TESIS DE LA UNIVERSIDAD DE ZARAGOZA

2018 112

María Sebastián Valverde

The action mechanism of prokaryotic FAD synthetases as a potential drug target for the treatment of bacterial infections

Departamento
Bioquímica y Biología Molecular y Celular

Director/es
MEDINA TRULLENQUE, MILAGROS

ISSN 2254-7606

Prensas de la Universidad
Universidad Zaragoza

ISSN 2254-7606

Universidad Zaragoza
1542

Tesis Doctora

THE ACTION MECHANISM OF PROKARYOTIC FAD SYNTHETASES AS A POTENTIAL DRUG TARGET FOR THE TREATMENT OF BACTERIAL INFECTIONS

Autor

María Sebastián Valverde

Director/es

MEDINA TRULLENQUE, MILAGROS

UNIVERSIDAD DE ZARAGOZA

Bioquímica y Biología Molecular y Celular

2018

Abstract 1

Resumen 7

Chapter I:

Introduction 13

1. The need of new antibacterial targets 15

1.1. From the beginnings to the golden era in the development of antibiotics 15

1.2. The resistance era put in check our effectiveness against pathogens 16

1.3. What makes a drug target good? 17

1.4. Proteins involved in flavins synthesis are promising drug targets 18

2. Flavins and flavoproteins: past, present and properties 20

2.1. A brief history of flavins and flavoproteins 20

2.2. Flavins are heterocyclic molecules 21

2.3. Flavins exhibit versatile redox properties 23

2.4. Flavins show useful spectroscopic properties 24

2.4.1. Absorption in the UV depends on the redox state *24*

2.4.2. Flavins are fluorescent compounds *26*

2.5. Biosynthesis of FMN and FAD in different organisms 26

3. FMN and FAD biosynthesis in different types of organisms 27

3.1. Prokaryotes own bifunctional FAD Synthetases 30

3.2.The FAD Synthetase from *Corynebacterium ammoniagenes* is the best characterized member of the family 32

3.2.1. Kinetics of CaFADS and interaction with substrates and products *33*

3.2.2. The CaFADS is organized in two independent modules *35*

3.2.3. Notable conformational changes occur during the CaFADS RFK catalytic cycle *42*

3.2.4. CaFADS can be organized into a dimer of trimers *46*

3.2.5. Binding of ligands induces oligomerization in CaFADS *49*

3.3. Other prokaryotic FADSs 51

3.3.1. The FADS from Streptococcus pneumoniae: SpnFADS *51*

3.3.2. The FADSs from Listeria monocytogenes and Mycobacterium tuberculosis *54*

3.4. Bacterial diseases needing new efficient treatments 56

3.4.1. Streptococcus pneumoniae and pneumonia *56*

3.4.2. Mycobacterium tuberculosis and tuberculosis *60*

3.5. *Ca*FADS, *Spn*FADS and *Mt*FADS as drug targets 65
4. Objectives **67**

Chapter II:

Materials and Methods **69**

1. General techniques in Molecular Biology **71**
1.1. Production of thermo-competent cells 71
1.2. Transformation of thermo-competent cells through heat shock 71
1.3. Isolation of plasmid DNA 72
2. Production of the recombinant *Ca*FADS and its variants **72**
2.1. Over-expression of *Ca*FADS and its variants 72
2.2. Purification of *Ca*FADS and its variants 73
2.2.1. Preparation of the crude extract *73*
2.2.2. Fractionation with ammonium sulphate *73*
2.2.3. Phenyl-Sepharose affinity chromatography *73*
2.2.4. DEAE-Cellulose anionic interchange chromatography *74*
2.2.5. Size exclusion chromatography *74*
3. Production of Δ (1-182) *Ca*FADS **75**
3.1. Purification of Δ(1-182) *Ca*FADS 75
4. Production of *Spn*FADS **75**
4.1. Cloning and over-expression of *Spn*FADS 75
4.2. Purification of *Spn*FADS 76
4.2.1. Preparation of the crude extract *76*
4.2.2. His-trap affinity chromatography *76*
4.2.3. Cleavage of the His-Tag and His-trap/GS-trap chromatography *76*
5. Biophysical characterization of proteins **77**
5.1. Spectroscopic characterization 77
5.1.1. Absorption spectroscopy in the UV-visible *77*
5.1.2. Circular dichroism *77*
5.1.3. Analysis of the formation of flavin-FADS complexes through difference spectroscopy *78*
5.2. Analysis of the formation of quaternary organizations 79
5.2.1. Native electrophoresis *79*
5.2.2. Size exclusion chromatography *80*

5.2.3. Evaluation of the effect of substrates and products on the monomer-oligomer equilibrium *81*
5.3. Steady-state kinetic analysis of the RFK and the FMNAT activities 82
5.3.1. Qualitative study of the RFK, the FMNAT and the FADpp activities through Thin Layer Chromatography *82*
5.3.2. Quantitative analysis of the CaFADS riboflavin kinase (RFK) activity and determination of kinetic parameters through High Performance Liquid Chromatography (HPLC) *83*
5.3.3. Fluorometric characterization of the FMN adenylyl-transferase activity (FMNAT) of CaFADSs *87*
5.3.4. Analysis of the RFK and FMNAT activities of SpnFADS through HPLC *89*
5.3.5. Analysis of the FMNAT activity of SpnFADS using photorreduced FMN *90*
5.4 Kinetic study of the inhibition of the RFK activity of *Ca*FADS and *Spn*FADS by the products of the reaction 90
5.5. Pre-steady state kinetics: Stopped-flow spectrophotometry 92
5.5.1. Basis of the technique *92*
5.5.2. Determination of observed rate constants (k_{obs}) for different processes involving flavins and FADS *93*
5.5.3. Analysis of the data *94*
5.6. Determination of thermodynamic parameters for ligand binding to FADS through Isothermal Titration Calorimetry (ITC) 95
5.6.1. Basis of the technique *95*
5.6.2. Titration of FADS with a single ligand *96*
5.6.3. Titration of pre-formed binary FADS:ligand complexes *98*
6. Discovery of antibacterial drugs **100**
6.1. Activity-based high-throughput screening for *Ca*FADS 100
6.1.2. Identification of the activity inhibited by each of the primary HTS hits *101*
6.1.3. Determination of the potency of FMNAT hits *102*
6.1.4. Determination of the inhibition mechanism of selected in the FMNAT activity *102*
6.1.5 Thermodynamic characterization of binding of the selected FMNAT hits to CaFADS through ITC *103*
6.1.6. In-vivo determination of the antibacterial effect of the hits *104*

7. Statistical analysis of the data **105**
8. AFM measurements **105**
9. Crystallographic structures **105**
10. Culture of pathogenic microorganisms **105**
11. Software **105**

Chapter III:

Quaternary organization in a bifunctional prokaryotic FAD synthetase: Involvement of an arginine at its adenylyltransferase module on the riboflavin kinase activity **107**

1. Expression, purification and distribution profile of quaternary organizations for R66 *Ca*FADS variants **111**
2. Spectral properties of the R66 *Ca*FADS variants **115**
3. Effects of the mutations in the catalytic activities of *Ca*FADS **117**
4. Interaction parameters for *C*aFADS with flavins and ATP **119**
5. Crystal structure of the *Ca*FADS variants **125**
6. Discussion **126**

Chapter IV:

The trimer interface in the quaternary structure of the bifunctional prokaryotic FAD synthetase from Corynebacterium ammoniagenes **133**

1. Spectral properties of *Ca*FADS variants **137**
2. Size distribution of *Ca*FADS variants **140**
3. Effects of the mutations in the catalytic activities of *Ca*FADS variants **143**
4. *Ca*FADS variants interacting with flavins and ATP **145**
7. Crystal Structure of the *Ca*FADS variants **154**
6. Discussion **157**

Chapter V:

Kinetics and thermodynamics in the protein-ligand interactions in the riboflavin kinase activity of FAD synthetase from *Corynebacterium ammoniagenes* **161**

1. The RFK activity shows inhibition by the RF substrate as well as by the products of the reaction. **163**

2. Changes in flavin fluorescence upon binding allow studying the association and dissociation kinetics of flavinic ligands to the RFK module. 166

3. The thermodynamic diagram for the RFK-ligand interactions 170

4. Adenine and flavin nucleotide ligands cooperate in their binding to the RFK module 175

5. Discussion 177

Chapter VI:

The FAD synthetase from the human pathogen Streptococcus pneumoniae: a bifunctional enzyme exhibiting activity-dependent redox requirements 183

1. *Spn*FADS is purified free of flavin ligands 187

2. *Spn*FADS catalyzes the RFK, FMNAT and FADpp activities. 189

3. The reduced state of flavins is critical for the FMNAT activity but not for the RFK one. 189

4. *Spn*FADS does not bind oxidized flavins by itself 193

5. *Spn*FADS exists mainly as a monomer but other oligomeric states are populated during catalysis 196

6. Discussion 200

Chapter VII:

The RFK catalytic cycle of the FADS from *Streptococcus pneumoniae* 207

2. Fast kinetics in the pre-steady state RFK reaction of *Spn*FADS 213

3. Thermodynamics of the interactions of *Spn*FADS with its ligands 217

4. FLV and ANP ligands show cooperative effects in their binding to *Spn*FADS 221

5. Discussion 223

Chapter VIII:

Discovery of antimicrobial compounds targeting bifunctional FAD synthetases 231

1. Identification of Potential Inhibitors of the *Ca*FADS activities through HTS 235

2. Effect of the HTS hits on RFK and FMNAT activities of *Ca*FADS 235

3. The Inhibition Mechanisms of C24, C27 and C31 239

4. ITC constants for the *Ca*FADS interaction with C24, C27 and C31 245

5. Effect of the HTS hits on the RFK and FMNAT activities of *Spn*FADS 247

6. Effect of selected HTS hits on different bacterial cells 248
7. Discussion 249

Chapter IX:

General discussion 255

1. Quaternary organizations of bifunctional prokaryotic FAD synthetases 257
2. Catalytic cycles of *Ca*FADS and *Spn*FADS 259
3. Discovery of antibacterial drugs targeting bifunctional FADSs 261

Chapter X:

Conclusions 265

1. The FADS from *C. ammoniagenes* 267
2. The FADS from *S. pneumoniae* 268
3. Discovery of antibacterial compounds 269

Capítulo X:

Conclusiones 271

1. La FADS de *C. ammoniagenes* 273
2. La FADS de *S. pneumoniae* 274
3. Desarrollo de nuevos compuestos antibacterianos 275

Bibliography 277

Abbreviations 293

Abstract

Bacterial FAD synthetases (FADS) are bifunctional and bimodular proteins that carry out the synthesis of the essential cofactors FMN and FAD from Riboflavin (RF,vitamin B2). These proteins are organized in two almost independent modules, each of which performs one of the activities that lead to FMN and FAD synthesis. The C-terminus module transforms RF into FMN through its riboflavin kinase activity (RFK), while the N-terminus module catalyzes the FMN adenylyltransferase activity (FMNAT) that transforms FMN into FAD. Having into account the essential character of the FMN and FAD flavinic cofactors, and the differences between prokaryotic FADSs and the corresponding human enzymes (especially between the FMNAT module of the bacterial proteins and mammalian enzymes that transform FMN into FAD), these enzymes appear as potential drug target. Thus, these bifunctional proteins are worthy of being studied in detail, with the objective of shedding light on their catalytic cycles, and on their regulatory strategies, focusing on the dissimilarities between different members of the family.

In that way, in the present thesis we have tackled three main projects:

- The study of the structural determinants that modulate the oligomerization tendency of the FADS from the organism *Corynebacterium ammoniagenes* (*Ca*FADS). During its catalytic cycles, *Ca*FADS stabilizes different oligomeric assemblies, being of especial relevance the formation of a hexamer formed by a dimer of trimers. The head to tail disposition that the protomers adopt within such structure, suggests an active role of the dimer of trimers in channeling the FMN product from the RFK active site to the FMNAT one, to be subsequently transformed into FAD. To demostrate this hypothesis we produced and characterized point mutants in positions located in the interface between protomers. The studied residues apparently stabilized the dimer of trimers establishing salt bridges, Van der Waals contacts, or hydrophobic interactions with residues located at the other module of a neighboring protomer. Our results revealed that all the mutated variants were active and able to stabilize quaternary organizations, although many of them presented altered RFK and FMNAT activities, as well as ligand binding parameters and oligomerization tendency. Special attention requires the fact that mutations located at the RFK module altered the FMNAT activity and *vice versa*. These results only can be explained in the context of the dimer of trimers, where residues of different modules, which are very distant in the monomer, are in close contact within the trimer. These

results validate our hypothesis about the formation of oligomeric structures during the catalytic cycles of *Ca*FADS, where the protomers might adopt a head to tail disposition. Additionally, our study allows inferring the role that specific residues have in the RFK and FMNAT catalytic cycles of this enzyme.

- Comparative characterization of the RFK and FMNAT catalytic cycles of the FADSs from the organisms *C. ammoniagenes* and *Streptococcus pneumoniae* (*Ca*FADS and *Spn*FADS, respectively). Despite the overall similarities between bacterial FADSs, enzymes from different organisms display important behavioral differences. The study of such differences might provide us with the suitable tools to design species-selective compounds, able to neutralize a specific organism through the selective inhibition of its FADS without affecting the flora of the host. That is the case of *Ca*FADS and *Spn*FADS, which show great structural homology but important dissimilarities in their activities. Thus, we have addressed a first functional characterization of *Spn*FADS, identifying the three main differences of this protein regarding *Ca*FADS. Thus, contrary to *Ca*FADS, *Spn*FADS i) does not stabilize the dimer of trimers, ii) its FMNAT activity requires strong reducing conditions and iii) its RFK activity is not inhibited by excess of the RF substrate. Furthermore, a more detailed study of the RFK activity of both enzymes allowed us to identify the thermodynamic and kinetic determinants responsible of such differences. The integration of our data, and its interpretation in the context of the available crystallographic structures, bring to light the differential regulatory strategies adopted by these two enzymes.
- Development of new antibacterial drugs targeting bifunctional FADSs. Due to the emergence during the last decades of bacterial resistant strains, the need to find new antibacterial targets and drugs against them is a fact. In that way, because of their essential nature, and other good characteristics, we propose prokaryotic FADSs as exploitable targets for the development of new antibacterial drugs. In this work, we have optimized a protocol do identify potential inhibitors of these enzymes, using as model *Ca*FADS, and we have utilized this methodology to identify broad-spectrum or species-selective compounds. Our methodology starts with the identification of potential inhibitors using an activity-based high-throughput screening protocol, and the subsequent identification of the affected activity. The best inhibitors of the FMNAT activity (they are more probable to have no effect on the mammal proteins) were further characterized, and their inhibition mechanisms identified. Concurrently,

the effect of the hits of the screening was tested in different bacterial strains. In this project, we have identified promising compounds that could act either as selective drugs against FADS from a specific organism, or as broad-spectrum inhibitors.

Resumen

Las FAD sintetasas bacterianas (FADS) son enzimas bifuncionales y bimodulares cuya función es producir los cofactores esenciales FMN y FAD a partir de Riboflavina (RF o vitamina B2). Estas proteínas se organizan en dos módulos casi independientes, cada uno de los cuales lleva a cabo una de las actividades mediante las cuales se sintetizan FMN y FAD. El módulo C-terminal transforma RF en FMN mediante una actividad riboflavin quinasa, mientras que el módulo N-terminal cataliza la actividad FMN:adenililtransferasa que transforma el FMN en FAD. Debido al carácter esencial de los cofactores FMN y FAD y a las diferencias entre FADSs bacterianas y las correspondientes enzimas de mamíferos (sobre todo entre el módulo FMNAT de las enzimas bacterianas y las enzimas que transforman FMN en FAD en mamíferos), estas enzimas son potenciales dianas terapéuticas. Por este motivo, merece la pena profundizar en el estudio de las FADs bacterianas, en la comprensión de sus ciclos catalíticos y de sus estrategias regulatorias, centrándonos en las diferencias entre diferentes miembros de esta familia.

Por lo tanto, durante el desarrollo de la presente tesis doctoral hemos abordado los siguientes proyectos:

- Estudio de los determinantes estructurales que modulan el equilibrio de oligomerización de la FADS del organismo *Corynebacterium ammoniagenes* (*Ca*FADS). *Ca*FADS estabiliza durante sus ciclos catalíticos distintos ensamblados oligoméricos, siendo especialmente relevante la formación de un hexámero compuesto por un dímero de trímeros. En esta estructura los protómeros adoptan una disposición cabeza-cola, lo que sugiere que el dímero de trímeros podría tener un papel activo en la canalización del FMN desde el sitio RFK hasta el sitio FMNAT, donde será transformado en FAD. Para validar esta hipótesis, producimos y caracterizamos mutantes puntuales localizados en la interfase entre protómeros. Aparentemente, los residuos mutados estabilizaban el dímero de trímeros mediante la formación de puentes salinos, interacciones de Van der Waals o interacciones hidrófobas con residuos localizados en el módulo opuesto del protómero adyacente en cada trímero. Nuestros resultados revelaron que todas las variantes eran activas y capaces de estabilizar estructuras cuaternarias, aunque la mayoría de ellas muestran alteradas sus actividades RFK y FMNAT, así como los parámetros de interacción con los ligandos y la tendencia a la oligomerización. Mención especial requiere el hecho de que mutaciones localizadas en el módulo RFK modulaban la actividad

FMNAT y *viceversa*. Estos resultados sólo pueden explicarse en el marco del dímero de trímeros, en el que residuos de diferentes módulos están en estrecho contacto. Estos resultados validan la hipótesis de la formación de estructuras oligoméricas, en las que los protómeros adoptan una disposición cabeza-cola, durante los ciclos catalíticos de *Ca*FADS. Además, nuestros estudios permiten determinar el papel de residuos concretos en las actividades RFK y FMNAT de esta enzima.

- Estudio comparativo de los ciclos catalíticos RFK y FMNAT de las FADSs de los organismos *C. ammoniagenes* y *Streptococcus pneumoniae* (*Ca*FADS y *Spn*FADS, respectivamente). A pesar de las similitudes generales entre FADSs bacterianas, enzimas de diferentes organismos muestran importantes diferencias funcionales. El estudio de estas disparidades puede proporcionar las herramientas adecuadas para el diseño de compuestos selectivos de especie, que sean capaces de neutralizar un organismo específico mediante la inhibición selectiva de su FADS, sin afectar la flora del huésped. Este es el caso de *Ca*FADS y *Spn*FADS, que muestran gran homología estructural pero importantes diferencias en sus actividades. En este proyecto hemos llevado a cabo una primera caracterización funcional de *Spn*FADS, identificando tres importantes diferencias respecto a *Ca*FADS. De este modo y contrariamente a *Ca*FADS, *Spn*FADS i) no estabiliza el dímero de trímeros, ii) su actividad FMNAT requiere condiciones reductoras fuertes, y iii) la actividad RFK de *Spn*FADS no muestra inhibición por el sustrato RF. Asimismo, un estudio más detallado de la actividad RFK de ambas enzimas nos permitió identificar los determinantes cinéticos y termodinámicos responsables de las citadas diferencias. La integración de nuestros datos experimentales y su interpretación en el marco de las estructuras cristalográficas disponibles, ha arrojado luz sobre las diferentes estrategias reguladoras adoptadas por estas dos enzimas.
- Desarrollo de nuevos fármacos antibacterianos contra FADSs bifuncionales. Debido a la irrupción durante las últimas décadas de cepas bacterianas resistentes a antibióticos, la necesidad de nuevas dianas terapéuticas antibacterianas, así como de fármacos dirigidos contra ellas ha quedado manifiesta. De este modo, y debido a su carácter esencial, junto a otras características deseables, proponemos a las FADS procariotas como dianas terapéuticas explotables durante el proceso de búsqueda de nuevos antibióticos. En este proyecto hemos optimizado un protocolo para la identificación de potenciales inhibidores de estas enzimas, utilizando como modelo *Ca*FADS. Posteriormente hemos utilizado esta metodología para identificar

compuestos que podrían ser utilizados como drogas de amplio espectro o selectivas de especie. Nuestro protocolo comienza con la identificación de potenciales inhibidores mediante un cribado de alto rendimiento, basado en las actividades enzimáticas de la proteína y la consiguiente identificación de la actividad inhibida. Los mejores inhibidores de la actividad FMNAT (ya que es más probable que estos compuestos no afecten a las enzimas de mamíferos) fueron estudiados más detalladamente y sus mecanismos de inhibición determinados. Paralelamente, se comprobó el efecto bacteriostático de los compuestos identificados mediante el cribado en diferentes cepas bacterianas. En este proyecto hemos identificado compuestos prometedores que podrían usarse como inhibidores selectivos de la FADS de un organismo en concreto, y otros que podrían desarrollarse como fármacos de amplio espectro.

Chapter I

Introduction

1. The need of new antibacterial targets

1.1. From the beginnings to the golden era in the development of antibiotics

Antibiotics are chemical substances produced by various microorganisms and fungi (or its synthetic derivatives) that are able to kill or to inhibit the growth of bacteria and other microorganisms.

It is thought that antibiotics were used for the first time in China, more than 2500 years ago, where it was known that the application of moldy curd from soybean improved some kind of infections. Nevertheless, principles of antibiosis were not established until the 19th century, in 1877, when Louis Pasteur and Robert Koch reported the competitive inhibition of *Bacillus anthracis* growth by another bacillus [1, 2]. Twenty years later, in 1897 Ernest Duchesne discovered the penicillin while he was working with fungi from the *Penicillum* genus, although his discovery was unnoticed by the scientific community [3]. The next step in the antibiotics development took place in 1909, when Paul Ehrlich synthetically produced the compound arsphenamine and described its use in the treatment of syphilis [4]. One of the most important facts in the antibiotics development, came in 1929 from the hand of Alexander Fleming, who published in the "British Journal of Experimental Pathology" his findings about a substance produced by fungi of the genus *Penicillum,* that was able to inhibit the growth of the bacteria *Staphylococcus aureus* [5]. Unfortunately, Fleming failed in his attempts to isolate the so-called penicillin, and it was not until ten years later that Ernst Chain and Howard Walter Florey achieved to purify a form of this compound [6]. Their studies led them to win, together with Fleming, the Nobel Price in 1945. This β-lactam antibiotic was among the first medications effective against different bacterial infections caused by *Staphylococcus* and *Streptococcus*. The importance of this drug was capital during the Second World War, where the War Production Board did a great effort drawing a plan for the distribution of penicillin to Allied troops in Europe [7]. In 1939 René Dubos isolated gramidicin [8], one of the first commercial antibiotics that was also used during the Second World War. Since 1943 the use of antibiotics has become widespread for the treatment of different bacterial infections, being most of them developed during the so-called "antibiotic golden age".

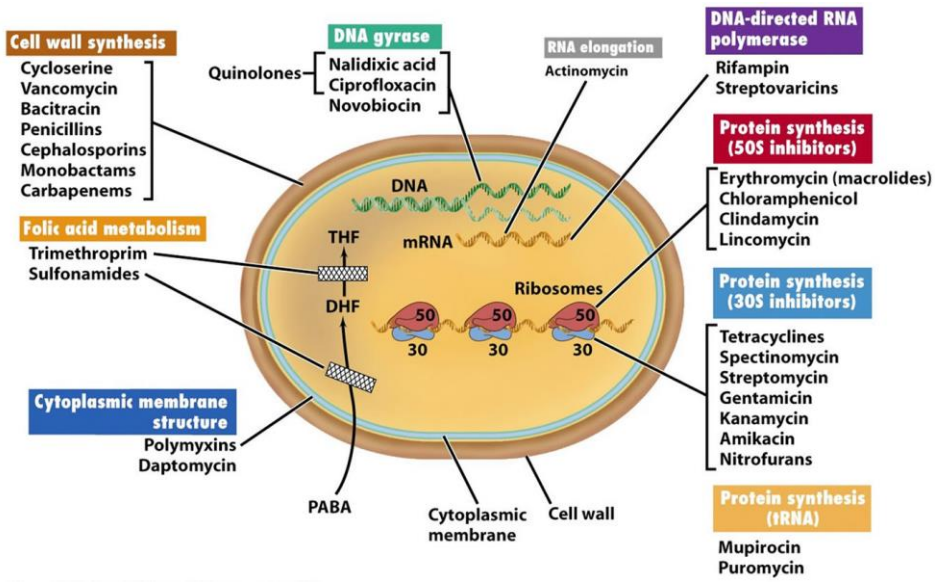

Figure 1.1. Action mechanisms of different types of antibiotics grouped according to their target. Figure from [9].

Nowadays, in rough outline, antibiotics can be classified attending to their targets [9]. In that way, we can distinguish among; i) antibiotics, such as penicillin and all generations of cephalosporins that affect the synthesis of the bacterial wall, specifically inhibiting the peptidoglycan synthesis [10], ii) those that alter the stability of the cellular membrane acting as detergents, being gramidicin an example of these drugs, iii) substances as actinomycin or sulphamides that prevent the synthesis of nucleic acids or proteins through the inhibition of the DNA polymerase or the nitrogenous bases synthesis, and iv) antibiotics that distinctivaly bind to the 30S or the 50S subunits of the bacterial ribosome, inhibiting the synthesis of proteins. To this last group belong the tetracyclines and the aminoglycosides (Fig. 1.1).

1.2. The resistance era put in check our effectiveness against pathogens

Bacteria always develop the molecular tools to acquire resistance. Thus, after the antibiotic golden era it came the resistance epoch, as a result of the indiscriminate use of antibiotics to treat human and animal infections, as well as in the agriculture (Fig. 1.2). These conditions have produced the mobilization of resistance elements in bacterial populations, and their capture by pathogens previously sensitive to antibiotics. Bacteria have acquired resistance to drugs through three main mechanisms [11]; i) the sequential capture of resistance genes through the mobilization and the horizontal transfer from environmental sources, ii) the over-

activation of intrinsic resistance mechanisms as efflux pumps [12], or the overexpression of the enzymes inactivated by antibiotics [13], and iii) the freezing of polymorphisms in antibiotic target genes that neutralize the effects on fitness of the drug-resistance mutations [14]. Due to the irruption of multidrug resistant pathogens, which are resistant to most or even all the known antibiotics, we are losing our ability to control infections using these drugs, and consequently, we have reached the post-antibiotic era (Fig. 1.2) [11].

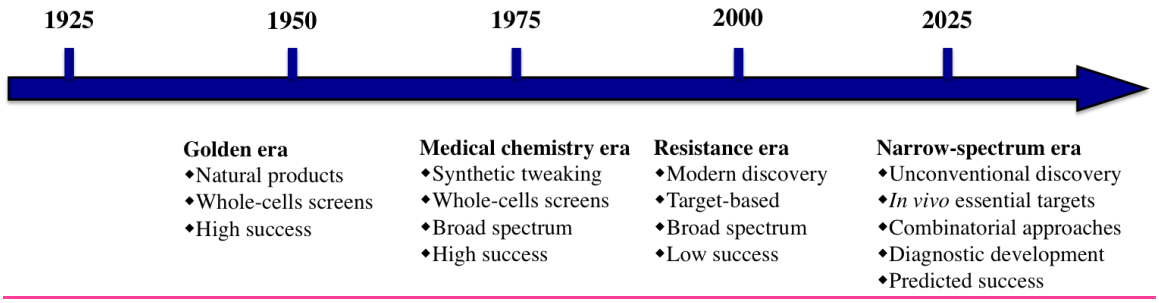

Figure 1.2. Timeline of the past and future of antibiotics development. The guidelines leading the research during each period of time are indicated, as also the efficacy of the developed drugs.

1.3. What makes a drug target good?

Since we have lost the potential to fight multidrug resistant pathogens using the available antibiotics, we need to elaborate new antibacterial strategies. The first step in the discovery of new drugs is the identification of good antibacterial targets. Therefore, first of all, the characteristics of good antimicrobial drug targets have to be established.

1) The target has to be involved in metabolic pathways that provide essential molecules for the survival of the pathogen. The inhibition of the target must interrupt the pathway, which finally leads to the death of the pathogen.

2) No alternative pathway must supply the metabolic route blocked by the inhibition of the target.

3) The drug target should have a low mutation rate. This feature hinders the appearance of resistances.

4) To favor the specificity of the drug and to avoid side effects in the host, the pathogen target protein must differ as much as possible from those in other microbes and in the host.

5) A 3D-structure of the target protein, or of a close homologous protein, should be available for druggability (capacity of a drug to bind the target with high affinity) assessment.

6) The target should have a favorable 'assayability' (capacity to be easily assayed) enabling high throughput screening.

7) Additionally, favorable predictions of potential side effects must be considered.

1.4. Proteins involved in flavins synthesis are promising drug targets

FMN and FAD are biomolecules that act as cofactors of a huge quantity of flavoproteins and flavoenzymes, which execute essential functions in all kind of organisms. Some of the processes that involve flavoproteins are, among others, protein folding [15], electron transport in the respiratory and photosynthetic chains, β-oxidation of fatty acids [16], nucleotide synthesis [17] and signal transduction during apoptosis [18] (Fig. 1.3). The lack of FMN and FAD leads to the accumulation of unfolded apoproteins, which are unable to perform their functions, and finally to the death of the organism. Regarding the points previously indicated, the synthesis of FMN and FAD perfectly fits the requirements of good antibacterial targets since;

1) The lack of FMN and FAD prevents from the very beginning all the pathways that involve flavoproteins. Since most of these processes are essential for survival, the final consequence of the inhibition of the flavins syntheses is cell death.

2) In bacteria there is a unique pathway for FMN and FAD synthesis that, in general, involves a single bifunctional protein, the prokaryotic FAD synthetase (FADS).

3) Enzymes hold a strict relationship between their structure and their function. Therefore, big insertions or deletions alter the protein function, while punctual mutations usually have two effects depending on their location. On the one hand, if the mutated residue is at the active site or indirectly affects its conformation, it is highly probable that the protein will lose the capacity to perform its function. On the other hand if the mutations are located in peripheral regions, the enzymatic efficiency will not be affected unless the mutation produces big structural rearrangements. Having into account that most of drugs that target enzymes affect their active sites, enzymes in general, and FADSs in particular, are less prone to generate resistances, since mutations causing resistance also might compromise the protein function.

4) The synthesis of FMN and FAD differs between mammals and prokaryotes. Mammals own two independent enzymes (a FMN adenylyl transferase and a riboflavin kinase), while bacteria have the single bifunctional (and bimodular) FADS. Although eukaryotic riboflavin kinases are structurally similar to the module that performs the same activity in bacterial FADSs, the prokaryotic module involved in FAD production is completely different from the corresponding eukaryotic enzyme. Therefore, drugs that target bacterial FADSs, and specifically their FMN adenylyltransferase domain, might not affect the mammalian homologous proteins, which would reduce the side effects caused by these drugs.

5) The crystallographic structures of some FADSs (those from the organisms *Thermotoga maritima* (*Tm*FADS), *Streptococcus pneumoniae* (*Spn*FADS) and *Corynebacterium ammoniagenes* (*Ca*FADS), PDBs 1T6Y, 3OP1 and 2X0K, respectively) are available, which facilitates the evaluation of their druggability.

6) FADSs show great assayability, since their activities can be easily followed registering the flavin fluorescence of substrates and products (see section 2.4 of this chapter). Hence, activity based high-throughput screenings can be used to identify potential drugs.

Consequently, once the potentiality as drug target of the FMN and FAD biosynthesis pathway has been set, this system must be understood in detail.

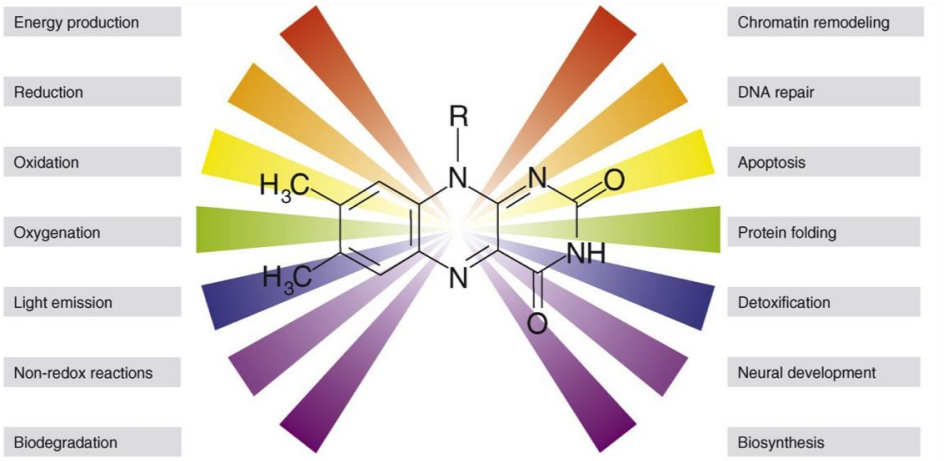

Figure 1.3. Overall structure of flavins and some biologically relevant processes they are involved in. Figure from [19].

2. Flavins and flavoproteins: past, present and properties

2.1. A brief history of flavins and flavoproteins

Nowadays, we know that flavins constitute a family of yellow compounds structurally derived from the 7,8-dimethyl-10-alkylisoalloxazine (Fig.1.3). However, these important compounds were unnoticed until 1897, when the English chemist Wynter Blyth observed a bright yellow pigment that could be isolated from cow milk [20]. Some years later, in the late 1920s and early 1930s, other yellow pigments were isolated from different sources and they were named lactoflavin, ovoflavin or hepatoflavin according to their founts. Those pigments were identified as a molecule that belongs to the vitamin B complex, the B_2 vitamin. In 1934 and 1935, respectively, Richard Kuhn and Paul Karrer published the structure of that vitamin and they chemically synthesized it [21, 22]. All previous names given to the molecule were then substituted by riboflavin (RF), regarding the ribityl side chain and the yellow color of the conjugated ring system (*flavus* in latin means yellow).

At the same time, in 1933, Otto Warburg during his research about the respiratory chain, isolated the "old yellow protein" which catalyzed the NADPH oxidation by oxygen [23], discovering in that way the first flavoprotein. Two years later Hugo Theorell observed that through precipitation, this yellow protein yielded two different fractions; a white precipitate and a yellow supernatant. Separately, neither the precipitate nor the supernatant were able to catalyze the NADPH oxidation [24]. The yellow fraction showed the same spectroscopic properties as RF, but RF did not restore the activity of the flavoprotein. Finally, Theorell solved the mystery when he realized that the flavin differed from RF in a phosphate group, attached to the terminal hydroxyl of the ribityl chain [24]. Today, this flavin is known as flavin mononucleotide or FMN. The main achievement of the Theorell´s work was that it demonstrated by the first time, and from a biochemical approach, the role of RF as a vitamin, since it acted as a cofactor during the enzymatic catalysis. Few years later Hans Krebs, during his studies about the amino-acids deamination, discovered another important flavoprotein; the D-amino acid oxidase [25]. As Theorell did in 1935, Warburg and Christian separated the apoprotein and the flavin cofactor, identifying this latter one as the flavin adenine dinucleotide or FAD, obtained as a product of the condensation of FMN and AMP [26]. FAD was synthesized years later, in 1954, in Cambridge by Christie and Todd [27].

Since its discovery in 1933 [23] until the date, lots of flavoproteins have been identified and characterized [28-34]. That fact together with the huge quantity of different processes they are involved in, evince the biological importance of these proteins.

2.2. Flavins are heterocyclic molecules

Flavins are heterocyclic compounds that contain an isoalloxazine ring, and more specifically, the flavins that we can find in living organisms derive from the 7,8-dimethil-isoalloxazine (Fig. 1.4).

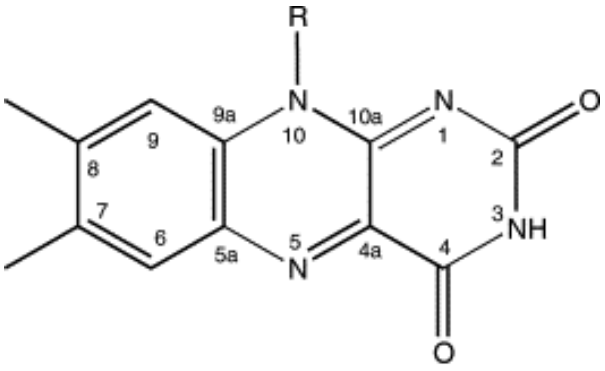

Figure 1.4. Chemical structure and atomic numbering of the 7,8-dimethil-isoalloxazine ring. R determines the nature of the flavin: R=CH3, lumiflavin; R=ribityl, riboflavin (RF); R=ribityl-5′-phosphate, flavin mononucleotide (FMN); R=ribityl-(9-adenosyl)-pyrophosphate, flavin adenine dinucleotide (FAD).

The oxidized flavin isoalloxazine ring is expected to be planar and shows two faces, named the *Re* and the *Si*. The *Re* face is that at the front when the benzene ring is at the left and N_{10} at the bottom of the molecule, being the *Si* face the back one in this position (Figure 1.5) [35].

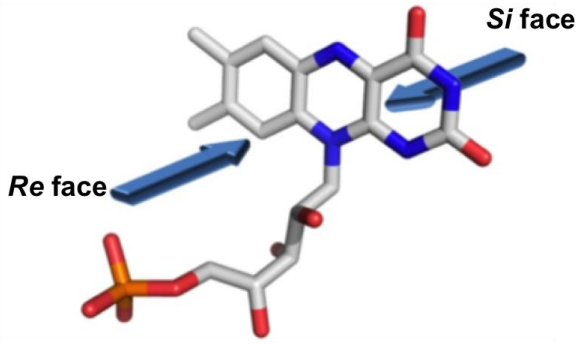

Figure 1.5. *Re* and *Si* faces of the isoalloxazine ring in FMN.

Among all the flavins that we can find in biological systems, there are three with especial relevance; RF or vitamin B_2 (7,8-dimethil-10-(1´-D-ribityl) isoalloxazine) and their derivatives, FMN or flavin mononucleotide (riboflavin 5´phosphate) and FAD or flavin adenine dinucleotide (Fig. 1.6).

Even though there is a broad distribution of flavins in the tissues, just a little amount stay as free flavins, being found much more frequently acting as cofactors and prosthetic groups of flavoproteins, which are involved in most cases in redox reactions (since FMN and FAD are able to accept or transfer one or two electrons at a time) [36-38]. Normally, FMN and FAD are not covalently bound to the protein, and the flavin-protein binding takes place mainly through the N(10)-ribityl side chain of the flavin [39]. For the vast majority of FAD-containing flavoproteins, the pyrophosphate moiety binds to the most strongly conserved sequence motif, indicating that pyrophosphate binding is an important determinant of molecular recognition [40]. In addition to their roles as cofactors, flavins can act as coenzymes of a family of oxidoreductases, named NAD(P)H:flavin-reductases, that catalyzed the FMN and FAD reduction, and exceptionally, also the reduction of RF by the nucleotide NAD(P)H [41, 42].

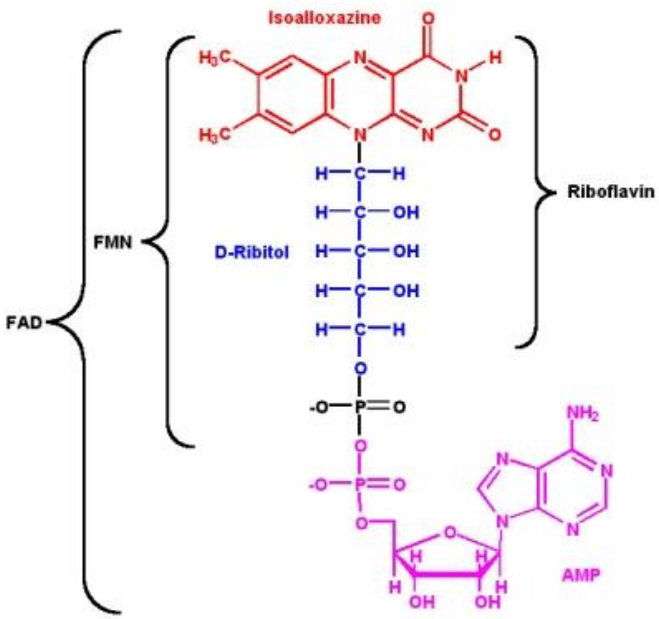

Figure 1.6. Chemical structure of the oxidized isoalloxazine ring (red) and of its three most biologically relevant derivatives; RF (with a ribityl chain attached to the N_{10}), FMN (formed through addition of a phosphate group to the 5´ carbon of the RF ribityl chain) and FAD (formed by condensation of FMN with a molecule of AMP).

2.3. Flavins exhibit versatile redox properties

One of the most important properties of RF, FMN and FAD, is their capacity to participate in redox reactions [43]. These flavins can interchange two electrons at a time, and additionally, under particular environments (as when are forming part of flavoproteins), also a single electron. In that way, they can act as intermediates, hitching reactions where one of the substrates can only accept or transfer one electron, and the other one needs to interchange two electrons at a time [36]. This valuable property is possible because flavins (within flavoproteins) can stabilize three different redox states; the oxidized form, the semi-reduced state or semiquinone (one electron reduction), and the fully two electrons reduced state or hydroquinone [44]. Consequently, flavoproteins can transfer just a single electron, a hydrogen atom or a hydride ion, being for this reason very versatile in terms of substrates modifications, and types of reactions in which they are involved. Additionally, flavins also show a pH-dependent equilibrium (Fig. 1.7) [45]. Nevertheless, all of the structures shown in figure 1.7 could not be found in physiological conditions, or within flavoproteins.

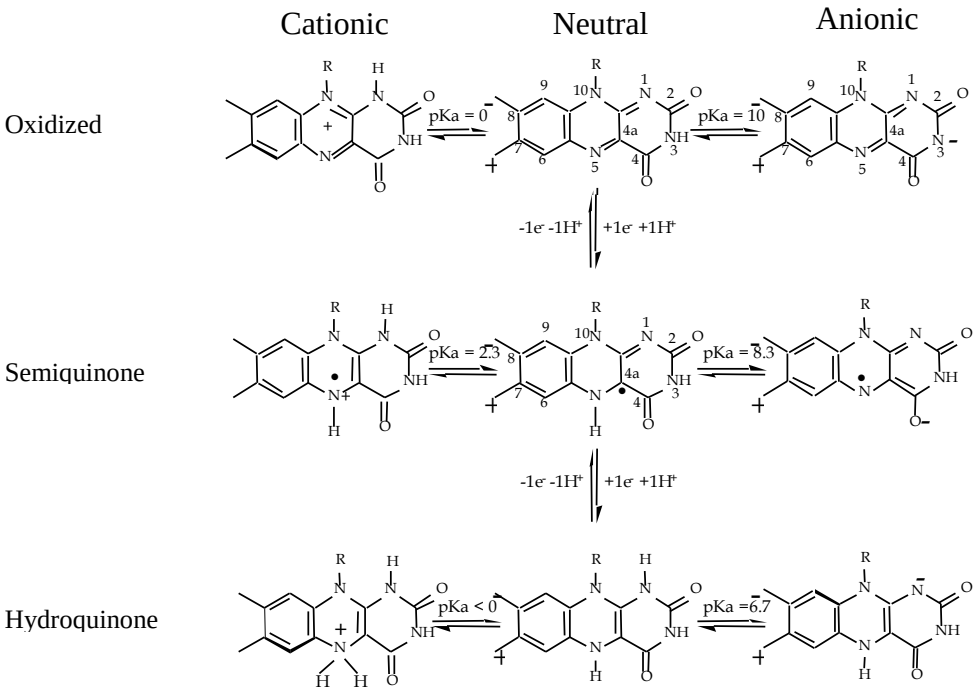

Figure 1.7. Redox states and acid-base equilibrium of the isoalloxazine ring. Figure modified from [44].

At pH 7.0 the oxidized state is stable against the oxygen, being the predominant form the neutral one. At neutral pH, the semiquinone state of the free flavin, which adds an electron with respect to the oxidized one [46, 47], is thermodynamically unstable, since only about 5% is stabilized as radical in a 50-50 mixture of the reduced and the oxidized forms [39]. The destabilization of the semiquinone state makes the reduction midpoint potential $E_{ox/sq}$ more negative than the $E_{sq/rd}$. For this reason, free flavins are only able to interchange two electrons at a time. Nevertheless, when flavins are part of flavoproteins, their midpoint redox potentials, which are both ~-200 mV for the free flavins [48], can be modified from -400 to +60 mV as a consequence of their isoalloxazine ring interaction with the protein [49]. For this reason, and depending on relative modulation of $E_{ox/sq}$ and $E_{sq/rd}$ values, some flavoproteins reach the stabilization of near to 100% of the semiquinone state. This is an interesting fact, because in these situations flavoproteins are able to mediate as intermediates in reactions where either one or two electrons are being transferred. Under physiological conditions and depending on the pH, the semiquinone state in flavoproteins can be found either in the anionic form, that presents red color or in the neutral blue one. Also under these conditions, the hydroquinone or reduced state of flavoproteins can only be found in the anionic and neutral forms [50]. Besides all these forms, electronic states where partial charge is transferred from or to one of the states previously described to a neighboring molecule can be found. They are known as charge-transfer states.

2.4. Flavins show useful spectroscopic properties

2.4.1. Absorption in the UV depends on the redox state

The absorption spectra of flavins are highly dependent on their redox state, since each form shows a particular electronic distribution. All oxidized flavins show high absorption in the UV and visible regions, with three maxima at wavelengths close to 265, 370 nm (band II) and 450 nm (band I) (Table 1.1, Fig. 1.8) [39]. The spectral shape is practically the same for RF and FMN, but shows little wavelength displacement and lower intensity for FAD, due to the formation of an internal complex between the isoalloxazine ring and the adenine of the molecule [51, 52]. The neutral semiquinone form exhibits a broad 500-650 nm band with a maximum around 589-600 nm, while the anionic semiquinone shows two maxima at 370 and 490 nm, and barely absorbs at wavelengths higher than 550 nm (Fig. 1.8) [53]. The

absorption of the bands I and II is bleached for the reduced flavins, that also present a shoulder around 290 nm (Fig. 1.8) [51].

Table 1.1. Position of the maxima and molar extinction coefficient for free oxidized flavins in 0.1 M phosphate pH 7.0. Data from [54].

	λ	ε ($mM^{-1}\cdot cm^{-1}$)	$\lambda_{band\ II}$	ε ($mM^{-1}\cdot cm^{-1}$)	$\lambda_{band\ I}$	ε ($mM^{-1}\cdot cm^{-1}$)
RF	266	32.5	373	10.6	445	12.5
FMN	266	31.8	373	10.4	445	12.5
FAD	263	38.0	375	9.3	450	11.3

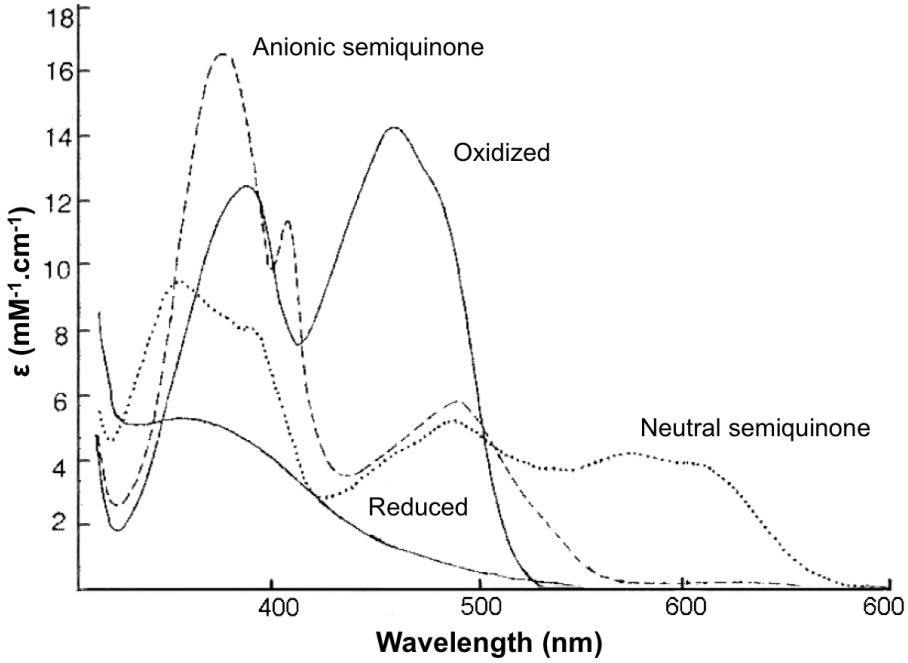

Figure 1.8. Characteristic absorption spectra of flavoproteins in different redox states. The completely reduced and oxidized forms are shown in solid lines, the neutral semiquinone in dotted line and the anionic semiquinone in dashed line. Figure modified from [39].

The absorption spectrum of flavins when forming part of flavoproteins, and that exhibited by the free flavins, are highly similar. Nevertheless, the protein environment usually induces small displacements in the position of the maxima and in their intensities, as well as the apparition of spectral shoulders. This makes the spectra of each flavoprotein unique.

2.4.2. Flavins are fluorescent compounds

Together with aromatic amino-acids, flavins are the most important fluorescent groups that can be found in proteins. The oxidized state of flavins exhibits a high quantum yield of fluorescence, being the maxima of absorption and emission around 440-450 and 525-530 nm respectively [55]. The quantum yield of fluorescence for RF and FMN at pH 7.0, is ten times higher than that of FAD. Once again, this effect is the result of the internal interaction between the isoalloxazine ring and the adenine group of the nucleotide (which quenches the fluorescence of the isoalloxazine ring). In aqueous solution this conformation is in equilibrium with the open fluorescent one [51, 52].

When FMN and FAD become part of flavoproteins their fluorescence can be moderately altered, completely disappear [56] or stay unaltered [57], depending on the manner in which the isoalloxazine ring gets allocated within the protein [51].

2.5. Biosynthesis of FMN and FAD in different organisms

Bacteria, fungi and plants have the ability to synthesize RF *de novo*, using five molecules of ribulose and one of GTP (Fig.1.9). Nevertheless, for some organisms, as animals, RF is a vitamin (vitamin B2) and they need to acquire it from the diet. Both the synthesis and the intake of RF are processes greatly regulated [58-60].

Independently on the endogenous or exogenous origin of RF, all the organisms show the ability to transform RF into FMN and FAD through two sequential reactions. Firstly, RF is phosphorylated to FMN by a riboflavin kinase activity (RFK, ATP:riboflavin 5´phosphotransferse, EC 2.7.1.26), which transfers a phosphate group from ATP to the C5´ ribityl chain (Eqn. 1.1). After the phosphorylation step, an ATP:FMN adenylyltransferase (FMNAT, EC 2.7.7.2) activity converts FMN into FAD (Eqn. 1.2).

$$RF + ATP \rightarrow FMN + ADP \qquad \text{Eqn. 1.1}$$

$$FMN + ATP \rightarrow FAD + PPi \qquad \text{Eqn. 1.2}$$

Although all organisms synthesize FMN and FAD from RF, they utilize different enzymes for that purpose.

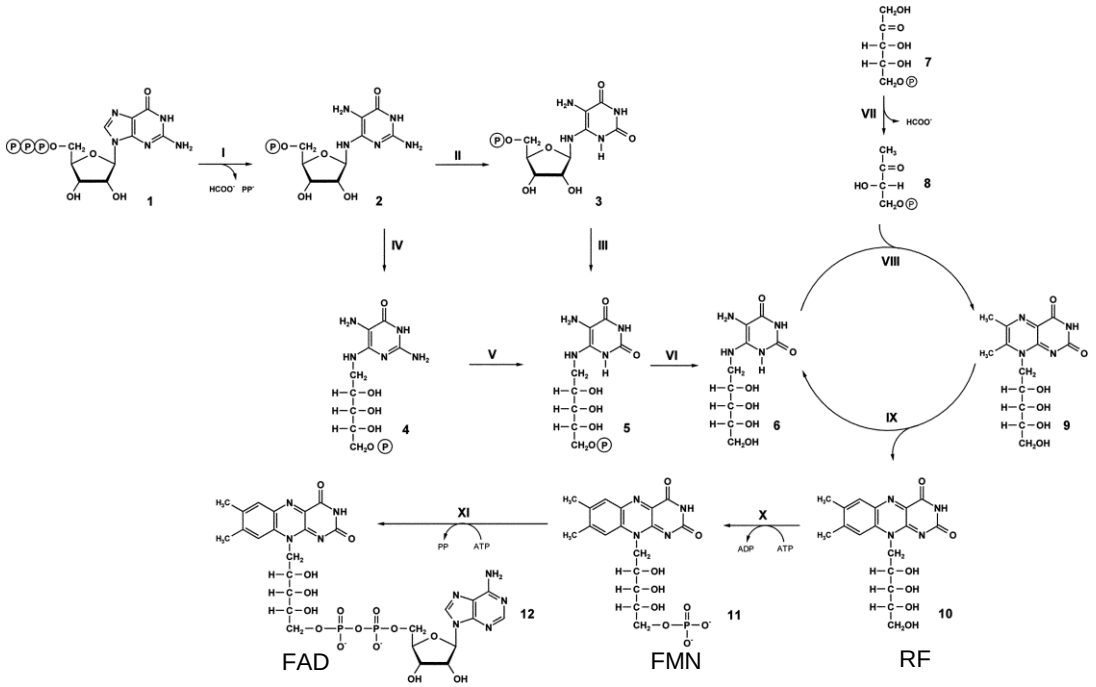

Figure 1.9. Pathway for FAD biosynthesis in prokaryotes. The enzymes involved in the metabolic route are: GTP cyclohydrolase II (I), 2,5-diamino-6-ribosylamino-4(3H)-pyrimidinone-5´-phosphate deaminase (II), 5-amino-6-ribosylamino-2,4(1H,3H)-pyrimidinone-5´-phosphate reductase (III), 5-Amino-6-ribitylamino-2,4(1H,3H)-pyrimidinedione phosphatase (VI), 3,4-dihydroxi-2-butanone-4-phosphate synthase (VII), 6,7-dimethil-8-ribityl-lumazine synthase (VIII), RF synthase (IX), RF kinase (X), FMN adenylyltransferase (XI). Eubacteria and plants produce RF through (II) and (III) while yeasts utilize path through (IV) and (V). The numbers indicate the following compounds: GTP (1), 2,5-diamino-6-ribosylamino-4(3H)- pyrimidinone-5´-phosphate (2), 5-amino-6-ribosylamino-2,4(1H,3H)-pyrimidinone-5´-phosphate (3), 5-Amino-6-ribitylamino-2,4(1H,3H)-pyrimidinedione-5´-phosphatase (5), 5-Amino-6-ribitylamino-2,4(1H,3H)-pyrimidinedione (6), ribulose-5-phosphate (7), 3,4-dihydrosi-2-butanone-4-phosphate (8), 6,7-dimethil-8-ribityl-lumazine (9), RF (10), FMN (11) and FAD (12). Figure modified from [61].

3. FMN and FAD biosynthesis in different types of organisms

Until some decades ago, the knowledge about the enzymes involved in FMN and FAD synthesis was relatively limited. Nowadays a great number of sequences of proteins that synthesize FMN and FAD is available, as well as the tridimensional structure of some of them. Comparative studies of these sequences, have allowed shedding light on some key aspects of the metabolism of flavins. In that way, it is now known that different organisms use dissimilar enzymes to perform the FMN and

FAD synthesis. Additionally, highly conserved consensus sequences, which might play essential roles during the catalysis, have been also identified.

Different organisms use distinct enzymes for FMN and FAD biosynthesis

Contrary to prokaryotes, yeasts, animals and, in general, non-photosynthetic eukaryotes, are unable to synthesize RF and they need to ingest it with diet [62, 63]. To transform RF into FMN and FAD, animals own two independent monofunctional enzymes; one catalyzes a RFK activity and the other a FMNAT one (Fig. 1.10). The first known eukaryotic gen codifying for a RFK activity (*FMN1*), was identified in *Saccharomyces cerevisiae*. This gen codifies for a membrane protein that shows sequences for its location in microsomes and in the inner mitochondrial membrane [64]. The first gen that putatively codified for a eukaryotic FMNAT was also identified in *S. cerevisiae*, in 1995. This protein was named as FAD1, and corresponds to a 35 kDa cytosolic protein [65]. After that, more eukaryotic RFKs and FADs have been identified. Sequence analyses revealed that monofunctional RKFs are ATP-dependent, and show greatly conserved the PTAN motif (Fig. 1.11) and a glutamic that acts as catalytic base. On their side, eukaryotic FMNATs belong to the A*denosine nucleotide α-hydroxilase-like* superfamily. Both proteins present different isoforms with mitochondrial and cytosolic locations [64, 66-68] (Fig. 1.10).

In plants the situation is more intricate, since additionally to the monofunctional RFK and FMNAT, two different bifunctional FAD synthetases have been found. One of them presents RFK activity in its C-terminus module, and hydrolase activity in its N-terminus one [69]. The other bifunctional enzyme shows a N-terminus module similar to prokaryotic FMNATs, and a shorter C-terminal module without the PTAN motif, that must perform a different activity but which is still unknown [70] (Fig. 1.10). These last proteins have been named as Plant-type FADSs. The monofunctional FMNATs and RFKs localize in the mitochondrion [71]. However, the location of the bifunctional enzymes with FMN hydrolase activity is still unknown, but they might be located in mitochondrion and chloroplast, since they have location sequences for those organelles.

Archaeas possess two monofunctional proteins. The RFK enzyme differs from the bacterial one in the nucleotide utilized as substrate, since contrary to other RFKs they are CTP-dependent. The archaeal FMNAT also belongs to the nucleotidyl-

transferase superfamily, although they do not present some of its characteristic motifs [72], and either ATP or CTP can be used as substrates.

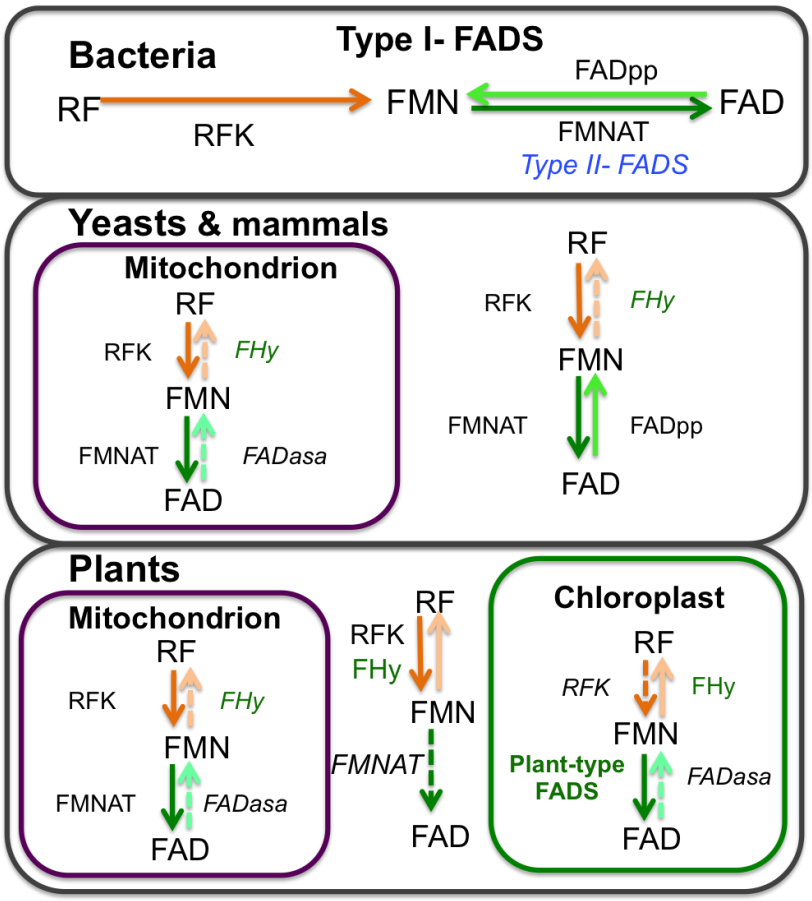

Figure 1.10. Distribution of the activities related to FMN and FAD synthesis in the subcellular locations of different organisms. Activities and enzymes shown in dot lines and italic, respectively, indicate that there are bioinformatics analyses that support the existence of the enzyme even though it has not been found experimentally. Activities in solid lines have been purified and characterized. Enzymes shown in black belong to the type I-FADS and those in green to the plant-type FADS. In addition to the type I-FADS, some bacteria are predicted to own a second type II-FADS (shown in blue). RFK (riboflavin kinase), FMNAT (FMN adenylyltransferase), FADasa (FAD hydrolase), FADpp (FAD pyrophosphorilase), FHy (FMN hydrolase). Figure modified from [73].

Most of bacteria possess bifunctional type-I FADSs, with a RFK module homologous to monofunctional eukaryotic proteins (that present the consensus PTAN motif and the catalytic glutamic residue) [74-76], and a FMNAT module different from mammalian eukaryotic FMNATs that belongs to the nucleotidyl-transferases superfamily [76, 77]. Additionally to the type-I FADS, a small group of bacteria also owns monofunctional enzymes with RFK and FMNAT activities, which

show sequence identity with the C-terminus and the N-terminus module, respectively, of bifunctional FADS [70, 78]. Finally, some bacteria, among them *Listeria monocytogenes*, *Lactobacillus plantarum* or *Oceanobacillus iheyensis*, besides the type-I FADS present another bifunctional protein that shows high sequence similitude with the previous one, but with a shorter RFK module that lacks the consensus PTAN motif [70]. These proteins have been named type-II FADS and even though their N-terminal domain is able to transform FMN into FAD, the function of the RFK module remains unknown [78, 79].

3.1. Prokaryotes own bifunctional FAD Synthetases

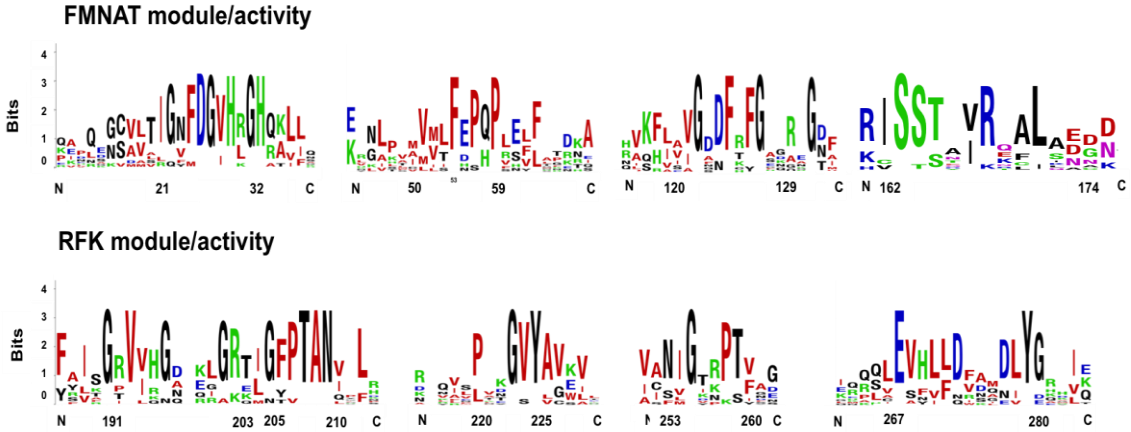

Figure 1.11. Primary structure of bifunctional Type I FADSs. Sequence logos for the bifunctional Type I FADS family consensus regions. The numeration of *Ca*FADS is used. The sequence logo was produced using the WebLogo server, http://weblogo.berkeley.edu [80].

Prokaryotic bifunctional proteins with RFK and FMNAT activities have been cloned and purified from bacteria. These type-I FADSs are organized in two different modules, each of them mainly related to one of the activities. The C-terminus module performs the RF phosphorylation, while the N-terminus one transforms FMN into FAD [74, 79, 81, 82]. The N-terminal FMNAT module of these FADSs presents several consensus sequences, GxFDGxHxGH and SS(T/S)x(I/V)R, which are also conserved in nucleotidyl-transferases, as well as own motifs FxP(H/Q)P and G(D/N)(F/Y/H)x(F/Y)G [76]. The C-terminus module of FADSs exhibits the several conserved consensus sequences, GxVxxGxxG, G(F/Y)PT(A/L/I/V)N, PxxG(V/I)(Y/F), PT(F/V/I), and (L/V/I)Ex(H/F/Y/N)x(F/L)(D/N)(F/W/Y)xx(D/N/E)(L/I/A/V)Y(G/D/N], as well as an invariant conserved acidic residue (Glu268 in

*Ca*FADS), which is proposed to act as catalytic base during the phosphorylation reaction. All these sequences are also conserved in eukaryotic RFKs [76].

The first tridimensional structure reported for a FADS was that from *Thermotoga maritima* (*Tm*FADS, PDB entry 1T6Y). In this 30 kDa protein, a single loop connects the two modules (Fig 1.12). The N-terminal module (residues 1-158) presents a characteristic nucleotide binding Rossman fold [83], while the C-terminus module (residues 158-293) folds into a β-barrel of six antiparallel β-strands, surrounded by 3 α-helixes perpendicularly oriented to the β-barrel [75]. The 3D structure does not show the disposition of some loops, probably because they are regions with great flexibility. Additionally, the crystallographic structure of the enzyme in complex with different ligands is available. This structure reveals that *Tm*FADS owns two adenine nucleotide binding sites (one in each module), and a single binding site for flavins located in the C-terminal module [74]. Nowadays, the structures of two additional bacterial FADSs are available; the FADSs from *Streptococcus pneumoniae* and *Corynebacterium ammoniagenes* (*Spn*FADS and *Ca*FADS, PDB entries, 3OP1 and 2X0K respectively), being *Ca*FADS the member of the family best characterized [70, 84-90].

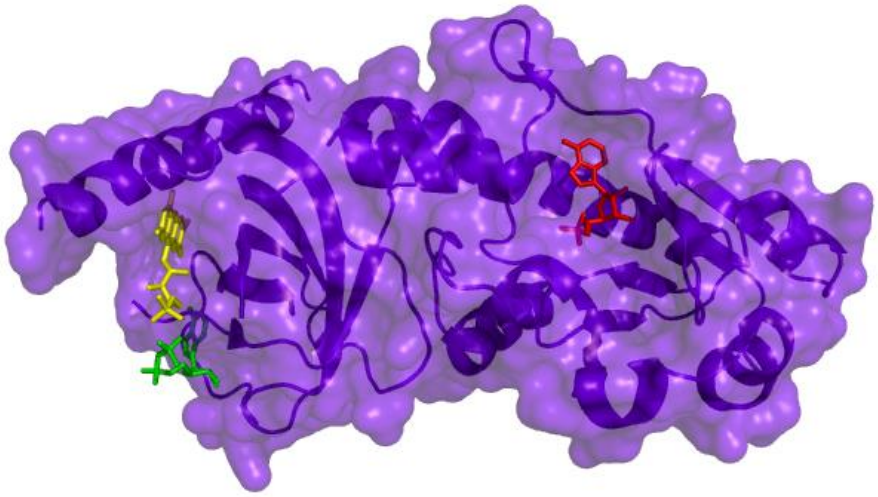

Figure 1.12. Overview of the crystallographic structure of the FADS from *T. maritima* (*Tm*FADS, PDB 1T6Y) in complex with FMN (yellow) and ADP (green) attached to the C-terminus module, and AMP (red) to the N-terminus domain.

3.2. The FAD Synthetase from *Corynebacterium ammoniagenes* is the best characterized member of the family

The FADS from *C. ammoniagenes* was described for the first time in 1976 as an enzyme that catalyzed the transformation of 5-deazariboflavin (5-dRF) into 5-deazaFAD (5-dFAD) [91]. However, it was not characterized until 1986, when Manstein and Pai achieved to purified it to homogeneity [82]. A single polypeptide chain of 338 residues constitutes the protein, which shows an apparent molecular weight of 38 kDa and an isoelectric point of 4.6. The *Ca*FADS catalyzes the RF phosphorylation in 5´ and the subsequent adenylylation of FMN, exhibiting wide specificity for flavin substrates. It seems that the important elements of flavins for binding to this enzyme are: the position 3 of the isoalloxazine ring, the existence of a hydroxyl group at 5´ and a substitution at position 7 [92, 93]. However, the protein is absolutely specific for ATP [82]. The phosphorylation reaction is irreversible while the adenylylation can be reverted to transform FAD into FMN in the presence of PPi (FADpp activity) [81] (Fig. 1.13).

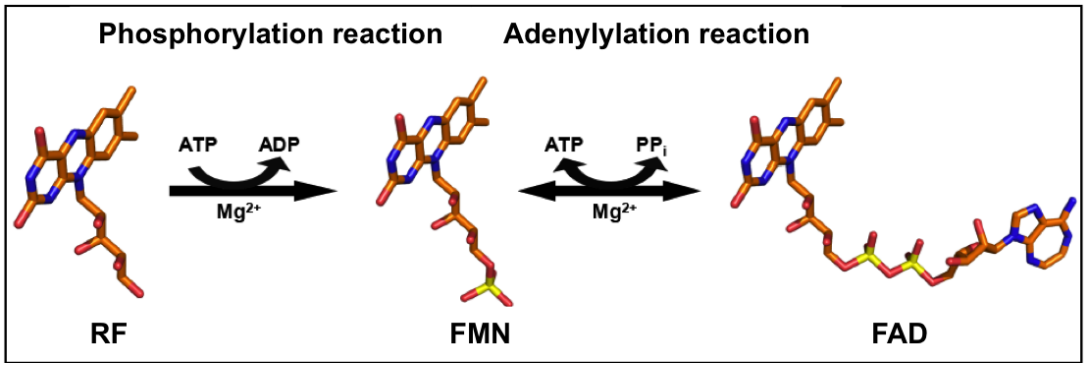

Figure 1.13. Reactions catalyzed by the *Ca*FADS.

The FMNAT reaction is $MgCl_2$ dependent, and it does not occur in the absence of the ion, while it was reported that the RFK activity can take place even in the absence of Mg^{2+} [82]. Nevertheless, the optimum Mg^{2+} concentration for each reaction differs, being 0.4 mM for the RFK activity [82] (0.75 mM according to [94]) and 10 mM for the FMNAT one. Consequently, through modification of the ion concentration either one reaction or the other one can be favored, since the RFK activity decreases at $MgCl_2$ concentrations higher than 0.8 mM [82]. The optimum pH and temperature were 7.8-8 and 35-37 ºC for the RFK reaction and 7.0-7.4, 37-40 ºC for the FMNAT one [94].

3.2.1. Kinetics of CaFADS and interaction with substrates and products

Kinetic parameters for the RFK and the FMNAT activities of CaFADS

Kinetic constants for the both RFK and FMNAT activities of *Ca*FADS have been determined [88]. For the RFK reaction, the enzyme shows different behaviors depending on the saturating substrate. At saturating ATP, the reaction rate is inhibited when the RF substrate concentration is higher than 7.5 µM (Fig. 1.14B), being the values reported (at 37ºC, in 20 mM PIPES, pH 7.0, 0.8 mM $MgCl_2$) for the Michaelis constant (K_m^{RF}), the inhibition constant (K_i) and the catalytic constant (k_{cat}) <13 µM, 4 µM and <302 min^{-1}, respectively. For this reason it is not possible to work under saturating RF conditions, therefore a RF concentration at which the protein shows the 80 % of it maximal velocity was selected for future characterizations (for those experiments that require a constant RF concentration). Under these conditions (5 µM RF) the protein shows a Michaelis-like kinetic profile when varying ATP, being the K_m^{ATP} and the k_{cat} values 13.7 µM and 68 min^{-1} respectively (Fig. 1.14A) [88].

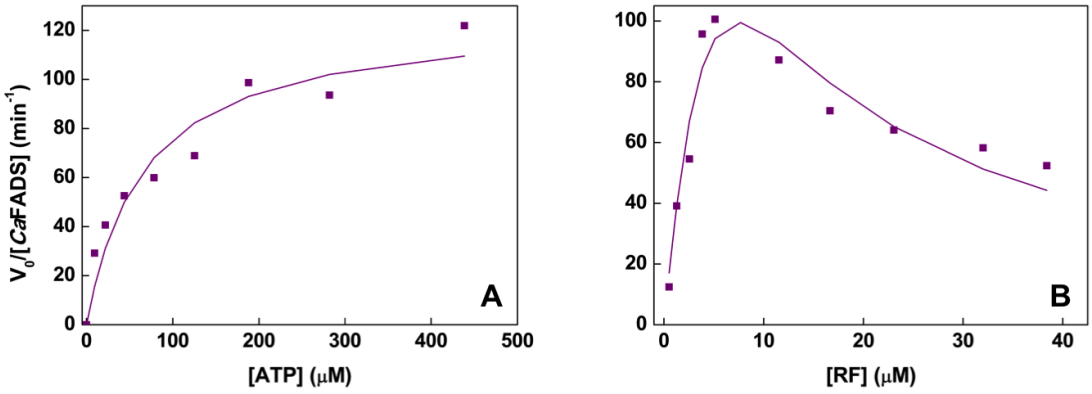

Figure 1.14. Steady state kinetic behaviors for the RFK reaction of *Ca*FADS (RF+ATP→FMN+ADP). (A) Reaction rates measured at 5 µM RF (concentration at which the protein shows the 80 % of its maximal rate) as a function of the ATP substrate. (B) Reaction rates at saturating ATP concentration as a function of the RF substrate. Measurements performed at 37ºC, in 20 mM PIPES, pH 7.0, 0.8 mM $MgCl_2$.

It has been suggested that the inhibitory effect produced by the RF excess might be related to the formation of non-productive enzyme-substrate (or enzyme-products) complexes, that might not be able to evolve [95]. Nonetheless, until the moment the nature of these complexes remains unclear. Some possible explications would be that the products of the reaction, ADP and FMN establish a highly stable *Ca*FADS:FMN:ADP complex, where ADP would hinder the initiation of a new

catlytic cycle; or maybe the excess of RF might provoke the binding of two molecules of this flavin, preventing the incorporation of the other substrate of the reaction. Therefore, more detailed kinetic studies are required to elucidate the nature of the inhibition suffered by the *Ca*FADS RFK reaction.

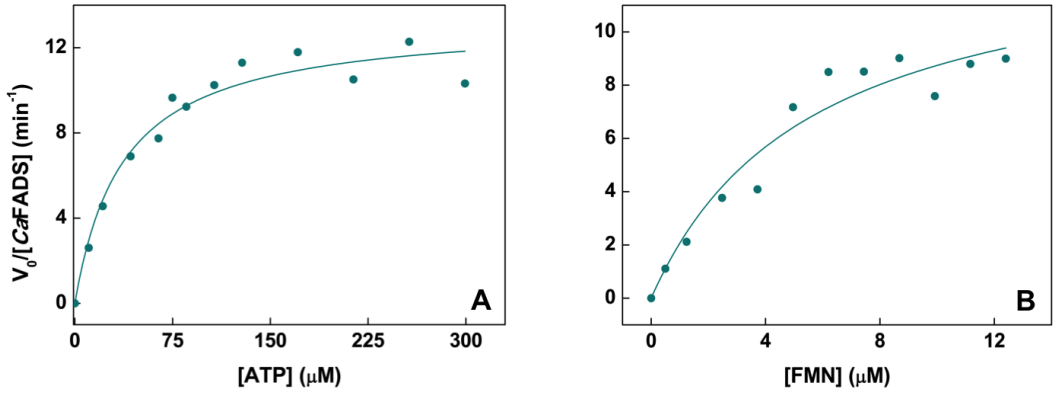

Figure. 1.15. Steady state kinetics behaviors for the FMNAT activity of *Ca*FADS (FMN + ATP →FAD + PPi) at (A) as a function of ATP at saturating FMN and (B) as a function of FMN at saturating ATP. Measurements performed at 37ºC, in 20 mM PIPES, pH 7.0, 10 mM $MgCl_2$.

Regarding the FMNAT reaction of *Ca*FADS, no inhibition has been observed neither at high concentrations of FMN nor of ATP. In this case the enzyme shows kinetic profiles that perfectly fit the Michaelis-Menten model (Fig. 1.15), being the values reported, at 37ºC, in 20 mM PIPES, pH 7.0, 10 mM $MgCl_2$, for the kinetic constants K_m^{ATP}, K_m^{FMN} and k_{cat} of 35.7 µM, 1.2 µM and 17.0 min^{-1}, respectively [88].

Thermodynamic parameters for the CaFADS interaction with substrates and products

Early studies postulated a single site for flavin binding, shared by the RFK and the FMNAT activities, and two independent binding sites for the adenine nucleotide ligands, each of them involved in one of the activities [81]. Nevertheless, subsequent studies about substrates binding through ITC provided new information that led to postulate a new interaction model [84].

*Ca*FADS has two independent ATP binding sites in the presence of Mg^{2+}, while in the absence of the ion only a single binding site is observable [84]. A single

binding site is detected both for FMN and FAD, while *Ca*FADS presents two binding sites for RF. Calorimetric titrations performed in the presence of ADP, revealed that this adenine nucleotide induces the formation of an additional independent binding site for FMN, demonstrating that *Ca*FADS holds two binding sites for adenine nucleotides and two for flavin nucleotides. This ITC study also allowed determining the values of the dissociation constant (K_d), for the interaction of *Ca*FADS with all of its ligands (Table 1.2). These experiments also suggested that the FMN and ADP products show positive cooperation, since the presence of one favors the binding of the other [84].

Table 1.2. Dissociation constants for the interaction between *Ca*FADS and its substrates and products. Data from [90]. The titrations were performed in 20 mM PIPES, pH 7.0, 10 mM $MgCl_2$, unless otherwise stated.

	K_d^{RF} (μM) (N)	K_d^{FMN} (μM) (N)	K_d^{FAD} (μM) (N)	K_d^{ATP} (μM)[a] (N)	$K_d^{ATP:Mg2+}$ (μM) (N)
***Ca*FADS**	24.1[b]	7.8	0.7	5.5	30.2
	(2)	(1)	(1)	(1)	(2)
***Ca*FADS:ADP**	Site 1	0.06			
	Site 2	0.9			

N indicates the number of binding sites observed for each ligand
[a] Experiments performed in the absence of Mg^{2+}.
[b] K_d averaged value for two independent binding sites.

3.2.2. The CaFADS is organized in two independent modules

The overall structure of CaFADS

The analysis of the *Ca*FADS primary structure reveals that this protein shows all the consensus sequences of RFKs and prokaryotic FMNATs (Figs. 1.11 and 1.16) [76]. The crystallographic structure of the *Ca*FADS has been obtained at 1.95 Å resolution (PDB 2X0K) [85]. The asymmetric unit contains two chains of 338 residues similarly folded. *Ca*FADS is a ~70-Å prokaryotic type-I FADS that presents two structural domains. The N-terminus FMNAT module (residues 1-186) shows an α/β dinucleotide binding domain with a Rossmann fold topology [83]. This module owns a parallel β-sheet compound by six strands (β1n–β6n) and five α-helixes (α1n-α5n) arranged at both sides of the β-sheet. At the end of the module a small subdomain built by a β-hairpin (β7n and β8n) and two short α-helixes (α6n and α7n)

can be found (Fig. 1.17). The C-terminal module (residues 187-338) folds in a ~25-Å diameter globular domain, formed by a β-barrel with six antiparallel β-strands (β1c-β6c), a long α-helix (α1c) and seven loops connecting them (Fig. 1.17). Three salt bridges (His186-Asp321, Asp273-Arg315 and Arg292-Arg310) and hydrophobic interactions stabilize the relative position between the β-barrel and the α1c helix. The main differences between the *Ca*FADS RFK module and eukaryotic RFKs, such as those from *Homo sapiens* (*Hs*RFK) and *Schizosaccharomyces pombe* (*Sp*RFK) [96, 97], are found in the loops that connect secondary structure elements. *Ca*FADS owns a 12 residues insertion in L3c (Leu232-Val246) that is only observed in corynebacteria and mycobacteria [85]. Additionally, loops L1c or Flap I (Val193-Thr208) and L4c or Flap II (Pro258-Glu263), *Ca*FADS numbering, show different conformations in *Ca*FADS and eukaryotic kinases [85, 96-98]. These loops are involved in the stabilization of nucleotides and flavins [85]. Another important difference is the position of Pro207 and Thr208 located at the 207-PTAN-210 consensus sequence of RFK and FADS families [76]. *Ca*FADS also holds a 15 residues loop, named L7c (Ala324-Ser338), that shows two different conformations (Fig. 1.18) and that it is not found neither in the monofunctional *Sp*RFK (PDB entry 1N05) nor in *Hs*RFK (PDB entry 1Q9S)

Figure 1.16. Primary structure of *Ca*FADS. The residues that belong to the N-terminus and C-terminus modules are shown in orange and blue, respectively. Consensus sequences of each module are highlighted in red and purple respectively.

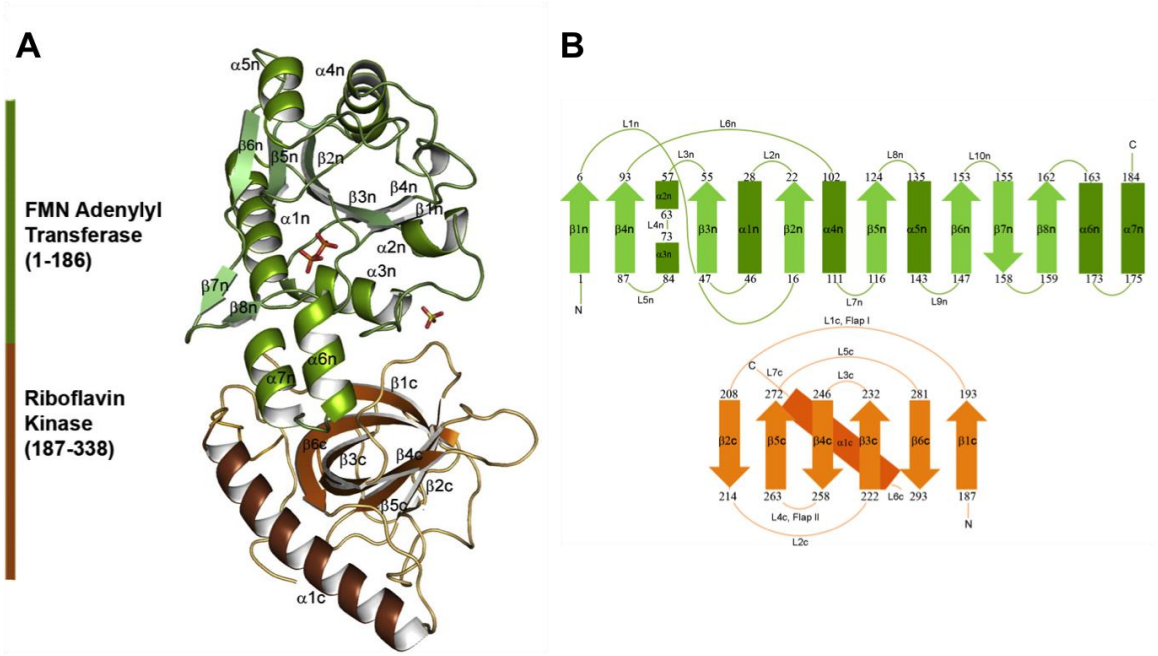

Figure 1.17. (A) Overall structure of the *Ca*FADS showing the different secondary structure elements. Sulfate and PPi are displayed as sticks. (B) Scheme of the *Ca*FADS topology, with the names assigned to every element of secondary structure. The C-terminal or RFK domain is displayed in orange, while the N-terminal or FMNAT one is shown in green. Figure from [85].

The RFK and FMNAT modules interact with each other through H-bonds and the formation of a hydrophobic core that provides rigidity to the interface between modules. Loop L2c, which is implicated in these interactions, is a α-helix in eukaryotic RFKs. This difference seems to be a distinctive feature of bifunctional FADSs, since this region is affected by the existence of the FMNAT module [85]. Special attention deserves the interaction between the His186 of the FMNAT module with the Glu286 located at the RFK one, seeing that the Glu residue is greatly conserved in the RFK family [74-76] (Fig. 1.11).

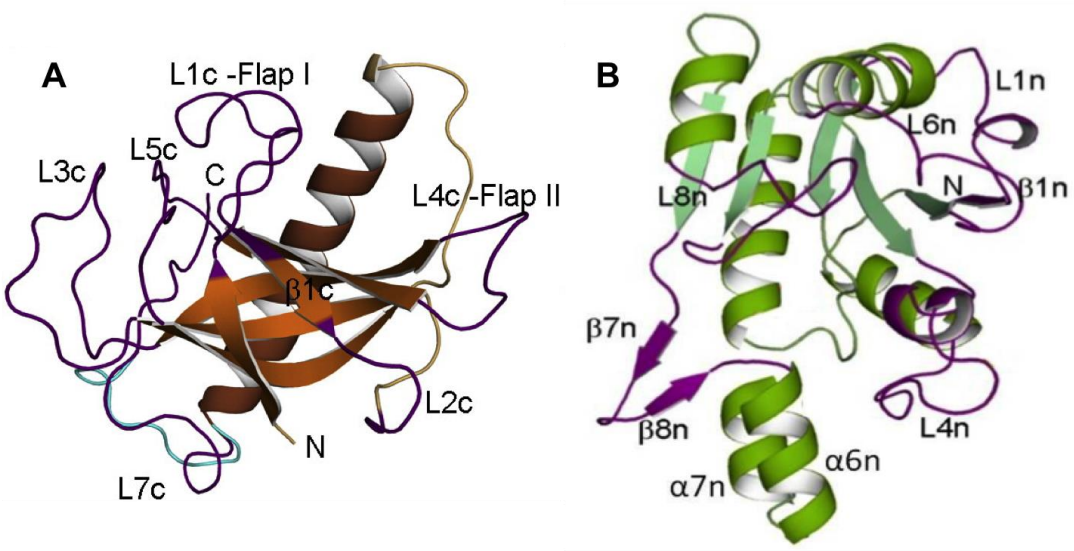

Figure 1.18. Detailed cartoon representation of the RFK (A) and FMNAT (B) modules of *Ca*FADS, with the nomenclature for their structural motifs. RFK and FMNAT modules are represented in orange and green, respectively, with their loops in purple. The alternative conformation of the loop L7c, in the RFK module, is shown in light blue. Figure modified from [85].

The active site at the FMNAT module of CaFADS

The FMN synthesized in the RFK module needs first to be released, to then bind to the FMNAT N-terminal domain to be transformed into FAD. In that way, the ATP adenine moiety is close enough to the FMN, and the adenylyl group can be transferred. Furthermore, this FMNAT module also performs the reverse reaction, this is the transformation of FAD and PPi into FMN and ADP. The surface of the FMNAT module shows an open cavity (Fig. 1.19) between the C-terminus of β3n, β2n and β5n, the α1n-helix, the small subdomain and the α2n-helix. This cavity is completed by the loop that connects β5n and α5n. The positively charged residues His28, His31, His57, Arg161, and Arg168 conform the central part of the cavity, contributing to the stabilization of the negative charges of the phosphate groups of substrates and products (Fig. 1.19C) [85].

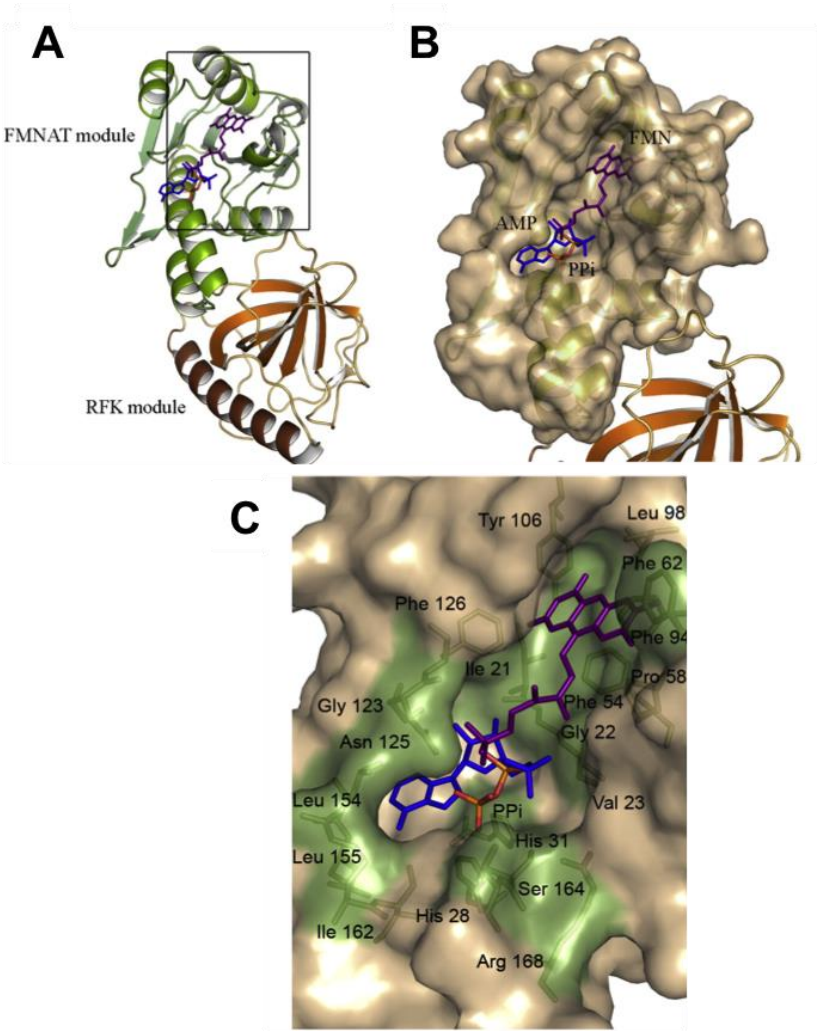

Figure 1.19. Active site of the FMNAT module of *Ca*FADS with modeled interactions with ligands. (A) Cartoon representation of the FMNAT module. AMP, PPi and FMN are shown in orange, blue and purple sticks, respectively. (B) Same view of the N-terminal module than in (A), but showing its molecular surface. (C) Detail of the binding cavity at the FMNAT module. The residues involved in ligands binding are shown in green. Figure from [85].

Sequence and structural analysis of Type I bacterial FADSs suggest that residues His28, His31, Asn125 and Ser164, which belong to the greatly conserved 28-HxGH-31, 123-Gx(D/N)-125 and 161-xxSSTxxR-168 motifs (Fig. 1.11 and 1.16), might play a key role in the FMNAT activity, through the stabilization of the phosphate groups of the substrates [76]. These residues might be also implicated in the formation of the catalytically ternary complex, and in the FMNAT and FADpp activities [76, 77]. A mutagenic study where these positively charged residues were replaced by negative ones [90], confirms this hypothesis since *Ca*FADS variants

showed altered FMNAT and FADpp activities. In addition, the binding parameters that describe the interaction of the variants with the ligands of the FMNAT activity also differed from those reported for WT *Ca*FADS. All together, these data confirmed the implication of these motifs in the formation of the catalytically competent complex as well as in the FMNAT and FADpp catalytic events [90]. Special mention deserves Asn125, which is the catalytic base of the FMNAT reaction. Thus, mutagenic studies in which N125A and N125D variants were characterized revealed the importance of this residue, since both variants did not performed the FMNAT activity, and they showed altered interaction parameters with the substrates of this reaction.

The flavin binding site at this domain is a wide open cavity that might allow different allocations of the isoalloxazine ring. For the moment, crystal structures reported at this site have only been obtained in the presence of the PPi product, but some models have been produced to show the putative binding of adenine and flavin nucleotides [85]. Hydrophobic contacts with Phe54, Phe62, Phe94, Tyr106 and Phe126 might stabilize the isoalloxazine ring within the flavin cavity [85]. Mutagenic studies, where these aromatic residues were substituted by others of different nature, confirmed their relevance. Phe62 affects the affinity of the binding site at the FMNAT module for the substrates and the products, as well as the conformation of the catalytic complex. Tyr106 and Phe128 are directly involved in the organization of the FMNAT cavity, and might be implicated in the conformational changes required for the FMNAT and FADpp reactions [78].

The active site at the RFK module of CaFADS

Although at the beginning of this Thesis crystal structure of *Ca*FADS in complex with ligands were reduced to that containing the PPi product of the fMNAT reaction, a model for the allocation of the substrates and products within the RFK module was proposed. For this modeling, the available structures of monofunctional RFKs with ligands, such as *Hs*RFK in complex with FMN and ADP (PDB 1Q9S), and the model for *Sp*RFK in complex with FMN and ADP (PDB 1N05) were considered [96, 97]. A posterior study where the structure of the isolated *Ca*FADS RFK domain was obtained in complex with some of its ligands corroborated the model [99].

Crystal structures of *Hs*RFK and *Sp*RFK in the presence of ligands, suggested large conformational changes during this catalytic cycle [96, 98]. These changes involved the Flap I and Flap II regions (L1c and L4c, respectively, in *Ca*FADS) that open the nucleotide binding site (which is closed and inaccessible to the ATP in the apo form) and close the flavin cavity after RF binding. This catalytically active conformation approaches the O5´-hydroxyl of RF to the catalytic base Glu268 (*Ca*FADS numbering), facilitating the Mg^{2+} coordination with the oxygens from ATP phosphates and with the Asn210 (numeration for *Ca*FADS) from the consensus PTAN motif [85].

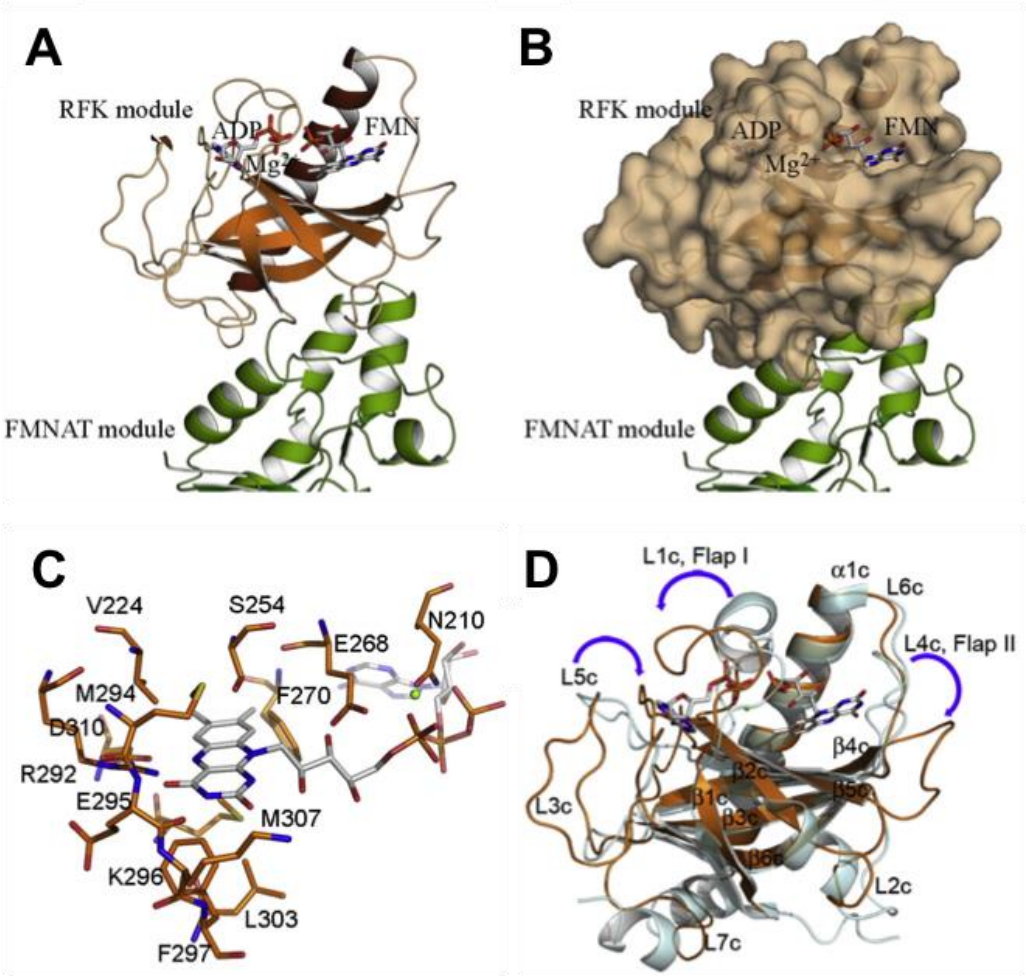

Figure 1.20. Active site of the *Ca*FADS RFK module. (A) Representation of the ligands within the active site of the RFK domain (orange). (B) Same view than (A) but with the RFK module represented in surface. (C) Detail of the flavin binding site with the highly conserved residues predicted to interact with FMN. (D) Superimposition of the RFK domains of *Ca*FADS (orange) and *Hs*RFK (blue). L3c apparently induces the displacement of L5c. The blue arrows indicate the expected movements of L5c, L1c and L4c according to those observed for *Hs*RFK. Figure from [85].

According to the structure of other members of the RFK family, the RFK active site of *Ca*FADS is placed outside the β-barrel, at the opposite side of the interface between modules (Fig. 1.20A). Within the *Ca*FADS RFK module, the highly hydrophobic region given by residues Val224, Phe270, Met294, Phe297, Leu303, and Met307, provides an accurate environment to stabilize the isoalloxazine ring (Fig. 1.20B). Additionally, H-bonds between Arg292 or Glu295 and N3, O4 and N5 of the flavin ring might also stabilize it. The poor density found for residues conforming L4c (259-261) and a solvent-exposed Phe260, suggest that in *Ca*FADS this loop is highly flexible, and upon RF binding could suffer conformational changes, similar to those observed for monofunctional RFKs [85]. The adenine moiety of the adenine nucleotide substrate binds in a pocket, between the N-terminus of β2c and the C-terminus of β5c, with L5c (Leu272-His281) surrounding its ring (Fig. 1.20C). The phosphates (and the Mg^{2+} that stabilizes its negative charges) are located between L1c and β1c. However, the *Ca*FADS adenine nucleotide binding site at the RFK module is small and closed, preventing the direct nucleotide access. It needs to be highlighted that contrary to other RFKs, in *Ca*FADS L1c-Flap-I is folded towards L5c, with the side chain of Thr208 occupying the adenine binding site of ATP. The conformation of L1c, L3c and L5c is stabilized by polar and hydrophobic interactions, including six H-bonds. When comparing the *Ca*FADS RFK module with monofunctional RFKs, in the apo-form of *Sp*RFK, the adenine nucleotide binding site is also blocked, but in this case only the position of Flap-I produces the closed conformation [96]. All these data suggested that the conformational changes during the RFK catalytic cycle of *Ca*FADS are more intricate than those reported for the monofunctional RFKs, since a concerted movement of the loops L1c, L3c and L5c of *Ca*FADS is required for the opening of the cavity and for the ATP binding, as well as the conformational rearrangement of the PTAN motif (Fig. 1.20C) [85].

3.2.3. Notable conformational changes occur during the CaFADS RFK catalytic cycle

Crystallographic structures of the isolated RFK module of *Ca*FADS in complex with some of its ligands are now available (binary RFK:ADP complex, PDB entry 5a88 and ternary RFK:ADP:FMN complex, PDB entry 5a89). In a recent study, which completes the structural information with computational analyses and kinetic

and binding information, a model for the structural rearrangements occurring during the RFK catalytic cycle has been proposed [99].

The structure of the RFK module in the apo form of the *Ca*FADS significantly differs from those found for the binary RFK:ADP-Mg^{2+}, and the ternary RFK:FMN:ADP-Mg^{2+} complexes. Both complexes exhibit important structural rearrangements that affect the conformation of the 207-PTAN-210 motif, as well as the majority of the protein loops with the only exception of L2c.

As indicated in the previous section, in the apo-protein the adenine nucleotide binding site of the RFK module is closed, due to the conformation of L1c, L3c and L5c, which interact with each other (Fig. 1.21B). The formation of the ternary complex induces a conformational change in L1c that is displaced to α1c, while part of it becomes a short helix. In that way, L1c loses its interaction with L3c and L5c, which move to the opposite direction expanding the adenine nucleotide cavity (Figs. 1.22C and 1.21B). The binary and the ternary complexes show the same disposition of these three loops, therefore the structural rearrangements are induced by the binding of the adenine nucleotide regardless of flavin binding. Molecular Dynamics (MD) simulations of the free RFK module show that in solution loops L3c, L5c and particularly L1c establish an open-close equilibrium for the adenine nucleotide binding site. These simulations also reveal that the presence of either flavin or adenine nucleotides increases the opening probability of the cavity [99]. Regarding the flavin binding site of the RFK module, L4c is disarranged in the binary complex and as a consequence the flavin binding cavity is open and wide (Fig. 1.21A). In contrast, FMN binding induces a change in the size, shape and solvent accessibility of the cavity (Fig. 1.21B) [99].

We focus now on the relative position in the different structures of the consensus 207-PTAN-210 motif that stabilizes the ATP phosphates and the Mg^{2+} ion during the reaction. In the free enzyme, the side chain of the Thr208 is occupying the position where the adenine ring is located both in the binary and in the ternary complexes (Fig. 1.22E). Therefore, the ADP/ATP binding necessarily undergoes a huge conformational change that results in the opening of the adenine nucleotide cavity. Considering that in the ternary complex Thr208 is the only residue interacting with FMN, ADP-Mg^{2+} and with the Glu268 catalytic base, this residue seems to be crucial for the competent binding of ligands within the active site. Site-directed mutagenesis studies where T208A and T208D variants were characterized confirmed the

relevance of this residue [88]. Another residue that also executes a key role in the conformation of the ternary complex active site is Asn210, also from the PTAN motif. The Asn210 side chain interacts with FMN, Mg^{2+} and Glu268, setting the geometry of the catalytically competent complex, and contributing to maintain the phosphate of the ATP donor and the OH acceptor of the RF in the accurate position [99]. MD simulations show that the presence of either the flavin or the adenine nucleotides is not sufficient to induce the Thr208 conformational change. Moreover, these simulations suggest that the coordination of its side chain with ADP/ATP through the Mg^{2+} ion is the most probable determinant for the achievement of the catalytically competent geometry of the PTAN motif.

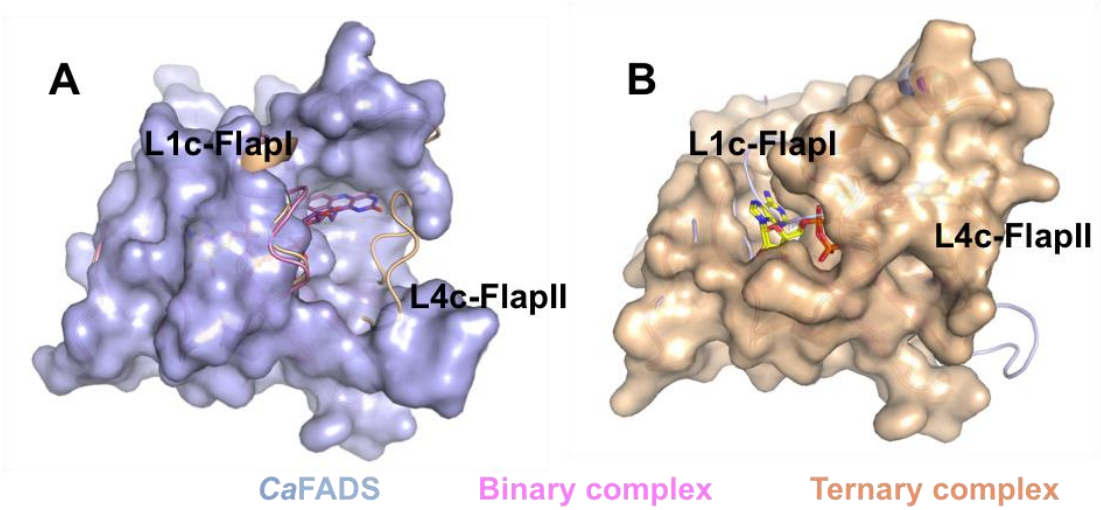

Figure 1.21. Surface view of both the flavin and the adenine nucleotide binding sites at the RFK module. (A) Superposition of the free *Ca*FADS RFK structure with the binary and ternary complexes. The free protein is shown in blue surface while both complexes are displayed in cartoon. In the free RFK, the flavin binding site is open and the adenine nucleotide binding site is closed. (B) Superposition of the same structures is shown as cartoon and the ternary complex as brown surface. In this case the adenine nucleotide cavity is open in both complexes, while the flavin cavity is closed only in the ternary complex. Figure from [99].

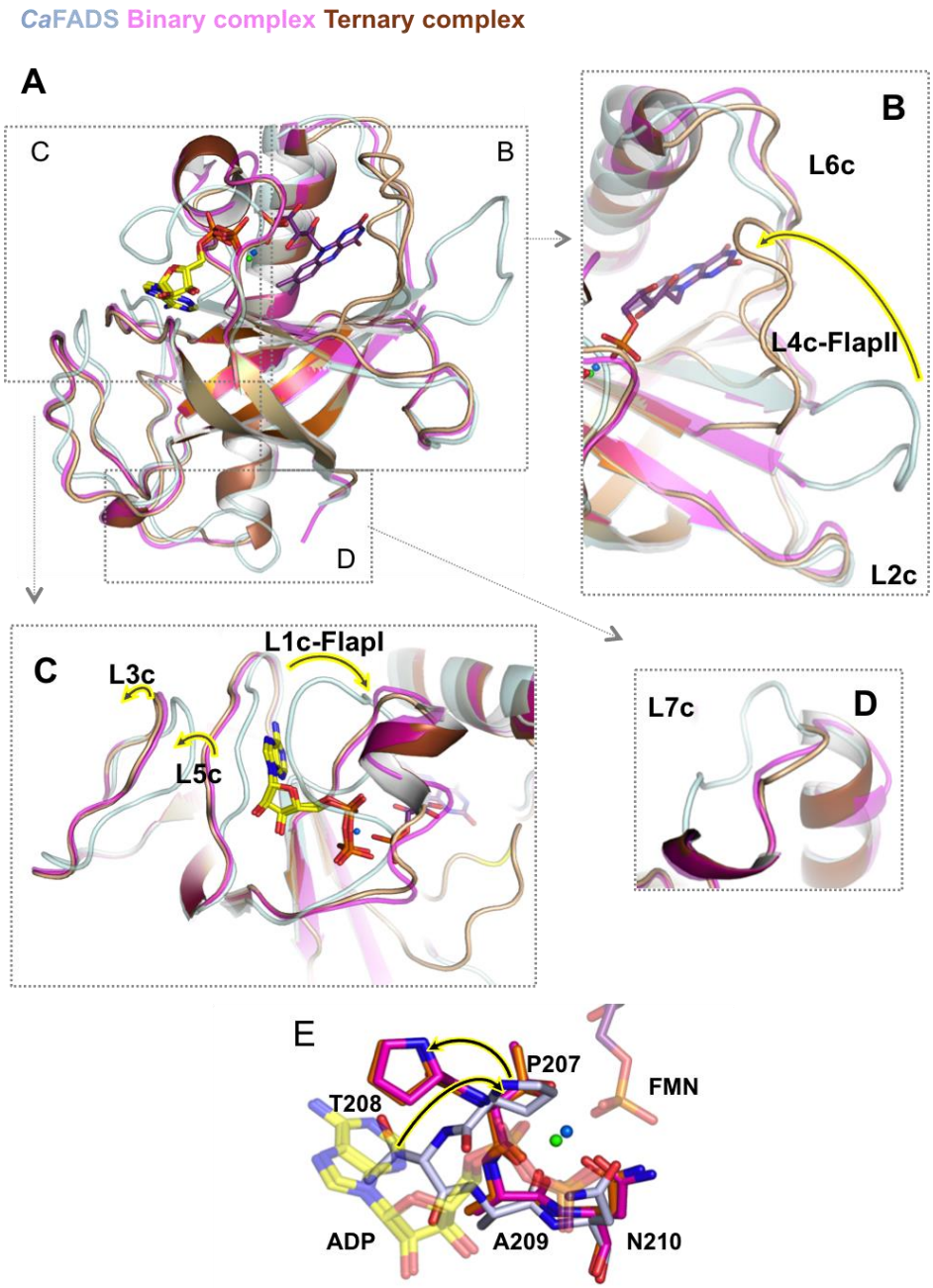

Figure 1.22. Superposition of the free *Ca*FADS RFK domain (light blue), the binary complex (light pink) and the ternary complex (brown). (A) Overall view of the alignment of the three structures. The most significant differences are highlighted with squares. (B) Detail of the flavin binding site indicating with a yellow arrow the displacement of loop L4c that closes the flavin cavity in the ternary complex. (C) Zoom into the adenine nucleotide binding site. Conformational changes of loops L1c, L3c and L5c are indicated with yellow arrows. (D) Detail of the position of L7c in the free protein and in both complexes that share the same conformation of that loop. (E) Conformation of the PTAN

motif in the three structures. The conformational change of Pro207 and Thr208 can be appreciated. Figure from [99].

All these data suggest that binding of ligands induces the conformational changes required during the catalytic cycle of the RFK module. Nevertheless, several aspects of this cycle still need to be clarified, such us; do the substrates of the RFK reaction bind the module sequentially or an induced-fit is required? or Has the Mg^{2+} cation a role in this process? Additionally, the inhibition of the RFK reaction by substrates and products is a topic worthy of study.

3.2.4. CaFADS can be organized into a dimer of trimers

A structural analysis of the crystal structure of the *Ca*FADS suggested the existence of an A_3B_3 hexameric organization in solution (being A and B the two chains of the asymmetric unit of the *Ca*FADS crystal) (Fig. 1.23). Such oligomeric state would consist on two trimers (A_1-A_2-A_3 and B_1-B_2-B_3, one on top of the other). Within each trimer, the three protomers show a head-tail disposition. The trimers are stabilized through contacts of different nature between 20 side chains (18 H-bonds, 18 hydrophobic contacts and 3 salt bridges) (Fig. 1.24A). The interface between trimers shows electrostatic complementarity (Fig. 1.23B). Moreover, 14 H-bonds, 4 salt bridges and 12 hydrophobic contacts strengthen the hexamer [85].

We focus now on the relative position in the different structures of the consensus 207-PTAN-210 motif that stabilizes the ATP phosphates and the Mg^{2+} ion during the reaction. In the free enzyme, the side chain of the Thr208 is occupying the position where the adenine ring is located both in the binary and in the ternary complexes (Fig. 1.22E). Therefore, the ADP/ATP binding necessarily undergoes a huge conformational change that results in the opening of the adenine nucleotide cavity. Considering that in the ternary complex Thr208 is the only residue interacting with FMN, ADP-Mg^{2+} and with the Glu268 catalytic base, this residue seems to be crucial for the competent binding of ligands within the active site. Site-directed mutagenesis studies where T208A and T208D variants were characterized confirmed the relevance of this residue [88]. Another residue that also executes a key role in the conformation of the ternary complex active site is Asn210, also from the PTAN motif. The Asn210 side chain interacts with FMN, Mg^{2+} and Glu268, setting the geometry of the catalytically competent complex, and contributing to maintain the phosphate of the ATP donor and the OH acceptor of the RF in the accurate position

[99]. MD simulations show that the presence of either the flavin or the adenine nucleotides is not sufficient to induce the Thr208 conformational change. Moreover, these simulations suggest that the coordination of its side chain with ADP/ATP through the Mg^{2+} ion is the most probable determinant for the achievement of the catalytically competent geometry of the PTAN motif.

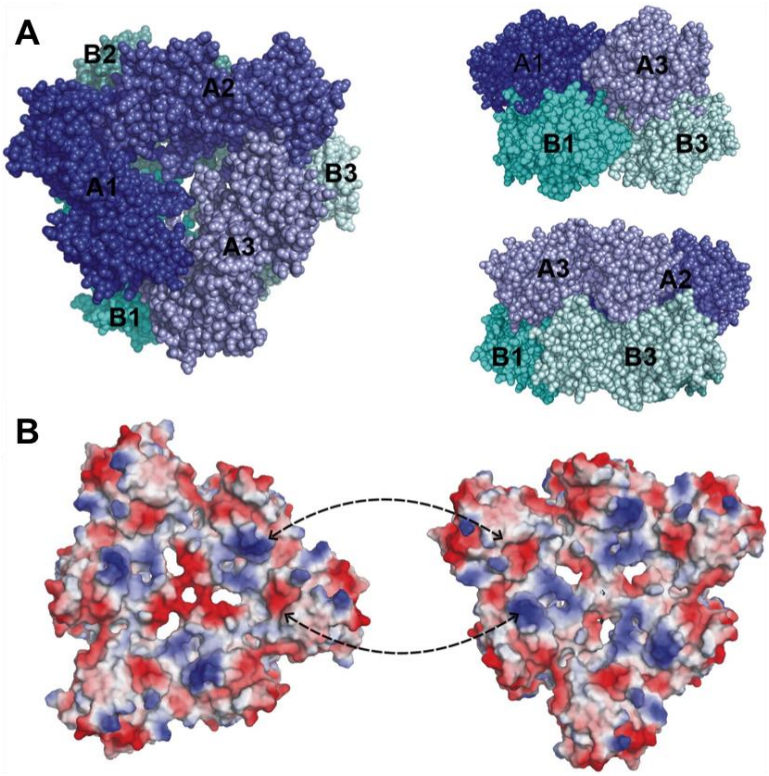

Figure 1.23. Oligomeric state of *Ca*FADS. (A) Spatial representation of the dimer of trimers. Left, view through the 3 crystallographic axis. Right, lateral view of the hexamer. (B) Electrostatic potential of the *Ca*FADS hexamer along the interaction surfaces of the two trimers (negative, positive and uncharged residues are shown in red, blue and white respectively). The arrows show the positions with electrostatic contacts between trimers for the formation of the hexamer. Figure from [85].

The *Ca*FADS trimeric state approaches the RFK and FMNAT active sites by placing the active centers of different protomers in close contact, which modifies the active site environment and its solvent accessibility (Fig. 1.24). That way, in the trimer, the RFK cavity appears partially closed by α2n and L4n of the neighboring protomer, specifically by the side chains of Phe62, Leu63, Pro64 and Arg66 (Fig. 1.24A and D). Arg66 from the FMNAT module would establish a salt-bridge with the catalytic base Glu268 at the RFK site. Additionally, the FMNAT catalytic site is

also modified by residues of the RFK module of a different protomer (Fig. 1.24A and C). Concretely, V300 would close the isoalloxazine cavity of the FMNAT module, while hydrophilic residues of L6c would block the ribityl binding site. Furthermore, the positive dipole of α1c would contribute to stabilize the phosphates of the substrates at the FMNAT module. Hence, in the proposed oligomeric state of the *Ca*FADS, each active site is composed of residues from its own module and also of residues from the other module of a different protomer [85].

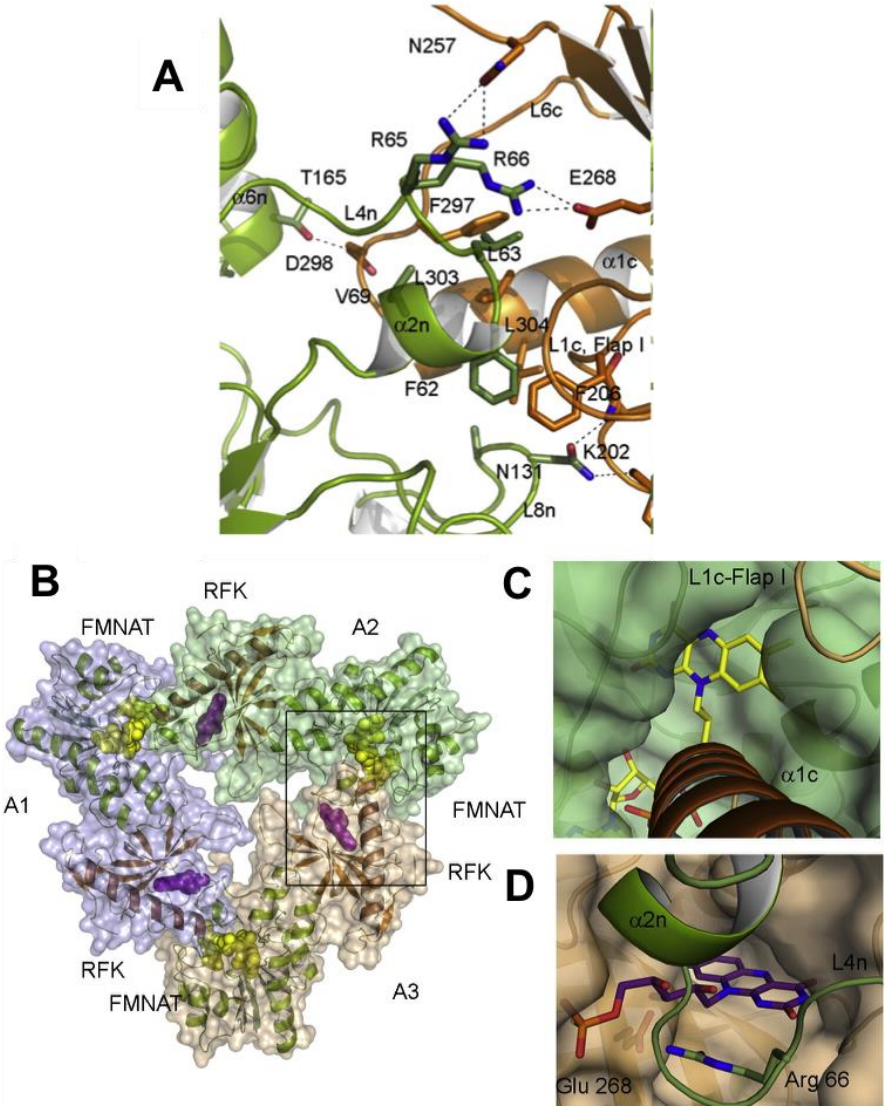

Figure 1.24. (A) Detail of the contact between the RFK and the FMNAT modules of different protomers within a trimer. (B) Cartoon representation of one of the trimers conforming the hexamer. The FMNAT module is shown in green while the RFK one is displayed in orange. Surface of each protomer is shown in different colors. The flavin products of the reactions are shown as spheres. (C) Detail of the active site at the FMNAT module. α1c and L1c of the RFK module of the neighboring protomer close the binding

site. (D) Detail of the active site of the RFK module. α2n and L4n of the FMNAT module of the neighboring protomer close the binding site. FMN and FAD are represented as violet and yellow sticks respectively. Figure from [85].

To further infer whether these oligomeric assemblies exit and have any role both at *in-vitro* and *in-vivo* levels, an analysis of the oligomeric states of *Ca*FADS was conducted. The study revealed the existence of such oligomers (in the same proportion), in both types of assays, indicating that the oligomerization process was relevant both at the molecular and cellular levels [100]. All this information suggests that the *Ca*FADS dimer-of-trimers might play a key role during its catalytic cycle.

3.2.5. Binding of ligands induces oligomerization in CaFADS

To determine whether the different ligands of *Ca*FADS influence the oligomerization tendency of the protein, an atomic force microscopy (AFM) study was performed [100]. In this study liquid, jumping mode (JM) AFM allowed visualizing single isolated *Ca*FADS molecules, estimating their molecular dimensions, as well as distinguishing between the C-terminus and the N-terminus modules.

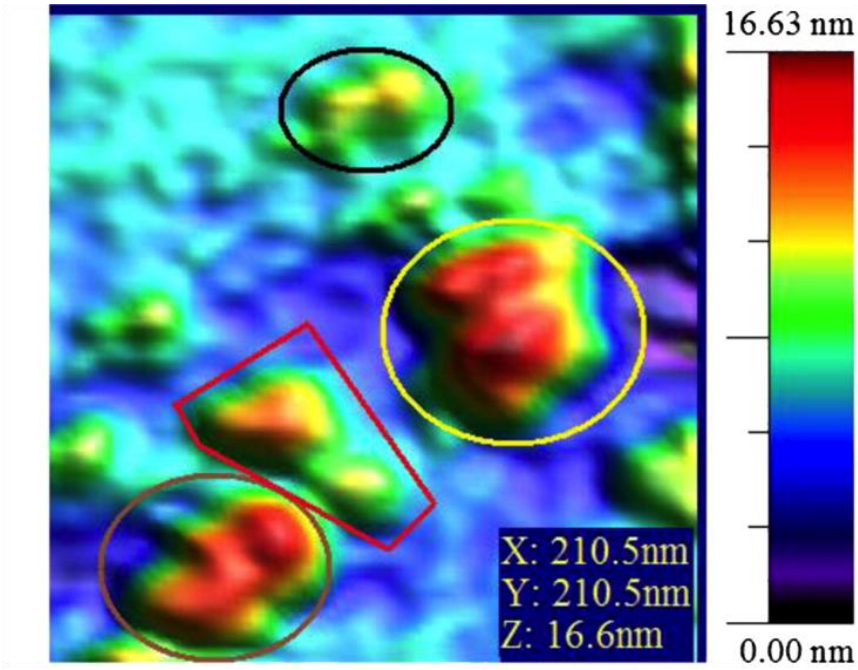

Figure 1.25. AFM topography images of *Ca*FADS after incubation with ATP:Mg^{2+}. The different species identified as monomer, dimer, tetramer and a dimer of trimers are rounded in black, red, brown and yellow respectively. Figure from [100].

Some substrates of the RFK (RF or ATP:Mg^{2+}), the FMNAT (ATP:Mg^{2+}), and the FADpp (FAD) activities of *Ca*FADS induced the oligomerization of the protein, yielding different oligomeric assemblies (Fig. 1.25) [100]. Some of these quaternary structures, such as dimers and an amorphous hexamer, might act as intermediates during the assembly of the organized dimer of trimers, which is specially favored by the presence of ATP:Mg^{2+}, and also by the products of the RFK reaction (FMN:ADP) (Fig. 1.26). Therefore, during the catalytic cycle, the quaternary organizations might be structured by the previous formation of dimers (supported by contacts between the RFK and FMNAT modules of different protomers) followed by packing of additional protomers to finally raise the dimer of trimers. Furthermore, the stabilization of the phosphate groups of ATP/ADP:Mg^{2+} at the RFK domain appeared as a determinant of the oligomerization process.

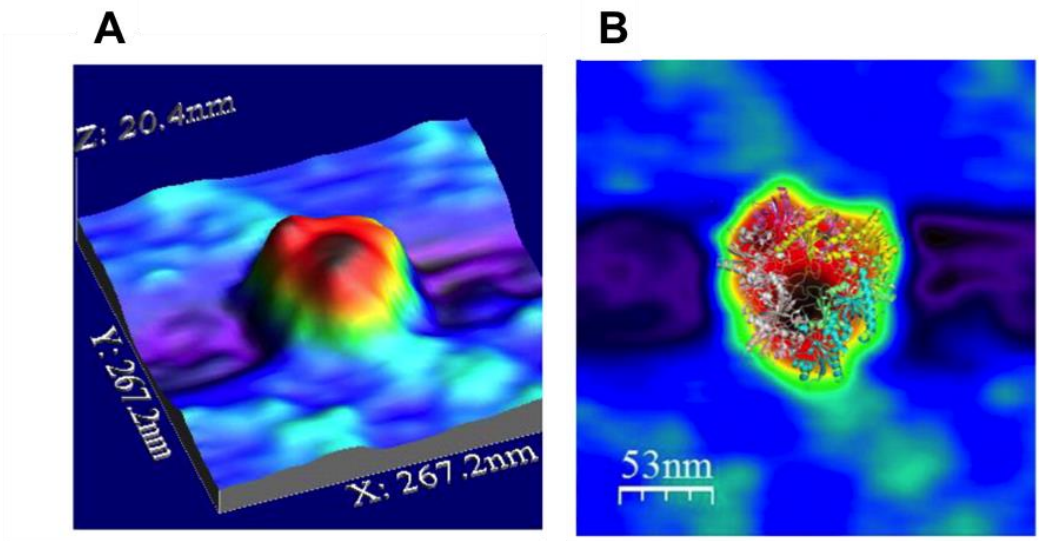

Figure 1.26. Topography image of *Ca*FADS upon incubation with the products of the RFK reaction (FMN and ADP:Mg^{2+}). (A) 3D image of a single organized dimer of trimers. (B) Superposition of the crystallographic *Ca*FADS hexamer and its 2D AFM image. Figure from [100].

Concerning other bifunctional FADSs, possibility of oligomerization has not been reported. The structural analysis of the FADSs whose structures are available (*Spn*FADS and *Tm*FADS), does not predict the formation of any quaternary organization. The main structural differences of *Ca*FADS regarding other FADSs are located in the β1n strand of the FMNAT module (absent in *Tm*FADS), and particularly in an insertion of 12 residues in the loop L3c (L232-V246), that is only present in *Corynebacteria* and *Mycobacteria* species [76]. As previously indicated,

the position of this insertion (also lacking in monofunctional RFKs), is stabilized in the monomeric *Ca*FADS by H-bonds that connect L3c and L5c. Additionally, L3c reinforces the interface between trimers within the hexamer. Therefore, besides all these elements that stabilize the dimer of trimers, L3c provides 3 more hydrophobic contacts (per protomer), between the three RFK modules of one trimer and residues from β1n and α3n at the FMNAT module of the other trimer. Hence, the absence of L3c in other FADSs might prevent the dimer of trimers stabilization, and consequently, the formation of oligomeric structures.

Collectively, these data hypothesized the implication of the organized dimer of trimers in the catalytic activities of *Ca*FADS. This implication is also supported by a site-directed mutagenesis study, that concludes that conformational changes at the RFK module produced by ligand binding affect the catalytic efficiency at the FMNAT module of *Ca*FADS of the neighboring protomer within the trimer [88]. In this study the substitution of the residues T208 and N210, both located in the consensus 207-PTAN-210 motif and of E268 (Figs. 1.10 and 1.16), altered the kinetic parameters for the RFK reaction, as well as substrates and products binding constants. Additionally, mutations of these residues, located at the RFK module of *Ca*FADS, also modulated the binding parameters at the FMNAT active site, and the catalytic efficiency of the FMN transformation into FAD [88].

3.3. Other prokaryotic FADSs

3.3.1. The FADS from Streptococcus pneumoniae: SpnFADS

The crystal structure of the FADS from *Streptococcus pneumoniae* (*Spn*FADS) was released in 2010 (PDB: 3OP1) (Fig. 1.27A). *Spn*FADS is organized in two different modules putatively related to each activity. The C-terminus module (residues 187-305), would perform the RFK activity, and it is constituted by a β barrel formed by six antiparallel β-strands (β1c- β6c), a long terminal α-helix (α2c) and an additional short α-helix (α1c), compound by 4 residues and located in loop I that connect β1c and β2c. Six loops connect these secondary structure elements (Fig. 1.27B). The N-terminal module (residues 1-186) folds into a α/β dinucleotide binding domain with the typical Rossman fold, and by homology with *Ca*FADS (Fig. 1.27B), it is predicted to catalyzed the FMNAT reaction. This domain is organized into six β-strands (β1n-β6n) and several α-helixes surrounding the β-strands connected by ten loops (L1n-L10n).

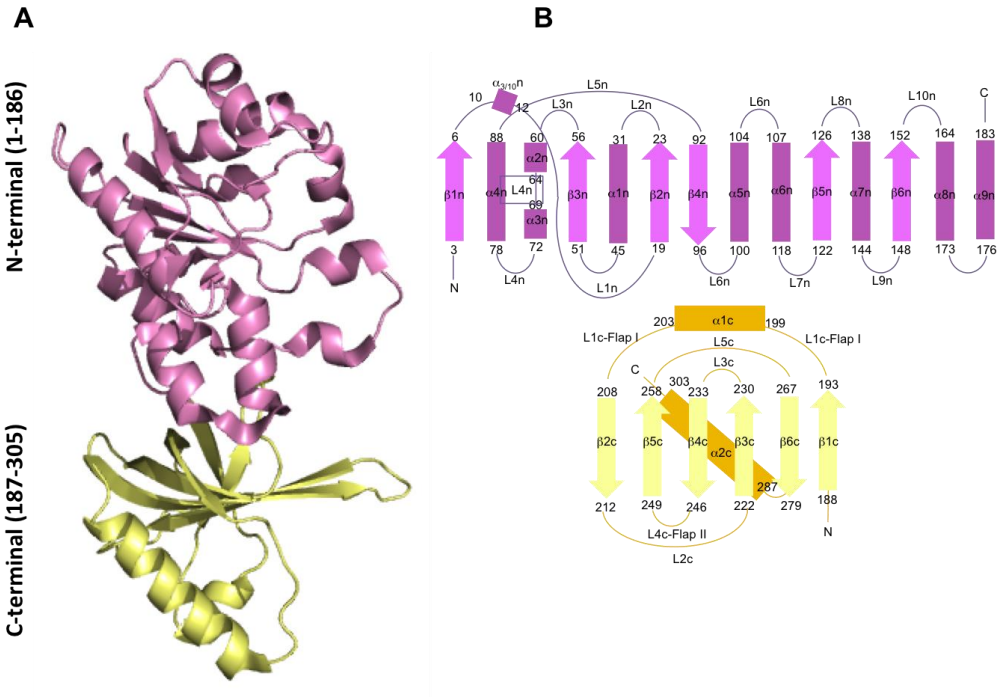

Figure 1.27. Structure of *Spn*FADS (PDB: 3OP1) (A) Cartoon representation of the 3D structure of *Spn*FADS with the N-terminal domain colored in pink and the C-terminal one in yellow. (B) Topology of the N-terminal module (pink) and the C-terminus one (orange). α-helix are displayed as solid dark rectangles and β-strands as light arrows. Loops connecting secondary structure elements are shown in thick lines. The numbers indicate residue positions.

Sequence analysis shows that *Spn*FADS contains all the typical features of prokaryotic FADSs (Figs. 1.28A and 1.11), and therefore it is expected to be able to perform the RFK, FMNAT and FADpp activities. *Spn*FADS shows 29% sequence identity with *Ca*FADS (Fig. 1.28A), and also owns the consensus sequences greatly conserved among prokaryotic FADSs. The N-terminus module presents the 30-HxGH-33, 161-xxSSTxxR-168 and 16-Gx(N/D)-128 motifs (*Spn*FADS numbering), which have been reported to play a key role in the FMNAT activity of *Ca*FADS through the stabilization of the ATP phosphates groups (Fig. 1.28A) [90]. Additionally, the *Spn*FADS C-terminal module also contains the 203-PTAN-207 motif (*Spn*FADS numbering), whose conformational change leads to the establishment of the catalytically competent complex in *Ca*FADS, and the Glu255 (*Spn*FADS numbering), that must act as catalytic base during RF phosphorylation [88]. Nevertheless, the relative position of these structural motifs, specifically the

orientation of the PTAN motif, meaningfully differs between both structures (Fig. 1.28C). On the other hand, it is noteworthy that the conformation of the PTAN motif in *Spn*FADS significantly resembles the position of this motif in the Δ(1-182)*Ca*FADS-FMN-ADP ternary complex (PDB: 5a89) (Fig. 1.28D). This important variance suggests that *Spn*FADS might require less structural rearrangements to acquire the catalytically competent complex than *Ca*FADS, as well as important differences in the RFK catalytic cycle.

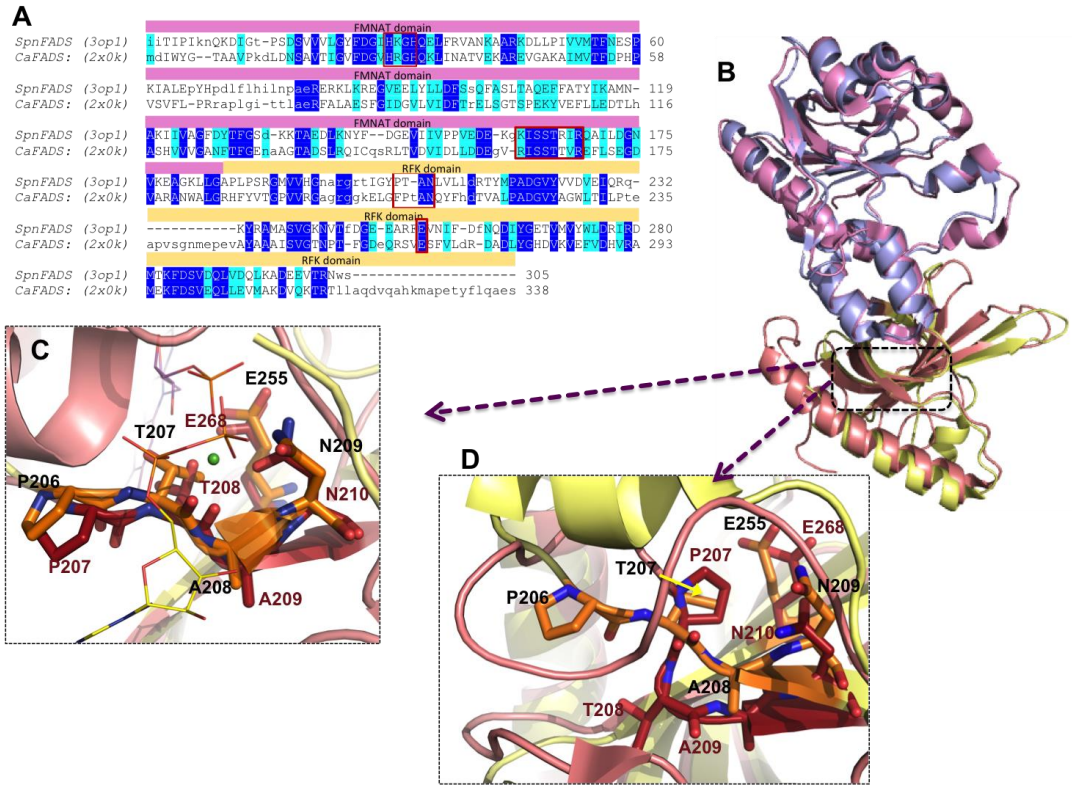

Figure 1.28. (A) Structural alignment of *Ca*FADS (PDB: 2X0K) and *Spn*FADS (PDB: 3OP1) performed by the SSM server (http://www.ebi.ac.uk/msd-srv/ssm/). Identical residues are shown in dark blue and conservative ones in light blue. Consensus motives at N-terminal (30-HxGH-33 and 160-xSSTxxR-168) and at C-terminal (103-PTAN-107 and E255, *Spn*FADS numbering) are highlighted with red boxes. (B) Superposition of the overall structures of *Spn*FADS (with its C and N-terminal domains colored in light pink and yellow, respectively) and *Ca*FADS (light blue and salmon, respectively). (C) Detail of the conformation of the PTAN motif in *Spn*FADS (CPK code with carbons in orange) and in the Δ(1-182)*Ca*FADS ternary complex with FMN and ADP (CPK code with carbons in maroon) FMN and ADP products are shown in purple and yellow lines, respectively. (D) Zoom into the PTAN motif residues and E255 of *Spn*FADS (shown in orange) and *Ca*FADS (in maroon).

3.3.2. The FADSs from Listeria monocytogenes and Mycobacterium tuberculosis

Crystallographic structures for the bifunctional FADSs from the pathogenic organisms *L. monocytogenes* (*Lm*FADS) and *M. tuberculosis* (*Mt*FADS) are not available. However, sequence alignments and structural models have been produced, using as models prokaryotic FADSs whose structure are known, mainly *Ca*FADS, *Spn*FADS and *Tm*FADS (PDB codes 2X0K, 3OP1 and 1T6Y, respectively) [78].

L. monocytogenes owns two different FADSs, named *Lm*$_1$FADS and *Lm*$_2$FADS. Sequences alignments revealed that *Lm*$_1$FADS is a type-I FADS, and shows all the consensus sequences assigned to RFK and FMNAT activities, in the C-terminal and N-terminal modules, respectively (Fig 1.29). *Lm*$_2$FADS presents in its N-terminal module the consensus sequences related to FMNAT activity, while its C-terminus module is degenerated, and does not show the consensus sequences displayed by RFKs (Fig 1.29). Therefore, the function of the C-terminal module of *Lm*$_2$FADS has not been predicted [78].

Lm$_1$FADS and *Lm*$_2$FADS have been purified, and their RFK and FMNAT activities have been measured both in the presence and in the absence of reducing environment [78, 79]. As it was expected, since *Lm*$_2$FADS lacks the consensus motifs of RFKs, only *Lm*$_1$FADS was able to transform RF into FMN, both under reducing and oxidizing conditions, although the catalytic efficiencies differed [78, 79]. Both proteins were able to transform FMN into FAD, but interestingly their redox requirements were different. *Lm*$_1$FADS only presented FMNAT activity under strong reducing conditions, while *Lm*$_2$FADS carried out this activity with and without the reducing agent, being more efficient under oxidizing environment [78].

In spite of the great efforts made to overexpress and purified *Mt*FADS, all the attempts to produce it have failed [78]. Sequence alignments performed for *Mt*FADS indicated that this protein also belongs to the bifunctional type-I FADSs, as it shows all the consensus motifs of this family of proteins (Fig 1.29). It is worth to notice the high identity percentage between *Mt*FADS and *Ca*FADS, as also the fact that FADSs from *Corynebacterium* and *Mycobacterium* genus are the only ones that have the 12-residues insertion in the RFK module, between L232 and V246 (*Ca*FADS numbering) [76].

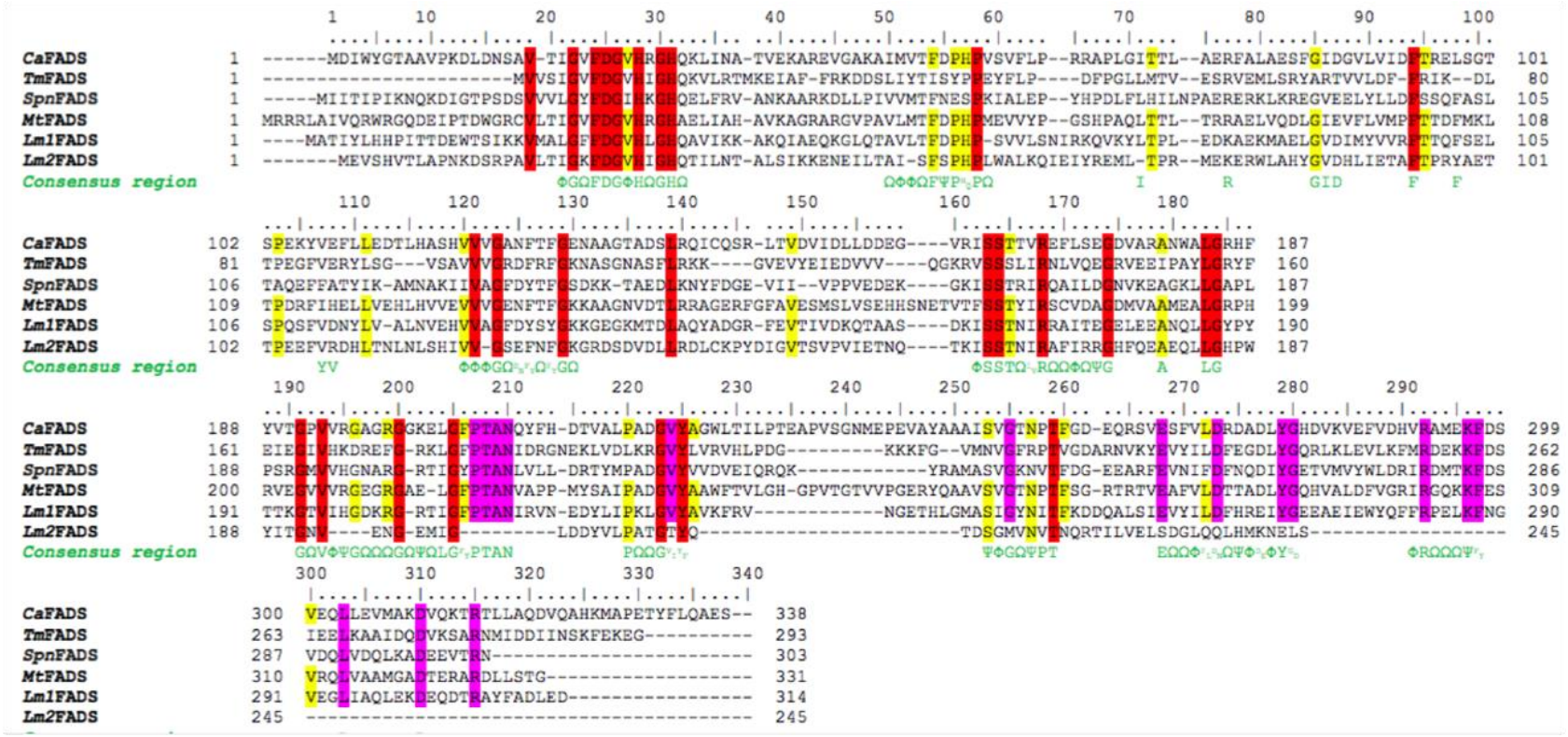

Figure 1.29. Sequence alignment of bifunctional FADSs from different organisms. Residues that are the same for all the five sequences are highlighted in red, those found in type-I FADSs but not in type-II FADS are shown in pink, and those present in *Ca*FADS, *Lm*$_1$FADS, *Lm*$_2$FADS, and in *Mt*FADS are displayed in yellow. The insertion Leu232-Val246 (*Ca*FADS numbering), observable only in *Corynebacterium* and *Mycobacterium* genus, is colored in gray. The consensus sequence and conserved residues among FADS family is displayed under the alignment. Symbols Φ,Ψ y Ω denote for hydrophobic, polar and any residue respectively. Figure modified from [78].

3.4. Bacterial diseases needing new efficient treatments

As we have discussed in Section 1, the apparition of multidrug resistant pathogens evinces the necessity to develop new antibacterial strategies and FADS are interesting drug targets in the discovery of antimicrobials.

3.4.1. Streptococcus pneumoniae and pneumonia

Streptococcus pneumoniae appears as a main problem for the public health both in developing and developed countries. This pathogen is responsible of a great variety of clinical profiles, being the causative agent of mild infections as otitis media or paranasal sinusitis, as well as of serious infections as septic arthritis, pneumonia, and brain abscesses [101]. Additionally, meningitis usually appears secondarily to pneumococcal infections. Pneumonia is the world´s leading cause of death among children under five, accounting for 15 % of deaths (data from the American Thoracic Society). Over the last two decades the incidence rate of systemic infections, such as meningitis, caused by *Streptococcus pneumoniae* have increased, and penicillin resistant strains have appeared as well [102].

Physiology, structure and genetics of S. pneumoniae

S. pneumoniae cells are Gram-positive, lancet-shaped, typically placed as pairs of cocci (diplococci). These bacteria require special culture conditions, needing enriched media as blood-agar. When cultured in that media they are alpha-hemolytic (under aerobic conditions) or beta-hemolytic (under anaerobic conditions). They neither form spores nor are motile. Concerning their metabolism, they are catalase negative and ferment glucose to lactic acid. *In-vitro* cultures require 5% carbon dioxide and a source of catalase to neutralize the produced peroxide hydrogen. In complex media, at 37ºC, *S. pneumoniae* has a generation time of 20-30 minutes. The pneumococcus is also able to produce autolysin, which is an enzyme that causes the culture to undergo autolysis. The autolysin kills the entire culture when it has grown to the stationary phase [102].

S. pneumoniae presents a capsule composed of polysaccharides that completely envelops the cells. During invasion, the capsule is a virulence determinant since it hinders phagocytosis by preventing the opsonization of the bacteria [103]. The cell

wall of *S. pneumoniae* is composed of peptidoglycan with teichoic acid attached, which is a virulence factor. With respect to surface proteins, the pneumococcus is estimated to contain more than 500 of them, either associated to the membrane or to the cell wall [104]. The latter group includes, among others, five penicillin-binding proteins, two neuroaminidases and an IgA protease. Additionally, twelve choline-binding proteins are non-covalently bound to choline motifs of the cell wall, constituting some of them virulence factors [105].

S. pneumoniae has a natural transformation system as mechanism for genetic exchange between related or unrelated bacteria, whose last consequence is the apparition of antibiotic resistances.

Pathogenesis and invasion cycle of the pneumococcus

S. pneumoniae causes diseases in humans, monkeys, rabbits, horses, mice and guinea pigs. 40 % of the population shows nasopharyngeal colonization by the pathogen.

The ecological niche for the pneumococcus is the nasopharynx. When the bacteria enter the nasal cavity, the negatively charged capsule protects them from being tapped in the mucous, and they can reach the epithelial surface. Many surface proteins are involved in the nasopharyngeal colonization, such us hyaluronidase, or CbpA [106, 107]. Once bacteria have entered the lower respiratory tract, the initiation of pneumonia requires escape from mucous defenses and migration of the bacteria into the alveolus (Fig. 1.30). For this purpose, bacterial neuraminidase cleaves mucin, and uncovers some glycoconjugates on the host cells, providing sites for bacterial attachment.

The strong adherence of bacteria to the alveolar epithelium, their subsequent replication and the initiation of host damage responses, collectively lead to the classic evolution of pneumonia. Innate immune defenses, together with products secreted by bacteria, and cell surface-anchored bacterial components drive this process. The toxin pneumolysin (that produces pore formation) disrupts the alveolar epithelium, while edema fluid accumulates in the alveolar space, as a result of the alteration of the vascular permeability [108]. During this early host response, *S. pneumoniae* sticks tighter to the alveolar epithelium through the use of several adhesins or pili [109].

The pneumococci together with other respiratory pathogens have developed a common strategy to advance mucosal disease to bacteremia, which is named "innate invasion". For this process the platelet-activating factor receptor located in the host cell surface, that binds phosphorylcholine at the bacterial surface, plays a key role. This binding initiates the uptake of *S. pneumoniae* into a vacuole that moves across the host cell spreading the bacteria all over the cell, where they can be released to seed the bloodstream [110]. When bacteremia (presence of bacteria in blood) happens, the risk of meningitis increases, since the pneumococcus can adhere specifically to cerebral capillaries, and once in the cerebrospinal fluid initiate the inflammatory response in the brain [102].

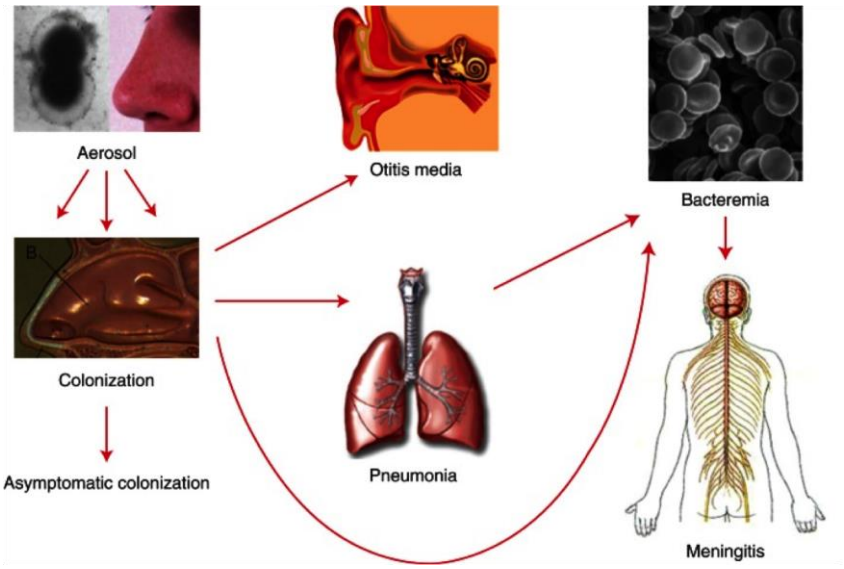

Figure 1.30. Progression of the pneumococcal disease. Figure from [111]

Epidemiology and emergence of antibiotic resistant strains

Pneumococcal infections cause more deaths than any other vaccine-preventable bacterial disease, being especially susceptible to the pathogen, children between 6 months and 4 years and adults over 60. It is estimated that 25 % of all community-acquired pneumonia (CAP) is caused by the pneumococcus [112]. Introduction of a conjugate vaccine has reduced the incidence of invasive disease [102, 113], although epidemics of disease have reappeared in locations such as chronic care hospitals, military camps and day care centers, which have not occurred since the pre-antibiotic era.

A matter of concern is the increased emergence of antibiotic resistance among the pathogens that cause CAP, and especially the pneumococcus, observed in the past

two decades. This phenomenon is occurring worldwide and involves all classes of antimicrobial agents to a greater or lesser extent [114, 115]. The Canadian Bacterial Surveillance Network shows the progressive rise of resistance among *S. pneumoniae* to penicillin, trimethoprimsulfamethoxazole, macrolides and fluoroquinolones. Data from a study of the Tracking Resistance in the United States Today also shows a steady rise in pneumococcal resistance against common antibiotics, as well as an increase in multidrug-resistant *S. pneumoniae* [116]. The incidence of penicillin-resistant pneumococcus increased from 0 in 1988 to 7 % in 2001, while the incidence of resistant strains to trimethoprim-sulfamethoxazole increased from 3.7 % to 12 % in the same period. Additionally the frequency of macrolide-resistant pneumococci has also increased; the number of erythromycin-resistant strains grows from 1.2 % to 13.1 %, and the number of clindamycin-resistant organisms increased from 1.2% to 5.8% (Fig. 1.31) [116]. Of greater concern is the rise of the frequency of multidrug-resistant *S. pneumoniae*, which means strains resistant to three or more antimicrobial classes, most commonly penicillin, trimethoprim-sulfamethoxazole, and macrolides [116].

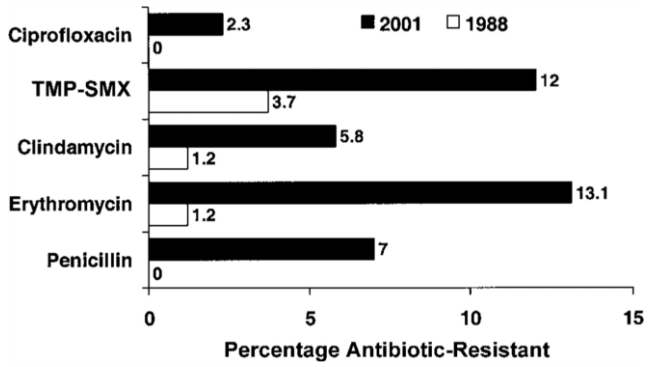

Figure 1.31. Antibiotic resistance trends for *Streptococcus pneumoniae* in Canada. TMP-SMX: rimethoprim-sulfamethoxazole. Figure from [116].

All these alarming data evince the necessity to develop new efficient antibacterial drugs against the pneumococcus. Here we proposed the rational design of new medicines targeting the FAD synthetase of *S. pneumoniae* (*Spn*FADS), which appears to be a strategy worthy to be explored [89]. Therefore, a first characterization of *Spn*FADS seems to be a good starting point to get this purpose.

3.4.2. Mycobacterium tuberculosis and tuberculosis

Tuberculosis (TB) is the world leading cause of death from bacterial infectious diseases. The disease affects 1.8 billion people/year, one third of the entire world population (data from the World Health Organization, 2015).

M. tuberculosis is the causative agent of TB. This bacterium was first described in 1882 by Robert Koch, who subsequently received the Nobel Prize in 1905 for this discovery, therefore the bacterium is also known as "Koch´s bacillus".

Physiology and structure of M. tuberculosis

M. tuberculosis is part of the *M. tuberculosis* complex, together with *M. bovis*, *M. bovis* BCG, *M. africanum* and *M. microti* [117, 118]. All these organisms share 99% of sequence identity, although they are very different regarding phenotype and pathogenicity [119].

M. tuberculosis is a non-motile rod shaped bacterium. This bacterium is an obligate aerobe, and a facultative intracellular parasite, normally of macrophages. It is a slow-growth bacterium and divides every 15-20 hours, for this reason it takes 4-6 weeks getting dense cultures. Under adverse conditions, *M. tuberculosis* can stay in a latent state, delaying its growing from some days to several years [118]. Regarding its culture conditions, two media can be used to grow this mycobacteria: Middlebrook´s medium, which was designed to protect organisms against a variety of toxic agents [120]; and Lowenstein-Jensen medium, which is an egg-based medium. In both media, colonies appear small and buff colored after 4-6 weeks of incubation. *M. tuberculosis* belongs neither to Gram-positive, nor to Gram-negative bacteria, since it does not show the chemical characteristics of either, although the cell wall contains peptidoglycan (murein). Gram stain on mycobacterium cells yields (and not always) very weakly Gram-positive stain, and therefore, cells are referred as "ghosts". Instead, acid-fast stains such as Ziehl-Neelsen, are used to identify the bacillus with a microscope.

The cell wall of M. tuberculosis

The mycobacterial cell wall requires special attention, since it is unique among prokaryotes, and one of the virulence determinants of mycobacteria. The wall has an external membrane that shows extremely low permeability [121, 122]. Chemically,

the wall is an intrinsically complex structure, made of peptidoglycan, lipids and different proteins [123, 124]. Over 60% of the cell wall are lipids, with three major components:

-Mycolic acids; that are alpha-branched lipids. These lipids are molecules highly hydrophobic that form a lipid shell around the organism, affecting the permeability of the cell wall. Mycolic acids are important virulence determinants, since protect the bacteria from the attack of cation proteins [125].

-Cord factor; is the primary glycolipid found on the surface of mycobacteria cells [126]. This molecule induces the disposition of the cells into long and slender formation. Cord factor is key for the survival of the pathogen within the hosts [127, 128], altering immune responses, inducing granulomas formation and inhibiting tumor growth [129].

-Wax-D; located in the cell envelope, is the major component of Freund´s complete adjuvant [130].

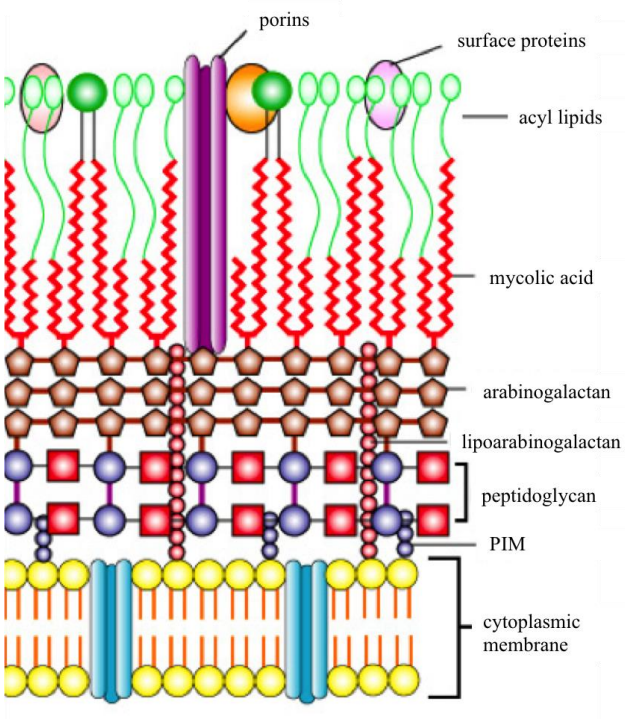

Figure 1.32. Structure and chemical composition of the cell wall of *M. tuberculosis*. Figure modified from Doc Kaiser's microbiology website Community College of Baltimore County.

Regarding the protein fraction, different membrane-associated proteins specific of *M. tuberculosis* have been identified, such as lipoproteins and antigens recognized by

B and T lymphocytes. The function of most of these proteins remained unclear, although they seem to play a key role in the functionalization of the cell wall [122].

Apparently, the mycobacterial cell wall is involved in mycobacteria resistance against different drugs. Additionally, differences in the composition of the mycolic acids might affect the fluidity and permeability of the bilayer. That fact would explain the different susceptibility to lipophilic drugs observed among mycobacterial species. Hydrophilic inhibitors are expected to cross the cell wall through porin channels (Fig. 1.32) [121].

Virulence factors

M. tuberculosis owns different and multifaceted virulence factors. This organism does not produce any toxins, but it shows a huge repertoire of structural and physiological properties, that contribute to its virulence. Among these pathogenicity determinants, we can highlight; growth within the macrophage [131], detoxification of reactive oxygen species [132], slow generation time and adherence factors [133].

Pathogenesis and invasion cycle of M. tuberculosis

M. tuberculosis is an exclusively human pathogen. The seriousness of the infection mainly depends on two parameters; the bacterial virulence, and the host resistance against the infection [134]. There are two types of infections, primary and post-primary. A complex network of interactions is established between the bacteria and the host, that can lead to the bacterial neutralization (no infection), to the log-term survival of the bacteria (latent infection), or to an active disease (primary tuberculosis) [135, 136].

During the infection the bacteria enter into the alveolar macrophages of the host through specific binding to different surface molecules [137, 138]. Through the activation of mechanisms that avoid the phagosome-lysosome fusion, the bacteria can survive and proliferate within the macrophage [139]. Then, the infection draws on through a granuloma formation, as a consequence of the migration of other immune cells to the infection spot [139]. The granuloma function is to content the pathogen, preventing their growth and spreading to the alveolar tissue and to the lungs, and also to focus the immune response [137]. After infection, macrophages die either through necrosis or apoptosis, although sometimes they survive. This last

fact would determine the result of the infection [140]. If the immune system detects and neutralizes the bacillus, the host will not develop the disease, while if the mycobacteria evade the immune response and survive, the infectious process will continue. In this situation, the host could develop the tuberculosis disease, or the bacteria could stay in a latent state, awaiting more favorable future conditions to continue the infection [141-143].

The diagnosis of tuberculosis requires detection of acid-fast bacilli in sputum through the Ziehl-Neelsen method. Therefore, bacteria must be cultured, which can take 4-6 weeks. The BACTEC system is a faster alternative (it takes 9-16 days) to detect the bacilli [144]. The presence of mycobacterial antibodies can also be detected through the tuberculin test, which consists on a skin test that uses as antigen a purified protein derivative [145].

Treatment and emergence of multi drug-resistant tuberculosis strains

To minimize the apparition of resistances, the tuberculosis treatment involves the use of multiple drugs to which the organisms are susceptible. Therefore, tuberculosis is normally treated using four different drugs; rifampin, isoniazid, pyrazinamide and ethambutol and/or streptomycin [146]. Tuberculosis treatment lasts 6-9 months. When this four-drugs treatment is used at the beginning of the therapy, the recovery probability of the patient is very high.

A different strategy against tuberculosis consists on vaccination. The actual anti-tuberculosis vaccine, *Bacillus Calmette-Guérin* (BCG), is a live attenuated vaccine used around the world. This vaccine protects against severe forms, although shows highly variable efficiency against pulmonary forms of tuberculosis, which are responsible for the spread of the bacillus. During the last decade, new candidates have been proposed as anti-tuberculosis vaccines, being the general objective to develop an effective vaccine, that protects against the pulmonary forms of the disease [147].

Resistance to anti-tuberculosis drugs can appear due to the mismanagement of these drugs [148]. Attending to the number of drugs to which the bacilli is resistant, we can distinguish between multidrug-resistant strains (the bacteria are resistant to at least two of the best drugs, normally isoniazid and rifampin, which are considered first-line drugs), and extensively drug resistant strains (the bacterial show resistance

against isoniazid and rifampin and also against any fluoroquinolone, and against at least one of the three second-line drugs) [149, 150]. Patients with extensively drug resistant tuberculosis usually have worse treatment outcomes.

Epidemiology

Approximately, one-third of the world´s population has been infected with *M. tuberculosis* (data from World Health Organization, 2011). Nevertheless, the 90-95% of infections do not progress to an active disease, but it is estimated that 8.6 million of chronic cases were active in 2012 (data from the World Health Organization http://www.who.int/tb/publications/global_report/en/). Tuberculosis is the second-most common cause of death from infectious disease, after those due to HIV. Tuberculosis has a greater incidence in developing countries, almost 80% of the population in Asia and Africa present positive results in the tuberculin test, while in USA only 5-10% of the population is tuberculin-positive [151] (Fig. 1.33). The control of TB disease is not easy due to different factors, such as the difficulty to develop an effective vaccine, the expensive and long diagnostic process and treatment and the emergence of drug-resistant strains in the 80s [151]. Tuberculosis appears then, as a main problem of public health, and the development of a vaccine, or the discovery of new effective anti-tuberculosis agents is a topic worthy of study and research.

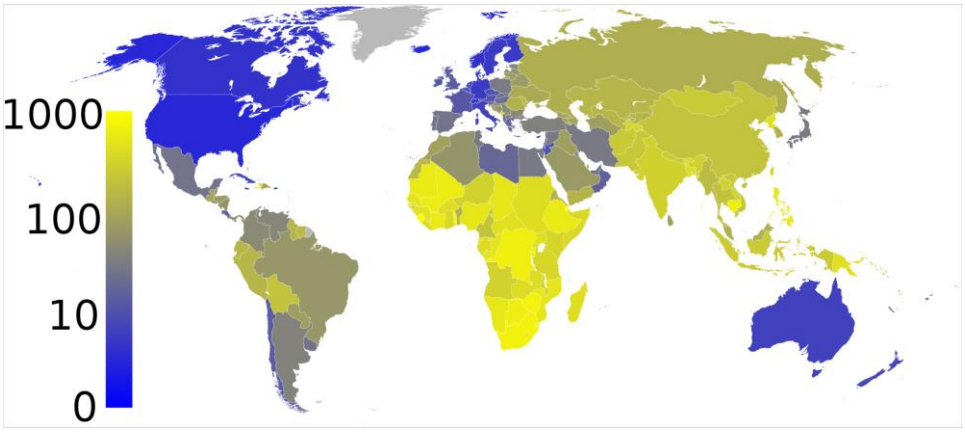

Figure 1.33. Number of cases of tuberculosis per 100000 people around the world. In 2007 countries of sub-Saharan Africa, and also of Asia were the ones that registered more new cases of tuberculosis.

3.5. *Ca*FADS, *Spn*FADS and *Mt*FADS as drug targets

The indiscriminate use of antibiotics has produced the apparition of immune bacteria. Thus, the apparition of multi-drug resistant microorganisms [11] forces us to find new antimicrobial drugs targeting new essential biomolecules. As previously said, FADSs seem good potential targets [89], since their selective inhibition produces lack of FMN and FAD, with the subsequent accumulation of the apo forms of essential flavoproteins that are unable to carry out their functions [32, 33, 152], and finally death [153, 154].

In that way, the selectively inhibition of the FADSs from *S. pneumoniae*, and *M. tuberculosis*, might be an effective strategy to neutralize these pathogens and to treat the diseases they produce. The RFK module of bacterial FADSs shows homology with eukaryotic RFKs but the FMNAT module does not [74, 85, 155, 156] (Fig. 1.34). Therefore, inhibiting this second module is the best option in the drug development process [89].

Unfortunately, until the date attempts to produce stable purified *Mt*FADS have failed, and *Spn*FADS shows some characteristics (low Tm, and need of reduced flavins for the FMNAT activity) that hinder performing some high throughput assays. Therefore, the use of *Ca*FADS, which is the member of the family best characterize [76, 84-86, 90, 95, 99] as model for both proteins, might be good as first approximation. *Spn*FADS presents only 29% sequence identity with *Ca*FADS, but it owns the consensus sequences of prokaryotic FADSs and both proteins show very similar structures (Fig. 1.28). *Mt*FADS sequence shows 45% identity with *Ca*FADS that increases up to 59% when considering conservative substitutions [76].

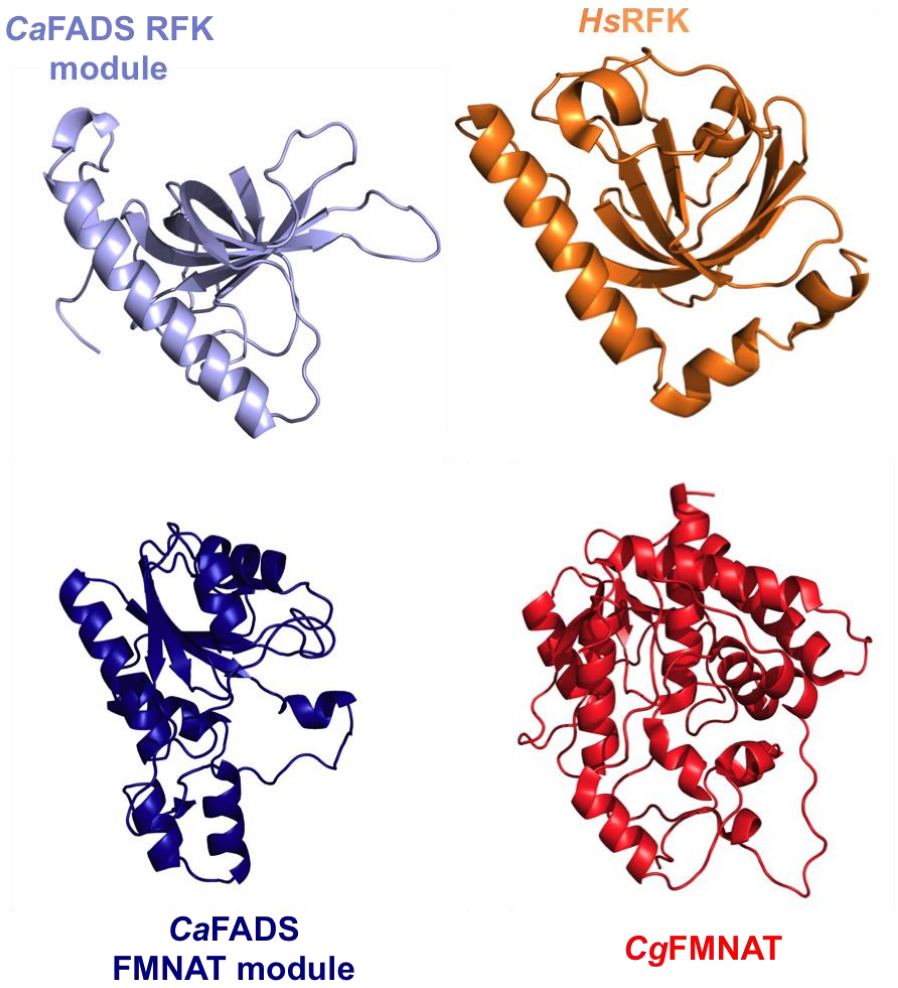

Figure 1.34. Cartoon representation of the overall structures for the RFK and FMNAT modules of *Ca*FADS, and the RFK and FADS enzymes from *Hs*RFK and *Candida glabrata* (*Cg*FMNAT), respectively. The RFK and FMNAT modules of the prokaryotic bifunctional *Ca*FADS are displayed in light and deep blue, respectively, while the monofunctional eukaryotic *Hs*RFK and *Cg*FMNAT are shown in orange and red, respectively. The *Ca*FADS RFK module shares structural elements and catalytic site with the correspondent monofunctional enzyme, but that is not the case of the *Ca*FADS FMNAT module and the eukaryotic *Cg*FMNAT. PDB codes 2x0k, 1q9s and 3fwk for *Ca*FADS, *Hs*RFK and *Cg*FMNAT, respectively.

4. Objectives

The main goal of this thesis is to further delve into the molecular mechanisms of prokaryotic bifunctional FADSs, focusing on the regulation of their catalytic properties and on the similarities and differences among species. This knowledge will help in settling the bases to the use of prokaryotic FADSs as targets in the development of antimicrobials. With these general aims, in this study we tackle the following partial goals:

- To determine the roles of residues at the trimer interface of the *C*aFADS dimer-of-trimers in the formation of oligomeric species, in the mechanisms of the enzyme catalytic cycles, and in the interaction with substrates and products.

- To propose a kinetic and thermodynamic model that explains the inhibition produced by excess of the RF substrate in the RFK activity of *Ca*FADS.

- To carry out the first functional characterization of the FADS from the human pathogen *S. pneumoniae*, including the description of its RFK and FMNAT catalytic cycles, its oligomerization tendency and the interaction with ligands.

- To set the bases of the different strategies adopted by *Ca*FADS and *Spn*FADS to regulate their RFK activities.

- To develop an activity-based High Throughput Screening (HTS) assay to discover inhibitors of the FMNAT activity of *Ca*FADS.

- To evaluate the potency of the identified HTS hits on the RFK and FMNAT activities of this enzyme, and to characterize the inhibition mechanism and the protein binding affinities of the best hits inhibiting the *Ca*FADS FMNAT activity.

-To evaluate the specificity of the inhibitors for *Ca*FADS FMNAT activity versus other prokaryotic and eukaryotic FADS.

Chapter II

Materials and Methods

1. General techniques in Molecular Biology

1.1. Production of thermo-competent cells

Competent cells are those that are able to take up extracellular DNA from their environment in a process called transformation. During the production of competent cells the cellular membrane is weakened due to the formation of pores, across which plasmid DNA gets internalized without provoking cellular collapse.

To produce competent cells, a chemical treatment with $CaCl_2$ was used [157]. A single *Escherichia coli* colony was grown in 1 ml of sterile Luria Bertani (LB) medium, containing no antibiotics. The culture was grown at 37ºC overnight (O.N.) with gently agitation. 10 ml of LB were inoculated with 100 µl of the culture and cells were grown in the same conditions until reaching the exponential phase, that is until getting an $O.D._{600\ nm}$= 0.3-0.6 AU. At this moment the culture was centrifuged for 10 min at 4ºC and the supernatant was discarded. Cells were resuspended in 0.05 M sterile $CaCl_2$ (1ml of $CaCl_2$ per 5 ml of culture) and incubated during 20 min in ice bath. 200 µl aliquots of competent cells were preserved in 20 % glycerol (v/v) and frozen at -80 ºC.

1.2. Transformation of thermo-competent cells through heat shock

For the transformation process, competent *E. coli* cells previously prepared and preserved at -80ºC were used. The transformation was performed through heat shock at 42 ºC. Cells were pre-incubated in ice bath to favor slow defrosting. 100 µl of defrosted competent cells were added to sterile eppendorf tubes containing the transforming DNA, typically 2-5 µl (40-100 ng) of plasmid DNA. Negative and positive controls were included. 10 µl of autoclaved water or 4 µl of plasmid DNA, showing high transformation efficiency, were added to the cells as negative or positive controls respectively. The mixtures were incubated in ice bath for 15 min and then at 42 ºC for 50 s, which produces the heat shock that originates the pores across which the DNA is taken. Immediately after, the samples were incubated in ice for 2 min. Finally, 900 µl of LB medium, without antibiotic and preheated at 37ºC, were added to each eppendorf tube under sterile conditions. The samples were then incubated at 37 ºC and 180 r.p.m. during 2 hours.

To check the success of the transformation a culture in solid medium was performed. The cells were grown in LB-agar plates containing the selection antibiotic, 30 µg/ml kanamycin for pET28a and 100 µg/ml ampicillin for pET15b. 100 µl of each

transformation sample were plated. The remaining volume was centrifuged and the precipitated was resuspended in 100 µl of LB medium that were plated again. The plates were incubated at 37ºC until apparition of colonies (14-18 h). The grown colonies assimilated the corresponding antibiotic resistance gene and therefore the transforming plasmid DNA.

1.3. Isolation of plasmid DNA

A single colony product of the transformation was inoculated in 10 ml of LB medium containing the selection antibiotic. The culture was incubated O.N. at 37ºC and 180 r.p.m. agitation. The extraction of the plasmid DNA was carried out using the GenElute™ Plasmid Miniprep Kit (Sigma-Aldrich®), based on cellular lysis methods in alkaline medium and plasmid purification through its union to a fiberglass matrix.

2. Production of the recombinant *Ca*FADS and its variants

All the plasmids codifying WT *Ca*FADS and the variants here analyzed were produced in advance to the start of this thesis.

Gen *ribF* codifying the WT protein had been cloned in the expression plasmid pET28a (+) under the promoter of the phage T7, between the *Ncol/BamHI* restriction sites [76]. The different variants of the protein were produced by the company Mutagenex (www.mutagenex.com) introducing the appropriate mutations in the construct *Ca*FADS-pET28a (+).

2.1. Over-expression of *Ca*FADS and its variants

Culture of WT *Ca*FADS and of its variants (including Δ(1-182) *Ca*FADS) were initiated either from 100 µl of liquid cultures preserved in glycerol at -80 ºC, or from a colony in LB-agar solid medium. In both situations 10 ml of LB medium containing 30 µg/ml kanamycin were inoculated with the bacteria and incubated at 37ºC for ~8 h under 180 r.p.m. agitation. After that, the pre-cultures were transferred to containers with 200 ml of LB medium and 30 µg/ml kanamycin, and were incubated O.N. in the same conditions. The following morning, 2 l Erlenmeyer flasks containing each one 1 l of medium, were inoculated with 10 ml of the overnight cultures and were incubated until reaching $O.D._{600nm}$= 0.5–1 AU. In that moment the expression of the proteins was induced through addition of Isopropyl β-D-1-thiogalactopyranoside (IPTG) at a final concentration of 1 mM. Then, the cultures were incubated O.N. at 37 ºC under agitation. The cells were harvested at 4 ºC by several rounds of 10 min centrifugations at 18000 x

g. The precipitate was wash with 0.15 M NaCl and the cells were centrifuged again. The supernatant was discarded and the cellular pellet was preserved at -20ºC. Generally, the yield was 5-7 g of cells per liter of culture.

2.2. Purification of *Ca*FADS and its variants

2.2.1. Preparation of the crude extract

E. coli cells overexpressing *Ca*FADS, or its variants, and produced according to section 2.1. were resuspended in 5-10 ml of lysis buffer (100 mM Tris/HCl, pH 8.0, 10 mM EDTA, 12 mM β-mercaptoethanol, 1μM PMSF) per gram of cell. Cells were broken through ultrasonic treatment at 4ºC in a sonicator DRH UP200 DR Hielsher, using 16 cycles of 45 s with 1 min rest between them. Then, the lysis solution was centrifuged at 4 ºC and 48000 x g for 45 min. The yellow color of the supernatant (crude extract) is due to a flavin initially bound to the *Ca*FADS, which has been identified as FAD [76].

2.2.2. Fractionation with ammonium sulphate

The resulting crude extract was fractionated through addition of 45 % ammonium sulphate in ice bath (25.8 g per 100 ml of crude extract). The salt addition was performed under mild stirring of the solution, to avoid the apparition of higher local concentrations. The precipitated fraction was removed by centrifuging the extract at 4 ºC and 48000 x g for 45 min.

2.2.3. Phenyl-Sepharose affinity chromatography

The crude extract was loaded upon a Phenyl-Sepharose High Performance column (Amersham Biosciences, GE Healthcare) previously equilibrated with 50 mM Tris/HCl, pH 8.0, 45 % ammonium sulphate. The column was washed with 50 mM Tris/HCl, pH 8.0, 13.5 % ammonium sulphate until the yellow flavin, released from *Ca*FADS [76], has completely eluted. Then, the protein was eluted through linear 13.5→0 % ammonium sulphate reverse gradient in the same buffer. Absorbance at 280 nm was registered while 6-8 ml fractions were collected. Fractions corresponding with peaks containing protein were analyzed through 17 % SDS-PAGE, and those containing more and purer *Ca*FADS were selected. The selected fractions were dialyzed against 50 mM Tris/HCl, pH 8.0.

2.2.4. DEAE-Cellulose anionic interchange chromatography

A second DEAE-Cellulose anionic interchange chromatography was performed. The dialyzed protein was loaded upon the column previously equilibrated with 50 mM Tris/HCl, pH 8.0. The column was washed with 50 mM Tris/HCl, pH 8.0, 0.1 M NaCl and then the protein was eluted using a linear 0.1→0.5 M NaCl gradient in the same buffer. 6 ml fractions were collected while absorbance at 280 nm was recorded. Once again, fractions corresponding to peaks that contain protein were analyzed by 17 % SDS-PAGE. Fractions containing the pure *Ca*FADS were selected and dialyzed against 20 mM PIPES, 10 mM $MgCl_2$, pH 7.0.

2.2.5. Size exclusion chromatography

*Ca*FADS is purified as a mixture that contains monomeric protein and small proportions of other oligomeric species [85]. These different species were separated through size exclusion chromatography, using the Superdex^{TM} 200 10/300 GL column, previously calibrated with the Gel Filtration Calibration Kit LMW (both from GE Healthcare). The mobile phase was 20 mM PIPES, 10 mM $MgCl_2$, pH 7.0. The pure monomeric *Ca*FADS was preserved at -20 ºC (Fig. 2.1).

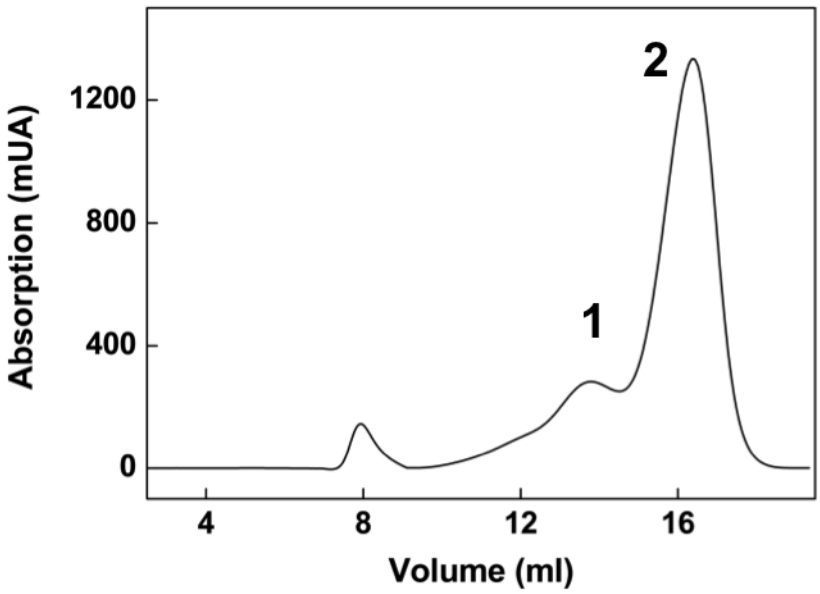

Figure 2.1. Elution profile for the separation by size exclusion chromatography of the different oligomeric (1) and monomeric (2) species from a pure sample of *Ca*FADS. The peak showing an elution volume of 8 ml corresponds to denatured protein. The mobile phase was 20 mM PIPES, 10 mM $MgCl_2$, pH 7.0.

3. Production of Δ (1-182) *Ca*FADS

E. coli cells overexpressing Δ(1-182) *Ca*FADS were produced as indicated in 2.1.

3.1. Purification of Δ(1-182) *Ca*FADS

The RFK module of *Ca*FADS was purified following a modification of the protocol described for the full-length protein (section 2.2) [84].

After preparation of the crude extract through sonication, a fractionation with 20 % ammonium sulphate (10.6 g per 100 ml of crude extract) was performed. The supernatant was loaded onto a Phenyl-Sepharose column previously equilibrated with 50 mM Tris/HCl pH 8.0 20 % ammonium sulphate, which allowed eliminating the flavin bound to the protein as well as other protein impurities. The purest fractions, which presented impurities of higher molecular weight, were concentrated in saccharose for 16 hours and then loaded in the Superdex^{TM} 200 10/300 GL column (GE Healthcare). This column has been previously equilibrated with 50 mM Tris/HCl pH 8.0, 150 mM NaCl. The purity of the different fractions was determined by 14 % SDS-PAGE. Fractions containing the pure RFK module were dialyzed against 20 mM PIPES pH 7.0, and quantified using the theoretical extinction molar coefficient in water at 279 nm (14.44 mM^{-1} cm^{-1}). The pure protein was preserved at -20 ºC.

4. Production of *Spn*FADS

4.1. Cloning and over-expression of *Spn*FADS

The DNA sequence encoding *Spn*FADS (accession number ADM84672, SPAP_1083), containing the *Nde*I and *Xho*I restriction sites and codon optimized for its expression in *E. coli,* was synthetically produced by Gen-Script. This DNA sequence was cloned into a modified pET-15b vector (Novagen) that contains an N-terminal His_6-Tag sequence followed upstream by a site for a PreScission Protease (GE Healthcare). The final construct was sequenced by *Sistemas Genómicos* (www.sistemasgenomicos. com). The BL21 Star ^{TM} (DE3) *E. coli* strain (*Invitrogen*) was transformed with the construct following the protocol described in 1.2. The transformed cells were grown at 37 ºC in 2xTY medium (1.6 % tryptone, 1% yeast extract and 0.5 % NaCl), containing ampicillin 100 μg/ml (which was the selection antibiotic in this case) until reaching an $O.D_{600}$ ~0.6. Then the expression of the protein was induced through addition of 1 mM IPTG at 18 ºC during 20 hours. After that, cells were harvested by centrifugation at 4 ºC.

4.2. Purification of *Spn*FADS

4.2.1. Preparation of the crude extract

E. coli cells containing overexpressed *Spn*FADS were resuspended in 2 ml of lysis buffer (20 mM sodium phosphate pH 7.4, 10 mM imidazole, 1mg/ml lysozyme, 0.1 mg/ml DNAse and 0.2 mM protease inhibitor) per gram of cells. After 30 min incubation, cells were broken by ultrasonic treatment at 4ºC in a sonicator DRH UP200 DR Hielsher, using 10 cycles of 30 s with 30 s rests between them. The cellular pellet was discarded by 4 rounds of 20 min centrifugations at 4 ºC and 19000 x g.

4.2.2. His-trap affinity chromatography

The supernatant, which contains the soluble protein, was loaded onto a His-Trap affinity column (HisTrap HP, GE Healthcare), previously equilibrated with 20 mM sodium phosphate pH 7.4, 10 mM imidazole and 0.5 M NaCl. The column was washed with the same buffer and the flow-through discarded. Then the protein was eluted through linear 10→500 mM imidazole gradient in the same buffer. Absorbance at 280 nm was registered while 3 ml fractions were collected. Fractions corresponding with peaks containing protein were analyzed through 17 % SDS-PAGE and those containing the purest *Spn*FADS were selected. Buffer was exchange to 25 mM Tris/HCl, pH 7.4, 0.15 M NaCl, using a HiPrep Desalting Column (GE Healthcare).

4.2.3. Cleavage of the His-Tag and His-trap/GS-trap chromatography

The protein was quantified using the Bradford assay [158] and the His_6-Tag was removed by 48 hours incubation at 4ºC with the PreScission protease (GE Healthcare). 2 mg of protease per 10 mg of protein were added. To eliminate both the remained His_6-Tagged *Spn*FADS and the protease, which is fused with GST to facilitate its elimination, the solution was loaded onto the HisTrap HP and GST Trap (GE Healthcare) columns connected as shown in Fig. 2.2.

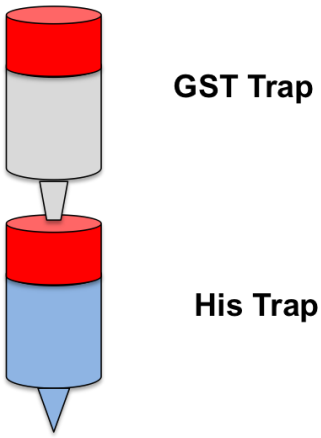

Figure 2.2. Disposition of the GST Trap and the HisTrap columns along purification of *Spn*FADS.

5. Biophysical characterization of proteins

5.1. Spectroscopic characterization

5.1.1. Absorption spectroscopy in the UV-visible

Absorption spectra in the UV-visible region were routinely recorded for all the proteins to check their integrity and to calculate their concentrations. The spectra were registered between 250 and 700 nm at 25 ºC in 20 mM PIPES pH 7.0 using a Cary 100 spectrophotometer (Agilent Technologies). Quartz cuvettes with a 10 mm light path were used, being the scan velocity 200 $nm.min^{-1}$.

Proteins were quantified according to the Beer-Lambert equation:

$$Abs = \varepsilon.c.l \qquad \text{Eqn. 2.1.}$$

Where Abs is the registered absorbance at a given wavelength, ε the molar extinction coefficient at that particular wavelength and l the light path of the cell. The extinction molar coefficients, at 278 nm, were 27.8 $mM^{-1}.cm^{-1}$ for the WT *Ca*FADS and all its variants, with the only exceptions of Δ (1-182) *Ca*FADS and F206W variant whose theoretical coefficients were 14.44 and 33.9 $mM^{-1}.cm^{-1}$, respectively. The theoretical extinction molar coefficient for *Spn*FADS was 28.8 $mM^{-1}.cm^{-1}$.

5.1.2. Circular dichroism

Circular dichroism (CD) spectra for the WT *Ca*FADS and all its variants, as well as for *Spn*FADS, were recorded to check their correct folding. The far UV region of the spectrum provides information about the secondary structure of the proteins, while the near UV region depends on the aromatic residues and their environment [159-161].

Therefore this last spectral region procures information about the tertiary structure of the proteins [162].

CD spectra were recorded at 25 ºC in a spectropolarimeter Chirascan (Applied Photosystem Ltd.). The CD spectra in the far UV region were registered between 190 and 260 nm using a 0.1 cm light path quartz cuvette. The protein concentration was ~5 μM and the buffer 5 mM PIPES, pH 7.0, 10 mM $MgCl_2$. Low buffer concentration was used since organic buffers absorbs in this spectral region, saturating the detector at high concentrations. Near UV-CD spectra were obtained also at 25 ºC between 260 and 600 nm. In this case a 0.4 cm light path quartz cuvette was used, being 20 μM the protein concentration and the buffer 20 mM PIPES, pH 7.0 10 mM $MgCl_2$. The resolution was 5 nm, both for near and far UV-CD spectra. The number of measurements per point was 10 s in the case of the far UV region and 16 s for the near UV. CD spectra were corrected resting the signal corresponding to the buffer. The CD-signal was expressed as mean residue ellipticity (MRE, [θ mr]):

$$[\theta_{mr}] = \frac{\theta}{10.c.l.(N-1)} \qquad \text{Eqn.2.2.}$$

Where θ is the signal (mdeg), c is the protein concentration, l the light path of the cuvette and N the number of residues of the protein.

5.1.3. Analysis of the formation of flavin-FADS complexes through difference spectroscopy

Difference spectroscopy allows observing changes in the absorption spectra of some ligands when they are interacting with proteins [163]. When the ligands are flavins, these variations are consequence of perturbations in the dielectric environment of the isoalloxazine ring, produced by residues of the protein close to it. Comparing the spectra obtained for the variants with those registered for the WT, differences in the way in which flavin and *Ca*FADSs interact can be detected [164].

Difference spectra for the flavin-*Ca*FADS complexes were obtained, both in the presence and in the absence of ADP. The spectra were recorded at 25ºC in a double beam spectrophotometer Cary 100 (Agilent Technologies), using two cuvettes of 1 cm light path. In a typical experiment the sample cuvette contains 600 μl of ~5 μM *Ca*FADS while the reference one contains the same volume of buffer. Sequential additions of the same volume of ~20 μM flavin were performed over both cells, until saturation of the protein was reached. For the experiments performed in the presence of ADP, it was added to 450 μM at both the reference and sample cuvettes. All the

experiments were carried out in 20 mM PIPES, pH 7.0, 10 mM $MgCl_2$. After each addition and previously to recording the spectra, all the samples were incubated at 25ºC for 3 min.

5.2. Analysis of the formation of quaternary organizations

As indicated in section 2.2.5, *Ca*FADS stabilizes oligomeric assemblies [85, 100]. To determine the role that the mutated residues play in the stabilization of such structures, size exclusion chromatographic assays were performed, as well as native electrophoresis and atomic force microscopy (AFM) experiments. The influence of the different substrates and products in the formation of the oligomeric assemblies was also analyzed through these methods.

The same techniques were also used to elucidate whether *Spn*FADS forms macromolecular assemblies.

5.2.1. Native electrophoresis

Different fractions of WT *Ca*FADS and of its variants were analyzed at 4 ºC by native electrophoresis using 10 % polyacrylamide gels without SDS (N-PAGE). Gels were pre-run for one hour to eliminate remainders of acrylamide. 20 µl of each sample (containing loading buffer (SB) without SDS) were loaded into the gel. A potential difference of 90 mV was applied until the disappearance of the coomasie front. Protein spots were visualized with coomasie stain. Since in native electrophoresis the mobility of the proteins depends on their weight and also on their charge, results only procure qualitative information about the presence of oligomeric states, and its molecular weights cannot be estimated (Fig. 2.3).

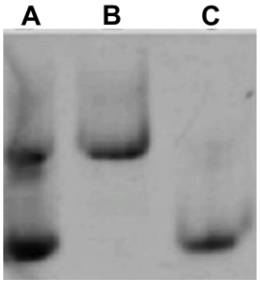

Figure 2.3. 10 % native gel (N-PAGE) showing: (A) Mixture fraction containing monomeric and oligomeric *Ca*FADS, (B) Oligomeric *Ca*FADS and (C) monomeric *Ca*FADS.

5.2.2. Size exclusion chromatography

To separate and analyze the different oligomeric assemblies, 500 µl of ~100 µM *Ca*FADS samples were loaded onto a SuperdexTM 200 10/300 GL column (GE Healthcare), previously equilibrated with 20 mM PIPES, pH 7.0, and calibrated with the Gel Filtration Calibration Kit LMW (GE Healthcare). The column was connected to an Akta Prime FPLC System (GE Healthcare). The obtained chromatograms were fit to a set of Gaussian functions (Origin 8.0, OriginLab) (Fig. 2.4) to determine the number of components, their estimated masses and relative areas. Taking into account the difficulty derived from the different hydrodynamic radius of the different protein organizations (monomer, dimer, trimer, tetramer, hexamer; different volumes and shapes) [165] for unequivocally correlating them with the elution volumes, averaged values have been taken for peaks mainly considered as monomeric or quaternary assemblies.

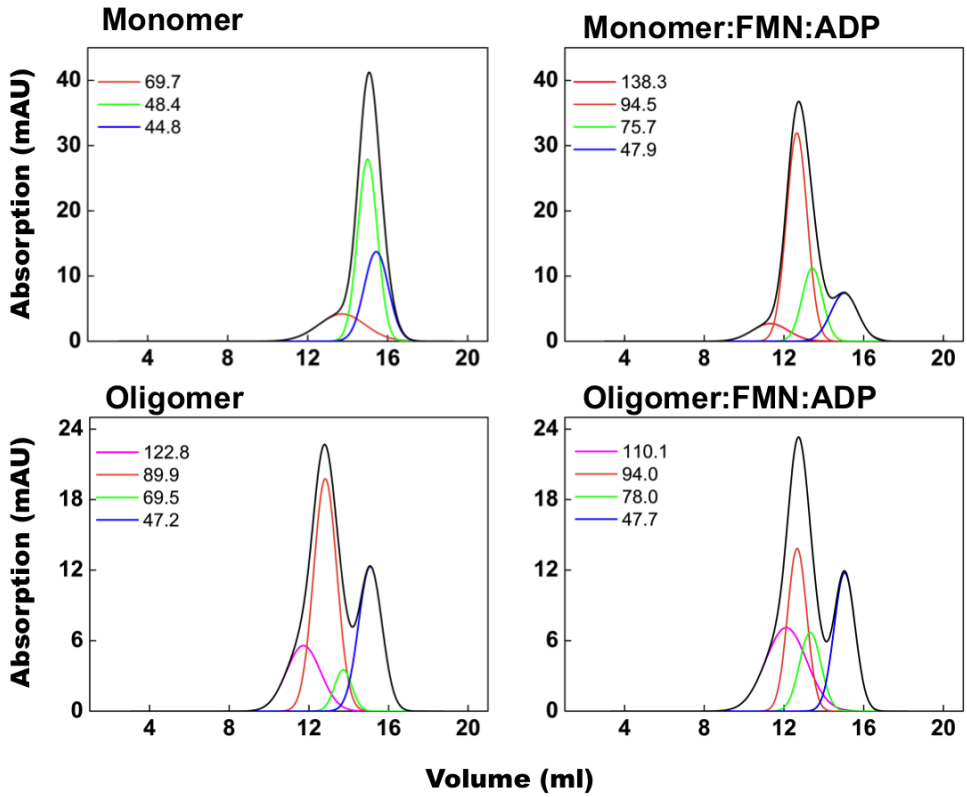

Figure 2.4. Example of fitting analysis to Gaussian functions of the gel filtration chromatograms, obtained for the *Ca*FADS variant E301K, after incubating the samples at the indicated conditions. The chromatograms are shown in black lines and the different populations assigned by the Gaussian analysis in colored lines. The legend shows the calculated molecular weight for the maxima peak of each population. Chromatograms obtained at 4ºC, in 20 mM PIPES, pH 7.0.

5.2.3. Evaluation of the effect of substrates and products on the monomer-oligomer equilibrium

The purpose of this study was to determine the effect that the flavin (RF and FMN) and the adenine nucleotide (ADP and ATP) ligands have in the monomer-oligomer equilibrium of *Ca*FADS.

Monomeric and oligomeric *Ca*FADS samples, obtained through exclusion molecular chromatography (see section 2.2.5), were incubated at 25ºC for 30 min with different combinations of ligands. Reaction mixtures contained 25 μM *Ca*FADS (monomeric or oligomeric fraction), and the ligand (or combination of ligands) that was being studied, at a final concentration of 500 μM for ADP and ATP or of 100 μM for RF and FMN. The final reaction volume was 20-25 μl for the analysis by electrophoresis and 500 μl for the size exclusion chromatography.

For the experiments performed in the presence of a cross-linker, the samples were prepared in 50 mM Tris/HCl, pH 8.0, 10 mM $MgCl_2$. 2 mM bis(sulfosuccinimidyl)suberate (BS3) was added to the samples after its incubation with the ligand, and the resulting mixture was incubated for 30 min at room temperature. The Cross-linking reaction was stopped through addition of the quenching buffer (500 mM Tris/HCl pH 8.0) at a final concentration of 50 mM. Once again samples were incubated for 15 min.

The amount of monomer and oligomer in the samples was analyzed through different techniques according to the protocol used for its preparation.

- The samples produced in the absence of the cross-linker were analyzed by N-PAGE as we have indicated in section 5.2.1.
- The samples which were exposed to the cross-linker were examined by 10% SDS-PAGE. Denaturant electrophoresis was used since the cross-linker avoids breaking of non-covalent interactions that stabilize oligomeric structures. These interactions do not remain under denaturant conditions in the absence of the cross-linker. Loading buffer was added to the samples, which were boiled for 5 min before loaded onto the gel. 20 μl of each sample (containing loading buffer with the SDS denaturing agent), were loaded into the gel. A potential difference of 90 mV was applied until the disappearance of the coomasie front. Protein spots were visualized with coomasie stain. To estimate the weight of the different proteins, a molecular weight patron was included in one of the lanes.

- Both types of samples were finally analyzed through molecular exclusion chromatography as described in 5.2.2. In addition this technique allows estimating the molecular weight of each species.

5.3. Steady-state kinetic analysis of the RFK and the FMNAT activities

5.3.1. Qualitative study of the RFK, the FMNAT and the FADpp activities through Thin Layer Chromatography

The RFK, the FMNAT and the FADpp activities of *Ca*FADS and *Spn*FADS were qualitatively assayed by separation of the flavins produced during these reactions through Thin Layer Chromatography (TLC) [166, 167].

200 µl of reaction mixtures containing 50 µM RF or FMN, 250 µM ATP, 0.8 or 10 mM $MgCl_2$ (for the RFK or FMNAT reactions respectively), 1 µM *Ca*FADS or *Spn*FADS in 20 mM PIPES pH 7.0, were incubated at 25 ºC for 30 min. The reactions were stopped by boiling the samples for 5 min. To determine the effect that a reducing environment has in the RFK and FMNAT activities of *Spn*FADS, these reactions were also performed at different concentrations of sodium dithionite (0-16 mM).

Separation of flavins within the supernatant reaction mixtures was carried out through TLC in 200 x 200 x 0.25 mm glass sheets coated with SIL G-25 silica gel (Macherey- Nagel). Dipole-dipole interactions, between the adsorbent and the molecule that is being analyzed, are the predominant ones in separations by silica gel. Under these conditions the flavins elution order is RF-FMN-FAD (Fig. 2.5), since more polar molecules interact in a stronger way with the polar Si-O bonds of the silica gel, and show smaller retardation factors (R_f) than the less polar components [167].

150 µl of the reaction mixtures were loaded on a sheet previously activated at 110 ºC for 1 hour. A patron sample (a RF-FMN-FAD mixture) was included. Samples were applied at a distance of 2 cm from the border of the sheet, and separated enough to avoid their mixing. The application of the samples was performed in several times, loading 20 µl each time and drying between applications. A mixture of butanol:acetic acid:H_2O in proportion 12:3:5 was used as eluent. The chromatographic separation was executed during ~ 7 hours, in a tray hermetically closed that has been previously saturated with the eluent vapor. Flavin spots were visualized under UV light using a transiluminator.

FAD shows two different bands that correspond with its two molecular conformations (one open and the other one closed). One of these bands presents a very

small R_f value, while the displacement of the other is slightly higher than that of the FMN.

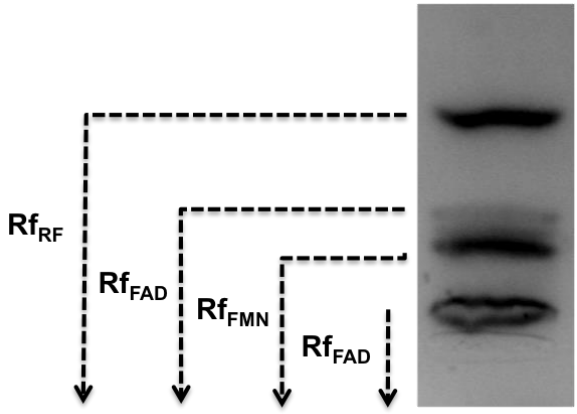

Figure 2.5. TLC separation of the flavins of the patron sample containing 50 μM RF, FMN and FAD, using as eluent a 12:3:5 mixture of butanol:acetic-acid:H_2O.

5.3.2. Quantitative analysis of the CaFADS riboflavin kinase (RFK) activity and determination of kinetic parameters through High Performance Liquid Chromatography (HPLC)

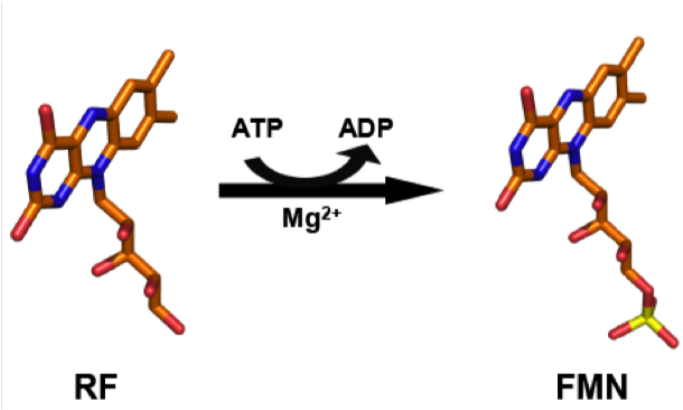

Figure 2.6. RF transformation into FMN catalyzed by the RFK activity of *Ca*FADS.

Chromatographic conditions for separation of flavins

The *Ca*FADS RFK activity (Fig. 2.6) was quantitatively analyzed by separating the flavins produced during this reaction through High Performance Liquid Chromatography (HPLC) [168]. For that purpose, an Alliance HPLC (Waters) system equipped with a 2707 Autosampler injector (Waters) and with a 2475 Multi-Wavelength fluorescence detector (Waters) was used. The chromatographic conditions for the flavin separation are displayed in Table 2.1.

Table 2.1. Chromatographic conditions for flavin separation from reactions mixtures through HPLC.

Stationary Phase	HSS T3 (4.6x150mm, 3.5 µm, Waters)[a]
Mobile Phase	5mM ammonium acetate, 40% methanol pH 6.0
Method	Isocratic
Flux	1ml/min
Detection System	Fluorescence, λ_{ex}=470 nm; λ_{em}=530 nm (gaining10)

[a]To prolong its lifespan, the column is preceded by a pre-column of the same material (4.6 x 20mm, 3.5 µm, Waters).

Under these conditions, flavin chromatograms were solved in 7 min, being the retention times 2.3, 3.5 and 5.5 for FAD, FMN and RF, respectively (Fig. 2.7).

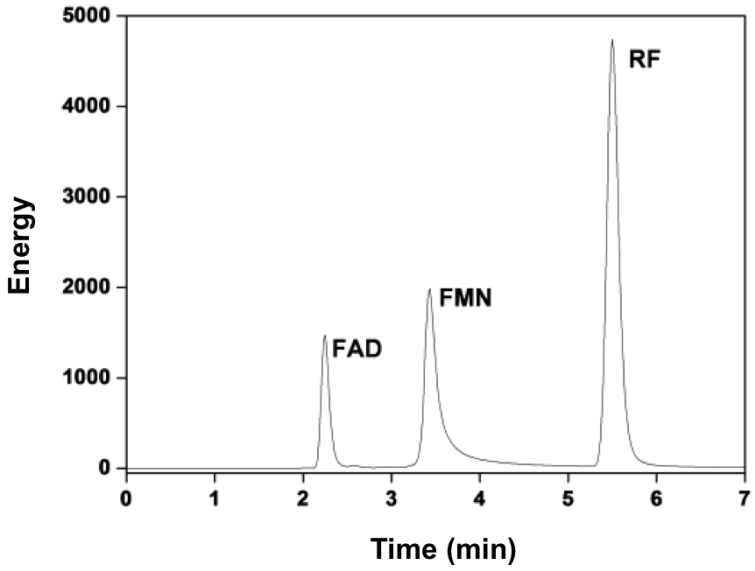

Figure 2.7. Retention times for the different flavins under the conditions specified in Table 2.1.

Flavins were quantified using calibration lines that relate the area of each peak with the corresponding flavin concentration (Fig. 2.8).

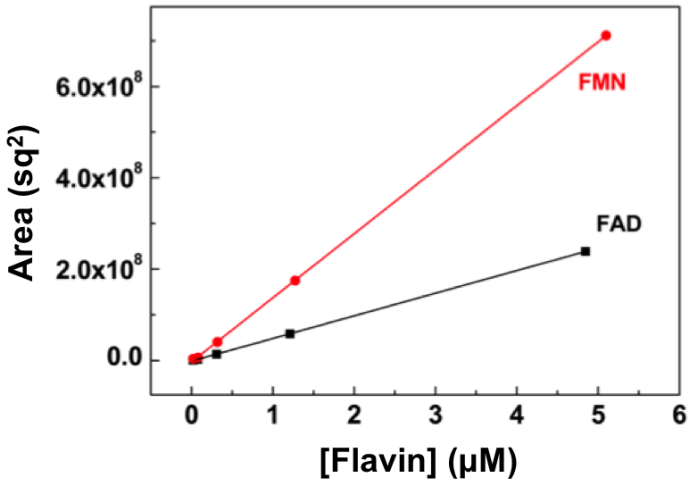

Figure. 2.8. Calibration lines for FMN and FAD quantification under the conditions specified in Table 2.1.

Experimental procedure and analysis of the results

The steady-state RFK activity of *Ca*FADS was analyzed by quantifying the amount of RF transformed during this reaction. Since there is no way to avoid the second reaction of the enzyme, the transformed RF was calculated as the addition of the FMN plus the FAD present at the end of the reaction.

For that purpose, sets of reaction mixtures containing 0.5-30 µM RF, 10-400 µM ATP in 20 mM PIPES, pH 7.0 and 0.8 mM $MgCl_2$ were prepared in a final volume of 500 µl. The reactions were performed in the presence of 0.8 mM Mg^{2+}, because at this concentration the *Ca*FADS shows the maximum value for its RFK activity, while its FMNAT one is minimized [94]. The samples were pre-incubated at 25 ºC and then the RFK reaction was initiated through addition of ~ 50 nM *Ca*FADS (final concentration). The samples were incubated for 1 min and then, the reaction was stopped by boiling the samples for 5 min. The denatured protein was eliminated through centrifugation.

To separate the different flavins present in the mixture, aliquots of 20 µl of each reaction sample were loaded into the HSST3 column (Table 2.1). The FMN and FAD concentrations were calculated using their corresponding calibration lines (Fig 2.8), obtained in the same chromatographic conditions (Table 2.1).

To determine kinetic parameters, measurements were carried out varying the concentration of one of the substrates, while keeping constant and at saturating concentration the second one. The reaction set performed at fixed concentration of RF was interpreted using the Michaelis-Menten model (Fig. 2.9A) [169]. For these

measurements, ~ 5-7 μM RF was used (concentration for which the enzyme shows the 80% of its maximal apparent activity). The reactions containing saturating ATP and variable RF concentrations did not show this hyperbolic behavior, but they presented a profile characteristic of inhibition by substrate (Fig 2.9B). Therefore, the experimental data were fit to a model that describes the substrate inhibition effect produced in enzymes with bi-substrate kinetics (Fig 2.9B) [170].

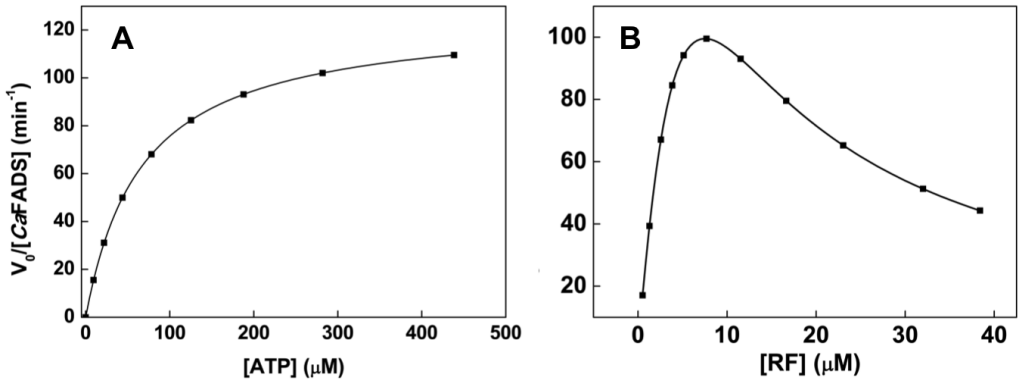

Figure 2.9. Kinetic profiles dependences for the RFK activity of *Ca*FADS (A) as a function of ATP at saturating concentration of RF (Michaelis-like kinetic) and (B) as a function of RF at saturating concentration of ATP (profile characteristic of enzymes showing inhibition by substrate). Measurements performed at 25 ºC, 20 mM PIPES, pH 7.0, 0.8 mM $MgCl_2$.

Mathematical analysis of the results

Kinetic parameters for the reactions that show a Michaelis-like saturation profile (Fig. 2.9A), were obtained by fitting the velocities, obtained as a function of the substrate concentration, to the Michaelis-Menten equation (Eqn. 2.3) [169].

$$v_0 = \frac{V_{max}\cdot[S]}{K_m+[S]} \qquad \text{Eqn. 2.3.}$$

Where v_0 is the initial velocity for each reaction sample, V_{max} is the maximum rate achieved by the system, K_m is the concentration of substrate for which the reaction rate is half of the V_{max}, and [S] the substrate concentration.

When inhibition by the RF substrate was detected (Fig. 2.9B), the kinetic parameters for the RFK reaction were obtained fitting the initial rates to the general equation for substrate inhibition (Eqn 2.4) [170].

$$v_0 = \frac{V_{max}^{app} \cdot [S]}{K_m^{app} + [S] + \frac{[S]}{K_i^{RF}}} \qquad \text{Eqn. 2.4.}$$

Where K_i^{RF} is the inhibition constant for the RF substrate. V_{max} and K_m are apparent values, since due to the inhibitory effect of the RF, it is not possible to work at saturating concentration of this substrate.

The turnover number, or k_{cat}, (maximum number of substrate molecules transformed per unit of time and per molecule of enzyme) was calculated using Eqn. 2.5.

$$k_{cat} = \frac{V_{max}}{[E]} \qquad \text{Eqn. 2.5.}$$

The k_{cat}/K_m relation provides information about the catalytic efficiency of the enzyme.

5.3.3. Fluorometric characterization of the FMN adenylyl-transferase activity (FMNAT) of CaFADSs

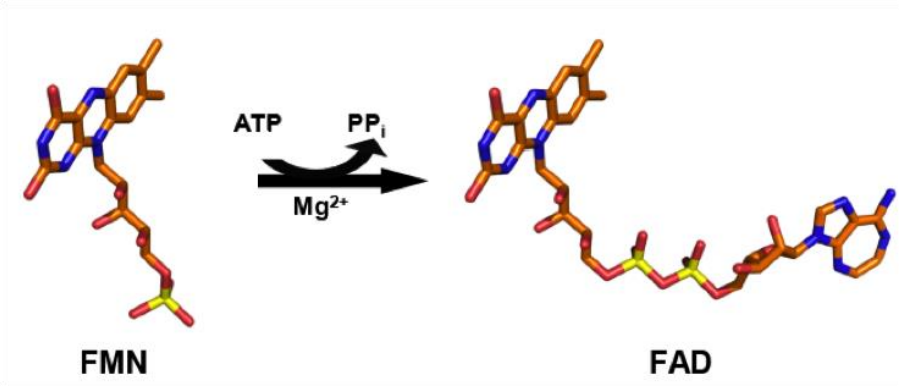

Figure 2.10. FMN transformation into FAD catalyzed by the FMNAT activity of *Ca*FADS.

As indicated in section 2.4.2, FMN and FAD are fluorescent molecules with different quantum yields. Consequently the transformation of the first one into the second can be followed in a continuous assay, by measuring the decrease of the flavin fluorescence [155].

Experimental procedure

Two sets of reactions were prepared, keeping constant and saturating the concentration of ATP while varying the concentration of FMN and vice versa. Reactions performed at ATP saturating concentration contained 0.5-30 µM FMN, while the ATP concentration was 10-350 µM for those experiments carried out at saturating FMN. All the experiments were carried out at 25 ºC in 20 mM PIPES, pH 7.0, 10 mM $MgCl_2$, with a final volume of 1 ml. The reaction was initiated through addition of ~100

nM *Ca*FADS. The fluorescence was registered during 30 s using a Varian Cary Eclipse Fluorescence spectrophotometer (Agilent Technologies) (Fig 2.11). The excitation and emission wavelengths were 420 and 530 nm, respectively.

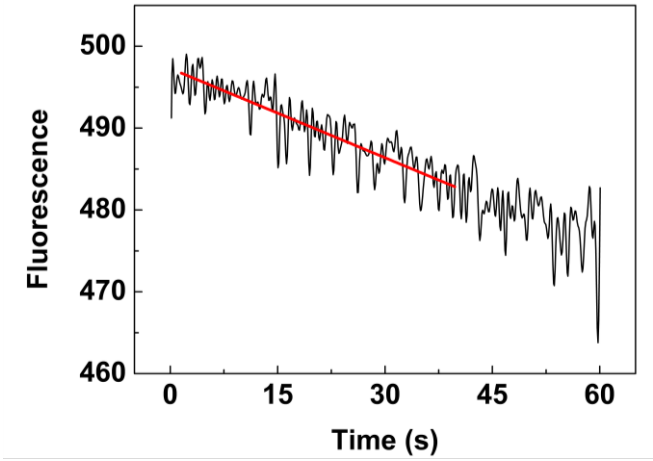

Figure 2.11. Evolution of the flavin fluorescence upon FMN transformation into FAD by *Ca*FADS. Kinetic trace (black) recorded at 25ºC, in 20 mM PIPES, pH 7.0, 0.8 mM $MgCl_2$. The fitting of the initial lineal stretch to a line is shown in red, the slopes of the fitted lines will be used to calculate initial velocities at the different concentrations of each substrate.

To determine the initial velocity (v_0) for each reaction sample, calibration lines (Fig. 2.12) for FMN and FAD were separately obtained under the experimental conditions indicated above. Fluorescence constants were calculated from the slope of the calibration lines, being the constant for FMN (K_{FMN}) ~10 times higher than the one for FAD (K_{FAD}).

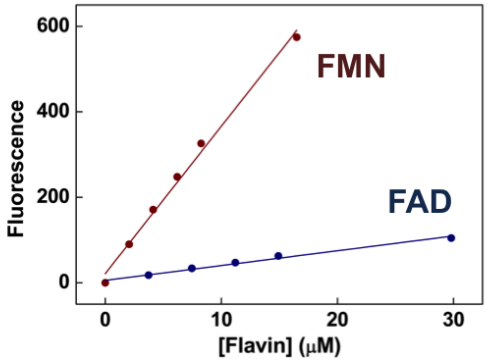

Figure 2.12. Calibration lines for FMN (maroon) and FAD (blue), which relate the fluorescence intensity to the flavin concentration. Data obtained at 25ºC, 20 mM, pH 7.0, 10 mM $MgCl_2$.

Mathematical analysis of the results

The rate of FAD formation, or initial velocity (v_0), for each reaction sample was determined from the fluorescence decrease during the measurement time as ΔF/Δt using Eqn. 2.6.

$$v_0 = \frac{\Delta F}{\Delta t.(K_{FMN} - K_{FAD})} \qquad \text{Eqn. 2.6.}$$

Where K_{FMN} and K_{FAD} are the slopes obtained from their corresponding calibration lines (Fig. 2.12).

The v_0 values obtained for the FMNAT reaction of *Ca*FADS, both at saturating ATP and FMN concentrations, showed a Michaelis-Menten kinetic profile (Fig. 2.9) [169]. Therefore, the kinetic parameters for this activity were calculated by fitting of the experimental data to Eqn. 2.3.

5.3.4. Analysis of the RFK and FMNAT activities of SpnFADS through HPLC

Both the RFK and the FMNAT activities of *Spn*FADS were quantitatively assayed through HPLC, using the experimental procedure and chromatographic conditions specified in section 5.3.2.

The RFK reaction was measured at 25 ºC in 20 mM PIPES, pH 7.0, 0.8 mM $MgCl_2$. The reaction samples were prepared using the protocol and substrates concentrations described in section 5.3.2, and the data processed as indicated in that same section. Initial velocities (v_0) showed a Michaelis-Menten saturation profile both at ATP and RF saturating concentrations (Fig. 2.9A, Eqn. 2.3) [169].

The results of the TLC experiment described in section 5.3.1 revealed that the FMNAT reaction of *Spn*FADS only takes places under strong reducing conditions. This fact prevents determining this reaction by the continuous fluorimetric assay used for the FMNAT activity of *Ca*FADS, since reduced flavins have not fluorescent properties [55]. Therefore, kinetic parameters for this activity were obtained in 20 mM PIPES, pH 7.0, 10 mM $MgCl_2$, by quantifying the products of the reaction through HPLC (chromatographic conditions indicated in 5.3.2), using a modification of the protocol described above, consisting on all samples being prepared in the presence of 3 mM sodium dithionite. The FMN and ATP concentrations were that detailed in 5.3.3 for *Ca*FADS. V_{max} and K_m were obtained by fitting the v_0 values to the Michaelis-Menten model (Fig. 2.9A, Eqn. 2.3) [169].

5.3.5. Analysis of the FMNAT activity of SpnFADS using photorreduced FMN

The FMNAT activity of *Spn*FADS only takes place under strong reducing conditions. To elucidate whether reduced flavins are needed for the FMNAT activity, or the protein requires the reducing environment, the reaction was measured using reduced FMN and oxidized protein. Reaction mixtures containing 500 μM ATP, 15 μM FMN, 2 μM 5-deazaRF (5-dRF) and 0.8 mM Mg^{2+}, in a final volume of 1 ml were deoxygenated during 1 h through Argon bubbling in the dark (to avoid FMN degradation). Once oxygen was displaced from the samples, previously deoxygenated *Spn*FADS was added at a final concentration of 100 nM. Then samples were illuminated during 15 s to photo-reduce FMN (the triplet state of light excites 5-dR that quickly evolves to a radical state, which returns to the fundamental state by ceding an electron to FMN) [171]. After 3 min of additional incubation the system was open to the air. Samples were boiled for 5 min to precipitate the protein and then centrifuged. Flavins presented in the supernatant were identified using the Alliance HPLC system (as indicated in 5.3.2).

5.4 Kinetic study of the inhibition of the RFK activity of *Ca*FADS and *Spn*FADS by the products of the reaction

The RFK activity of *Ca*FADS shows an inhibition pattern when the RF concentration increases. To identify whether products of the reaction might also contribute to the inhibition and to elucidate their mechanisms of action, a kinetic inhibition study was carried out [172-174].

The inhibitory effect of the products of the RFK activity was evaluated using reaction mixtures containing 0-20 μM FMN, 1-30 μM RF, and 350 μM ATP when analyzing the FMN effect, or 0-400 μM ADP, 10-350 μM ATP, and 5 μM RF when examining the inhibition by ADP. Reactions were initiated through addition of the enzyme at a final concentration of ~ 40 nM, followed by 1 min incubation and finally, reactions were stopped by bowling the samples at 100ºC for 5 min. The precipitated protein was eliminated through centrifugation. The flavin composition of the supernatant was analyzed using the Alliance HPLC system, following the protocol described in 5.3.2, and the data were analyzed as described in that section. All the experiments were performed by triplicate.

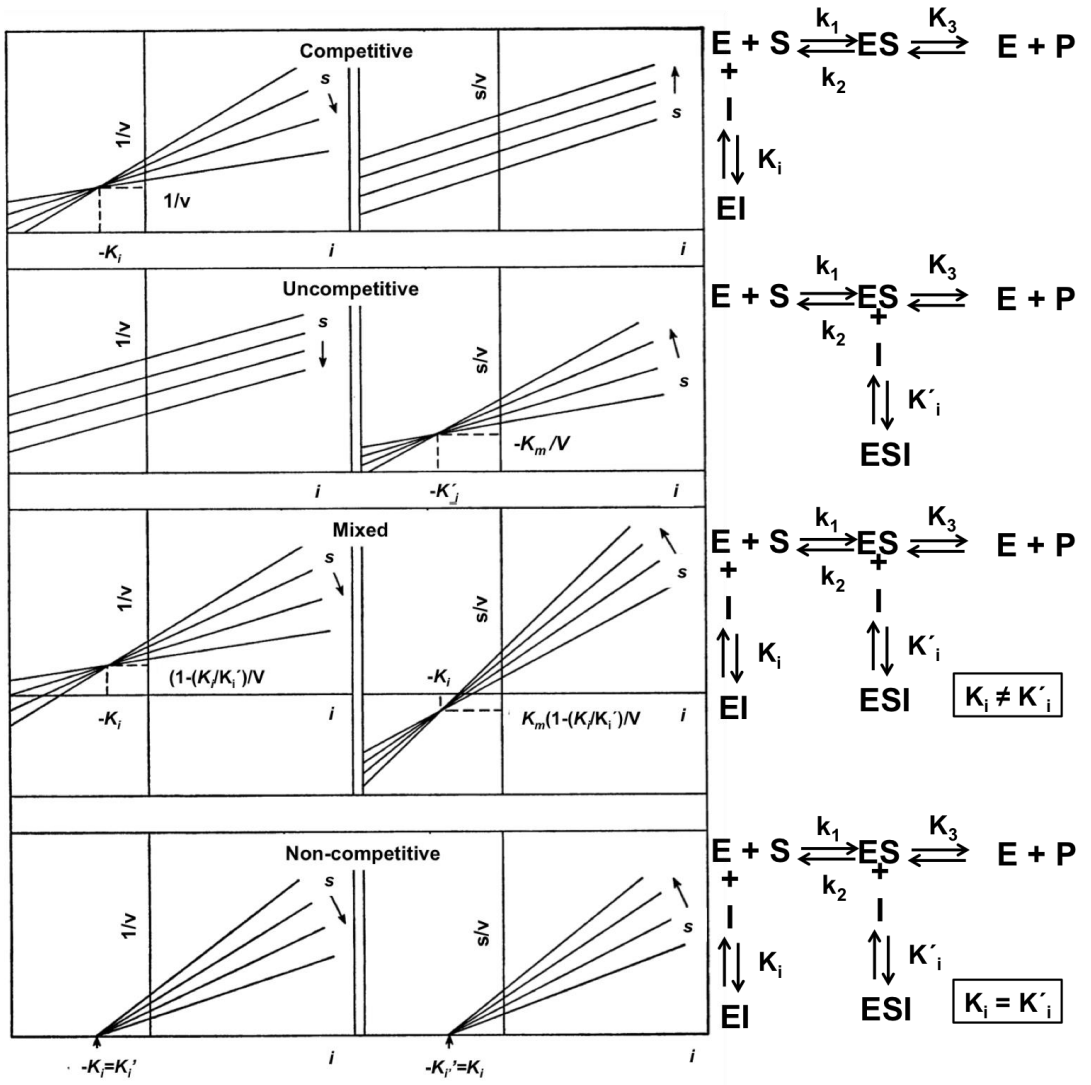

Figure 2.13. Characteristic plots for the common inhibition types. Left, plots of 1/v against inhibitor concentration (Dixon plots) and right, s/v against inhibitor concentration for all the types of inhibition. In every case the intersection point between lines provides an estimation of K_i and K_i' [172].

The inhibition mechanisms performed by FMN and ADP, were identified by evaluating the effect of both products in the K_m and k_{cat} values, obtained by the independent fitting of data sets to the Michaelis-Menten model. Additionally, Dixon plots and Cornish-Bowden representations were used to reveal the type of inhibition (Fig. 2.13) [172]. Finally, the different data sets were globally fit using the Lineweaver-Burk equations for competitive, uncompetitive and mixed inhibitors (Eqns. 2.7, 2.8 and 2.9), respectively [173].

$$\frac{[e]}{v_0} = \frac{\left[1+\frac{[I]}{K_i^P}\right]K_m}{k_{cat}}\frac{1}{[S]} + \frac{1}{k_{cat}} \quad \text{Eqn. 2.7.}$$

$$\frac{[e]}{v_0} = \frac{\left[1+\frac{[I]}{K_i^P}\right]K_m}{k_{cat}} + \frac{K_m}{k_{cat}}\frac{1}{[S]} \quad \text{Eqn. 2.8.}$$

$$\frac{1}{V_0} = \frac{\left(1+\frac{[I]}{K_i}\right)\cdot K_m}{V_{max}}\frac{1}{[S]} + \frac{\left(1+\frac{[I]}{K'_i}\right)}{V_{max}} \quad \text{Eqn. 2.9.}$$

Where v_0 is the determined observed rate constant at each experimental condition, $[e]$ is the enzyme concentration in the assay, [S] is the concentration of the inhibitory substrate, and K_i^P is the corresponding product inhibition constant [175]. Estimated errors in k_{cat}, K_m, K_i and K_i values are, in general, within ±15 % of its value, but when inhibitory concentrations of RF were present errors increased due to the similar K_i^{RF} and K_m^{RF} values.

5.5. Pre-steady state kinetics: Stopped-flow spectrophotometry

Kinetic measurements using stopped-flow spectrophotometry allow to visualize fast individual processes taking place in the course of a reaction and to determine their velocities [176-178]. Some of these processes can be ligand binding or dissociation, conformational changes or the reaction itself.

5.5.1. Basis of the technique

Stopped-flow is a fast mixing technique that allows studying very fast reactions (occurring in milliseconds to seconds). The stopped-flow equipment (Fig. 2.14) has two identical reaction syringes (A and B) that contain the reactants, and their pistons are connected to a valve moved by compressed air. The exit of both syringes (after passing by another valve each) are joined and arrive to a mixing chamber. The exit of the chamber is connected to another syringe, which is the stop syringe. The process starts through fast emptying of the stop syringe when compressed air pushes its piston (1), and continues with the subsequent impulse of the pistons (2) that makes both syringes liberating the same volume. Then, solutions contained in the reaction syringes are mixed at the measuring chamber the exit, where the reaction takes place. Using an appropriate detector, such as fluorescence, absorbance or circular dichroism, the kinetic of the reaction can be determined in the measuring chamber. The main difference between conventional techniques for measuring reaction kinetics and stooped-flow is the death time. Stopped-flow allows determining processes occurring within

milliseconds to seconds, making possible to get kinetic parameters in the pre-steady state.

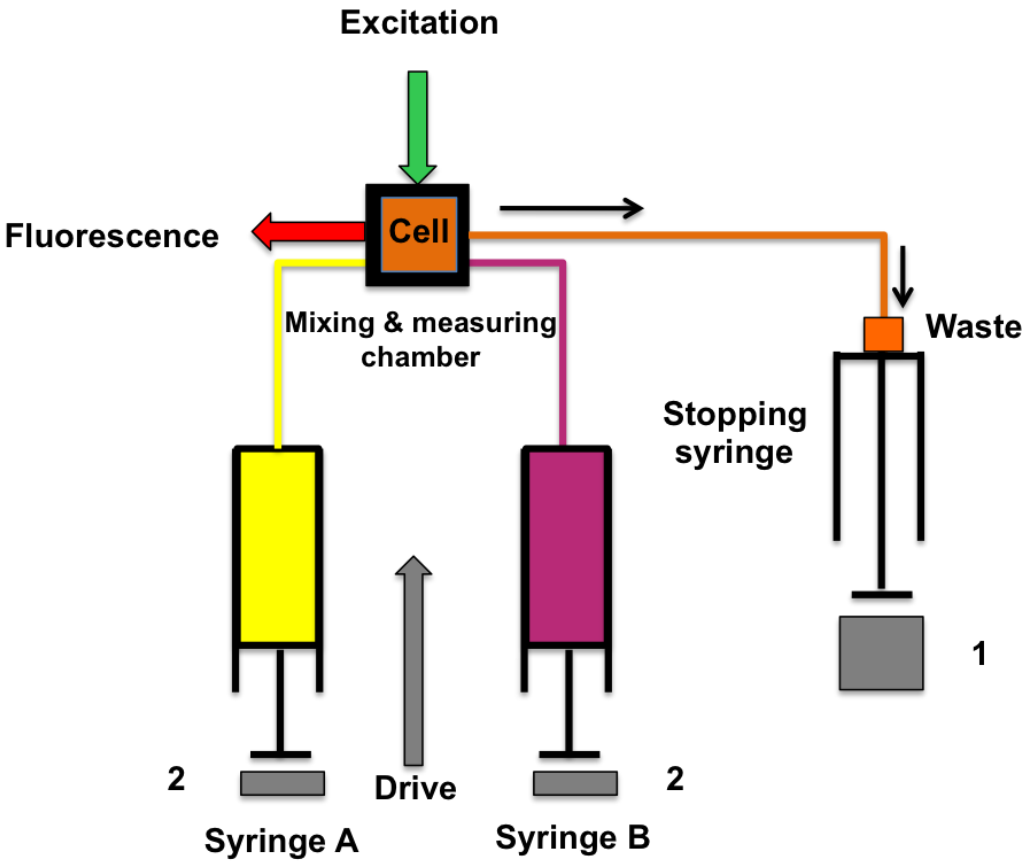

Figure 2.14. Diagram of the stopped-flow equipment, showing its different components. Syringes A and B contain the reactants that are going to be mixed in the mixing and mearuring chamber. 1 and 2 denote for the stop and drive pistons, indicating the order in which they are activated. The arrows indicate the direction of the flow. In our case the light source and the detector are perpendicularly placed, since the measured magnitude is fluorescence.

5.5.2. Determination of observed rate constants (k_{obs}) for different processes involving flavins and FADS

Stopped-flow measurements were performed to identify the different steps that take place during a single cycle of the enzymes and to get apparent kinetic constants for each of these processes. It is necessary to clarify that the registered magnitude is the fluorescence of flavin, therefore only the processes affecting the environment of the isoalloxazine ring [51], and consequently the flavin fluorescence, might be observed.

Stopped-flow measurements were performed on an Applied Photophysics SX17.MV spectrophotometer linked to an Acorn computer using the Xscan software from Applied

Photophysics. The fluorescence of the flavins was measured in a continuous assay being the excitation wavelength 445 nm while the emission was recovered using a 530 nm filter. The selected voltage was 350 V and 800 points were taken in every measurement. Measures were carried out at 25ºC in 20 mM PIPES, 0.8 mM $MgCl_2$, pH 7.0. Either *Spn*FADS, or the *Ca*FADS RFK module (0.2 μM) were mixed with reaction samples varying the concentration of FLV (herein for either RF or FMN) −0.05-5 μM− both in the absence of adenine nucleotides and in the presence of saturating concentration of ANP (herein for either ATP or ADP ligands). Control experiments were also recorded in the same buffer but in the absence of $MgCl_2$. All the concentrations indicated are the final ones in the reaction cell. Every kinetic trace was recorded until getting at least three reproducible traces.

5.5.3. Analysis of the data

Kinetic traces related to changes in fluorescence were fit to exponential processes (Eqn. 2.10), where each exponential term describes at least a different process. When a particular process is not finished in the measure time frame a linear term can be added to the equation to account for it (Eqn. 2.11).

$$y = \sum A_i e^{-k_{obs,i} \cdot t} \qquad \text{Eqn. 2.10.}$$

$$y = \sum A_i e^{-k_{obs,i} \cdot t} + bt \qquad \text{Eqn. 2.11.}$$

Where A_i and k_{obsi} are the amplitude and the observed rate constant, respectively, for each of the processes that contribute to the overall fluorescence change and b is the slope of an unfinished process during the measure time.

When k_{obs} values showed a linear dependence with the flavin concentration they were fit to an one step model (Eqn. 2.12), which describes the association-dissociation equilibrium of enzyme-flavin complexes.

$$k_{obs} = k_{on}[flavin] + k_{off} \qquad \text{Eqn. 2.12.}$$

Where k_{on} and k_{off} are the kinetic constants for the complex formation and dissociation respectively.

Due to the well-known deterioration that flavins undergo when exposed to light, we also evaluated the flavin photobleaching decay produced under our stopped-flow experimental conditions. Due to this effect, the RF and FMN fluorescence linearly decays along the time. The slopes for these kinetic traces show an inverse linear

dependence with flavin concentrations, with slopes corresponding to rates of $4.6 \cdot 10^{-3} \pm 1.8 \cdot 10^{-4}$ min^{-1} and $4.1 \cdot 10^{-3} \pm 1.8 \cdot 10^{-4}$ min^{-1} for RF and FMN, respectively (Fig. 2.15).

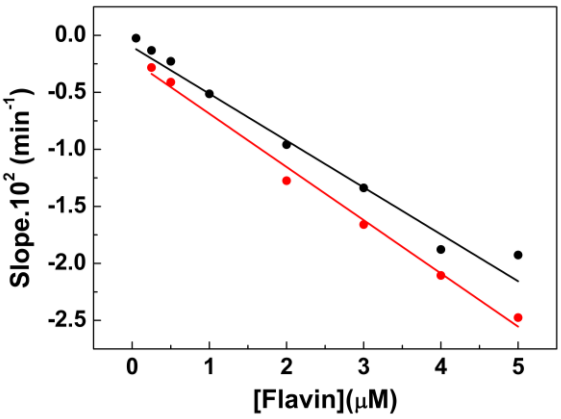

Figure 2.15. Slopes for linear fluorescence decays on the flavin concentration for samples containing RF (black), FMN (red). Data obtained in 20 mM PIPES pH 7.0, 10 mM $MgCl_2$.

5.6. Determination of thermodynamic parameters for ligand binding to FADS through Isothermal Titration Calorimetry (ITC)

5.6.1. Basis of the technique

Isothermal Titration Calorimetry (ITC) is an analytical technique that allows determining thermodynamic parameters for the interaction between two molecules [179-181]. Since binding processes usually involve liberation or absorption of heat, the nature of the interaction can be characterized through the quantification of the interchanged heat. ITC experiments are carried out in a calorimeter at constant pressure and temperature, and allow directly calculating the binding enthalpy (ΔH), the equilibrium association constant (K_a) and the stoichiometry for the binding (N) [179, 182].

An isothermal titration calorimeter is composed of two identical cells (sample and reference cells) surrounded by an adiabatic jacket (Fig. 2.16). Thermocouple circuits detect differences of temperature between the reference cell, which is filled with water, and the sample cell, which contains the molecule to be titrated. Prior to addition of the titrating ligand, a constant power is applied to the reference cell. This produces a feedback circuit that activates a heater located on the sample cell. During the experiment, perfectly known aliquots of the titrating ligand are added to the sample cell that contains the other ligand, producing heat to be either taken up or released. The

measured magnitude is the time-dependent input of power required to maintain both cells at the same temperature.

5.6.2. Titration of FADS with a single ligand

Experimental procedure

ITC measurements were performed using a high precision Auto-ITC200 MicroCal calorimeter (Malvern) thermostated at 25 ºC (or at 20 ºC for *Spn*FADS titrations). The reference cell contained distilled water while the sample cell contained 207 µl of a ~25 µM protein solution. The concentration of the titrating ligand in the syringe was 10-15 times higher, that is ~250 µM in the case of flavins or 300 µM in the case of ADP and ATP. Due to the low solubility of RF, a saturated solution of this ligand, ~200 µM, was used. Both the ligand and the protein were dissolved in the same buffer, 20 mM PIPES pH 7.0 and variable concentrations of $MgCl_2$; 0, 0.8 or 10 mM depending on the experiment. This buffer was selected because of its low ionization enthalpy, which prevents any buffer influence on the observed binding enthalpy caused by de/protonation events. Up to 19 injections of 2 µl were added to the calorimetric sample cell and mixed using a stirring speed of 1000 r.p.m.

To elucidate whether *Spn*FADS is able to bind reduced flavins, ITC experiments were performed in the presence of a reducing agent. Since the Auto-ITC200 MicroCal calorimeter has some parts that could be damaged in the presence of such agents, these titrations were performed using a high precision VP-ITC system (MicroCal LLC). The experimental sets were similar to those described above. Thus, 25 µM *Spn*FADS were titrated at 20 ºC with FMN ~200 µM or FAD ~300 µM. Both the protein and the ligands were dissolved in 20 mM PIPES, pH 7.0, 0.8 mM $MgCl_2$, 4 mM sodium dithionite, 10 mM glucose, 0.5 U/ml glucose oxidase, and degassed. Each titration was initiated by a 4 µl injection followed by 25–28 stepwise injections of 10 µl. Glucose and glucose oxidase were added to avoid the oxidation of sodium dithionite by molecular oxygen, which would liberate unspecific oxidation heat, masking the one corresponding to the flavin:protein interaction.

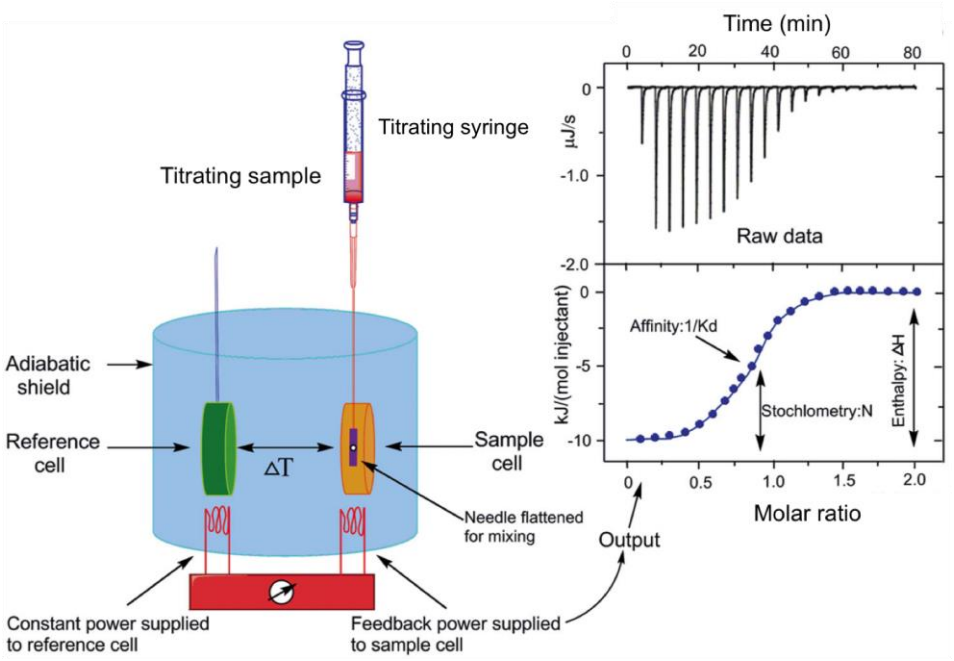

Figure 2.16. Diagram of a typical ITC experiment. The sample cell contains the protein while the reference one contains buffer or water. The measured magnitude is the power applied to maintain both cells at the same temperature. Addition of the titrating ligand to the sample cell produces liberation or absorption of heat, depending on if the reaction is exothermic or endothermic. The interchanged heat is proportional to the increment of the ligand fraction bound to the protein. The great signal observed during the first additions is due to the majority of the ligand being bound to the protein. During the following additions the protein is saturated and the signal decrease because less heat is interchanged [179].

Analysis of thermograms

The heat evolved after each ligand injection was obtained from the integral of the calorimetric signal ($\mu cal \cdot s^{-1}$ *vs* time). The heat derived from the binding process was calculated as the difference between the binding heat and the corresponding dilution heat. This last was estimated as a constant heat throughout the experiment and included as an adjustable parameter in the analysis. Finally, the $kcal.mol^{-1}$ values for each injection were represented versus the molar fraction of ligand as [ligand]/[FADS]. The resulting data were fit to a different mathematical model, depending on the number of binding sites, Eqn. 2.13 and Eqn. 2.14 for a single binding site and for two binding sites, respectively.

The differential heat associated to each injection (i) results from the difference between the total heat accumulated after the injection i, and that corresponding to the injection i-1.

$$q_i = Q_i - Q_{i-1}\left(1 - \frac{v}{V_0}\right) = V\left[[ML]_i - [ML]_{i-1}\left(1 - \frac{v}{V_0}\right)\right]\Delta H \qquad \text{Eqn. 2.13}$$

$$q_i = Q_i - Q_{i-1}\left(1 - \frac{v}{V_0}\right) =$$

$$= V\left[\left[[ML]_i - [ML]_{i-1}\left(1 - \frac{v}{V_0}\right)\right]\Delta H_1 + \left[[ML]_i - [ML]_{i-1}\left(1 - \frac{v}{V_0}\right)\right]\Delta H_2\right]$$

Eqn. 2.14

The dilution factor is considered through the (1-v/V_0) term. The thermodynamic parameters K_a, ΔH and N, in the case of Eqn. 2.13 and K_{a1}, K_{a2}, ΔH_1, ΔH_2, N_1 y N_2, for Eqn. 2.14 were obtained through non-lineal regression of the experimental data to the corresponding equations, implemented in Origin 7.0. Estimated errors were in general ~0.3 kcal/mol for ΔH and ± 10% for K_a.

Calculation of thermodynamic parameters from ITC experiments

The association constant (K_a), the enthalpy change (ΔH), and the stoichiometry of the binding (N) were obtained as just described. The dissociation constant (K_d), the free energy change (ΔG), and the entropy change (ΔS) were obtained from the previous ones using basic thermodynamic relationships (Eqns. 2.15, 2.16 and 2.17).

$$\Delta G = -RTlnK_a \qquad \text{Eqn. 2.15}$$

$$\Delta G = \Delta H - T\Delta S \qquad \text{Eqn. 2.16}$$

$$K_d = \frac{1}{K_a} \qquad \text{Eqn. 2.17}$$

Where K_a is the association constant obtained from the fitting, ΔG, ΔH and ΔS are the free energy, the enthalpy and the entropy contributions to the binding , respectively and R is the universal gas constant ($1.987 \cdot 10^{-3}$ kcal/mol K).

Usually when N~2 there was not enough information in the titrations for using a model with two different binding sites and averaged binding parameters are given. Normally, the estimated errors were ~ 15 % in K_d and ± 0.3 kcal/mol in ΔG, ΔH and –TΔS.

5.6.3. Titration of pre-formed binary FADS:ligand complexes

Titrations with FLV ligands of mixtures containing the enzyme prebound to ANP ligands were also carried out, as well as titrations with ANP of mixtures of the enzyme

prebound to FLV ligands. The methodology and the data treatment were the same as the ones described above.

Determination of cooperativity constants between flavin and adenine nucleotide ligands

Some bi-substrate proteins show cooperativity effects between their ligands [183]. Cooperative ligands change the affinity of the protein for the other ligand. For instance, considering a system where a protein has two ligands, A and B. A and B are cooperative ligands if the binding of A alters the affinity of the protein for B, and *vice versa*. Cooperativity effects can be positive, if the binding of A increases the protein affinity for B (*and vice versa*) [184], or negative, if the affinity for the second ligand decreases [185, 186]. Cooperation effects can be related to conformational changes, induced by binding of one of the ligands that somehow favors or hinders the binding of the other one [184].

To determine the cooperation coefficients (α) between the ANP ligands and the FLV ones, sets of six experiments were carried out. Solutions of the ANP ligands were used to titrate mixtures, located in the calorimetric cell, containing the RFK module at six different FLV concentrations (0-180 µM). These experiments allowed to determine the apparent association constants for the ANP ligand, $K_a^{app,ANP}$, at each concentration of the FLV one.

Mathematical processing of the data

Values were fit to the equation describing the dependency of $K_a^{app,ANP}$ as a function of the FLV concentration and α (cooperativity constant for the heterotropic interaction between ANP and FLV) (Eqn. 2.18) [183].

$$K_a^{app,ANP} = K_a^{ANP} \cdot \frac{1+\alpha.K_a^{FLV}.[FLV]}{1+K_a^{FLV}.[FLV]} \qquad \text{Eqn. 2.18}$$

Being $K_a^{app,ANP}$ the association constant for the ANP ligand at each [FLV], K_a^{FLV} the association constant for the FLV one, and [FLV] the concentration of flavin in the calorimetric cell.

Additionally, particular titrations performed at saturating FLV concentration (150 µM) were fit to a homemade model that considers the influence of the FLV ligand on the protein affinity for the ANP one [187], yielding similar α values.

Experiments were performed in duplicate or triplicate. The errors considered in the measured parameters (±15% in K_d and K_a values, ±0.3 kcal mol^{-1} in ΔG, ΔH and $T\Delta S$ and ±20% in α) were taken to be larger than the standard deviation between replicates and the numerical error after fitting analysis.

6. Discovery of antibacterial drugs

As mentioned previously, the *Ca*FADS shows sequence and structural homology with other prokaryotic FADSs. Therefore, *Ca*FADS can be a good target (section 1.3, Introduction) model in the development of new antibacterial drugs against pathogenic microorganisms [89]. Particularly, due to the homology of *Ca*FADS with the *Mt*FADS (showing 45% homology), the first protein seems to be an optimal model for the second one [89].

6.1. Activity-based high-throughput screening for *Ca*FADS

HTS is a drug discovery process that has become very popular in the last decades, since it allows the assaying of a large number of potential biological modulators against a chosen target. This methodology automates the screening process and it is useful to discover ligands for enzymes, receptors or other pharmacological targets [188, 189]. Different properties can be exploded to perform a HTS. For instance ligand binding to the target can be detected through variations on its Tm using thermal upshift assays [190, 191], or we can identify compounds that inhibit the activity of the target through an activity-based HTS [192, 193]. Additionally, this process also allows directly assaying the effect of the compounds in cells [194].

To find *Ca*FADS inhibitors, we performed the HTS of the Prestwick Chemical Libary® that contains 1040 compounds. These compounds have been approved by the Food and Drug Administration (FDA) and by the European Medicines Agency (EMA), and they have been selected for their known bioavailability and safety in humans. The screening was activity based, what means that we directly determine how the compounds affected any of the activities of the protein or both of them. In this assay, the measured magnitude was the flavin fluorescence. As indicated in section 5.3.3, FMN transformation into FAD involves a linear decrease of the fluorescence along the time. Therefore, when the RFK or the FMNAT activities are inhibited, less FAD is produced and consequently the fluorescence decrease (registered in a specific time interval) is less pronounced.

Measurements were carried out using a multimode microplate reader, Synwergy™ HT Biotek, with BRAND plates- pure Grade™ (96-well plates). To optimize the conditions of the assay, a previous study was performed using constant concentrations of RF, ATP and *Ca*FADS (~5 µM, ~50 µM and ~ 0.4 µM respectively), and variable concentrations of $MgCl_2$ (0.2-10 mM) and DMSO (0%-12.5% v/v). Additionally, different instrumental sensitivities were tried to select the one that produces the highest signal but without saturating it. Optimum conditions were 2.5% DMSO, 10 mM $MgCl_2$ and sensitivity 70.

Experiments were executed in 96-well plates. Reaction mixtures contained 5 µM RF, 0.4 µM *Ca*FADS, 10 mM $MgCl_2$, in PIPES 20 mM, pH 7.0, and the corresponding compound of the chemical library (dissolved in DMSO) at a concentration of 250 µM. Reactions were initiated through addition of 50 µM ATP, being the final volume 100 µl. Controls, which contained the reaction mixture but not any compound, were added both to the first and last rows. Flavin fluorescence in each well was registered at 25 ºC, every 50 s during 15 min. Excitation and emission wavelengths were 440 and 530 nm, respectively.

The slope of the resulting line, recoded between 0 and 6 min, was calculated for every compound and also for the controls, as the fluorescence increase per time unit ($\Delta F/\Delta t$). Those compounds that decreased the reaction rate bellow the average reaction rate of the controls minus the standard deviation (Eqn. 2.19), were preselected as potential inhibitors, and herein known as primary HTS hits.

$$\frac{\Delta F_{compound}}{\Delta t} < \frac{\Delta F_{controls}}{\Delta t} - SD_{controls} \qquad \text{Eqn. 2.19}$$

6.1.2. Identification of the activity inhibited by each of the primary HTS hits

As previously indicated in section 3.5 (Introduction), the HTS hits that showed lowest rates for the FMNAT activity, affecting to a lesser degree the RFK one, are the preferable ones to continue the study.

Since the only detectable fluorescence change is that produce during the FMNAT activity, the primary HTS hits might inhibit the RFK activity, the FMNAT one, both of them, or be a false positives also known as pan assay interference compounds (PAINS), which tend to nonspecifically react with numerous targets. Therefore, to determine which of the *Ca*FADS activities was inhibited, both reactions were assayed through HPLC in the presence of the HTS hits. The experimental procedure is similar to that

described in section 5.3.2, but in this case, reaction mixtures contained 50 µM ATP, 5 µM RF, 0.4 µM *Ca*FADS in 20 mM PIPES, pH 7.0, 0.8 mM $MgCl_2$ and 250 µM of each HTS hit (when assaying the RFK activity), or 50 µM ATP, 5 µM FMN, 0.4 µM *Ca*FADS in 20 mM PIPES, pH 7.0, 10 mM $MgCl_2$ and 250 µM of each HTS hit (when assaying the FMNAT one). Those HTS hits that decreased the FMNAT activity by more than 5 %, without significantly affecting the RFK one (remaining reaction rate higher than 75%) were selected as FMNAT hits to continue the study.

Similarly, the HTS hits were also assayed against *Spn*FADS, following a modification of the procedure described above, consisting on when measuring the FMNAT activity 3 mM sodium dithionite was added to the reaction media.

Data were processed as indicated in section 5.3.2.

6.1.3. Determination of the potency of FMNAT hits

The half maximal inhibitory concentration (IC_{50}) of a compound reflects the concentration at which an enzyme shows the half of its maximal activity. The lower the IC_{50} is, the more potent the compound is as inhibitor.

Once we have selected the FMNAT hits, this activity was assayed at different concentrations of the compound (0-100 µM). Experiments were performed as specified in section 5.3.2. Positive controls (without any compound) were included in every reaction set. To avoid differences in the percentage of DMSO among samples, DMSO was added to the samples so that:

$$V_{DMSO} + V_{hit} = 12.5\ \mu l \qquad \text{Eqn. 2.20}$$

where V_{DMSO} and V_{hit} are the volumes of DMSO and the assayed compound, respectively. 12.5 µl corresponds to the 2.5 % of the final reaction volume, which was 500 µl.

Experiments were performed in triplicate, and data were processed as indicated in section 5.3.2. The FMNAT hits that presented lowest residual activity and IC_{50} were selected to be furthermore characterized.

6.1.4. Determination of the inhibition mechanism of selected in the FMNAT activity

Experimental procedure

To identify the inhibition mechanism performed by selected FMNAT hits (C24, C27 and C31), this reaction was evaluated in the following conditions. Reaction mixtures

containing 0-100 µM of each compound, 1-20 µM FMN and 400 µM ATP were used when analyzing the inhibitory effect of the compound regarding the FMN substrate, while 5-400 µM ATP, 15 µM FMN, when analyzing the effect of the inhibitor regarding the ATP substrate. All the experiments were carried out in 20 mM PIPES, 10 mM $MgCl_2$, pH 7.0, being the final reaction volume 500 µl. The reactions were initiated by addition of the enzyme at a final concentration of ~40 nM, followed by 1 min incubation. Finally, reactions were stopped by bowling the samples at 100ºC for 5 min, and the precipitated protein was eliminated through centrifugation. The flavin composition of the supernatant was analyzed using the Alliance HPLC system, as we described in 5.3.2. All the experiments were performed in triplicate.

Analysis of the data

The inhibition mechanisms of the selected compounds were identified by evaluating their effect in the K_m and k_{cat} values obtained as indicated in section 5.3.2. Additionally, the different data sets were fit to Lineweaver-Burk equations for competitive, uncompetitive, mixed and non-competitive inhibition (Eqns. 2.7, 2.8, 2.9 and 2.21), respectively).

$$\frac{1}{V_0} = \frac{\left(1+\frac{[I]}{K_i}\right)}{V_{max}} + \frac{\left(1+\frac{[I]}{K_i}\right)K_m}{V_{max}}\frac{1}{[S]} \qquad \text{Eqn. 2.21}$$

6.1.5 Thermodynamic characterization of binding of the selected FMNAT hits to CaFADS through ITC

Beside the affinity that a compound has for its target, ITC experiments also provide additional valuable information such as the enthalpic and entropic contributions to the binding free energy. Depending on the thermodynamic term (that is ΔH or ΔS) that dominates the interaction between a ligand and a protein, we can distinguish between "enthalpic" or "entropic ligands" [195, 196]. The binding of the first type of ligands is favored by the formation of a great number of electrostatic interactions, such as H-bonds or Van der Waals forces. On the other hand, the binding of "entropic ligands" is directed by entropic contributions, being the hydrophobic effect an important determinant for these interactions. This information is essential to determine the suitability of potential bioactive compound, and also for its future improvement through rational design.

ITC experiments were performed to characterize the affinity of the protein for the selected compounds, as also the thermodynamic parameters that drive the interaction. The experimental procedure and the data processing were those indicated in section 5.5.2. In these experiments, ~400 µM of each compound were used to titrate ~25 µM *Ca*FADS. However, when saturation of the protein was not reached, higher concentrations of compounds were employed,

6.1.6. In-vivo determination of the antibacterial effect of the hits

To determine the effect that the hits have in the cellular growth, the HTS hits were tested in *C. ammoniagenes* cells. The assay was based on the redox reactions that take place in living cells. Resazurin, which is blue in its oxidized form, but when it is reduced inside metabolically active cells change into pink, was used as indicator. Therefore, the color change produced in the course of the experiment, is a measurement of the cellular viability [197, 198].

Experiments were carried out in 96-well plates, BRAND plates®-pure Grade TM. 100 µl of the corresponding culture media were added to each well. Within a column, 4 different concentrations of each HTS hit (75-600 µM) were prepared through serial dilutions. The first column of each plate was the positive control, and no compound was added to it. The last columns of each plate contained the negative controls, and were included to detect contaminations by other microorganisms. These last wells neither contained cells nor any compound. All the wells, except those of the last column, were inoculated with 100 µl of culture, which contained the cells at a concentration of 10^6 CFU/ml. Cells were incubated at 30ºC for 24 hours. After that, 20 µl of 0.01% (0.1 mg/ml) resazurin solution, were added to each well, and cultures were incubated 24 hours more.

Positive and negative controls were checked to verify that cells have grown in positive controls (pink), and that they have not grown in the negative ones (blue). When the compound had inhibited the cellular growth in a well, the resazurin did not change from blue to pink.

Similarly, the HTS hits were also assayed against *M. tuberculosis* and *S. pneumoiniae* cells. In these experiments the cell concentration of the inoculum was $5 \cdot 10^5$ CFU/ml and plates were incubated for 10 hours (*S. pneumoniae*), and 6 days (*M. tuberculosis*), before the addition of the resazurin.

7. Statistical analysis of the data

Along this thesis, results are expressed as the mean ± the standard deviation (SD) or as the mean ± the standard error (SE) of the regression. When it was convenient, one-way analysis of variance (ANOVA) was performed to determine statistical significance. Statistical analyses were carried out using the GraphPad Software (GraphPad Prism 7), and the Turkey test with a 95% confidence interval.

8. AFM measurements

All the AFM experiments included in this thesis were performed by the group of the Dr. Anabel Lostao, in the Laboratorio de Microscopias Avanzadas at the Instituto de Nanociencia de Aragón de la Universidad de Zaragoza.

9. Crystallographic structures

The crystallographic structures displayed in the results chapters of this thesis were obtained by Dr. Beatriz Herguedas and/or Dr. Marta Martinez.

10. Culture of pathogenic microorganisms

Pathogenic bacterial strains were grown in the following culture media:

-*S. pneumoniae*: brain-heart infusion medium (BHI) supplemented with 4 % bovine serum albumin (BSA), (Gibco).

-*M. tuberculosis*: Middlebrook 7H9 culture medium (Difco) supplemented with 10% ADC (0.2% dextrose, 0.5% V fraction BSA and 0.000·% bovine catalase) (BD Difco) and with 0.5% glycerol (Scharlau).

In-vivo assays using *S. pneumoniae* and *M. tuberculosis* were carried out by Ernesto Anoz-Carbonel in the Centro de Investigación Biomédica de Aragón and with the collaboration of Dr. Jose Antonio Ainsa.

11. Software

The analysis of the most of the data, and the production of the charts were made using the programs Origin 7.0 and Origin 8.0 (OriginLab). Structures were produced with the PyMol software (PyMol) [199].

Chapter III

Quaternary organization in a bifunctional prokaryotic FAD synthetase: Involvement of an arginine at its adenylyltransferase module on the riboflavin kinase activity

As previously indicated, the crystal structure of *Ca*FADS showed a quaternary organization composed of a hexameric structure formed by a dimer of trimers (Figs. 1.21 and 1.22), which was stabilized by H-bonds, salt-bridges, and hydrophobic contacts [85]. The head-tail disposition of the monomers within each trimer approaches the RFK and FMNAT catalytic sites of neighboring protomers, placing them at a distance and orientation compatible with channeling of FMN between modules during FAD biosynthesis [85]. The physiological relevance of this quaternary organization was further supported by its observation at single molecule level, by the identification of oligomeric species in *C. ammoniagenes* cells as well as by the fact that binding of some substrates induces the interconversion between the monomer and the dimer of trimers [100]. Several structural elements contribute to stabilize each trimer within the hexamer; loop L4n in the FMNAT-module together with loops L1c and L6c, and helix α1c in the RFK-module conform the interface between two protomers and help to build the RFK- and FMNAT- active sites (Fig. 3.1). Especially relevant is the salt-bridge formed between R66 (situated at L4n) and the catalytic base of the RFK activity, E268, conserved in FADS and RFK families [88]. Mutations at E268 affect the binding parameters and the catalytic efficiency at the FMNAT active site of *Ca*FADS, supporting the relevance of this interaction [88].

Here, we evaluate the roles of R66 in both the RFK and FMNAT activities, as well as in the stabilization of the quaternary organization. For this purpose, we produced and characterized two *Ca*FADS variants at R66 that prevent formation of the salt-bridge: one completely eliminating the side-chain, R66A variant, and other replacing its positive charge by a negative one, R66E variant. Even though the complexity of the system, which includes two catalytic processes and an oligomerization equilibrium occurring within the same time scale, characterization of such variants indicates that in *Ca*FADS R66 contributes to sustain the RFK activity, to maintain the geometry of the FMNAT and RFK active sites and to stabilize the dimer of trimers.

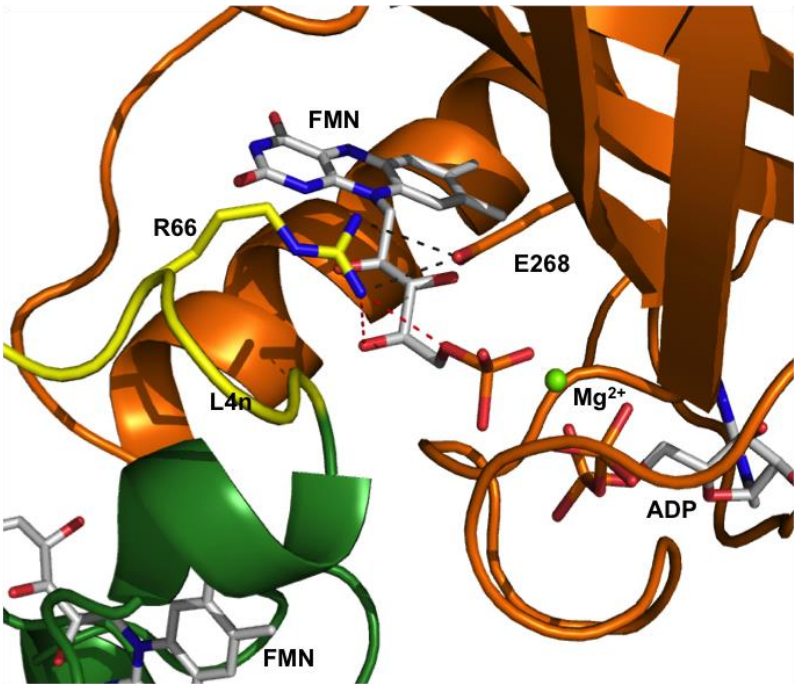

Figure 3.1. Cartoon detail of the head-tail disposition between the RFK-module and the FMNAT-module of contiguous protomers within the *Ca*FADS trimer (PDB code: 2X0K). Positions of the products of the reaction, FMN and ADP:Mg^{2+}, at the RFK-module were predicted based on the structure of the complex for human RFK (PDB code: 1P4M), and that of the FMN substrate at the FMNAT-module was modeled as previously described [85]. The interactions established by the R66 side-chain with the RFK-module are shown in black dashes, while those predicted with the modeled FMN are shown in red dashes. The RFK-module and the FMNAT-module are colored in orange and green respectively. L4n is highlighted in yellow. R66 and E268 side-chains are shown in sticks and CPK colored. Modeled FMN and ADP molecules are CPK colored sticks with carbons in grey. Mg^{2+} is shown as a green sphere.

1. Expression, purification and distribution profile of quaternary organizations for R66 *Ca*FADS variants

The expression level for the variants was similar to that of WT *Ca*FADS. R66A and R66E *Ca*FADSs show three bands when analyzed by N-PAGE, similarly to the WT [100], but differences in the relative intensities of bands for the higher molecular weight species suggested changes in their relative distribution (Fig. 3.2). To analyze the oligomeric state of the different variants we used gel filtration chromatography. WT *Ca*FADS showed several populations (Fig. 3.3A), with the main contribution corresponding to the monomer and the other peaks assigned to the dimer, trimer, and hexamer and higher aggregates (Fig. 3.4), as previously described [100]. When similarly analyzed, the R66E and, particularly, R66A *Ca*FADS showed a considerable increase in the amount of oligomeric species, as well as a displacement of the monomeric peak to smaller elution volumes (Fig. 3.3A). Therefore, mutations at R66 modulate the trend of the protein to organize its quaternary structure.

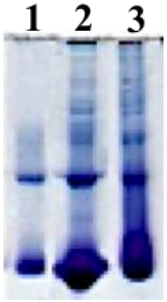

Figure 3.2. Species detected by N-PAGE after the purification of WT (lane 1), R66E (lane 2) and R66A (lane 3) *Ca*FADS.

To further study this modulation, the isolated samples corresponding to either monomeric or oligomeric species were loaded again into the gel filtration column (Fig. 3.3). In the absence of ligands, the monomer peak (Fig. 3.3A, peak 2) remained mainly monomeric for all variants (Fig. 3.3B). On the other hand, we had previously shown that WT *Ca*FADS stabilizes quaternary organizations in the presence of the products of the RFK reaction, FMN and ADP [100]. When both R66 variants were analyzed in similar conditions, the amount of oligomeric species decreased, particularly for the R66 variant (Fig. 3.3C). In addition the gel filtration profile of the oligomeric peaks (Fig. 3.3A, peak 1) in the presence of the products of the RFK activity (FMN and ADP) did not show the typical profile observed in the WT *Ca*FADS protein (Fig. 3.3D). Therefore, all the filtration data indicate that the point mutation at R66 modify the

equilibrium between monomeric and oligomeric species in the presence of the products of the RFK reaction.

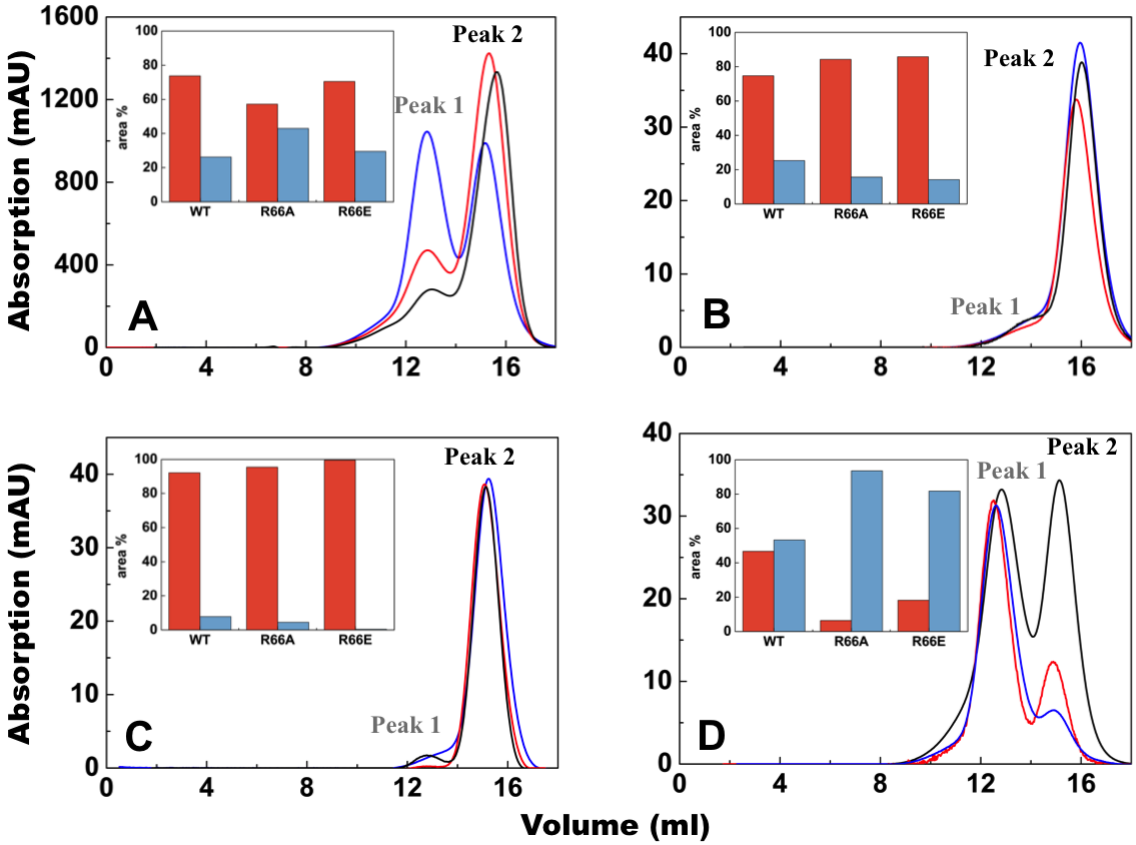

Figure 3.3. The quaternary organization of WT, R66A and R66E *Ca*FADSs. Elution profiles obtained after passing through a Superdex^{TM} 200 10/300 GL column in 20 mM PIPES, pH 7.0: (A) the just purified samples, (B) the monomeric fraction (peak 2) after incubation with 0.8 mM $MgCl_2$, (C) the monomeric fraction (peak 2) after incubation with 25 µM FMN and 200 µM ADP and (D) the oligomeric fraction (peak 1) after incubation with 25 µM FMN and 200 µM ADP. The corresponding profiles for WT, R66A and R66E are shown as black, blue and red lines, respectively. The insets show the percentage of monomeric (red, peak 2) and oligomeric (blue, peak 1) fractions obtained from the chromatograms.

To quantify the effects of these mutations on the oligomeric state and on the conformation of *Ca*FADS oligomers, we used AFM (Fig. 3.5E). This single molecule technique had been successfully used before not only to analyze the oligomeric state of the WT protein, but also to determine the topology of the oligomers and the effects on those of different ligand combinations [100]. Whereas the WT enzyme was mainly visualized as a homogeneous distribution of monomers in the absence of ligands [100] R66A and R66E *Ca*FADS immobilized samples showed a mixture of species where

monomers accounted for the 34 and 44% of the total molecules, respectively (Table 3.1, Fig. 3.5, panel 1). The remaining species –with similar ratio in both variants- correspond to dimers (~40%) (Fig. 3.5, panel 1), tetramers (~15%) (Fig. 3.5, panel 2) and amorphous hexamers (~4%) (Table 3.1, Fig. 3.5 panels 3-4). Upon addition of the products of the RFK activity, FMN and ADP, the WT enzyme stabilized more than 70% of the molecules as a homogeneous compact dimer of trimers [100] However, similar treatment of the R66E and R66A variants did not promote this quaternary organization: for R66E the ligands induce formation of dimers and amorphous hexamers and for the R66A stabilization of tetramers and amorphous hexamers (Table 3.1, Fig. 3.5). It is also remarkable that while the WT dimers adopt mainly a head-tail disposition [100], the dimers of variants, whose modules are less distinguishable than in the WT molecule, usually do not show such disposition. Altogether, these data indicate that the mutations introduced at R66 have a negative impact on the establishment of the functional dimer of trimers in *Ca*FADS, as well as on the formation of the monomer:trimer:hexamer equilibrium upon ligand binding.

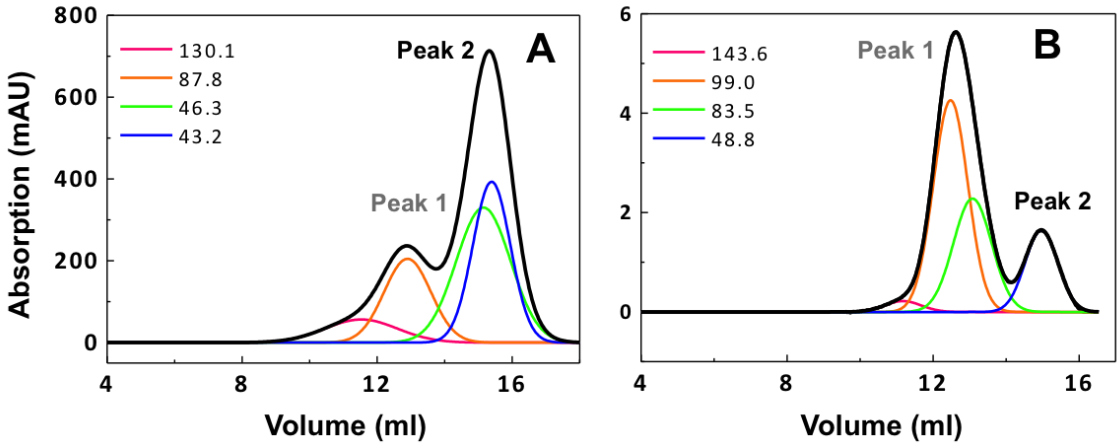

Figure 3.4. Fitting analysis to a set of Gaussian functions of the chromatograms obtained for R66E *Ca*FADS, right after its purification (A) and after incubation of the obtained oligomeric peak (peak 1) with FMN and ADP:Mg^{2+} (B). The chromatograms obtained in each elution are indicated in black lines and the different populations assigned by the Gaussian analysis are indicated in colored lines. The calculated molecular weight for the peak maxima of every population is shown.

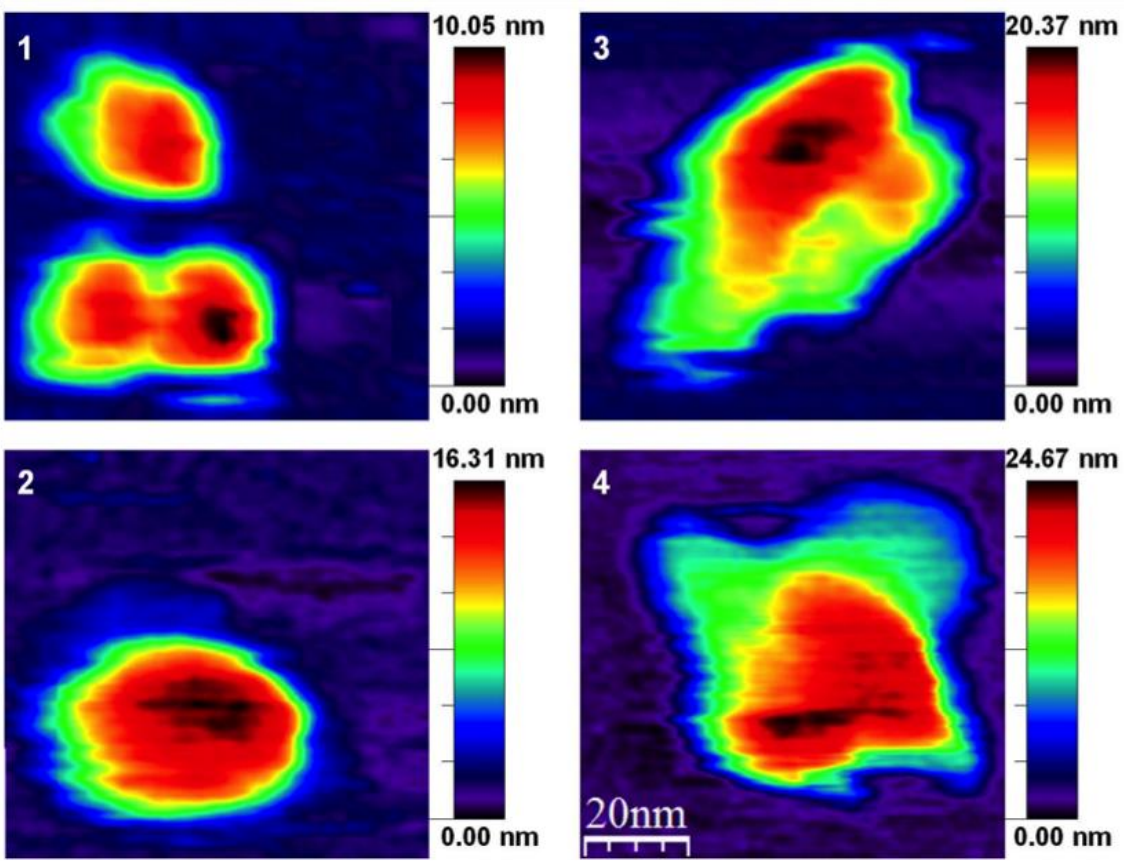

Figure 3.5. AFM topography images of R66A samples upon incubation with ADP:FMN:Mg^{2+}. Samples of 0.5 µM proteins were diluted in 20 mM PIPES, pH 6.0, and 2 mM DTT. ADP, FMN and $MgCl_2$ were added at 250 µM, 50 µM and 0.8 mM, respectively. Panels show the different representative features found at the images identified with the accurate profile functions of the WSxM software as monomers (above) and dimers (1), tetramers (2), and incomplete or amorphous (3) and not compact hexamers (4). The associates found in the R66E samples were very similar (not shown). The oligomers are shown in a proportional scale in the X-Y plane while the corresponding Z-scales appear in colors. All measurements were performed in 20 mM PIPES, 2 mM DTT and pH 6.0.

Table 3.1. Relative association ratios estimated for purified monomeric WT, R66E and R66A *Ca*FADSs at different conditions in AFM samples. Protein samples of 0.5 µM were diluted in 20 mM PIPES, pH 6.0, 2 mM DTT. ADP, FMN and $MgCl_2$ were added at 250 µM, 50 µM and 0.8 mM, respectively. Features correspond to image units, while molecules refer to the amount of individual protein monomers in the corresponding image units. Error associated to percentage determination was ±5-10%.

			Association state (%)				
*Ca*FADS variant	Ligands	Units	Monomers	Dimers	Tetramers	Amorphous hexamers	Dimer of trimers
WT	–	Features	97	3	–	–	–
		Molecules	94	6	–	–	–
	ADP-Mg^{2+} FMN	Features	30	28	2	–	40
		Molecules	9	17	2	–	72
R66A	–	Features	56	34	8	2	0
		Molecules	34	42	19	5	0
	ADP-Mg^{2+} FMN	Features	56	27	14	3	0
		Molecules	31	30	29	10	0
R66E	–	Features	65	30	4	1	0
		Molecules	44	41	12	3	0
	ADP-Mg^{2+} FMN	Features	54	39	5	2	0
		Molecules	33	48	13	6	0

2. Spectral properties of the R66 *Ca*FADS variants

Far-UV CD spectra of the *Ca*FADS variants were similar to those of the WT protein, indicating that the mutation had no impact on the secondary structure of the enzyme (Fig. 3.6A). Near-UV CD showed spectra with similar shape to that of the WT protein (a broad negative 260-300 nm band with minima at 284 and 291 nm) [84], but alterations in the overall and relative intensity of the minima suggest local changes in the environment of some of the aromatic side-chains contributing to the signal, putatively tryptophans (Fig. 3.6B).

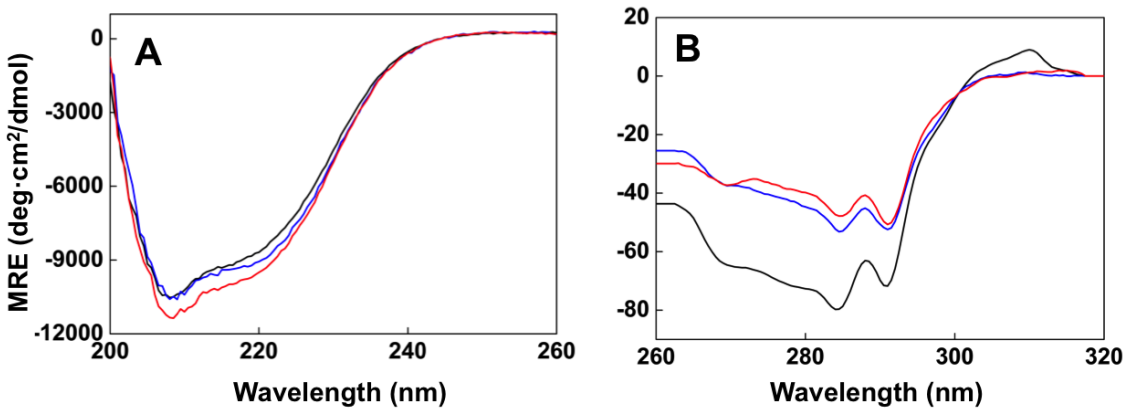

Figure 3.6. Circular dichroism spectra (molar ellipticity by residue) of (A) 5 µM *Ca*FADS in 5 mM PIPES, 10 mM $MgCl_2$, pH 7.0 in the far-UV (cuvette path length, 0.1 cm) and (B) 20 µM *Ca*FADS in 20 mM PIPES, 10 mM $MgCl_2$, pH 7.0 in the near-UV (cuvette path length, 0.4 cm). Spectra were recorded at 25 °C. The corresponding spectra for WT, R66A and R66E are shown as black, blue and red lines, respectively.

Titration of R66A and R66E *Ca*FADSs with RF, FMN and FAD produced visible difference spectra (Fig. 3.7, left panels), indicating that both variants bind the isoalloxazine ring of these flavins in at least one of the two flavin binding sites reported for the WT enzyme [84, 88]. The magnitude of the difference spectra suffered a significant increase when saturating FMN concentrations were added to the already preformed R66A and R66E *Ca*FADS:ADP complexes (Fig. 3.7, right panels). In a previous study of the WT protein we saw this increase was related to the formation of a binding site for FMN at the RFK-module in the presence of the adenine nucleotide [88, 90]. Moreover, in the case of the mutants the magnitude of the difference spectra also increased noticeably upon titration of the preformed *Ca*FADS:ADP complex with RF and FAD (Fig. 3.7B and 3.7F), indicating that in the mutants the presence of ADP favors RF and FAD binding.

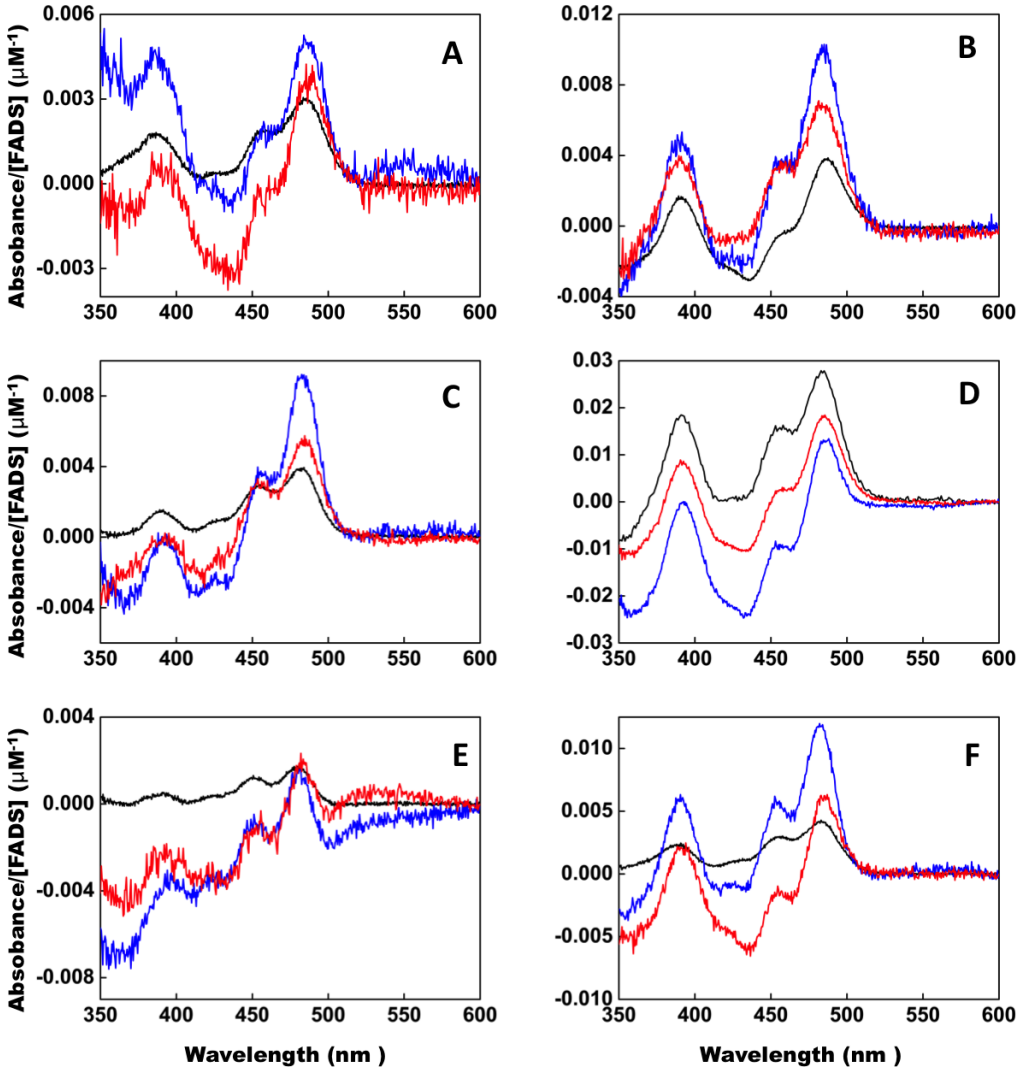

Figure 3.7. Visible difference spectra obtained upon titration of WT (black), R66A (blue) and R66E (red) *Ca*FADSs (panels on left column) and their preformed *Ca*FADS:ADP complexes (panels on right column) with saturating concentrations of (A and B) RF, (C and D) FMN and (E and F) FAD. Spectra were recorded in 20 mM PIPES, 10 mM $MgCl_2$, pH 7.0 at 25 ºC.

3. Effects of the mutations in the catalytic activities of *Ca*FADS

To determine whether the mutations at R66 of *Ca*FADS were able to prevent its catalytic activities, we analyzed the products of the two reactions using TLC. These assays confirmed that both *Ca*FADS mutants retain the ability to catalyze the RFK and FMNAT reactions.

Further on, we determined the kinetic parameters for the RFK and FMNAT activities. First we studied the RFK activity by quantifying the amount of RF transformed at 25 ºC by the amount of FMN plus FAD present in the reaction mixture

after 1 min of reaction (Table 3.2). For WT *Ca*FADS the steady-state parameters were similar to those previously reported at 37 ºC [88, 90]. Variants at R66 exhibited strong RF dependent inhibition profiles at saturating ATP concentration, as also reported for the WT, which prevented determination of the kinetic parameters in the case of R66A *Ca*FADS. Kinetic analyses indicate noticeable decreases in $^{app}k_{cat}^{RF}$ for both variants as well as in $^{app}K_m^{RF}$ for R66E (Table 3.2). The similar decrease in both parameters for R66E *Ca*FADS produces minor changes in the catalytic efficiency for the transformation of RF. On the contrary, catalytic efficiency significantly decreases for the transformation of ATP when RF is kept constant, particularly for R66A *Ca*FADS. This behavior is mainly a consequence of the decrease in the $^{app}k_{cat}$ value (6.5- and 15-fold reduction for R66E and R66A, respectively). Therefore, R66, situated at the FMNAT-module of *Ca*FADS, considerably contributes to modulate the activity taking place at the RFK-module.

Table 3.2. Steady-state kinetic parameters for the RFK (RF → FMN (+ FAD)) and the FMNAT activities (FMN → FAD) of the *Ca*FADS variants. Parameters obtained at 25 ºC in 20 mM PIPES, pH 7.0, and 0.8 mM and 10 mM $MgCl_2$, respectively, for the RFK and FMNAT activities. Estimated errors in k_{cat} and K_m are within ±10%.

RFK activity	$^{app}k_{cat}$[a] **(min^{-1})**	K_m^{RFa} **(μM)**	K_i[a] **(μM)**	$^{app}k_{cat}$[a]/ K_m^{RFa} **(min^{-1} μM^{-1})**	$^{app}k_{cat}$[b] **(min^{-1})**	K_m^{ATPb} **(μM)**	$^{app}k_{cat}$[a]/ K_m^{RFa} **(min^{-1} μM^{-1})**
WT	408.1	11.7	4.85	34.9	155.5	28.2	5.5
R66A	>30[c]	nd[c]	<<0.5[c]	nd[c]	10.9	87.0	0.13
R66E	42.1	0.89	8.2	47.3	23.8	21.5	1.1

FMNAT activity	k_{cat} **(min^{-1})**	K_m^{FMN} **(μM)**	K_m^{ATP} **(μM)**	k_{cat}/ K_m^{FMN} **(min^{-1} μM^{-1})**	k_{cat}/ K_m^{ATP} **(min^{-1} μM^{-1})**
WT	5.5	10.1	22.4	0.54	0.25
R66A	8.5	0.69	15.8	12.3	0.54
R66E	4.5	0.38	31.1	11.8	0.14

[a] Determined at saturating ATP concentrations. Strong inhibition by RF substrate prevents the determination of real parameters and these correspond to apparent ones; $^{app}k_{cat}$ and $^{app}K_m$. Estimated errors in $^{app}k_{cat}$ and $^{app}K_m$ can increase up to ±35% due to the larger K_i values.

[b] Parameters estimated using a RF concentration exhibiting ~80% maximal before inhibition is detected.

[c] Although the variant is active, the strong inhibition caused by RF prevents mathematical determination of the kinetic parameters, and only minimal and maximal values for $^{app}k_{cat}$ and K_i can be provided.

Similarly, the effects of the R66 mutations on the *Ca*FADS FMNAT kinetic parameters were determined by following the transformation of FMN into FAD at 25 ºC. The FMNAT activity of WT *Ca*FADS in 10 mM $MgCl_2$ followed a Michaelis-Menten model with k_{cat}, K_m^{FMN} and K_m^{ATP} of 5.5 min^{-1}, 10.1 μM and 22.4 μM, respectively (Table 3.2), indicating a slightly slower reaction at 25 ºC than the previously reported at 37 ºC [88, 90]. Mutations at R66 hardly produce effects on the k_{cat} for this activity (Table 3.2), slightly modulate K_m^{ATP} (within a 1.5-fold factor) and considerably decrease K_m^{FMN} (14- and 25-fold reduction for R66A and R66E, respectively). This makes the R66A and R66E *Ca*FADS variants more efficient than the WT in transforming FMN. These observations indicate that R66 modulates the catalytically competent binding of FMN during the FMNAT activity.

4. Interaction parameters for *Ca*FADS with flavins and ATP

In order to deep into the effect produced by the mutations on ligand binding, we used ITC in 10 mM $MgCl_2$ to determine the thermodynamic parameters for the formation of the complexes of R66A and R66E *Ca*FADS with flavins. Thermograms revealed the ability of RF, FMN and FAD to bind to the enzyme, but relatively low occupancy was observed for all the flavins (Fig. 3.8). The unusual low flavin occupancy could not be related to contaminations or defective folding, but rather to the establishment of non-productive quaternary organizations decreasing the accessibility of flavins to their binding sites. Even though several observations clearly indicate two different RF binding sites; i) RF stoichiometry for R66A *Ca*FADS resulted twice as large as that of FMN and FAD and ii) in R66E *Ca*FADS thermodynamic parameters were determined for two independent sites (Tables 3.3 and 3.5). The affinity for RF increased in R66E *Ca*FADS relative to the WT (Table 3.5), while its affinity for FMN and FAD decreased (K_d^{FMN} and K_d^{FAD} increased up to 11-fold and 40-fold, respectively (Fig. 3.8A and 3.8B, Table 3.5). R66A *Ca*FADS showed a similar behavior but milder effects. Changes in affinity for flavins resulted in general as a consequence of mutations having a slight negative impact on the enthalpic favorable contribution, while the entropic contribution became less unfavorable or even favorable for RF (Fig. 3.9A, 3.9B and 3.9C, Table 3.3). Taking into consideration the previous studies confirming that under the employed experimental conditions FMN and FAD preferentially bind to the FMNAT-module [84, 88, 90], our data indicate that mutations at R66 modify the organization of the flavin

substrates at the FMNAT-module of *Ca*FADS. Similarly, data for RF also suggest changes in the RF binding architecture at the RFK-module.

R66A and R66E *Ca*FADS mutants showed two ATP binding sites in the presence of Mg^{2+} and a single ATP binding site in its absence (Fig. 3.8C), as reported for the WT protein [84, 88, 90]. Regarding ATP affinity, the mutations produced more relevant changes in the absence of the metal ($K_{d,av}^{ATP:Mg2+}$ 1.3-fold higher and 2-fold lower, and $K_{d,av}^{ATP}$ 3-fold and 10-fold higher for R66A and R66E, respectively) (Table 3.5), indicating changes in the ATP binding conformation at the FMNAT-module. Although these patterns indicated that ATP binding is enthalpically driven with an opposing entropic contribution, the magnitude of both contributions to the binding was in general smaller than in the WT (Fig. 3.9D, Table 3.3). These results indicate that R66 contributes to the ATP binding at both the FMNAT-module and the RFK-module.

In WT *Ca*FADS the adenine nucleotide promotes stabilization of FMN at the RFK-module and increases its affinity at the FMNAT-module [84]. Therefore, we also investigated the interaction of FMN and RF to the preformed R66A and R66E *Ca*FADS:ADP complexes (Fig. 3.8D). Under these conditions mutations neither prevented RF nor FMN binding at any of the two identified sites and occupancy for each site was close to the maximum (Table 3.5). Moreover, they had a slight positive impact on RF affinity, at least in one of the binding sites, and a slight negative impact on FMN affinity. Thermodynamic profiles for binding of RF and FMN to the *Ca*FADS:ADP pre-formed complex for both mutants were similar to those for the WT protein: binding generally driven by favorable enthalpic contributions with small favorable entropic contributions at both sites (Fig. 3.9E, Table 3.4). This is in contrast with contributions driving the interaction of FMNA at the FMNAT-module in the absence of the adenine nucleotide (compare Fig. 3.9B with Fig. 3.9E, and Table 3.3 with Table 3.4) [84, 88]. Regarding RF, it is worth to notice that the mutations modulated the enthalpic and entropic contributions to the binding at one of the sites. Altogether, these profiles confirm that, in general, mutations modulate favorable interactions at the FMNAT site and induce favorable interactions at the RFK-module, with replacement of R66 by Glu also having a negative impact on the entropic contribution to the binding.

Table 3.3. Thermodynamic parameters for the interaction of WT, R66A and R66E *Ca*FADSs with flavins and ATP as determined by ITC. Data obtained at 25 ºC in 20 mM PIPES, pH 7.0, and, unless otherwise stated, 10 mM $MgCl_2$. Errors in Δ*G*, Δ*H* and –TΔ*S* were ±0.3 kcal/mol, taken in general larger than the standard deviation between replicates and the numerical error after fitting analysis.

	FADS:RF			**FADS:FMN**			**FADS:FAD**		
	Δ*G*	**Δ*H***	**-TΔ*S***	**Δ*G***	**Δ*H***	**-TΔ*S***	**Δ*G***	**Δ*H***	**-TΔ*S***
	(kcal/mol)	**(kcal/mol)**	**(kcal/mol)**	**(kcal/mol)**	**(kcal/mol)**	**(kcal/mol)**	**(kcal/mol)**	**(kcal/mol)**	**(kcal/mol)**
WT[a]	-6.3[b]	-7.5[b]	1.2[b]	-7.0	-35	28	-8.4	-26	18
R66A	-5.9[b]	-4.1[b]	-1.9[b]	-5.7	-24	18	-7.8	-25.0	17.2
R66E	Site 1 -7.6 Site 2 -6.3	0.5 -4.8	-7.2 -1.5	-5.5	-21	15	-6.2	-27.6	21.4

	FADS:ATP:Mg^{2+}			**FADS:ATP without Mg**		
	Δ*G*	**Δ*H***	**-TΔ*S***	**Δ*G***	**Δ*H***	**-TΔ*S***
	(kcal/mol)	**(kcal/mol)**	**(kcal/mol)**	**(kcal/mol)**	**(kcal/mol)**	**(kcal/mol)**
WT[a]	-6.2	-30	23	-7.0	-32.3	25.3
R66A	-6.0	-31.8	25.8	-6.6	-16.8	10.1
R66E	-6.6	-8.3	1.7	-6.0	-15.5	9.5

[a] Data from[88, 90].
[b] Data correspond to an average of two independent binding sites.

Table 3.4. Thermodynamic parameters for the interaction of RF and FMN with the preformed *Ca*FADS:ADP complexes. Data obtained at 25 ºC in 20 mM PIPES, pH 7.0, and 10 mM $MgCl_2$. Errors in ΔG, ΔH and $-T\Delta S$ were ±0.3 kcal/mol, taken in general larger than the standard deviation between replicates and the numerical error after fitting analysis.

	FADS:ADP:RF						**FADS:ADP:FMN**					
	Site 1			**Site 2**			**Site 1**			**Site 2**		
	ΔG (kcal/mol)	**ΔH (kcal/mol)**	**$-T\Delta S$ (kcal/mol)**	**ΔG (kcal/mol)**	**ΔH (kcal/mol)**	**$-T\Delta S$ (kcal/mol)**	**ΔG (kcal/mol)**	**ΔH (kcal/mol)**	**$-T\Delta S$ (kcal/mol)**	**ΔG (kcal/mol)**	**ΔH (kcal/mol)**	**$-T\Delta S$ (kcal/mol)**
WT	-8.3[b]	-4.9[b]	-3.5[b]				-10.0[a]	-4.1[a]	-6.0[a]	-8.2[a]	-4.5[a]	-3.8[a]
R66A	-10.4	-9.6	-0.8	-8.8	-5.5	-3.3	-8.6	-3.4	-5.2	-7.8	-5.6	-2.2
R66E	-10.2	-11.4	1.2	-8.8	-6	-2.8	-8.2	-2.2	-6.0	-7.8	-7.1	-0.6

[a] Data from[88, 90]. [b] Data correspond to an average of two independent binding sites.

Table 3.5. Parameters for the interaction of WT and mutated *Ca*FADS forms with RF, FMN, FAD and ATP, and for RF and FMN interaction with the preformed *Ca*FADS:ADP complexes, determined by ITC. The stoichiometry for the interaction is shown in brackets. Data obtained at 25 ºC in 20 mM PIPES, pH 7.0, and unless otherwise stated, 10 mM $MgCl_2$. Estimated errors in K_d are ±15%

	***Kd* (μM)**								
	FADS:RF		**FADS:FMN**	**FADS:FAD**	**FADS:ATP**		**FADS:ADP:RF**		**FADS:ADP:FMN**	
					$MgCl_2$	Without $MgCl_2$	Site 1	Site 2	Site 1	Site 2
WT	24.1 (2)[a,b]		7.8 (1)[a]	0.74 (1)[a]	30.2 (2)[a,b]	3.9 (1)[a]	0.79 (2)[b]		0.04	0.90
R66A	45.6 (<2)[b]		66.2 (<1)	1.9 (<1)	40.0 (2)[b]	13 (1)	0.03	0.35	0.49	1.80
R66E	Site 1 5.0 (<1)	Site 2 22 (<1)	89.0 (<1)	30.2 (<1)	14.7 (2)[b]	38 (1)	0.03	0.36	0.94	2.07

[a] Data from[88, 90]. [b] Data correspond to an average K_d ($K_{d,av}$) of two independent binding sites

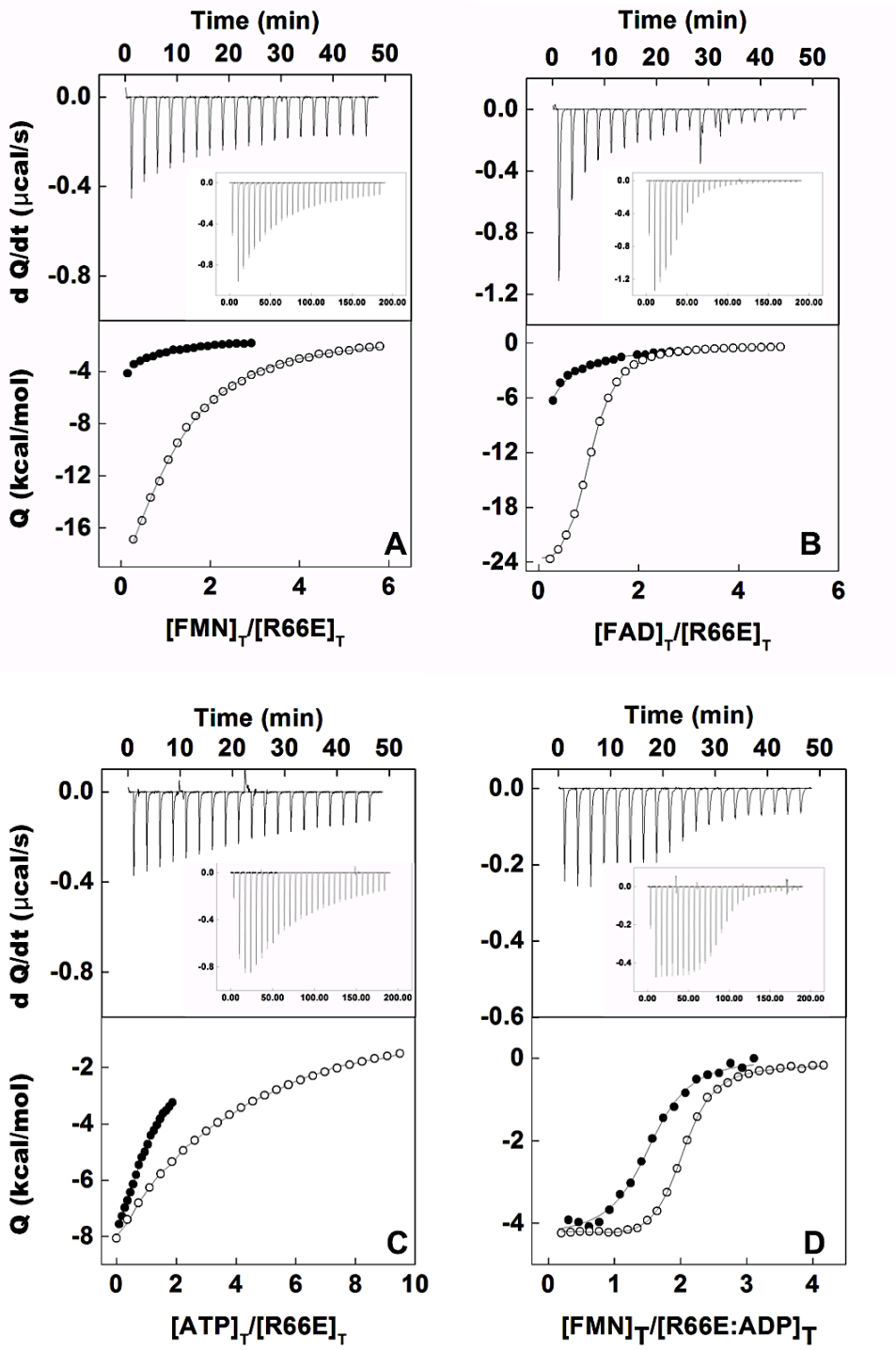

Figure 3.8. Calorimetric titrations of *Ca*FADS with (A) FMN, (B) FAD and (C) ATP, and of the preformed *Ca*FADS:ADP complex with (D) FMN. The upper panels show the thermograms for R66E and WT *Ca*FADS (inset) interaction and lower panels show the corresponding binding isotherms with integrated heats for R66E (●) and WT (○) *Ca*FADSs. Experiments were carried out at 25ºC in 20 mM PIPES, 10 mM $MgCl_2$, pH 7.0.

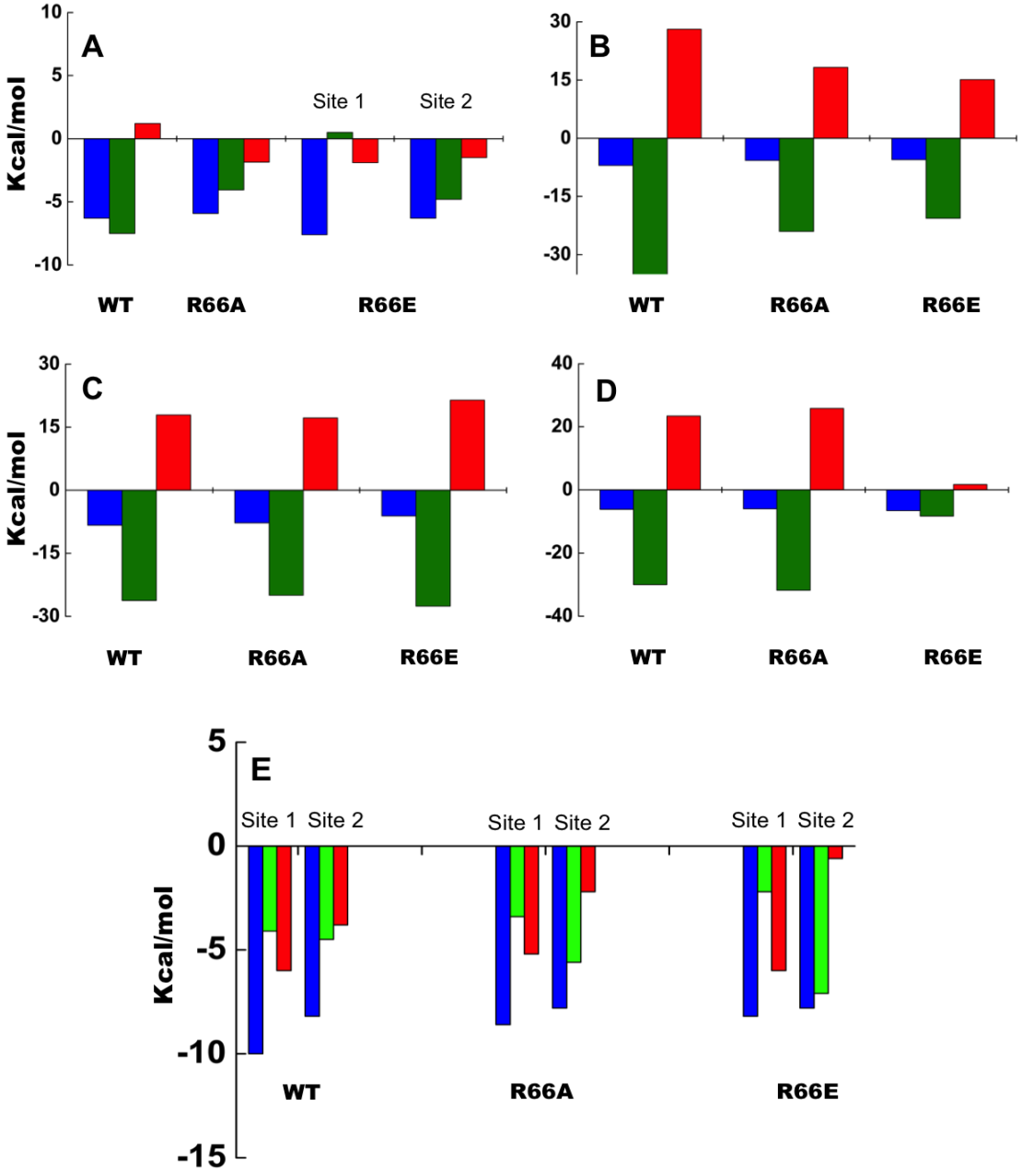

Figure 3.9. Thermodynamic dissection of the interaction of R66A and R66E *Ca*FADS with (A) RF, (B) FMN, (C) FAD and (D) ATP, as well as of the preformed R66A and R66E *Ca*FADS:ADP complexes with (E) FMN. All measurements were carried out in 20 mM PIPES, 10 mM $MgCl_2$, pH 7.0. The binding Gibbs energy (ΔG), enthalpy (ΔH), and entropy ($-T\Delta S$) are represented in dark blue, green and red, respectively. In (E) the energetic profiles for both independently detected binding sites are displayed separately.

5. Crystal structure of the *Ca*FADS variants

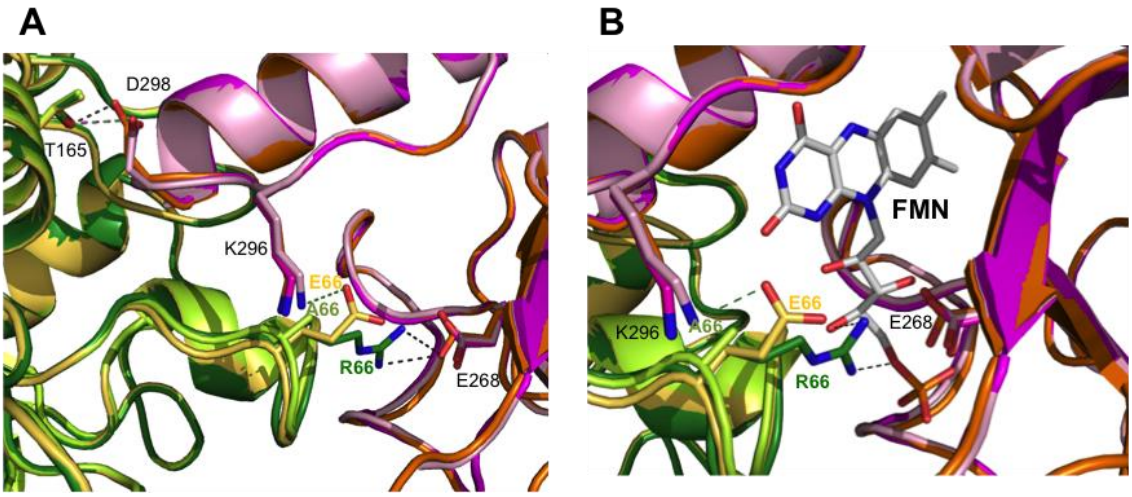

Figure 3.10. Structural effects induced by R66 replacement in the interactions stabilizing the *Ca*FADS trimer interface. Head-tail disposition between the RFK-module (orange) and the FMNAT-module (dark green) of two contiguous protomers in the WT *Ca*FADS trimer (PDB code 2x0k), with the superposition of the respective RFK- and FMNAT-modules of R66A (in magenta and lemon green, respectively, PDB code 4uze) and R66E *Ca*FADS (in pale pink and yellow, respectively, PDB code 4uzf). (A) Key interactions established by position 66 at the interaction surface between the RFK-module and the FMNAT-module of contiguous protomers are shown in black for WT, magenta for R66A and green for R66E *Ca*FADS. (B) Model showing the expected position of the FMN, product of the RFK reaction, at the RFK-module (based on PDB code: 1P4M) and the detail of the K296-E66 (green) and R66-FMN (black) interactions present in R66E and WT *Ca*FADSs, respectively. Key residues are shown in sticks and CPK colored. Modeled FMN in the RFK-module is colored in CPK sticks with carbons in gray.

The overall structures of R66A and R66E *Ca*FADSs (PDB codes 4uze and 4uzf respectively) hardly differ from that of the WT (A chains shows r.m.s.d values of 0.121 and 0.151 Å, for 288 and 293 C□ atoms, respectively) [85, 86]. Model for R66A *Ca*FADS showed all residues, *i.e.* 1-338, whereas in model for R66E residues 258-263 in chain A and 260-262 in chain B were not refined due to the lack of local electron density. The PISA server predicted for both variants a stable hexameric assembly in solution with similar stability parameters to the WT, but the R66E *Ca*FADS trimeric assembly (A_3 or B_3) was not predicted as stable in solution (Table 3.5). The variants show slight differences when looking at the interface between the RFK- and the FMNAT-modules of neighboring protomers within each trimer (Fig. 3.10A). The

shorter and non-charged A66 side-chain in the R66A variant cannot interact with E268 of the neighboring protomer. In the R66E variant the OE1 atom of E66 establishes a salt-bridge with K296 on loop L6c of the FMNAT-module of the neighbor protomer, neutralizing the introduced negatively charge and taking it far from the expected binding sites for the ATP phosphates and the ribityl chain of RF during RFK catalysis (Fig. 3.10B). In both variants the R65 side-chain and the regions where conformational changes are predicted during catalysis at the RFK-module (loop L4c-FlapII (residues 258-263) and, to a lesser extent, loop L1c-FlapI (193-208)) show higher B factors than in the WT [85]. Finally, changes in the orientation of T165 and, particularly, of D298 are observed regarding their conformations in the WT structure.

Table 3.6. Predicted stability parameters for quaternary organizations inferred from the PISA server.

	Specie	Hexamer (A_3B_3)	Trimer B_3 (A_3)	Dimer (AB)
Surface area sq.·Å	WT	82800	45020 (44480)	31390
	R66A	81760	44570 (43760)	30730
	R66E	82140	44920 (44160)[a]	30820
Buried area sq.·Å	WT	19770	6550 (6520)	2800
	R66A	18680	5770 (6350)	2750
	R66E	19050	593º (6170)[a]	2910
ΔG_{int} [b] kcal/mol	WT	-189.0	-73.0 (-72.0)	-52.7
	R66A	-201.4	-78.4 (-78.3)	-52.8
	R66E	-188.2	-72.3 (-70.1)[a]	-50.2
ΔG_{diss} [c] kcal/mol	WT	22.5	3.1 (2.7)	12.4
	R66A	20.8	4.4 (0.1)	9.8
	R66E	19.0	-0.2 (1.2)[a]	12.4

[a] These structures might not be stable in solutions.
[b] Indicates the solvation free energy gain upon formation of the assembly. The value is calculated as difference in total solvation energies of isolated and assembled structures. This value does not include the effect of satisfied H-bonds and salt bridges across the assembly's interfaces.
[c] Indicates the free energy of assembly dissociation. The free energy of dissociation corresponds to the free energy difference between dissociated and associated states. Positive values of ΔG^{diss} indicate that an external driving force should be applied in order to dissociate the assembly, therefore assemblies with $\Delta G^{diss}>0$ are thermodynamically stable.

6. Discussion

Specific self-association of enzymes is very common in living organisms. Oligomers provide structure and stability, regulate activity by modulating conformation and accessibility of binding sites, facilitate concentration and channeling of molecules,

generate links between different cellular components, transmit signals or regulate ligands homeostasis. In many oligomers the active sites are formed at the subunit interface, while in others, conformational changes are propagated from the interface to catalytic sites [200-202]. Active site residues are usually conserved among species since they are constrained by the specific chemical functionality to catalyze the reaction, but residues that make up the subunit interface evolve as rapidly as the overall protein sequence. Quaternary organizations have been related to the function in several members of the nucleotidyltransferase superfamily [203-206]. Stabilization of quaternary organizations in the prokaryotic FADS family has already been shown for *Ca*FADS [85, 100] but characterization of other family members is reduced to the structures for the FADSs from *Thermotoga maritima* (*Tm*FADS, PDB 1MRZ) and *Streptococcus pneumoniae* (*Spn*FADS, PDB 3OP1) [74]. Moreover, recent data from our laboratory indicate that this later enzyme might stabilize dimers (unpublished results). The main structural difference between *Ca*FADS and *Spn*FADS is an insertion of 12 residues in the L3c (L232-V246, RFK-module) only present in sequences of the *Corynebacterium* and *Mycobacterium* genus (Fig. 1.29). This loop reinforces the interface between trimers in the formation of the dimer of trimers and might be an enabling determinant contributing to mediate interactions between protomers [207]. The second most important difference is the conformation of loop L4n at the FMNAT module (L63-T73). This loop contains R66 and situates at the interface between trimers in the dimer of trimers (Fig. 3.1). In *Tm*FADS the corresponding loop and the preceding α2n helix are displaced towards the α6n helix (Fig. 3.11A), while in *Spn*FADS part of the loop folds into a short α helix (Fig. 3.11B). Non conserved motifs are present in sequences of loop L4n itself and all type of residues are at the equivalent position of R66 in *Ca*FADS. However, the loop usually contains at least two prolines and a group of polar residues with lack of a motif in distribution (Fig. 3.11) [76]. Both facts suggest that L4n might be involved in highly flexible interactions with other protein regions. Even though mutations at R66 in *Ca*FADS do not prevent the formation of oligomeric species, experimental data and theoretical evaluation of structures revealed a negative impact on the stabilization of putatively functional quaternary organizations, trimers and hexamers, as well as on their regulation by ligand binding (Figs. 3.2, 3.3 and 3.5, Tables 3.1 and 3.3). Surface and charge complementarities within this organization result considerably decrease in the mutants regarding the WT enzyme (Table 3.6 and Fig. 3.12), which might favor other types of quaternary arrangements. These

observations indicate that R66 is involved in the establishment and stability of the compact dimer of trimers of *Ca*FADS, but is far from being a single determinant of the enzyme quaternary organization.

Noticeably, kinetic parameters for R66A and R66E *Ca*FADS mutants point to a relevant role for this arginine in modulating the enzyme RFK catalytic efficiency; R66 particularly contributes to maintaining a high turnover and to moderate the large inhibitory effect produced by the RF substrate (Table 3.2). Changes in the affinity of ligands and in the magnitude of the enthalpic and entropic contributions for their binding to the mutants, showed that R66 contributes to place: i) flavins at the FMNAT-module, ii) ATP at the FMNAT-module of one protomer and iii) ATP at the RFK-module of the neighboring protomer within the trimer (Fig. 3.8 and 3.9, Tables 3.5 and 3.3). Both replacements prevent direct interaction of position 66 with the E268 catalytic base of the neighboring protomer within each trimer (Fig. 3.10A), as well as the expected interaction with the ribityl chain of RF during its phosphorylation in this second protomer (Fig. 3.10B) [85, 88]. Thus, lack of a side-chain in A66 position of the R66A variant prevents any contribution of this position to ligand binding at the RFK module, while the E66 side-chain in the R66E variant is located far from the catalytic site (Fig. 3.10B). Therefore, R66 plays a key role in modulating the orientation of the E268 catalytic base and of the reacting atoms during the RFK activity, as previously hypothesized [85]. Nevertheless, the role of R66 in the chemistry of the RFK activity of *Ca*FADS might hardly extrapolate to other members of the prokaryotic FADS family, since this position is not conserved between species [76]. This might be in agreement with other members of the family stabilizing organizations different from the trimer, where a different relative orientation between protomers would be expected and a residue different from that at position 66 in *Ca*FADS might be involved in bridging the catalytic base. To test this hypothesis we should wait to the characterization of other enzymes of the family.

Changes in the efficiency of the FMNAT activity for FMN upon replacing R66 seem to be a consequence of a different interaction mode for substrates/products relative to the WT enzyme (Tables 3.2, 3.5 and 3.3, Fig. 3.9), indicating that R66 plays a role in their accommodation for the production of the catalytic competent complex. However R66 and the loop L4n are relatively far from the FMNAT active site, and exposed either to the solvent in the monomer or to the neighboring protomer within the trimer. Therefore, *a priori* they are not expected to participate in the conformation of the flavin

binding site at the FMNAT module, unless conformational changes in loop L4n are produced (as observed in *Tm*FADS and *Spn*FADS, (Fig. 3.11A and 3.11B). Structures for R66A and R66E variants do not reveal important conformational changes in loop L4n that might occlude/expose the ligand binding site (Fig. 3.11C), but the mutations alter the electrostatic potential surface at one of the sites of the binding cavity (Fig. 3.12A). This observation might explain on one hand the very low occupancy for binding of flavins to the free mutants and on the other the full occupancy of flavins when binding to preformed *Ca*FADS:ADP complex and of ATP:Mg^{2+} when binding to the free enzyme These facts suggest that: i) binding of AT(D)P:Mg^{2+} to the variants might overcome the negative effect introduced by the mutations in the *Ca*FADS ability to bind flavins at the FMNAT site, and ii) the integrity of the adenine nucleotide binding sites at the RFK- and FMNAT-modules is maintained.

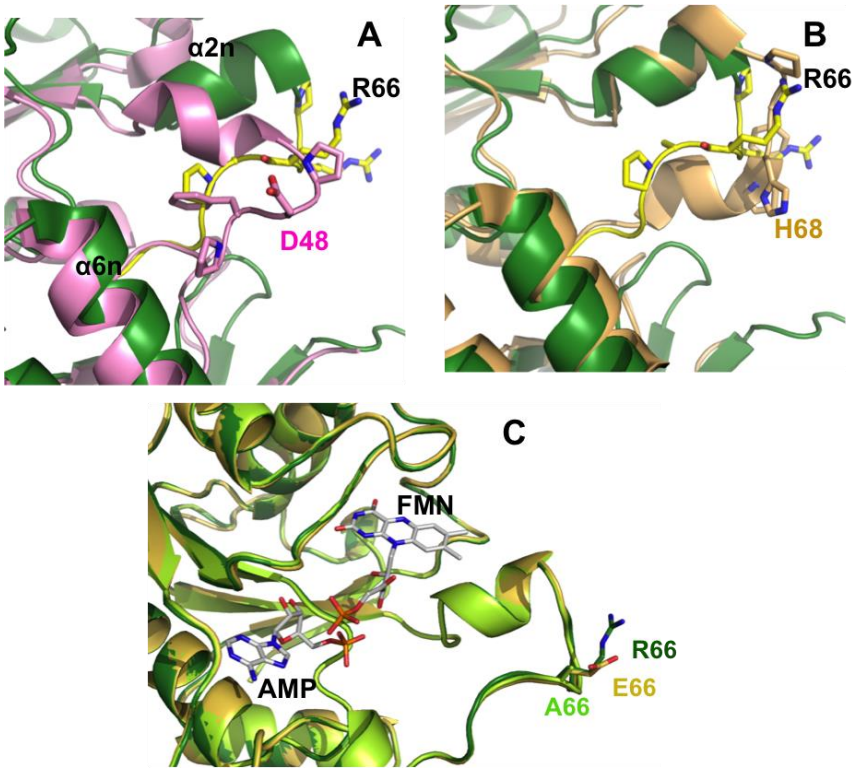

Figure 3.11. Comparison of the conformation of the residues forming the loop L4n in *Ca*FADS (protein in green, L4n in yellow) with those found in the structures of (A) *Tm*FADS (PDB 1MRZ, pink) and (B) *Spn*FADS (PDB 3OP1, wheat). Equivalent residues to R66 are highlighted. (C) Detail of the conformation of side-chain at position 66 regarding modeled ligands at the FMNAT-module of one *Ca*FADS protomer. WT, R66A and R66E *Ca*FADS are colored in dark green, lemon green and yellow, respectively. Modeled FMN and AMP ligands are in CPK sticks.

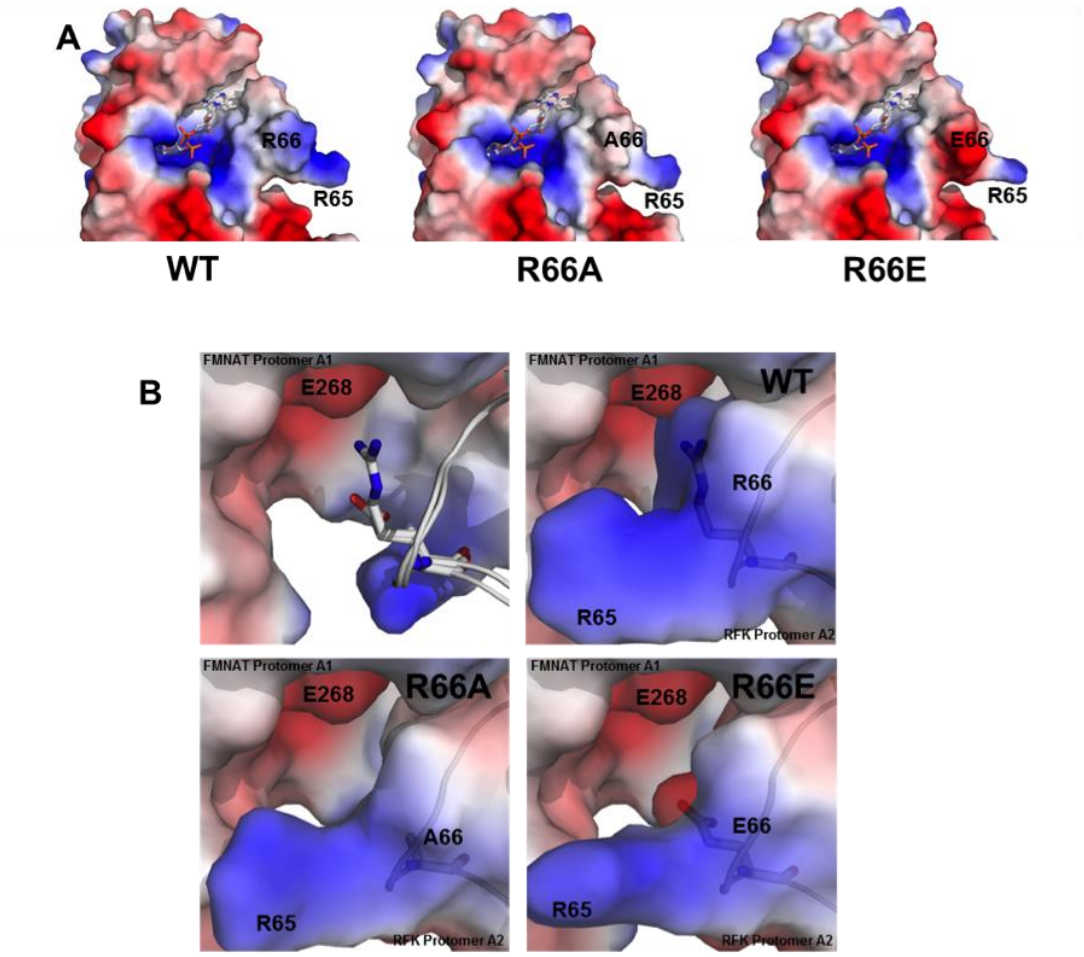

Figure 3.12. Effects on the electrostatic potential surface of *Ca*FADS upon replacement of R66. (A) Electrostatic potential surface of one protomer in the surroundings of the FMNAT catalytic site of WT, R66A and R66E *Ca*FADSs. Modeled FMN and AMP ligands are in CPK sticks. (B) Electrostatic potential surface at the interface between the FMNAT-module and the RFK-module of neighboring protomers within the trimer. The first panel shows protomer A1 in electrostatic potential surface, while the RFK-module of protomer A2 is shown for the three variants in cartoons with residue at position 66 in sticks. Rest of panels show the RFK-module of protomer A2 as electrostatic potential surface for each variant.

Both catalytic and ligand binding behaviors of these variants indicate that the mutation of R66 situated at the FMNAT-module of *Ca*FADS affects the activity catalyzed by the RFK-module. These observations can be explained considering the quaternary of the enzyme into the dimer of trimers, particularly in each trimer. A negative effect on the binding properties of flavins at the FMNAT-module of *Ca*FADS was already described when mutations at E268 also disrupted the R66-E268 salt-bridge [88]. The magnitudes of the enthalpic and entropic contributions to FMN, FAD and ATP binding in WT *Ca*FADS indicate that these ligands induce a large number of

interactions as well as the displacement of numerous well-ordered water molecules on the protein surface upon binding (Table 3.3). Considering that FMN:ADP:Mg^{2+} and ATP:Mg^{2+} have been reported as inducing the formation of the dimer of trimers [100], the large values of the enthalpic and entropic contributions observed for ligand binding may reflect the overall coupled process; ligand binding and assembly of the dimer of trimers. Moreover, changes in conformation of the quaternary organizations in the mutants further support the contribution of the two effects (Fig. 3.9, Table 3.3).

Chapter IV

The trimer interface in the quaternary structure of the bifunctional prokaryotic FAD synthetase from Corynebacterium ammoniagenes

Many biological processes take place through the formation of protein oligomers or multiprotein assemblies as a response to conformational changes, being that an extended mechanism for protein activity modulation [208-210]. Protein-protein association or dissociation processes can be regulated by the binding of partner proteins, metal cofactors or small allosteric effectors, as well as by conformational modifications coupled to geometry changes after a catalytic event [211]. Regarding the protein of our study, the *Ca*FADS, the formation of such species might regulate cellular processes, such as flavin delivery to apo-flavoproteins or those dependent on flavin homeostasis [212, 213]. The assembly takes place through self-association and self-dissociation processes as response to conformational changes induced by the substrates of the two enzymatic activities: FMN-adenylyltransferase (FMNAT) and particularly riboflavin kinase (RFK) [100]. Thus, as previously shown, the head-tail disposition of the monomers within each trimer of the *Ca*FADS dimer-of-trimers approaches the RFK and the FMNAT catalytic sites of neighboring protomers (Fig. 4.1A), placing them at adequate distance and orientation for FMN channeling between modules during FAD biosynthesis [85].

Different structural elements have been proposed to stabilize such quaternary organization through H-bonds, electrostatic and hydrophobic interactions. Some of these elements are: loop L3c located in the FK domain and composed by residues 231-246, loop L4n at the FMNAT module and loops L1c-FlapI and L6c (both in the RFK module) that together with the helix α1c of the same domain, conform the interface between two protomers of the trimer and contribute to the building of the active sites (Fig. 4.1A) [85]. In addition, L1c-FlapI, L6c and α1c, together with loop L4c-FlapII, conform the closed conformation of the RFK flavin-binding site. This conformation is reached after substrate/product binding triggering dramatic conformational changes (Fig. 4.1B) [99].

In the present chapter, we analyze at the molecular level the structural determinants that stabilize the trimer interfaces by evaluating the effect produced through the mutation of residues at L1c-FlapI (K202, E203, and F206), L6c (D298), and α1c (V300, E301 and L304) of *Ca*FADS, which contribute to the trimer stabilization through electrostatic and hydrophobic interactions (Fig. 4.1A) [85]. As we have just indicated, these secondary structural elements also contribute to build the active sites for FMN and FAD synthesis of two contiguous protomers (Fig. 41A) [85] and are involved in important conformational changes contributing to flavin binding at the RFK module

(Fig. 4.1B) [99]. Therefore, the introduced mutations are expected to somehow alter the formation of the oligomeric structures or the catalytic activities of the enzyme.

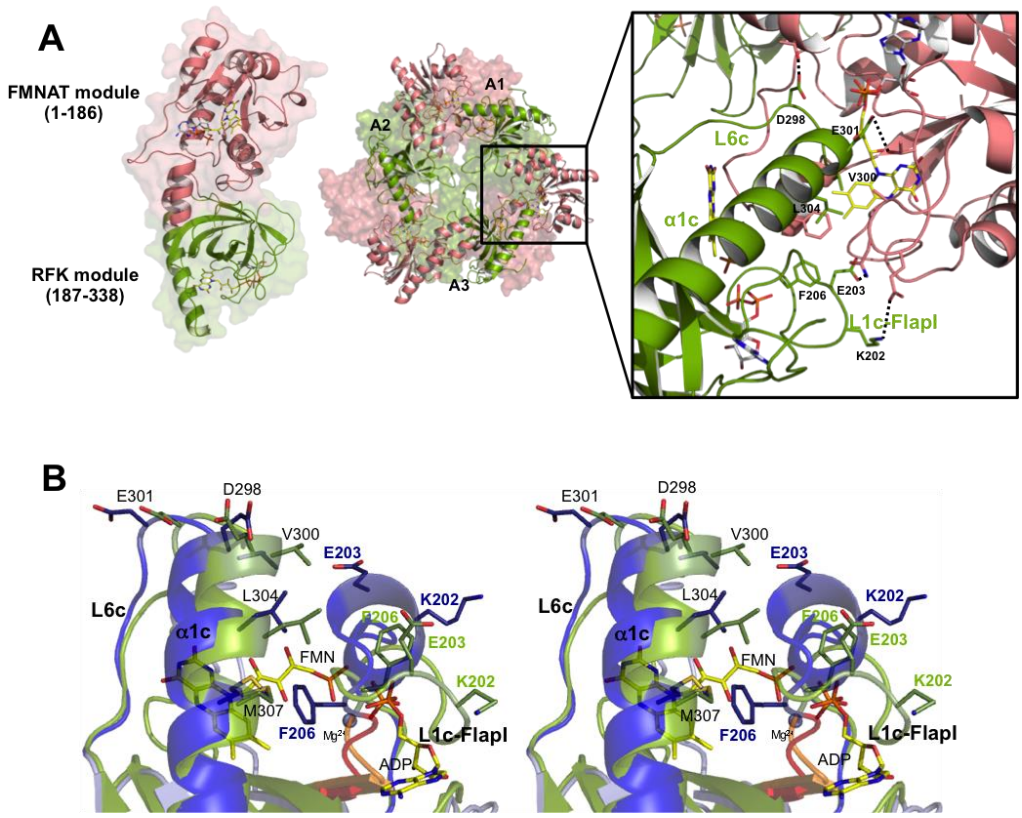

Figure 4.1. Structure of *Ca*FADS. (A) Cartoon representation of the *Ca*FADS monomer (PDB code: 2x0k) and of the dimer of trimers model predicted by the PISA server (one of the trimers is represented as a surface). The RFK-module and the FMNAT-module are colored in green and pink, respectively. The right panel shows a detail of the head-to-tail disposition between the RFK and FMNAT modules of neighboring protomers, within each one of the trimers. Residues involved in the stabilization of the trimer are shown as sticks and the ones mutated in the present work are labelled. H-bonds and salt-bridges established by these residues are indicated with dotted lines. Predicted positions for flavin and adenine nucleotide ligands are shown as sticks with carbons in yellow and gray, respectively. (B) Cross-eye stereo view of the superposition of the RFK modules of *Ca*FADS (PDB code: 2x0k; green) and the ternary complex *Ca*FADS RFK:FMN:ADP:Mg^{2+} (PDB code: 5a89; blue). Relevant residues are shown in sticks. FMN, ADP (in sticks CPK colored with C in yellow) and Mg^{2+} (blue sphere) are from the ternary complex structure. Backbones of the PTAN motifs (207-210 residues) of *Ca*FADS and the ternary complex are highlighted in orange and red, respectively.

1. Spectral properties of *Ca*FADS variants

The expression levels of all variants are similar to that of WT *Ca*FADS (10-17 mg per g cells). Most mutants primarily purified as monomers, with a small population of oligomeric species (Fig. 4.2), similar to WT *Ca*FADS [87, 100]. Far-ultraviolet (UV) circular dichroism (CD) spectra were similar to those of the WT [84] indicating minor impact of the mutations on the enzyme's secondary structure (Figs. 4.3A and 4.3B). However, some mutations considerably decreased the intensity of the near-UV CD signal (Figs. 4.3C and 4.3D), suggesting local changes in the region contributing to the signal.

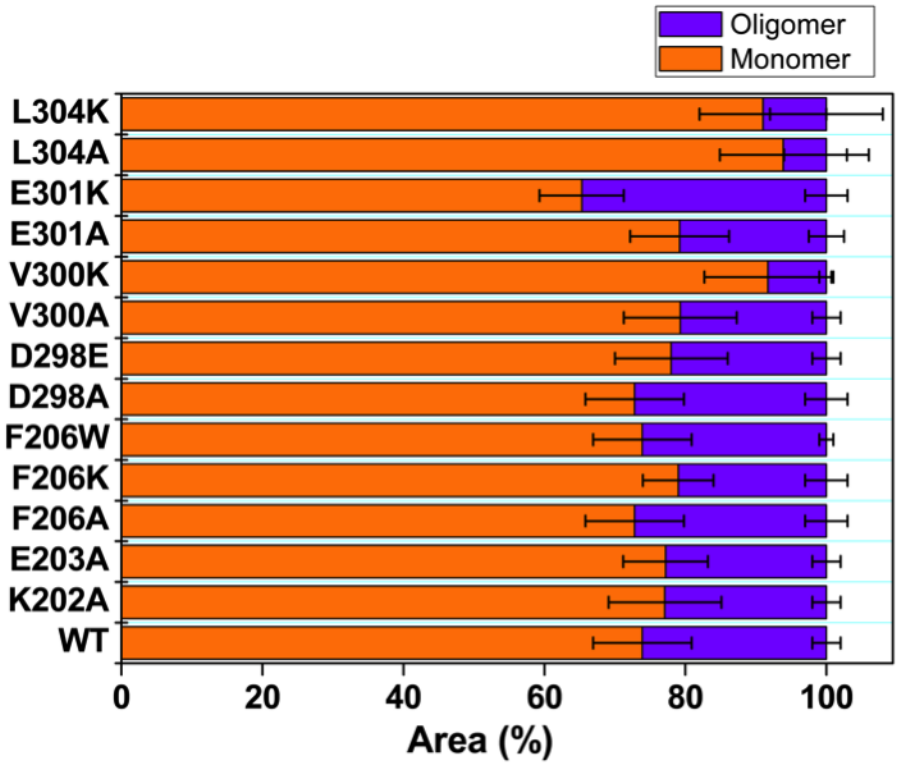

Figure 4.2. Relative area of the monomeric and oligomeric species detected after passing the just purified variants of *Ca*FADS at ~20 µM through a Superdex™ 200 10/300 GL column in 20 mM PIPES, 0.8 mM $MgCl_2$, pH 7.0. The one-way ANOVA test (n=3, confidence interval 95%) did not show statistically significant differences regarding the WT.

Visible difference spectra monitored during titration with flavins indicated that all the *Ca*FADS variants interact with RF, FMN and FAD (Fig. 4.4). Noticeably, while mutations at charged residues increase the magnitude of the difference spectra in comparison to the WT enzyme, the opposite effect was observed for mutations at hydrophobic residues. The most significant changes of peak shapes in the spectra were

observed when titrating with FAD and FMN, particularly for the F206W, D298E and E301K variants (Figs. 4.4C and 4.4F), suggesting different environments of the isoalloxazine ring in the flavin binding site at the FMNAT-module. The increase in the magnitude of the difference spectra upon titration of the preformed WT *Ca*FADS:ADP:Mg^{2+} complex with FMN (~8-times higher than in the absence of ADP) is related to the formation of the FMN binding site at the RFK module [84, 87, 88]. Noticeably, this effect was smaller for most of our variants and undetectable for E301K (Figs. 4.4G and 4.4H). Calorimetric results (discussed below) indicate that, as reported for the WT, all variants maintain two binding sites for FMN in the presence of ADP. Difference spectra suggest that the mutations alter the closed conformation of the flavin isoalloxazine binding site at the RFK module, as described for WT [99].

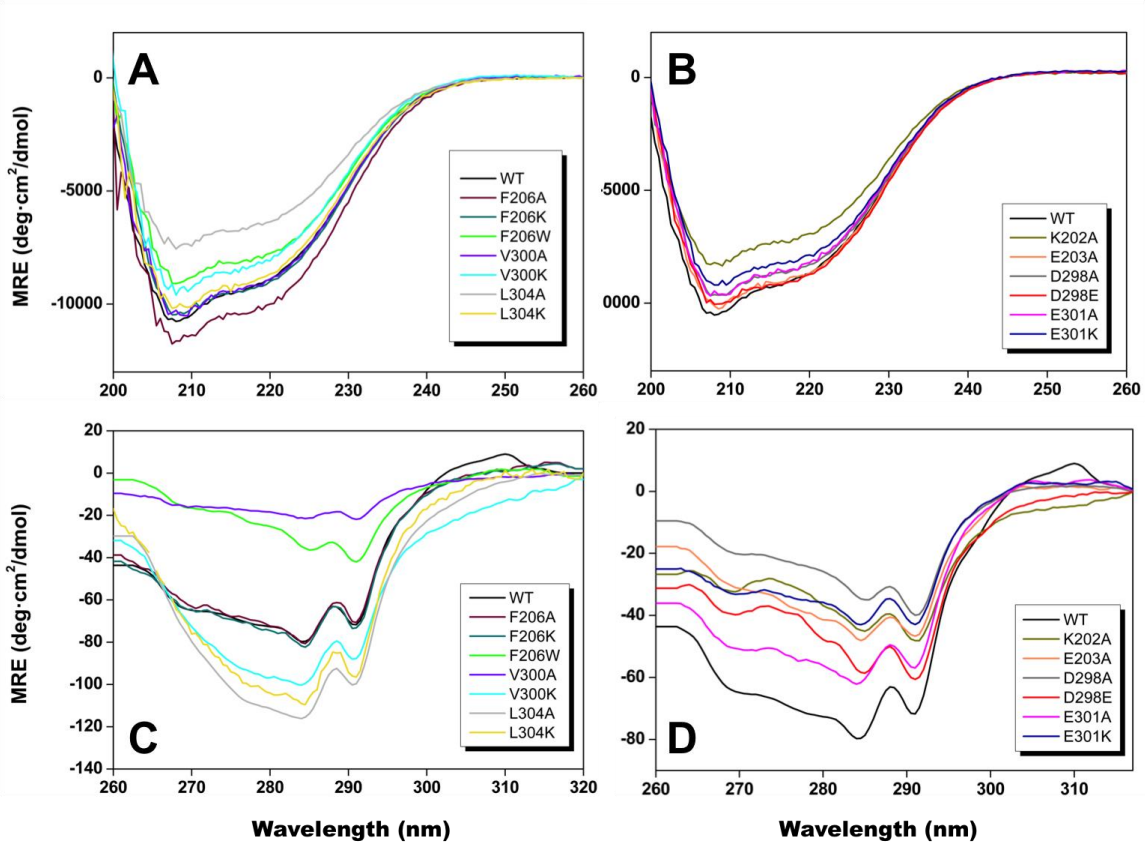

Figure 4.3. Circular dichroism spectra (molar ellipticity *per* residue) (A and B) in the far-UV region and (C and D) in the near-UV region for the different *Ca*FADS variants. Spectra were recorded in 20 mM PIPES, 10 mM $MgCl_2$, pH 7.0 at 25 °C.

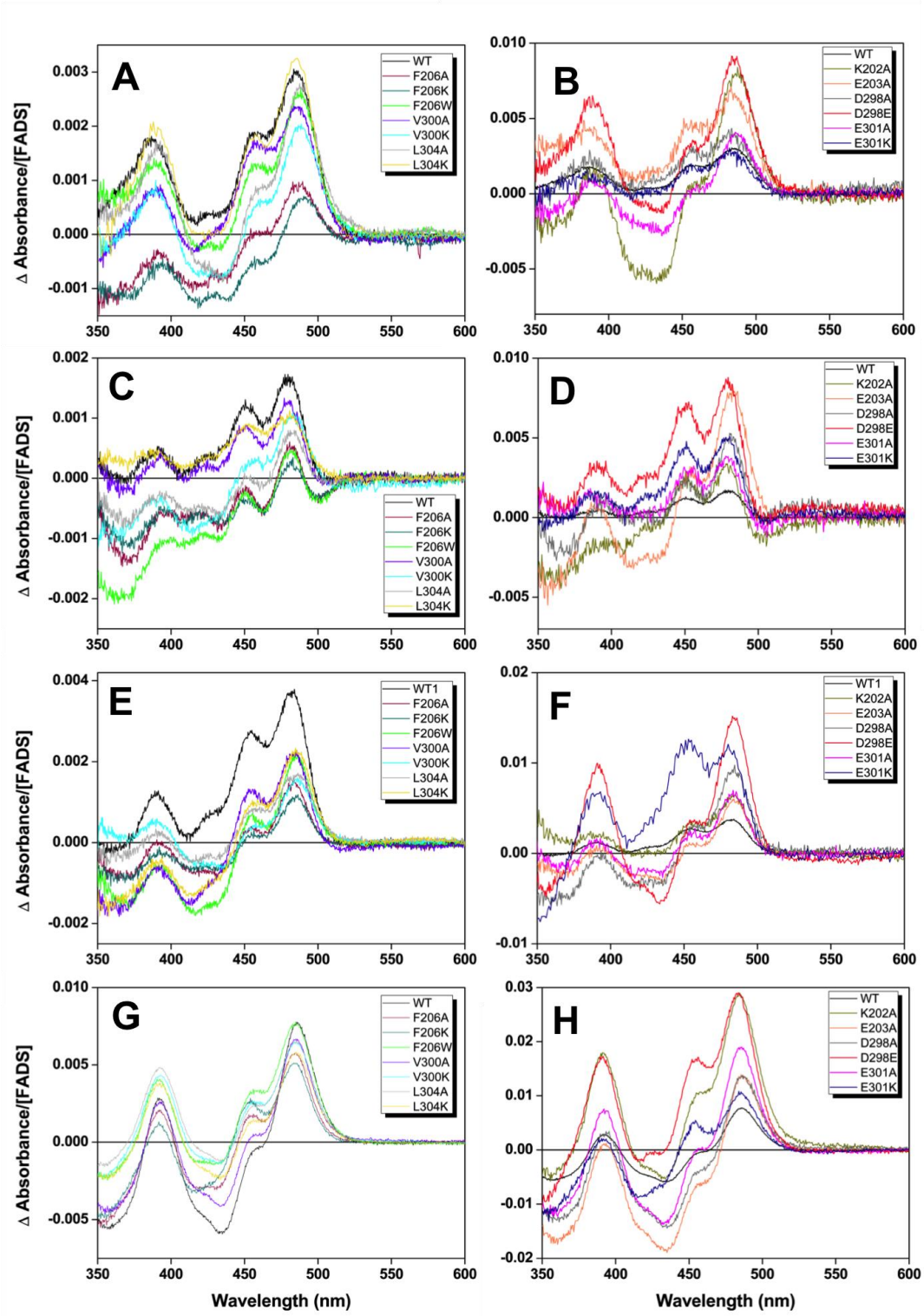

Figure 4.4. Visible difference spectra obtained upon titration the different *Ca*FADS variants with saturating concentrations of (A and B) RF, (C and D) FAD, (E and F) FMN and (G and H) FMN in presence of ADP:Mg^{2+}. Spectra were recorded in 20 mM PIPES, pH 7.0 at 25 °C.

2. Size distribution of *Ca*FADS variants

Previous studies showed that monomeric WT *Ca*FADS, incubated with the products of the RFK activity (FMN and ADP in the presence of Mg^{2+}), stabilizes a transient dimer of trimers, which mostly dissociates into the monomer form upon the ligands' removal by gel filtration chromatography [87, 100]. This is due to the protomers of *Ca*FADS rapidly assembling in response to ligand binding, and disassembling when ligands are eliminated. However, a small fraction of oligomers always remain after gel filtration, which probably reflects the presence of poorly fit assemblies with a large kinetic barrier to dissociation. This might be a consequence of the thermodynamic complexity of the system (see text below and corresponding Figs. 4.2 and 4.5), forming other assemblies than the transient dimer of trimers [87, 100]. In practice, these observations allow the evaluation of whether the introduced mutations modulate assembly and disassembly profiles of WT *Ca*FADS [100]. Taking advantage of this, we next studied whether the mutations influence the *Ca*FADS monomer-oligomer interconversion associated to the binding and dissociation of ligands. We used freshly purified fractions containing either monomeric or oligomeric (which included all oligomeric fractions isolated by gel filtration of freshly purified variants) species and independently incubated them with the products of RFK activity. Monomeric and oligomeric species in the absence of ligands were similarly treated but used as controls. Gel filtration chromatography was then used to remove ligand and separate monomers and oligomers and quantify their relative percentages (Figs. 4.5 and 4.6). For all variants, in the absence of ligands, samples that began as freshly prepared monomers eluted again mostly as monomers (peak labelled 2 in Figs. 4.5A, 4.6A and 4.6B). Variants, when prepared as monomers that had been incubated with the products of the RFK activity, were also isolated mainly as monomers after gel filtration (Figs. 4.5B, 4.6C and 4.6D), as has been reported for WT *Ca*FADS. The only exception was E301K *Ca*FADS, which recovered less than 20% of the monomer.

When oligomeric fractions (the peak labelled 1 in the chromatograms) were similarly treated in the absence of ligands, the monomer/oligomer ratio was ~0.8 for WT, with no statistically relevant differences for most of the variants (Figs. 4.5E, 4.5F and 4.6C). This agrees with the large amount of oligomeric assemblies that remain, which, as mentioned above, possess a large kinetic barrier to disassembly [87, 100].

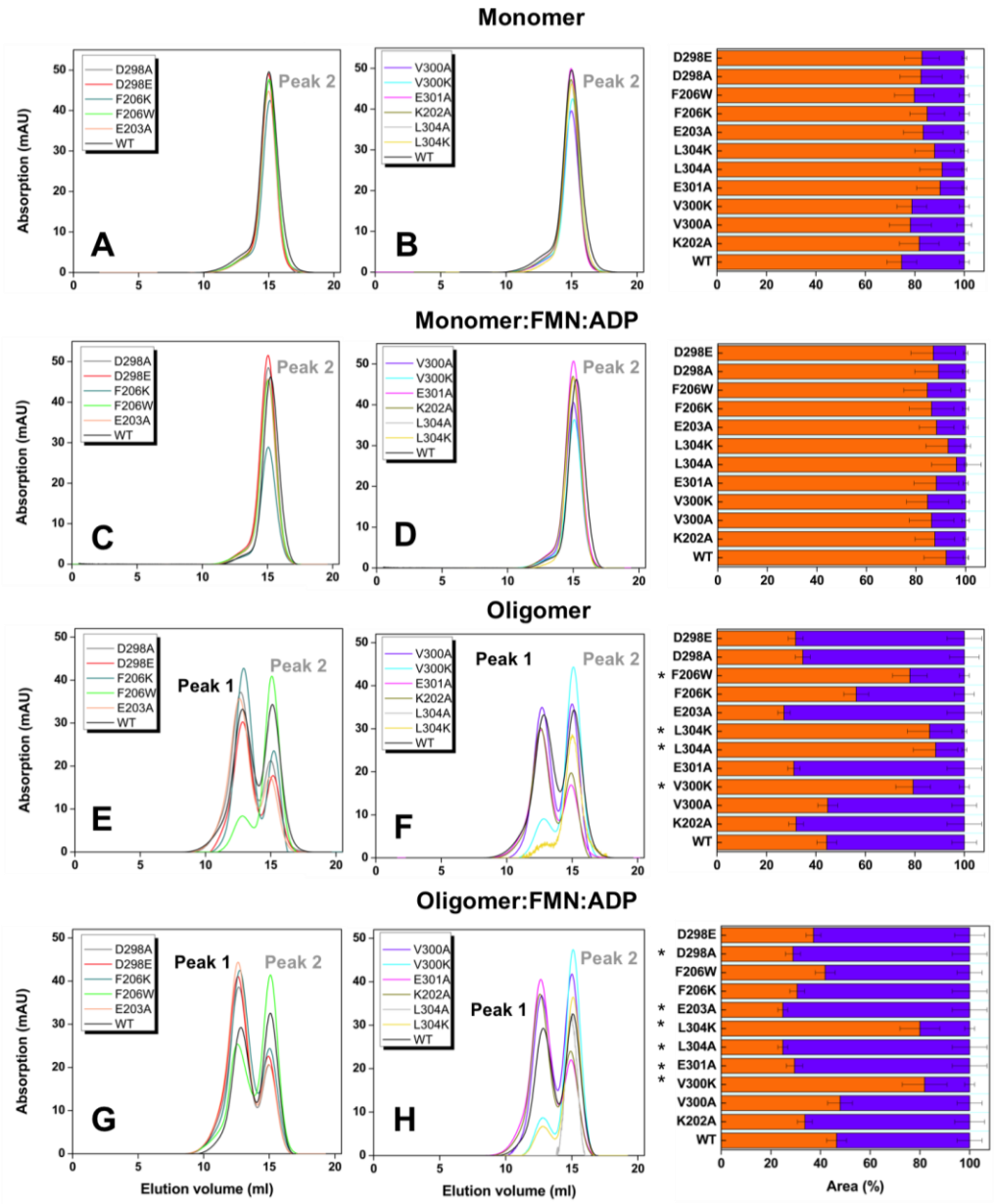

Figure 4.5. Gel filtration elution profiles of purified monomeric and oligomeric fractions of the different *Ca*FADS variants under different conditions. (A and B) The peak corresponding to the monomeric form. (C and D) The band corresponding to the oligomeric forms. (E and F) The peak corresponding to the monomeric form incubated with 25 µM FMN and 200 µM ADP. (G and H) The band corresponding to the oligomeric forms incubated with 25 µM FMN and 200 µM ADP. Panels on the right show the corresponding percentages of monomer (peak 2) in orange bars and the bulk of oligomeric species (peak 1) in violet obtained from each chromatogram, with * indicating values showing statistically significant differences to the WT ones as determined by the one-way ANOVA test (P < 0.002; n=3, confidence interval 95%). All samples contained 15-20 µM of protein, 20 mM PIPES, 0.8 mM $MgCl_2$, pH 7.0, and where incubated 10 min at room temperature before passing through a Superdex™ 200 10/300 GL column in the same buffer.

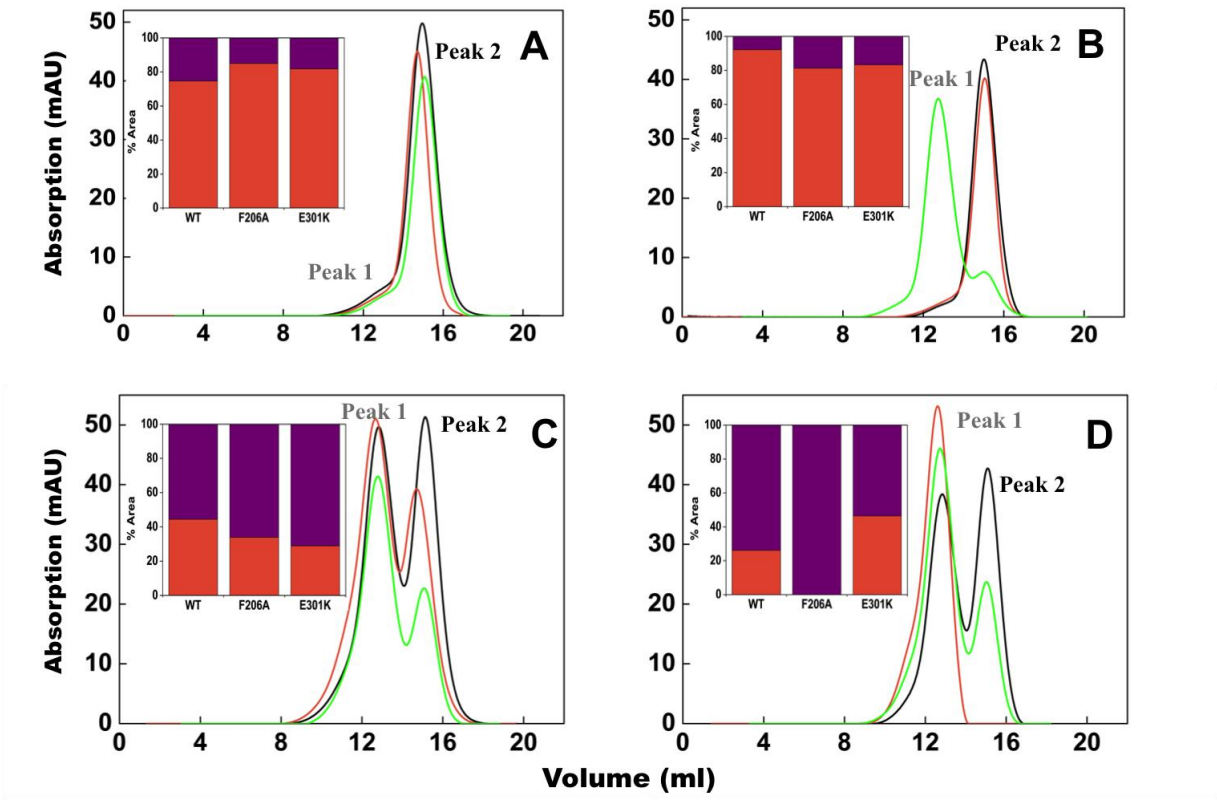

Figure 4.6. Gel filtration elution profiles of monomeric and oligomeric samples of WT (black line), F206A (orange line) and E301K (green line) *Ca*FADSs after incubation under different conditions. (A) The peak corresponding to the monomeric form, which was used as a control. (B) The peak corresponding to the monomeric form, after incubation with 25 μM FMN and 200 μM ADP. (C) The band corresponding to the oligomeric forms, which was also used as a control. (D) The band corresponding to the oligomeric forms, after incubation with 25 μM FMN and 200 μM ADP. The insets show the percentage of monomer (represented by the peak labelled peak 2) and the bulk of oligomeric species (labelled as peak 1) obtained from the chromatograms, with * indicating values that show statistically significant differences from the WT, as determined by the one-way ANOVA test ($P < 0.002$; n=3, confidence interval 95%). All samples contained 15-20 μM of protein, 20 mM PIPES, 0.8 mM $MgCl_2$, pH 7.0, and were incubated 10 min at room temperature before passing through a Superdex™ 200 10/300 GL column in the same buffer.

Nevertheless, this ratio significantly increased for the F206W, V300K and L304 variants, indicating the greater conversion of such assemblies into monomers (panel to the right of Figs. 4.5E and 4.5F). Finally, when the original oligomeric fractions were treated with FMN and ADP, most of the variants exhibit monomer/oligomer ratios similar to the corresponding control. However, no traces of monomer were detected for the F206A variant (Fig. 4.6D), indicating that this mutation prevents recovery of misfit

assemblies by ligand binding and dissociation. In contrast, the V300K and L304K mutations clearly promote the recovery of the monomeric form (Figs. 4.5E and 4.5F). Altogether, these data indicate that point mutations introduced at F206 in L1c-FlapI and V300, E301 and L304 in α1c modulate the reestablishment of monomeric forms as well as the type of assemblies that are produced.

3. Effects of the mutations in the catalytic activities of *Ca*FADS variants

Qualitative analysis of RFK and FMNAT reactions by thin layer chromatography (TLC) indicates that all the variants retained both catalytic activities (not shown).

The RFK activity was quantitatively analyzed by monitoring the conversion of RF into FMN and FAD (because there is no way to fully avoid FMNAT activity) (Table 4.1). At saturating ATP concentrations, all the variants exhibit the WT-like RF-inhibition kinetic profile (not shown). The calculated inhibition constants suggest that only mutation L304A slightly reduces the RF inhibitory effect (see K_i in Table 4.1). while the effect is large enough for F206W, D298E, V300A and E301K variants to prevent determination of accurate kinetic parameters. All mutants except V300K and L304K reduce both k_{cat} (1.5-8 times lower than *Ca*FADS WT*)* and K_m^{RF} values (up to 4-fold lower), maintaining the catalytic efficiency of RF transformation within a factor of three from that of WT *Ca*FADS (Table 4.1). When determining the RFK activity as a function of ATP concentration, (experiments performed at RF concentrations producing 80% of the maximal measured activity), most of the variants show a significant $^{app}k_{cat}$ decrease (Table 4.1), except for F206A, F206K, V300K, L304A and L304K. Under such conditions, the introduced mutations significantly increased K_m^{ATP} in the cases of non-conservative mutations at F206 and E203A, and slightly decreased its value for V300K, L304A and L304K (4-7 times less). When RF is kept constant, most of the variants reduce the catalytic efficiency for ATP and only V300K and variants with mutations at L304 show higher efficiency, because of a stronger apparent affinity for ATP (Table 4.1). These observations indicate that although the mutated residues are not critical to maintain the RFK activity, they are in some way implicated in the adequate allocation of substrates during catalysis.

Table 4.1. Steady-state kinetic parameters for the RFK activity (RF + ATP → FMN + ADP) of the different *Ca*FADS variants (n=3; means ±SE). Data obtained at 25 °C in 20 mM PIPES pH 7.0, 0.8 mM $MgCl_2$.

	k_{cat} [a, b] (min^{-1})	K_m^{RF} [a, b] (μM)	K_i [a, b] (μM)	k_{cat}/K_m^{RF} [a, b] (min^{-1} μM^{-1})	k_{cat} [c] (min^{-1})	K_m^{ATP} [c] (μM)	k_{cat}/K_m^{ATP} [c] (min^{-1} μM^{-1})
WT	408 ±230	11.7 ±3.0	4.9 ±3.9	34.9 ±21.6	155 ±5	28.2 ±3.9	5.5 ±0.8
K202A	63.8 ±11.7	0.8 ±0.4 [e]	19.4 ±8.5	9.9 ±5.3	34.5 ±1.0 [e]	52.7 ±5.3	0.66 ±0.07
E203A	128 ±67	3.7 ±1.3	3.5 ±3.2	34.6 ±21.8	50.1 ±2.8 [e]	89.2 ±13.9 [e]	0.56 ±0.09
F206A	189 ±70	3.2 ±1.9	9.5 ±5.0	59.7 ±41.8	139 ±12	121 ±29 [e]	1.14 ±0.3
F206K	176 ±25	4.0 ±1.2	29.0 ±8.3	44.4 ±14.7	150 ±8	140 ±24 [e]	1.07 ±0.2
F206W	>50 [d]	n.d. [d]	n.d. [d]	n.d. [d]	70.2 ±6.0 [e]	24.7 ±11.1	2.84 ±1.3
D298A	78.4 ±18.9	0.7 ±0.4 [e]	8.7 ±3.9	9.1 ±5.6	32.2 ±0.8 [e]	26.6 ±2.8	1.2 ±0.13
D298E	>20 [d]	n.d. [d]	n.d. [d]	n.d. [d]	20.9±0.8 [e]	64.9±6.9	0.32 ±0.03
V300A	>50 [d]	n.d. [d]	n.d. [d]	n.d. [d]	69.7 ±1.4 [e]	37.5 ±2.5	1.86 ±0.13
V300K	359 ±145	9.7 ±6.4	31.8 ±24.1	36.8 ±28.5	187 ±10 [e]	7.25 ±2.9	25.8 ±10.4
E301A	53.0 ±15.9	0.1 ±0.3 [e]	18.0 ±11.9	10.2 ±30.7	36.7 ±1.1 [e]	30.9 ±4.1	1.2 ±0.2
E301K	>30 [d]	n.d.[d]	n.d.[d]	n.d.[d]	59.9 ±2.0 [e]	59.3 ±6.4	1.0 ±0.1
L304A	260 ±63	3.3 ±1.9	58.4 ±40.7[f]	78.8 ±49.2	177 ±10	4.0 ±3.0	44.3 ±33.3[f]
L304K	540 ±201	14.9 ±5.7	5.0 ±2.8	36.4 ±19.4	131 ±6	4.8 ±2.8	27.4 ±16

[a] Determined at saturating ATP concentrations.
[b] Inhibition by substrate prevented the determination of true parameters and these correspond to apparent constants; $^{app}k_{cat}$ and $^{app}K_m$. Estimated errors in $^{app}k_{cat}$ and $^{app}K_m$ values can increase up to ±35% for the larger K_i values.
[c] Parameters estimated using an RF concentration at which ~80% of maximal activity is exhibited.
[d] Despite these variants being active, the high degree of inhibition prevented mathematical determination of their kinetic parameters.
[e] Values showing statistically significant differences, $P < 0.002$, from the WT, as determined by the one-way ANOVA test (n=3, confidence interval 95%).
[f] Values showing statistically significant differences, $P < 0.02$, from the WT, as determined by the one-way ANOVA test (n=3, confidence interval 95%).

The effects of the mutations on FMNAT activity were similarly evaluated (Table 4.2). The mutations produced minor effects on the k_{cat} and K_m^{ATP} values (generally within a factor of two of those of the WT), but decreases in the K_m^{FMN} were, in general, more significant (up to 25-fold in the case of E301A). Thus, these variants were more efficient than WT in transforming FMN. These data suggest that mutated residues at the RFK module of *Ca*FADS modulate the catalytically competent binding of FMN during the FMNAT activity of the enzyme.

Table 4.2. Steady-state kinetic parameters for the FMNAT activity (FMN → FAD) of the different *Ca*FADS variants (n=3; means ±SE). Data obtained at 25 °C in 20 mM PIPES pH 7.0, 10 mM $MgCl_2$.

	k_{cat} (min^{-1})	K_m^{FMN} (μM)	K_m^{ATP} (μM)	k_{cat}/K_m^{FMN} (min^{-1} μM^{-1})	k_{cat}/K_m^{ATP} (min^{-1} μM^{-1})
WT	5.5 ±0.5	10.1 ±1.0	22.4 ±2.0	0.54 ±0.07	0.25 ±0.03
K202A	2.3 ±0.2 [a]	2.9 ±0.5 [a]	12.1 ±2.9	0.80 ±0.10	0.19 ±0.05
E203A	3.2 ±0.2 [a]	0.70 ±0.10 [a]	10.8 ±2.6	4.5 ±0.7 [a]	0.30 ±0.07
F206A	4.2 ±0.2 [a]	2.9 ±0.7 [a]	38.0 ±7.2	1.45 ±0.4	0.11 ±0.02
F206K	6.2 ±0.3	5.4 ±0.6 [a]	38.8 ±3.3	1.15 ±0.1	0.16 ±0.02
F206W	4.6 ±0.2	1.7 ±0.5 [a]	25.2 ±6.1	3.3 ±1	0.22 ±0.05
D298A	6.1 ±0.4 [a]	1.2 ±0.2 [a]	20.7 ±6.4	5.1 ±0.9 [a]	0.30 ±0.09
D298E	3.3 ±0.3	0.95 ±0.30 [a]	10.4 ±3.3	3.47 ±1.1	0.31 ±0.10
V300A	4.9 ±0.2	1.4 ±0.2 [a]	46.2 ±7.6 [a]	3.5 ±0.5	0.11 ±0.02
V300K	4.6 ±0.3	8.3 ±1.7	9.5 ±1.4	0.55 ±0.10	0.48 ±0.08
E301A	6.9 ±0.2	0.42 ±0.02 [a]	19.7 ±3.6	16.4 ±0.9 [a]	0.35 ±0.06
E301K	6.3 ±0.5	0.85 ±0.20 [a]	15.3 ±3.6	7.4 ±1.8 [a]	0.41 ±0.10
L304A	2.5 ±0.2 [a]	2.8 ±0.3 [a]	34.7 ±9.4	0.91 ±0.10	0.07 ±0.02
L304K	5.2 ±0.5	15.2 ±3.1 [a]	11.5 ±1.8	0.34 ±0.08	0.45 ±0.08

[a] Values showing statistically significant differences from the WT, as determined by the one-way ANOVA test ($P < 0.002$; n=3, confidence interval 95%).

4. *Ca*FADS variants interacting with flavins and ATP

Isothermal titration calorimetry (ITC) was used to determine the binding parameters that describe the formation of *Ca*FADS:flavin complexes (Table 4.3, Fig. 4.7). Upon titration with RF, a single binding site was detected for K202A, E203A, F206W, V300A and L304A *Ca*FADSs. Thermograms for F206A and V300K variants reveal that their interaction with RF, although observed in difference spectra (Fig. 4.4), is weak or occurs with a very low enthalpy change. The remaining variants exhibit the same binding stoichiometry as the native protein (two RF sites) but with altered affinities. F206K and D298A *Ca*FADSs present slightly higher affinity for RF (K_d values only 2- and 4.5-fold lower than WT, respectively), while replacement of E301 by Lys decreases the affinity (Fig. 4.7A, Table 4.3).

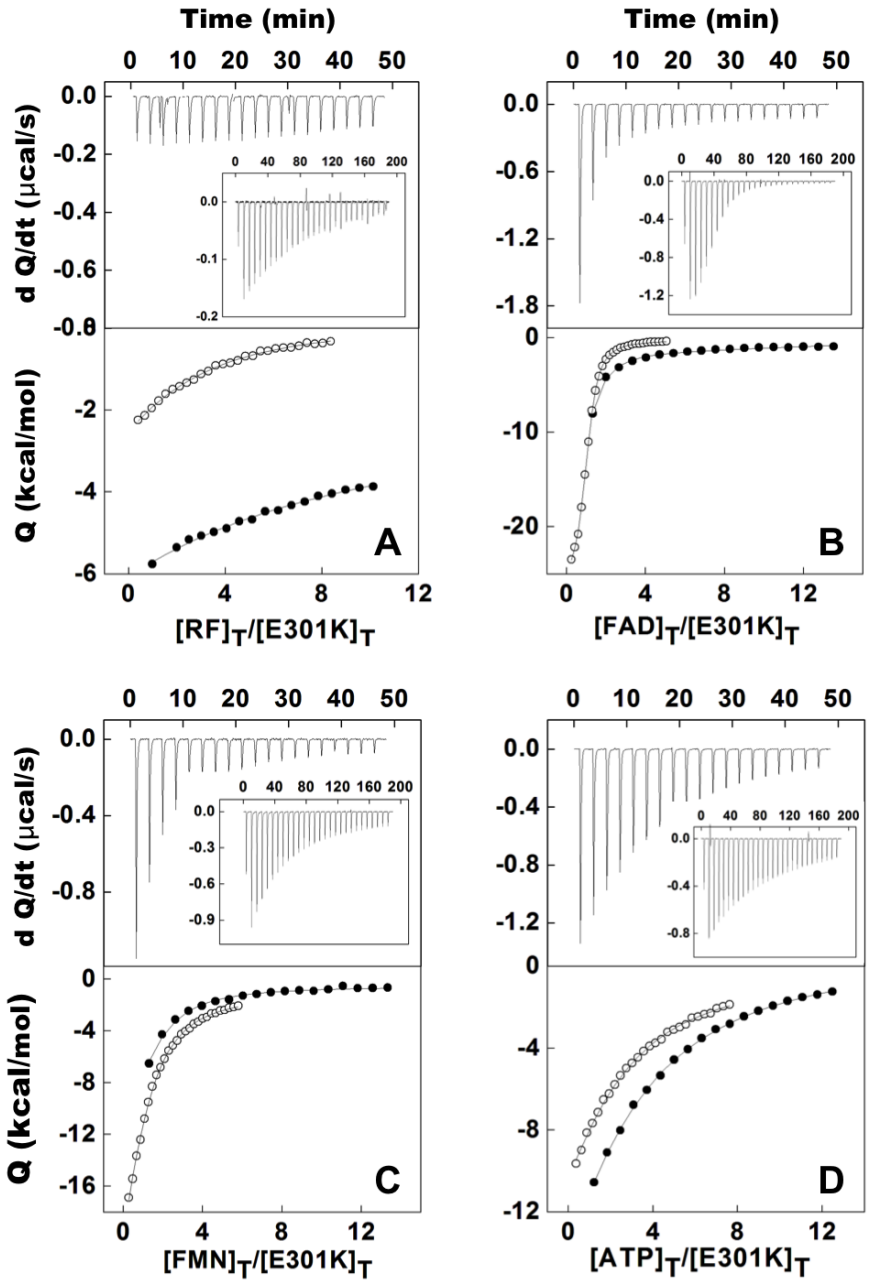

Figure 4.7. Calorimetric titrations of *Ca*FADS with: (A) RF, (B) FMN, (C) FAD and (D) ATP. Upper panels show thermograms for E301K and WT (inset) and lower panels show the corresponding binding isotherms with normalized integrated heats for E301K (●) and WT (○). Experiments carried out in 20 mM PIPES, 10 mM $MgCl_2$, pH 7.0, at 25 °C.

When studying the interaction of these variants with FAD and FMN, several demonstrate low occupancy for either one or both of these flavins (Table 4.3), suggesting non-productive assemblies that block flavin access to their binding sites [87]. Differences in FMN affinity were observed, with relatively weaker interactions for D298 and L304 variants, and a very low enthalpy change for V300K. Most of the

introduced mutations reduced FAD affinity, particularly E203A, L304A and L304K (K_d increases up to 80-fold relative to WT). In general, these differences in binding affinities reveal that the mutations modulate the interactions of flavins with their binding cavity in the FMNAT module.

When analyzing the interaction of the *Ca*FADS variants with ATP, in the presence of 10 mM $MgCl_2$, a single binding site was observed for K202A and L304A, while the rest of the variants retained the two independent ATP binding sites of WT *Ca*FADS [84, 90]. Mutations only produced minor effects in the average ATP affinity, with changes introduced at charged residues causing slight decreases and changes at some hydrophobic residues causing slight increases (Table 4.3). Thus, these mutated residues barely modulate ATP binding at either or both of the FMNAT or RFK modules.

We have also investigated the interaction of FMN with the preformed *Ca*FADS:ADP:Mg^{2+} complex. None of the mutations prevents the FMN binding to the two independent binding sites reported for WT [84]. In general, the mutations appear to disturb the FMN interaction at the high-affinity binding site, presumably the site in the FMNAT-module, demonstrating significantly higher K_d values for F206A, D298A, D298E and L304K (Table 4.3). Only the E203A, F206A, D298A and E301K mutations significantly decrease the affinity of the second FMN-binding site, putatively in the RFK module (K_d 10-15-fold higher) (Fig. 4.8, Table 4.3). These results suggest that E203, F206, D298, E301 and L304 modulate the interaction of the FMN substrate at both the RFK and FMNAT binding sites.

The large values of the enthalpic and entropic contributions reported for FMN, FAD and ATP binding to WT *Ca*FADS have been related to the formation of a large number of interactions, as well as the displacement of numerous well-ordered water molecules on the protein surface, as a consequence of both ligand binding and the assembly of the dimer of trimers [87]. The corresponding values for the mutants in this work are presented in Figures 4.9 and 4.10 and Tables 4.4 and 4.5. In short, these data indicate that these mutations noticeably modulate enthalpic and entropic contributions to ligand binding, with the mutations inducing, in general, the loss of favorable interactions at the FMNAT binding site and the formation of favorable interactions in the RFK module. These data further support the presence of differences between the conformations of the assemblies in these variants.

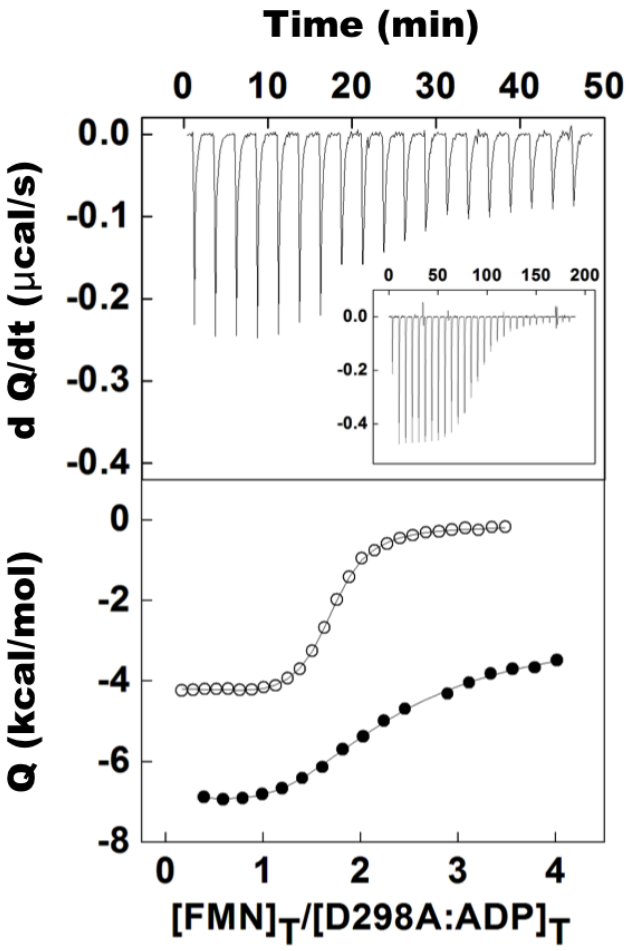

Figure 4.8. Calorimetric titration of the preformed *Ca*FADS:ADP:Mg^{2+} complex with FMN. The upper panel shows thermograms for the D298A and WT (inset) titrations and the lower panel displays the corresponding binding isotherms with normalized integrated heats for D298A (●) and WT (○). Experiments carried out in 20 mM PIPES, 10 mM $MgCl_2$, pH 7.0, at 25 °C.

Table 4.3. Interaction parameters for the interaction of WT and mutated *Ca*FADSs with RF, FMN, FAD and ATP, as determined by ITC (n=3; means ±SD). The stoichiometry for the interaction is shown in brackets. For those showing a stoichiometry of N=2, data correspond to an average K_d ($K_{d,av}$) of two independent binding sites. Data obtained at 25 °C in 20 mM PIPES pH 7.0, 10 mM $MgCl_2$.

	K_d (μM)					
	FADS:RF	**FADS:FMN**	**FADS:FAD**	**FADS:ATP**	**FADS:ADP:FMN**	
				10 mM $MgCl_2$	**FMNAT site**	**RFK site**
WT [a]	24.1 (2) ±3.6	7.8 (1) ±0.9	0.74 (1) ±0.10	30.2 (2) ±4.5	0.04 ±5 10^{-3}	0.90 ±0.10
K202A	31.4 (1) ±4.7	12.2 (<<1) ±1.0	6.4 (<<1) ±1.0	64.5 (1) ±16.9	0.01 ±1.5 10^{-3}	1.4 ±0.3
E203A	10.3 (1) ±2.3	7.2 (1) ±1.6	61.8 (1) ±15.2 [c]	43.4 (2) ±9.3	0.94 ±0.20	9.12 ±1.4 [c]
F206A	n.d. [b]	6.8 (1) ±3.8	1.9 (<<1) ±0.1	15.3 (2) ±2.4	1.2 ±0.7 [c]	9.71 ±2.7 [c]
F206K	7.6 (2) ±2.5	3.1 (<<1) ±0.5	11.5 (1) ±1.7	29.1 (2) ±8.0	0.10 ±0.03	0.39 ±0.06
F206W	10.3 (1) ±4.0	3.6 (<<1) ±1.1	0.68 (<<1) ±0.30	26.5 (2) ±11.0	0.05 ±0.01	0.85 ±0.30
D298A	5.3 (2) ±1.1	18.8 (1) ±2.9 [c]	3.0 (<<1) ±0.3	32.9 (2) ±2.7	1.2 ±0.2 [c]	12.09 ±2.1 [c]
D298E	17.9 (2) ±8.5	19.1 (1) ±1.8 [c]	3.7 (<<1) ±0.2	46.2 (2) ±14.5	1.4 ±0.3 [c]	3.4 ±0.6
V300A	22.6 (<<1) ±1.7	2.5 (<<1) ±0.5	2.2 (<<1) ±1.0	31.6 (2) ±9.1	0.10 ±0.005	3.1 ±0.5
V300K	n.d. [b]	n.d. [b]	4.0 (1) ±0.5	15.3 (2) ±2.4	0.22 ±0.03	2.2 ±0.4
E301A	58.0 (2) ±8.4	5.9 (1) ±0.7	2.4 (1) ±0.9	60.7 (2) ±9.5	0.35 ±0.07	4.7 ±0.6
E301K	142 (2) ±42[c]	13.6 (1) ±1.2	2.9 (1) ±0.4	60.2 (2) ±10.1	0.19 ±0.04	13.2 ±1.9 [c]
L304A	1.2 (1) ±0.4	18.3 (1) ±0.8 [c]	28.2 (1) ±3.3 [c]	17.6 (1) ±1.0	0.51 ±0.20	1.1 ±0.3
L304K	40.6 (2) ±7.7	37.1 (1) ±3.0 [c]	26.2 (1) ±1.0 [c]	39.6 (2) ±2.5	1.7 ±0.1 [c]	2.2 ±0.5

[a] Data from [88, 90]. [b] Despite these variants exhibiting different spectra upon mixing with the ligand, no heat exchange was detected in the corresponding ITC titration, indicating a very low binding enthalpy. [c] Values showing statistically significant differences from the WT, as determined by the one-way ANOVA test ($P < 0.002$; n=3, confidence interval 95%).

Table 4.4. Thermodynamic parameters for the interaction of WT and mutant *Ca*FADSs with flavins and ATP determined by ITC. Data obtained at 25 °C in 20 mM PIPES, 10 mM $MgCl_2$, pH 7.0. Δ*G*, Δ*H* and –TΔ*S* in kcal/mol. Standard errors in Δ*G*, Δ*H* and –TΔ*S* where ±0.3 kcal/mol, taken in general larger than the standard deviation between replicates (n=3) and the numerical error after fitting analysis.

	FADS:RF			**FADS:FMN**			**FADS:FAD**			**FADS:ATP**		
	Δ*G* (kcal/mol)	**Δ*H* (kcal/mol)**	**-TΔ*S* (kcal/mol)**	**Δ*G* (kcal/mol)**	**Δ*H* (kcal/mol)**	**-TΔ*S* (kcal/mol)**	**Δ*G* (kcal/mol)**	**Δ*H* (kcal/mol)**	**-TΔ*S* (kcal/mol)**	**Δ*G* (kcal/mol)**	**Δ*H* (kcal/mol)**	**-TΔ*S* (kcal/mol)**
WT	-6.3	-7.5	1.2	-7.0	-35	28	-8.4	-26	18	-6.2	-30	23
K202A	-6.1	-4.2	-1.9	-6.7	-21.5	15	-7.1	-31	24	-5.7	-56	50
E203A	-6.8	-1.6	-5.2	-7.0	-13	6.2	-5.7	-41	35	-5.9	-24	18
F206A	n.d.[a]	n.d.[a]	n.d.[a]	-7.1	-6.7	-0.4	-7.8	-29	21	-6.6	-17	10.9
F206K	-7.0	-0.5	-6.5	-7.5	-12.5	5.0	-6.7	-17	10	-6.2	-24	17.4
F206W	-6.8	-9.9	3.1	-7.4	-19	11	-8.4	-18	9.1	-6.2	-23	17
D298A	-7.2	-1.5	-5.7	-6.4	-23	16	-7.5	-40	32	-6.1	-27	21
D298E	-6.5	-4.3	-2.2	-6.4	-23	16	-7.4	-56	48	-5.9	-38	32
V300A	-6.3	-11.2	4.9	-7.6	-10	2.8	-7.7	-13	5.7	-6.1	-30	24
V300K	n.d.[a]	n.d.[a]	n.d.[a]	n.d.[a]	n.d.[a]	n.d.[a]	-7.4	-5.9	-1.5	-6.6	-4.8	-1.8
E301A	-5.8	-13	6.7	-7.1	-13	6.1	-7.7	-13	5.8	-5.7	-39	33
E301K	-5.2	-59	54	-6.6	-22	15	-7.5	-24	16	-5.7	-48	42
L304A	-8.1	-5.9	-2.2	-6.5	-7.8	1.3	-6.2	-21	15	-6.3	-26	20
L304K	-6.0	-32.1	26.1	-6.0	-8.2	2.1	-6.3	-17	11	-6.0	-12	6.0

[a] No heat effects were detected in these ITC titrations.

Table 4.5. Thermodynamic parameters for the interaction of FMN with the preformed WT and mutant *Ca*FADS:ADP complexes determined by ITC. Data obtained at 25 °C in 20 mM PIPES, 10 mM $MgCl_2$, pH 7.0. Δ*G*, Δ*H* and –TΔ*S* in kcal/mol Standard errors in Δ*G*, Δ*H* and –TΔ*S* where ±0.3 kcal/mol, taken in general larger than the standard deviation between replicates (n=3) and the numerical error after fitting analysis.

	FADS:ADP:FMN					
	Site 1			**Site 2**		
	Δ*G* (kcal/mol)	**Δ*H* (kcal/mol)**	**-TΔ*S* (kcal/mol)**	**Δ*G* (kcal/mol)**	**Δ*H* (kcal/mol)**	**-TΔ*S* (kcal/mol)**
WT	-10	-4.1	-6.0	-8.2	-4.5	-3.8
K202A	-11	-3.3	-7.7	-7.8	-3.7	-4.3
E203A	-8.2	-1.4	-6.9	-6.9	-2.3	-4.5
F206A	-8.1	-6.3	-1.8	-6.8	-8.0	1.1
F206K	-8.7	-1.7	-7.1	-9.6	-2.3	-7.3
F206W	-9.9	-3.2	-6.7	-8.3	-1.6	-6.7
D298A	-8.1	-3.9	-4.2	-6.7	-8.9	2.2
D298E	-8.0	-1.7	-6.3	-7.5	-3.1	-4.3
V300A	-9.5	-15	5.6	-7.5	-15	7.9
V300K	-9.1	-5.5	-3.6	-7.7	-6.6	-1.1
E301A	-8.8	-3.0	-5.8	-7.3	-4.6	-2.7
E301K	-9.2	-2.7	-6.5	-6.7	-3.2	3.5
L304A	-8.6	-4.3	-4.3	-8.1	-4.9	-3.2
L304K	-7.9	-2.3	-5.6	-7.7	-6.3	-1.4

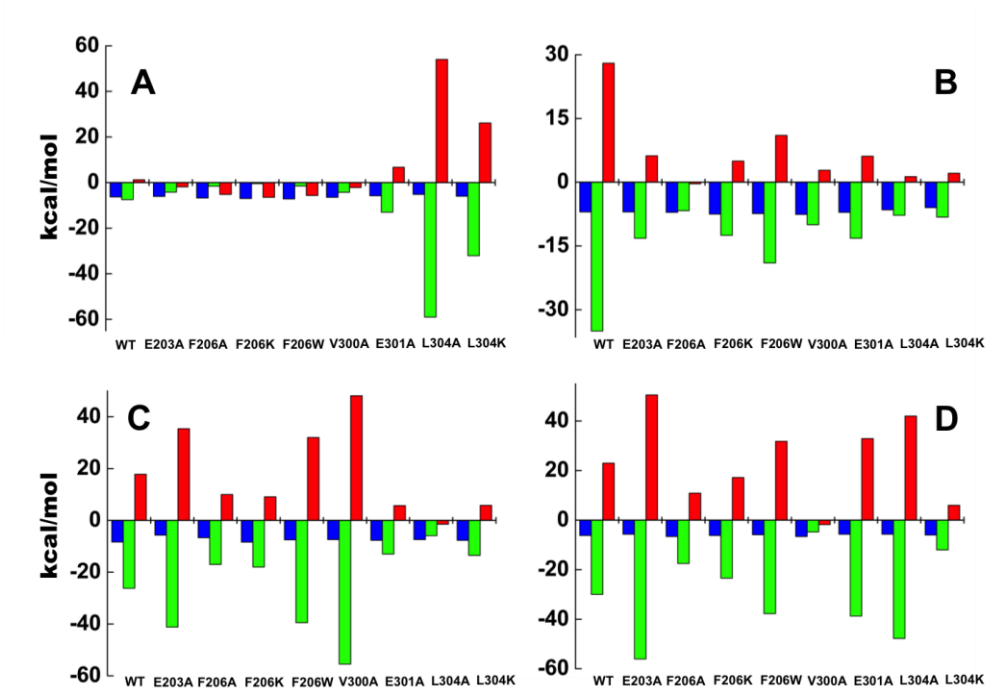

Figure 4.9. Thermodynamic dissection of the interaction of the different *Ca*FADS variants with (A) RF, (B) FMN, (C) FAD and (D) ATP in 20 mM PIPES, 10 mM $MgCl_2$, pH 7.0, at 25 °C. The binding Gibbs energy (ΔG), enthalpy (ΔH), and entropy ($-T\Delta S$) contributions to the binding are represented in blue, green and red bars, respectively.

These data show that the enthalpic contribution turns into more favorable and the entropic contribution into more unfavorable for variants at E301, particularly E301K, and for L304K when are compared with the WT (Fig. 4.9A, Table 4.4). For the rest of the variants RF binding is driven by the enthalpic contribution (more favorable than for WT *Ca*FADS) and by a favorable entropic contribution. FMN and FAD binding to WT *Ca*FADS is driven by a large enthalpic change with a big entropic cost (Fig. 4.9 panels B and C, Table 4.4). All the mutations made the enthalpic contribution for the *Ca*FADS:FMN interaction considerably less favorable, while the entropic contribution was less unfavorable (even favorable for F206A) (Fig. 4.9B, Table 4.5). Larger differences in both magnitudes were observed for the FAD interaction regarding WT; more favorable enthalpic and less favorable entropic binding contributions for E203A, D298A and D298E, less favorable enthalpic and less unfavorable entropic contributions for F206K, F206W, V300A and E301A, and a favorable entropic contribution for V300K (Fig. 4.9C, Table 4.4), resulting in an obvious example of enthalpy-entropy compensation. Regarding ATP binding two patterns for thermodynamic parameters were observed regarding the WT. F206, V300 and L304 variants showed less favorable

enthalpic and less unfavorable entropic contributions, while for the rest the magnitude of these parameters slightly increased (particularly for K202 and E301) (Fig. 4.9D, Table 4.4).

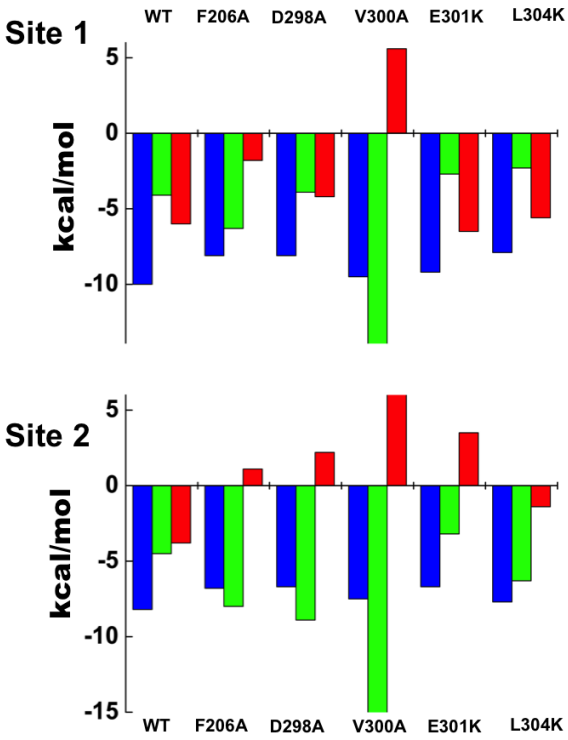

Figure 4.10. Thermodynamic dissection of the interaction of the mutated *Ca*FADS:ADP preformed complex with FMN. Profiles at the two FMN binding sites are displayed separately. The binding Gibbs energy (ΔG), enthalpy (ΔH), and entropy ($-T\Delta S$) contributions to the binding are represented in blue, green and red, respectively. Experiments carried out in 20 mM PIPES, 10 mM $MgCl_2$, pH 7.0, at 25 °C.

As reported for the WT [84, 88] these data show that FMN binding to the preformed *Ca*FADS:ADP:Mg^{2+} complex is driven, in general, by favorable enthalpic and entropic contributions at both sites (Table 4.5). This fact contrasts with the thermodynamic contributions driving FMN binding at the FMNAT module in the absence of ADP (compare Fig. 4.9B with Fig. 4.10 and Table 4.4 with Table 4.5). Changes in the magnitude of enthalpic and entropic contributions to the binding regarding the WT were particularly observed for V300A, for which the enthalpic contribution becomes more favorable and the entropic one becomes unfavorable at both sites (Table 4.5). A similar change in the entropic contribution was observed for mutations F206A, D298A and E301K when analyzing FMN binding at the RFK module (Table 4.5).

7. Crystal Structure of the *Ca*FADS variants

The overall structures of F206W, D298E and E301A *Ca*FADSs (5fnz, 5fo0 and 5fo1, respectively) are quite similar to that of the WT (A chains r.m.s.d. values 0.149, 0.152 and 0.251 Å, superimposing 274, 309 and 317 atoms, respectively). They all have two chains in the asymmetric unit and the relative positioning between the two modules of each protomer is identical to that of WT [85, 86]. All mutants contain residues 1 through 338, corresponding to the whole sequence, although in some high-mobility regions the lack of electron density prevents determining of the structural location of some residues. Thus, in the F206W structure, residues 200-204 in chain A and 201-202 in chain B from L1c, as well as residues 259-263 (in chain A) and 261-264 (in chain B) from L4c-FlapII, are not observed. The D298E structure lacks density for residues 259, 260, 261 and 262. The E301A structure shows all residues in chain A but lacks 260, 261 and 262 in chain B. All mutant structures contain, in addition, one sulfate ion and one pyrophosphate molecule, as ligands in each chain. The PISA server [214] predicts a stable dimer of trimers assembly in solution for the three variants, with similar stability as the WT; in contrast, prediction of a single stable trimeric assembly is uncertain (Table 4.6). Low beta factors at residues forming the interface between modules of a single protomer do not predict hinge movements in any of the variants, similarly to that reported for the WT enzyme [85].

For the F206W variant, the side chain of the introduced tryptophan was refined in slightly different conformations for each of the two molecules of the asymmetric unit. Both differ from those of F206 in the WT structure and in the substrate-bound complex (Figs. 4.11A, 4.11B and 4.11C). Moreover, residues 197-199 on L1c-FlapI of F206W *Ca*FADS were displaced relative to those of the WT (Figs. 4.11A and 4.11C), contributing to the opening of the cavity where ADP binds in the RFK module (Fig. 4.11B). Noticeably, these residues immediately precede the region that stabilizes a 3_{10} α-helix (199-204) in the ternary complex structure of the *Ca*FADS RFK module that contains the reaction products, FMN:ADP:Mg^{2+} (Fig. 4.11B). The PISA server predicts a dimer of trimers for the F206W structure, in which the orientations of F62 and W206 side chains from the two neighboring protomers differ from the WT, and the distance between the aromatic rings increases by 1.34 Å (Fig. 4.11D).

Table 4.6. Predicted stability parameters for quaternary organizations inferred from the PISA server.

	Specie	**Hexamer (A_3B_3)**	**Trimer B_3 (A_3)**	**Dimer (AB)**
Surface area	WT	82800	45020 (44480)	31390
sq.·Å	F206W	83020	45070 (44530)[a]	30730
	D298E	81150	44540 (43380)[a]	30540
	E301A	84750	45690 (45660)[a]	31750
Buried area	WT	19770	6550 (6520)	2800
sq.·Å	F206W	17440	5840 (5020)[a]	2760
	D298E	18930	5960 (6210)[a]	2820
	E301A	18780	5830 (6340)[a]	2750
ΔG_{int}[b]	WT	-189.0	-73.0 (-72.0)	-52.7
(kcal/mol)	F206W	-200.4	-75.1 (-67.2)[a]	-51.9
	D298E	-181.3	-69.9 (-67.0)[a]	-48.3
	E301A	-175.4	-66.5 (-71.8)[a]	-45.0
ΔG_{diss}[c]	WT	22.5	3.1 (2.7)	12.4
(kcal/mol)	F206W	27.2	8.7 (-1.2)[a]	16.3
	D298E	19.6	2.2 (-1.4)[a]	12.3
	E301A	21.8	-0.5 (6.6)[a]	8.1

[a] These structures may or may not be stable in solution

[b] Indicates the solvation free energy gain upon formation of the assembly, in kcal/mol. The value is calculated as difference in total solvation energies of isolated and assembled structures. This value does not include the effect of satisfied hydrogen bonds and salt bridges across the assembly interfaces.

[c] Indicates the free energy of assembly dissociation, in kcal/mol. The free energy of dissociation corresponds to the free energy difference between dissociated and associated states. Positive values of ΔGdiss indicate that an external driving force should be applied in order to dissociate the assembly, therefore assemblies with ΔGdiss>0 are thermodynamically stable.

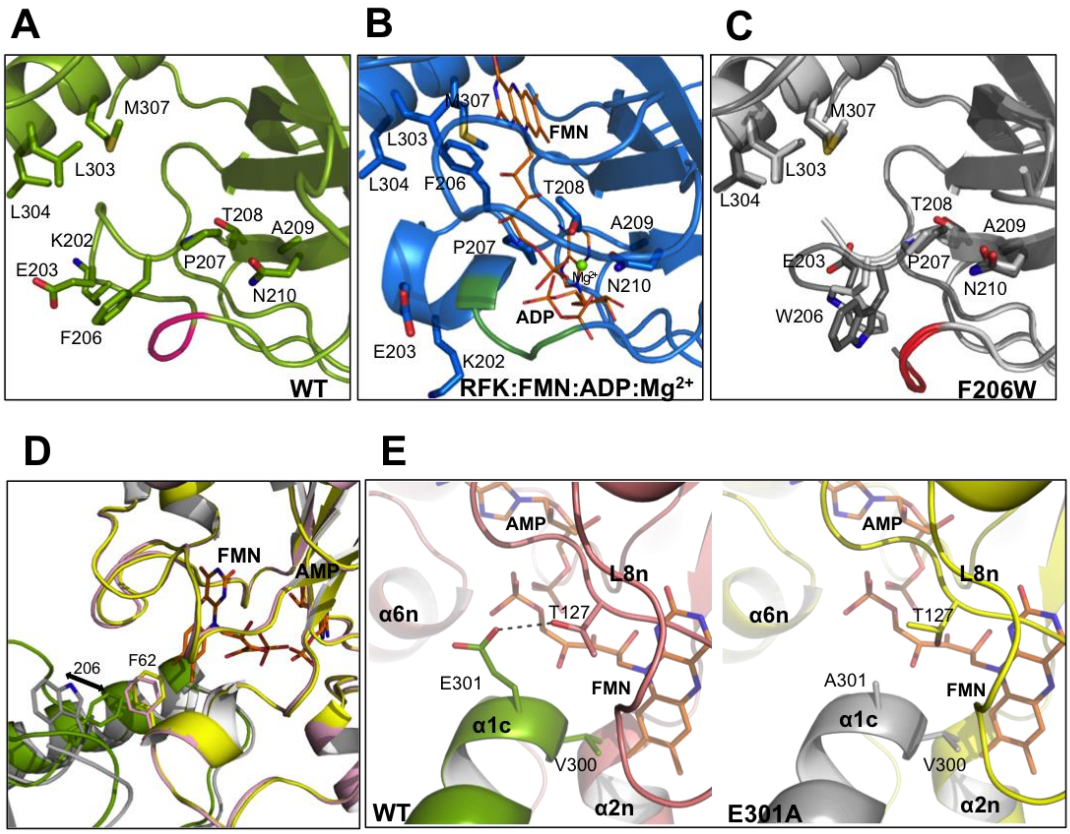

Figure 4.11. Structural analysis of *Ca*FADS variants. Detail of the RFK module around the F206 position in (A) WT *Ca*FADS (PDB code: 2x0k) (green), (B) the WT *Ca*FADS ternary complex with the reaction products (PDB code: 5a89) (blue) and (C) superposition of the two chains of the asymmetric unit (A light gray and B dark gray) in F206W *Ca*FADS with the two different conformations adopted by W206 (PDB code: 5fnz). Relevant residues are represented in sticks and CPK colored, and residues 197, 198 and 199 of L1c-FlapI are highlighted in pink, green and red, respectively. FMN and ADP ligands of the ternary complex are depicted as narrow sticks with orange carbons and the Mg^{2+} ion is shown as a green sphere. (D) Superposition of predicted macromolecular head-to-tail interfaces at the RFK and FMNAT modules of contiguous protomers within each trimer in WT *Ca*FADS (modules in green and pink, respectively) and in F206W *Ca*FADS (modules in gray and yellow, respectively). Residues 62 and 206 are shown in colored sticks. An arrow indicates the change in side chain conformations at position 206 in the mutant. (E) Detail of the predicted trimer head-to-tail interface region around position 301 in WT (left panel, RFK module in green and FMNAT module in pink) and E301A (right panel, RFK module in gray and FMNAT module yellow, respectively) *Ca*FADS variants. In (D) and (E) FMN and AMP ligands in the FMNAT module have been modelled as previously described and are shown in sticks colored with carbons in orange [85].

No differences were observed in the D298E *Ca*FADS structure relative to that of WT. Replacement of D298 with Glu allows carboxylic oxygen atoms to maintain their bond with T165 of the neighboring protomer in the trimer (Fig. 4.12). Finally, no conformational changes were observed in L6c or in the α1c helix, which contains the E301A mutation, when comparing this mutant's structure to that of the WT. However, the H-bond between E301 of one protomer and T127 on loop L8n of the neighboring protomer, which is predicted for the WT dimer of trimers, is not expected in this case (Fig. 4.11E).

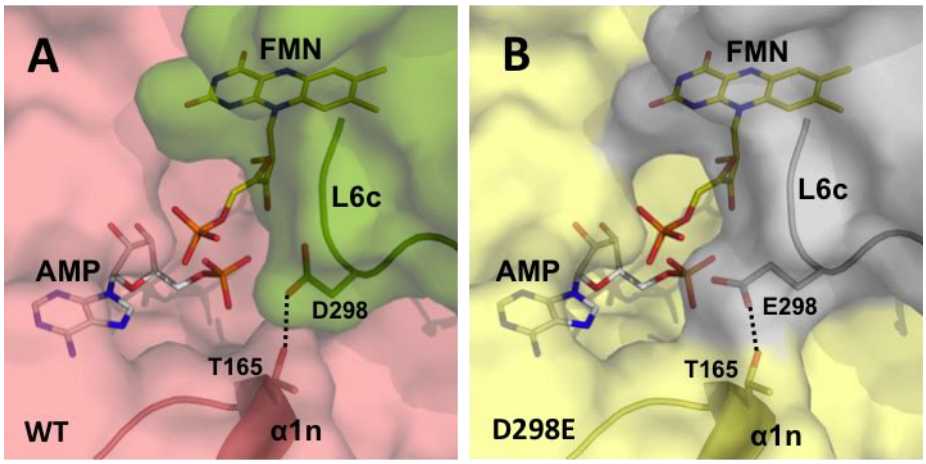

Figure 4.12. Detail at the macromolecular interfaces predicted by PDBePISA among the RFK- and FMNAT-modules of contiguous protomers within the trimers for (A) WT (modules in green and pink, respectively) and D298E (in grey and yellow, respectively) *Ca*FADSs. Modules are represented as surfaces with cartoon representation of secondary structure elements implicated in the interaction of the side-chain at position 298 with T165 (shown as colored sticks). Theoretical position for FMN and AMP ligands in the FMNAT module is shown in yellow and grey CPK sticks, respectively, accordingly to the model previously proposed for the interaction to WT *Ca*FADS [85].

6. Discussion

All studied variants with mutations in L1c-FlapI, L6c and helix α1c are active, as well as able to bind ligands and to stabilize transient quaternary assemblies. The lack of drastic changes prevents us from making conclusions regarding channeling between modules of different protomers, a question previously raised for the *Ca*FADS dimer of trimers [85]. Despite the fact that the effects are not drastic, point mutations, particularly in L1c-FlapI and helix α1c, affect the equilibria between *Ca*FADS monomeric/oligomeric assemblies, as well as kinetic and ligand binding parameters. All mutants also maintain the WT inhibition profile induced by an excess of the RF

substrate. This is a critical aspect of the regulation of the RFK activity in *Ca*FADS, to which product inhibition might also contribute [88, 90]. Work is underway to understand the different levels of inhibition occurring in this enzyme. Nevertheless, those studies are beyond the scope of the present work (although they will be addressed in the next chapter) since the variants presented here do not demonstrate statistically significant differences in K_i^{RF} relative to the WT (Table 4.1). Therefore, in this work, we emphasize interpreting the effects of mutations on the kinetic and binding parameters in view of the available structural information

Mutations in L1c-FlapI (K202, E203 and F206) modulated the kinetic parameters for the RFK activity of *Ca*FADS, as well as ligand binding parameters in the C-terminal module (Tables 4.1, 4.3 and 4.4). Therefore, although the relevant residues are not directly involved in catalysis, they somehow contribute to achieving the appropriate RFK catalytic geometry. This relationship is consistent with the recently reported structure for the *Ca*FADS RFK:FMN:ADP:Mg^{2+} ternary complex (Fig. 4.1B) [99]. Complex formation induces conformational changes in L1c-FlapI, β2c and the 207-PTAN-210 motifs, which displace Cαs of K202 and E203 by 8.1 and 7.2 Å, respectively. Concomitantly, the F206 side chain (highly conserved in FADS [76]) moves more than 7 Å to stack against M307 of helix α1c and the isoalloxazine ring of the flavin ligand [85, 99] (Fig. 4.1B). In these variants, K_m^{FMN} for the FMNAT activity, as well as thermodynamic parameters for ligand binding at the FMNAT module (Tables 4.2, 4.3 and 4.4), reveal the importance of L1c-FlapI residues in FMN and FAD binding in the N-terminal module. Moreover, the low fraction of protein that is capable of FAD and FMN binding that some of these variants exhibit is consistent with the coexistence of competent conformations in equilibrium with non-competent assembles that hinder flavin binding (Table 4.3) [87]. Furthermore, the strong effect of the E203A and F206A mutations on FMN binding at the FMNAT site in the *Ca*FADS:ADP:Mg^{2+} preformed complex (Tables 4.3 and 4.5) align with the observation that their monomer/oligomer ratios after purification differ from that of the WT (Fig. 4.2A). In the WT *Ca*FADS dimer of trimers, K202 and E203 stabilize salt-bridges with E130 and N131 from loop L8n of the neighboring protomer within the trimer, while F206 interacts with F62 of helix α2n (Fig. 4.1A) [85]. The mutation of K202 and E203 to Ala would prevent formation of the salt-bridges, while substitution of F206 by Ala or Lys will abrogate its hydrophobic interaction with F62. With the elimination of such interactions, the shape of the isoalloxazine hydrophobic cavity in the FMNAT site should change, as found

when evaluate this cavity in the dimer of trimers assembly for the F206W variant (Fig. 4.11D). This conservative substitution apparently reduces the amount of oligomeric assemblies able to bind FMN and FAD at the FMNAT site, relative to the WT, an effect that is clearly overcome in the ternary complex (Table 4.3). Altogether, these data indicate that L1c-FlapI and, particularly, F206, contribute to modulating the conformations and the catalytic properties of quaternary assemblies of *Ca*FADS, although the individual residues studied here are neither critical for catalysis nor key determinants in assembling the protein structure.

Mutations in L6c (D298) and the contiguous N-terminal helix α1c (V300, E301 and L304) considerably modulate k_{cat} and K_m^{RF} for the RFK activity as well as K_m^{FMN} for the FMNAT activity (Tables 4.1 and 4.2). In general, the mutations decreased the affinity for FAD and FMN, and V300A and D298 variants also show low flavin occupancy (Table 4.3). These results, together with the observed changes in the thermodynamic parameters (Figs. 4.9 and 4.10, Tables 4.4 and 4.5), indicate that these residues contribute to the binding of flavins in the FMNAT module as well as to the stabilization of quaternary assemblies. These mutations also affect the flavin binding in the RFK module, as seen in the decrease of the FMN affinities of their *Ca*FADS:ADP:Mg^{2+} complexes (Table 4.3). These effects (Tables 4.1 and 4.3) are consistent with recent studies that show that ligand binding and catalysis at the RFK site triggers dramatic conformational changes in L1c-Flap1, L4c-FlapII, L6c and helix α1c (Fig. 4.1B) [99].

Residues here mutated do not directly interact with the flavin substrate, but L6c and helix α1c regions are part of the hydrophobic core that closes the *re*-face of the isoalloxazine ring (Fig. 4.11B). In addition, L6c and the N-terminal end of helix α1c also contribute to closing the FMNAT flavin-binding site of the neighboring protomer within the *Ca*FADS trimer (Figs. 4.1A and 4.11E). In particular, D298 establishes H-bonds with T165 at α1n of the adjacent protomer [85], a residue reported as critical for substrate binding and FMN adenylylation (Fig. 4.12) [90]. D298 replacement by Ala would prevent this interaction, but in the D298E mutant, the introduced Glu can still retain it (Fig. 4.12). However, the presence of more than one orientation of carboxylic oxygens suggests that alterations to the FMNAT ligand-binding cavity within the dimer of trimers (Fig. 4.12) is a factor that determines the low flavin occupancy in the FMNAT sites of these variants (Table 4.3).

Among the residues mutated in helix α1c, only V300 is predicted to directly interact with the FMN isoalloxazine ring (1.38 Å) in the FMNAT module of the adjacent protomer [85] (Fig. 4.1A and 4.11E). Substitution of V300 by Ala or Lys will affect the hydrophobic interactions, which can explain the changes observed in FMN and FAD binding parameters (Tables 4.3 and 4.4). E301 and L304 are predicted to interact with T127 and A132, respectively, of L8n of the neighboring protomer FMNAT site (Figs. 4.1A, 4.11E) [85]. The lack of interactions between the side chain of residue 301 and T127 in the E301A mutant and the substitution of L304 by Ala would both affect the van der Waals contacts with L8n in the dimer of trimers, producing local effects at this loop that helps close the FMNAT substrate binding site. These mutations can also alter the positive end of the helix α1c dipole, which contributes to the stability of substrate phosphate groups and is located near the FMNAT substrate binding site (Fig. 4.11E) [85]. Since ligand binding and catalysis in the RFK module also trigger the conformational change of L6c and the bending of the helix α1c [99], it is very likely that interplay between RFK and FMNAT modules of protomers, within the trimer, will differ when introducing mutations at L6c and α1c (Figs. 4.2 and 4.5). However, we cannot further speculate until structures containing the FMNAT module in complex with ligands become available. All these structural considerations also explain the changes in kinetic and binding parameters of the FMNAT module for the *Ca*FADS mutants (Tables 4.1, 4.2 and 4.3), which suggest a different conformation for flavin binding, especially, for FMN (Table 4.4 and Fig.4.5).

Altogether, our data indicate that the secondary structural elements of the *Ca*FADS RFK module investigated herein tune protomer-protomer contacts within the trimer. This confirms the interplay between protein-protein assembly and catalysis, with a possible role of macromolecular interfaces contributing to flavin homeostasis [100]. In this direction, recent studies on the human FMNAT, FADS2, have proven direct delivery of the flavin cofactor to the recipient apoflavoprotein through heterologous protein-protein interactions [156]. If this mechanism also occurs in *Ca*FADS, we might envisage the possibility of macromolecular assemblies as part of a cell strategy to control the delivery of FMN and FAD to apoflavoproteins. However, the study of such new strategies lies beyond this work.

Chapter V

Kinetics and thermodynamics in the protein-ligand interactions in the riboflavin kinase activity of FAD synthetase from *Corynebacterium ammoniagenes*

Despite the fact that all the bacterial FADSs share function and structure, some functional differences have been found among them. For instance *Ca*FADS does not required reducing environment for its FMNAT activity while other FADS from pathogenic bacteria such as *S. pneumoniae* or *L. monocytogenes* require the presence of a reducing agent [79]. Another important difference is that the RFK activity of *Ca*FADS shows inhibition when RF concentration increases [88], while other members of the family do not show this behavior. These differences suggest dissimilar regulatory mechanisms that, as a last resort, might be related with the pathogenic/non pathogenic character of the microorganism. In the present study we focus on this second regulatory topic, and specifically we work with the isolated RFK domain of *Ca*FADS or Δ(1-182)*Ca*FADS. This isolated module has shown to be fully active and to show the same behavior that the complete enzyme [99]. Therefore, and due to the intrinsically difficulties inherent to some of the techniques here used, the isolated C-terminus domain seems to be perfect for the characterization of the regulation of the *Ca*FADS RFK activity. In addition available crystal structures of the RFK domain free and in complex with some of its products (which reveal necessary conformational changes during the catalytic cycle) let us to connect our results with the 3D structures [99].

In this chapter we present a complete study of the inhibition of the *Ca*FADS RFK domain both from the kinetic and the thermodynamic points of view, identifying the inhibitors of the enzyme and its course of action. Regarding to the kinetic approach, stopped flow spectrophotometry provides a deep sight of how the substrates and the products bind the enzyme before the equilibrium is reached and also of the conformational changes during the catalytic cycle, while kinetic measurements in the steady state yield the type of inhibition suffered by the enzyme and the inhibition constants. From the thermodynamic point of view, isothermal titration calorimetry experiments allow tracing the complex network of interactions between the enzyme and its ligands, identifying the most favorable pathways and the effect that one specific substrate or product has over the others.

1. The RFK activity shows inhibition by the RF substrate as well as by the products of the reaction.

The independently expressed RFK module of *Ca*FADS retains the ability to catalyze the phosphorylation of RF, and conserves the structural determinants responsible for the strong inhibition by its RF substrate (bold lines in Figs. 5.1A and 5.2A) [99]. Fitting of the observed steady-state rates either to the Michaelis-Menten equation (Eqn. 2.3) (Fig. 5.1A, bold line), or to the equation describing a dead-end inhibition by substrate excess (Eqn. 2.4) (Fig. 5.2A, bold line), allowed determining the apparent values for the constants that characterize the process with K_m^{ATP}, K_m^{RF}, K_i^{RF} and k_{cat} values of 60.3±11.5 µM, 10.4±1.6 µM, 1.9±0.2 µM and up to ~440 min^{-1}, respectively (Table 5.1).

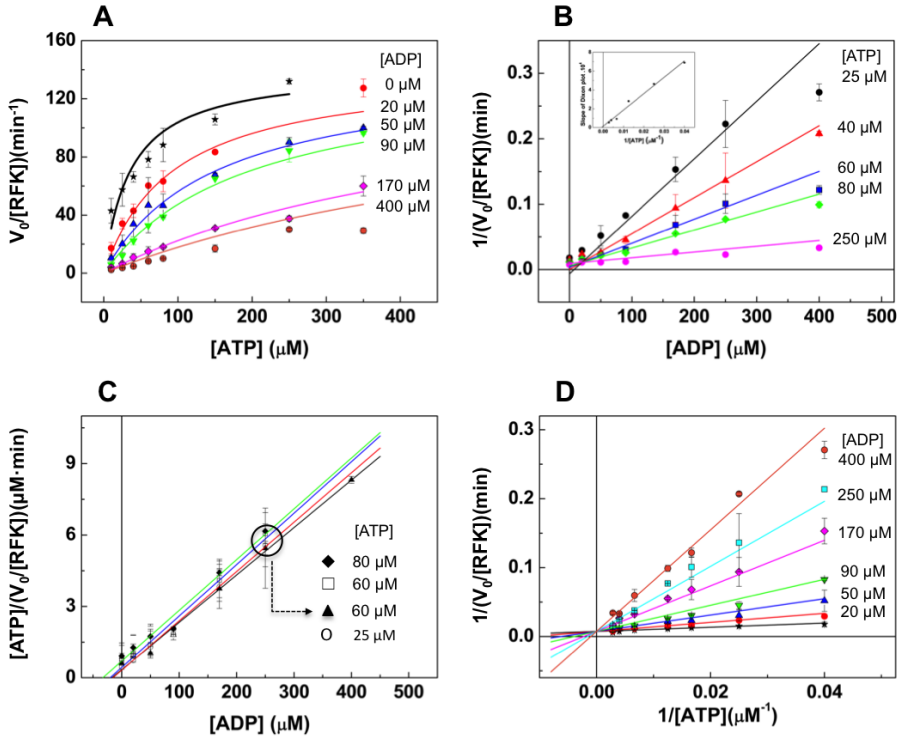

Figure 5.1. Inhibitory effects produced by the ATP substrate and the ADP product in the steady-state RFK activity of the RFK module of *Ca*FADS. (A) Michaelis-Menten plots as a function of the ATP substrate at different concentrations of the ADP product and the corresponding (B) Dixon plot with the representation of the slopes *vs.* 1/[ATP] in the inset, (C) Cornish-Bowden plot and (D) Lineweaver-Burk representation with global fit to the equation for competitive inhibition. Reaction rates were obtained in 20 mM PIPES, 0.8 mM $MgCl_2$, pH 7.0, at 25°C, with 5 µM RF (concentration for which the enzyme shows the 80% of its maximal apparent activity at saturating ATP), varying the concentration of the ATP substrate (10-350 µM) and the ADP product (0-400 µM).

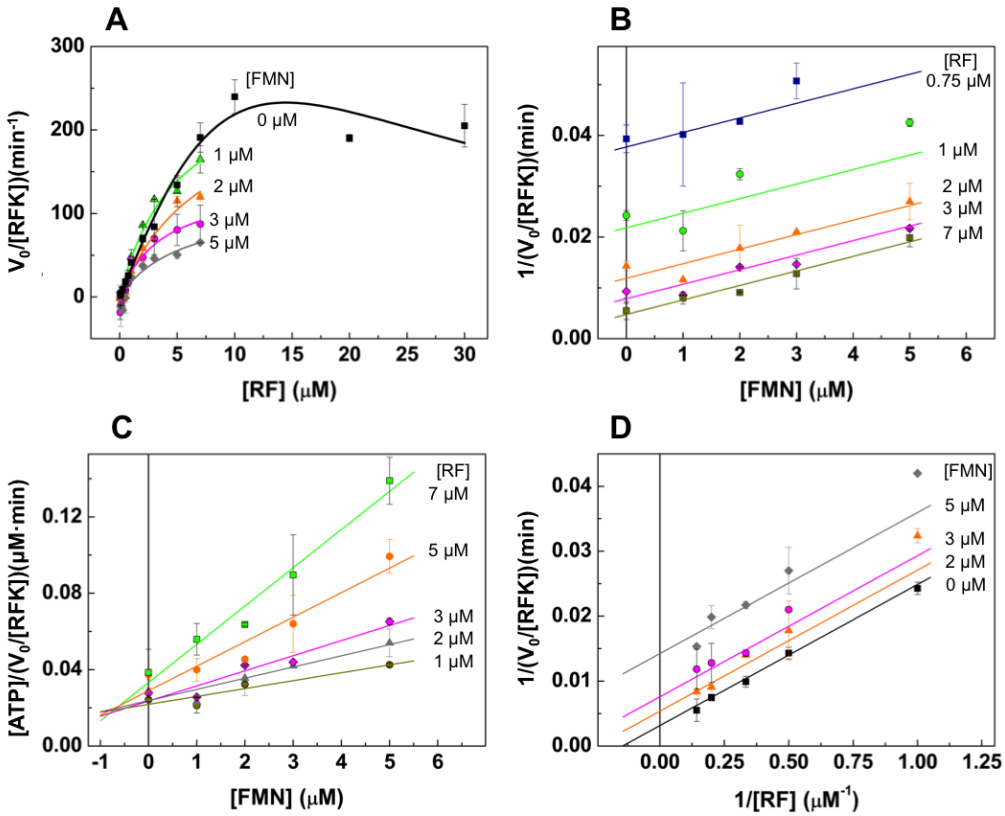

Figure 5.2. Inhibitory effects produced by the RF substrate and the FMN product in the steady-state RFK activity of the RFK module of *Ca*FADS. (A) Michaelis-Menten plots as a function of the RF substrate at different concentrations of the FMN product (high fluorescence yields in mixtures simultaneously containing RF and FMN prevented accurate determination of data over 7 µM RF) and the corresponding (B) Dixon plot, (C) Cornish-Bowden plot and (D) Lineweaver-Burk representation with global fit to the equation for uncompetitive inhibition. Reaction rates were obtained in 20 mM PIPES, 0.8 mM $MgCl_2$, pH 7.0, at 25°C and saturating ATP (350 µM ATP), varying the concentration of the RF substrate (0-30 µM) and the FMN product (0-7 µM).

To evaluate whether any of the products of the RFK reaction also produce inhibition, we analyze the evolution of steady-state rates at increasing concentrations of either ADP or FMN (Figs. 5.1 and 5.2). The fitting of the rates, obtained as a function of the ATP concentration while varying ADP concentration, to the Michaelis-Menten model, shows that while K_m^{ATP} values increase with ADP concentration, k_{cat} ones remain constant (Fig. 5.1A, Table 5.1). Dixon and Cornish-Bowden plots for these data were then used to identify the type of inhibition produced by ADP.

Table 5.1. Steady-state kinetic parameters describing the RFK activity of the RFK module and the inhibition by its different substrates and products. Data obtained at 25 °C in 20 mM PIPES, 0.8 mM $MgCl_2$, pH 7.0. Inhibition by the RF substrate prevented the determination of true parameters and data presented correspond to apparent constants.

Kinetic parameters as determined in the absence of products of the reaction

[ADP] (μM)	k_{cat} [a] (min^{-1})	K_m^{ATP} [a] (μM)	[FMN] (μM)	k_{cat} [b] (min^{-1})	K_m^{RF} [b] (μM)	K_i^{RF} [b] (μM)
0	162±8	60.3±11.5	0	443±47	10.4±1.6	1.9±0.2

Kinetic parameters as determined at different concentrations of reaction products

[ADP] (μM)	k_{cat} [a] (min^{-1})	K_m^{ATP} [a] (μM)	[FMN] (μM)	k_{cat} [b] (min^{-1})	K_m^{RF} [b] (μM)
20	162±13	114±20	1	278±39	5.0±1.1
50	138±8	137±18	2	266±53	7.7±1.4
90	170±8	257±23	3	139±28	3.6±0.9
170	168±66	697±276	5	116±39	5.5±2.1

Kinetic parameters determined by global fitting the Lineweaver-Burk equation

K_i^{ADP} [a] (μM)	k_{cat} [a] (min^{-1})	K_m^{ATP} [a] (μM)	K_i^{FMN} [b] (μM)	k_{cat} [b] (min^{-1})	K_m^{RF} [b] (μM)
17.0±3.3	133±32	40.3±11.9	1.4±0.2	318±33	6.9±0.4

[a] Parameters estimated using a RF concentration exhibiting ~80% maximal activity before the maximum experimentally detected as a function of RF concentration and saturating ATP.
[b] Determined at saturating ATP concentrations.

These data indicate that the RFK activity of *Ca*FADS is inhibited by the RF substrate, as well as by both products of the reaction, with ADP acting as a competitive inhibitor and FMN as an uncompetitive one.

The Dixon plot shows lines intersecting at negative values of the x-axis, while in the Cornish-Bowden representation lines are parallels (Figs. 5.1B and 5.1C). These plots reveal that the ADP product acts a competitive inhibitor. Representation of the slopes in the Dixon plot *vs* 1/[ATP] confirms a pure competitive inhibition (Fig. 5.1B, inset). Global fit of the data in the Lineweaver-Burk representation to the equation describing competitive inhibition (Eqn. 2.7), yields values of k_{cat}, K_m^{ATP} and K_i^{ADP} of 133±32 min^{-1},

40.3±21.9 μM and 17.0±6.4 μM, respectively (Fig. 5.1A and 5.1D, Table 5.1). In this case, the high affinity for the ADP product inhibitor considerably increases the estimated error for K_m^{ATP}. The fits to the Michaelis-Menten equation of the observed rates *vs* RF, in experiments carried out at saturating ATP and increasing FMN, show that k_{cat} values decrease, while K_m^{RF} ones do not significantly change (Table 5.1, Fig. 5.2A). This indicates that the FMN product also behaves as inhibitor of the RFK activity. In this case, the Dixon plot displays parallel lines (Fig. 5.2B), while lines intersect at negative values of the x-axis in the Cornish-Bowden graphic (Figs. 5.2B and 5.2C). These plots are typical of uncompetitive inhibitors. Global fit of the Lineweaver-Burk plots to the uncompetitive inhibition equation (Eqn. 2.8) yields 318±40 min^{-1} for k_{cat}, 6.9±0.4 μM for K_m^{RF} and 1.4±0.2 μM for K_i^{FMN} (Fig. 5.2D, Table 5.1).

2. Changes in flavin fluorescence upon binding allow studying the association and dissociation kinetics of flavinic ligands to the RFK module.

We used stopped-flow spectrophotometry to kinetically differentiate some of the steps implicated in the RFK reaction under pre-steady-state situations. These processes can be identified by changes in the fluorescence of the flavin isoalloxazine ring, property highly dependent on its environment [51]. Since RF and FMN share the same fluorescence spectra and yields [55], direct transformation of the first one into the second is not expected to be observed by this method. However, we should be able to detect processes inducing changes in the electronic environment of the flavin isoalloxazine; including flavin binding, flavin dissociation or even any conformational change around the isoalloxazine ring taking place along catalysis. When we mix FLV ligands with the protein in the stopped-flow equipment and follow flavin fluorescence evolution, we only detect slow linear fluorescence decays, whose slopes linearly decrease with the FLV concentration, and are consistent with the photobleaching range (rates of 4.5·10-3 ±1.2·10-4 min-1 for RF and 4.1·10-3±2.4·10-4 min-1 for FMN) (see methods and Fig. 5.3). These results reveal that the RFK module is not able to directly bind the FLV ligand, and/or to internalize its isoalloxazine ring into the active site in a competent enclosed conformation.

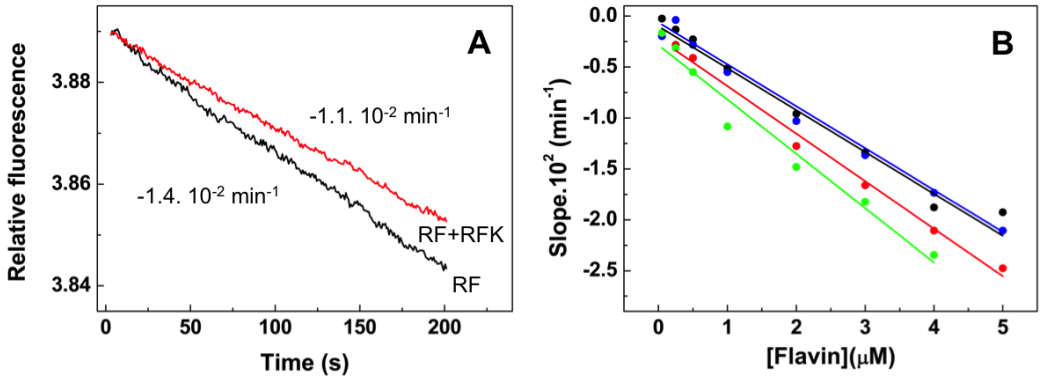

Figure 5.3. (A) Kinetic traces for the evolution of the RF fluorescence (1 μM) in the stopped-flow equipment follow zero order decays both in the absence (black line) and presence (red line) of the RFK module (0.2 μM). (B) Slopes of linear fluorescence decays on the flavin concentration for samples containing RF (black), FMN (blue), as well as RF (red) and FMN (green) in the presence of the RFK module. All show linear dependences on flavin concentrations with similar negative slopes. They, therefore, indicate that increasing flavin concentrations protect from photobleaching during measurements. Experiments were performed in 20 mM PIPES, 0.8 mM $MgCl_2$, pH 7.0 at 25ºC.

Kinetic traces were then recorded when the RFK module was mixed with different combinations of flavin and adenine nucleotide ligands. These traces show kinetic processes taking place in time frames considerably lower than those related to flavin photobleaching. The number of processes detected depends on the ligands present in the mixture (Fig. 5.4A-D). All the analyzed mixtures show a fluorescence decay in the 5 s time frame that fits to a single exponential process, allowing to determine the corresponding k_{obs1} values (Fig. 5.4A-D, see a highlighted example for FMN in Fig. 5.4B). This feature is not observed when flavins are independently mixed with either ANP ligands in absence of the RFK module (not shown), or with the RFK module in the absence of ANP ligands (Fig. 5.3A). Therefore, this process can be identified as the ANP ligand promoting changes in the polar environment of the flavin isoalloxazine ring, and must be related to flavin binding and/or to its internalization within the protein matrix. k_{obs1} values follow, in general, a linear dependency on FLV concentration (Fig. 5.4E). The fit of k_{obs1} values to Eqn. 2.11, yields the flavin association rates, k_{on}, as the slope, and the corresponding dissociation rate, k_{off}, as the independent term. These values are reported in Table 5.2, and show how at saturating concentrations of the ADP product, the RF binding is two times faster than the FMN binding. On the contrary, the

binding of the substrates of the RFK reaction, RF and ATP, is the slowest process. Thus, apparently, the products of the reaction bind the RFK module faster than the substrates and, as consequence, substrate binding appears slightly weaker (Table 5.2). Noticeably, k_{obs1} values for non-productive mixtures containing the FMN product and the ATP substrate are considerably slower than the rest and show a biphasic dependence on the FMN concentration that prevents the determination of k_{on} and k_{off} (Fig. 5.4D). This indicates that excess of FMN in the presence of ATP, hinders its own binding and/or a conformational change in the flavin environment.

Table 5.2. Pre-steady-state kinetic parameters for the binding and dissociation of flavins to the RFK module in the presence of adenine nucleotides. Experiments were carried out in 20 mM PIPES, 0.8 mM $MgCl_2$, pH 7.0. NA, not applicable.

Ligands combination	k_{on} **($min^{-1}\mu M^{-1}$)**	k_{off} **(min^{-1})**	K_d **(μM)**	ΔG **(kcal/mol)**
FMN-ADP	63.6 ± 2.1	96.9 ± 5.5	1.52 ± 0.10	-7.9 ± 0.5
RF-ADP	127 ± 3.4	109 ± 8	0.86 ± 0.08	-8.2 ± 0.1
RF-ATP	27.0 ± 0.9	97.6 ± 2.6	3.62 ± 0.15	-7.4 ± 0.3
FMN-ATP	NA	NA	NA	

After the initial decay, here related to flavin recognition in the presence of the ANP, experiments performed with ADP only show slow decays consistent with flavin photobleaching, which are therefore not assumed as part of the reaction. However, experiments carried out with mixtures of FLV and ATP show an exponential increase in fluorescence, characterized by k_{obs2}, (Fig. 5.4A, 5.4C and 5.4D) before the photobleaching decay starts. These observations suggest that after the initial interaction of ligands with the protein, a subsequent ATP-dependent conformational rearrange is produced in the flavin environment. Such rearrange brings back the isoalloxazine ring to the external media. Interestingly, both the amplitude and k_{obs2} values increase with flavin concentrations below 0.25-0.5 μM, but considerably decrease at higher flavin concentrations (Fig. 5.4C and 5.5). This biphasic profile agrees with excess of FLV ligands inhibiting the catalytic process (Fig. 5.2A). These data indicate that this second process is related to the release of the isoalloxazine ring to the solvent, which, according to the k_{obs2} values, appears the limiting step in the catalytic reaction.

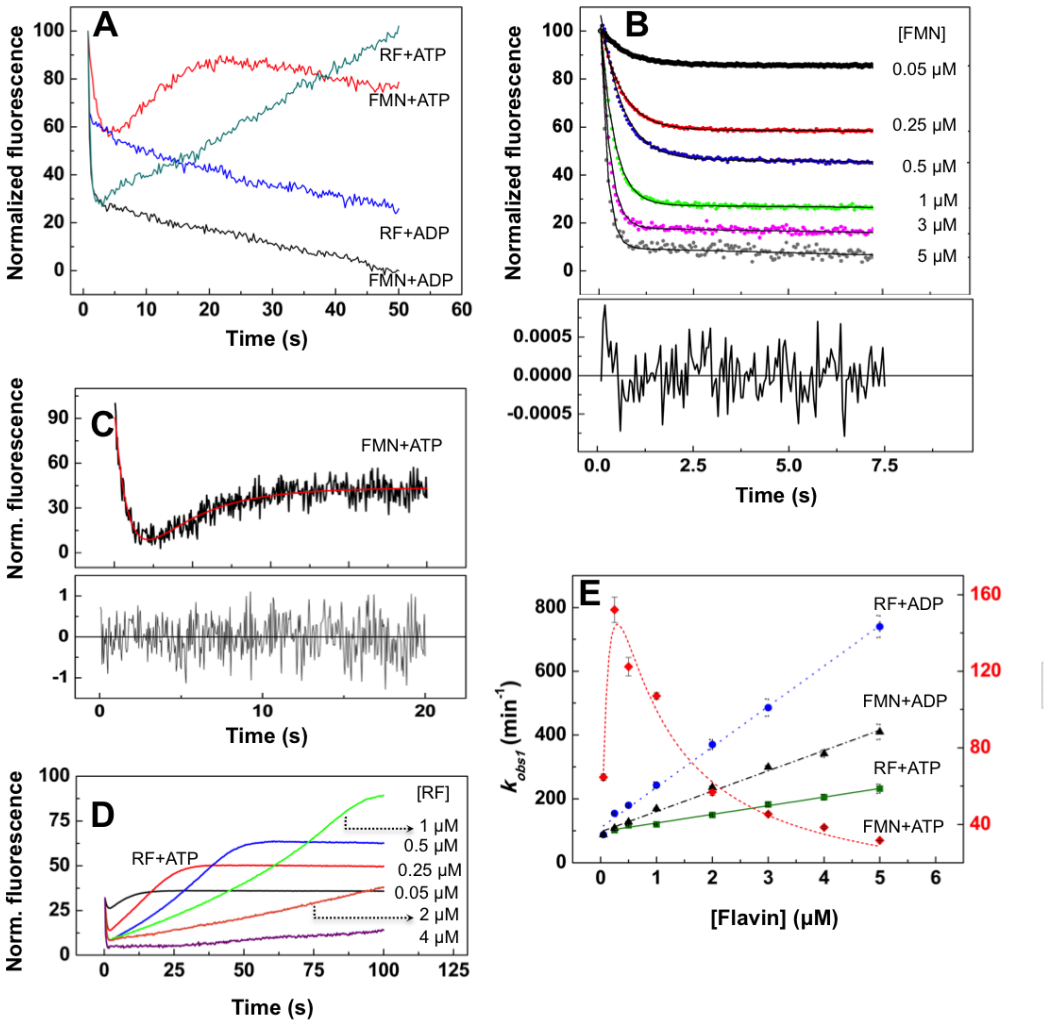

Figure 5.4. Pre-steady-state kinetic analysis of the binding of the flavins to the RFK module of *Ca*FADS. (A) Kinetic traces for the evolution of the flavin fluorescence upon mixing the RFK module (0.2 μM) with RF (1 μM) at saturating ATP (250 μM) and ADP (250 μM), as well as of FMN (1 μM) at saturating ATP (250 μM) and ADP (250 μM). (B) Evolution of kinetic traces on the FMN concentration for its interaction with the RFK module in the presence of 250 μM ADP. Traces are fit to a mono-exponential decay with steady-state. Residuals are shown at the bottom for fitting of 1 μM FMN data. (C) Dissection of the exponential processes for kinetic traces observed upon mixing the RFK module (0.2 μM) at saturating ATP (250 μM) with FMN (1 μM). The panel shows the fit to a two exponential process with its fitting residual at the bottom. (D) Traces obtained when mixing the RFK module (0.2 μM) at saturating ATP (250 μM) different with RF concentrations. (E) Evolution of k_{obs1} on the flavin concentration for the mixing of the RFK module with RF+ADP (●), FMN+ADP (▲), RF+ATP (RFK reaction, ■) and (C) FMN+ATP (◇). For those data showing linear dependences slopes are related with the k_{on} for the binding and the independent term with the k_{off}. All the experiments were carried out in the stopped-flow

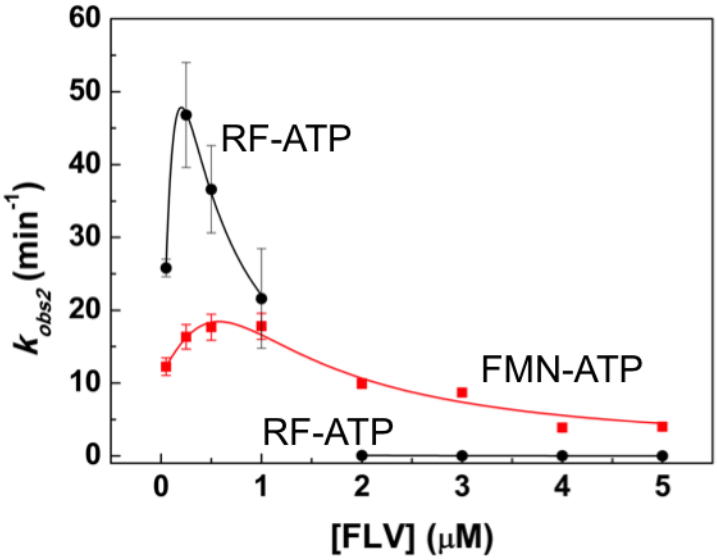

Figure 5.5. Evolution of k_{obs2} values on the FMN concentration for reaction mixtures of the RFK module with FMN+ATP (red) and with RF+ATP (black) follow a biphasic behavior with maximum ~0.5 μM FMN and ~0.25 μM RF. All the experiments were carried out in the stopped-flow equipment at 25ºC in 20 mM PIPES, 0.8 mM $MgCl_2$, pH 7.0 with 0.2 μM of the RFK module.

Altogether, and despite differences in experimental settings, these data show that the fast kinetic rates, k_{obs1} and k_{obs2}, for processes compatible with RFK catalysis (containing RF, ATP, and Mg^{2+}) are in the k_{cat} range (Figs. 5.4D-5.4E, Table 5.1). This indicates that the here depicted pre-steady-state kinetics are relevant for catalysis, being the final recovering of solvent accessibility of the flavin the limiting step of the reaction.

3. The thermodynamic diagram for the RFK-ligand interactions

We performed ITC experiments to verify that the observed pre-steady-state kinetic processes were significant to reach the thermodynamic equilibrium. Titrations with the different ligands (substrates and products) of either the isolated RFK module, or of its mixtures with either FLV or ANP ligands, provide values of the thermodynamic parameters (free Gibbs energy (ΔG), enthalpy (ΔH) and entropy ($-T\Delta S$), as well as the corresponding K_d) for each binary and ternary interaction. The corresponding numeric data are summarized in Table 5.3, while thermodynamic dissections and some examples of the titrations are displayed in Figs. 5.6 and 5.7. Titrations were performed in 0.8 mM $MgCl_2$ (conditions showing the highest efficiency for the RFK activity [82]) (Fig. 5.6A

and upper panel Table 5.3), as well as in the absence of $MgCl_2$ to avoid catalysis when both substrates, RF and ATP, are present (the catalytic reaction heat would mask the binding enthalpy) (Fig. 5.6B and lower panel in Table 5.3).

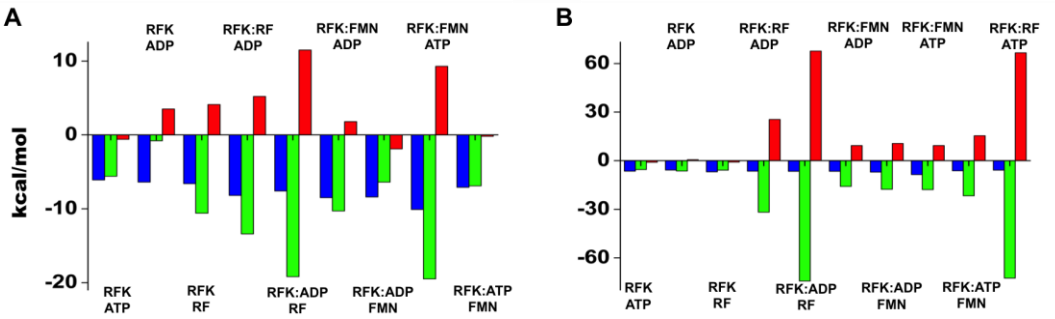

Figure 5.6. Thermodynamic dissection of the interaction of different ligands with either the free RFK module, or with the preformed mixtures of the RFK module with the different ligands (RFK:X). Parameters obtained (A) in the presence of 0.8 mM $MgCl_2$ and (B) in the absence of $MgCl_2$. Experiments were carried out in 20 mM PIPES, pH 7.0, at 25 °C. The binding Gibbs energy (ΔG), enthalpy (ΔH), and entropy ($-T\Delta S$) contributions to the binding are represented in blue, green and red bars, respectively.

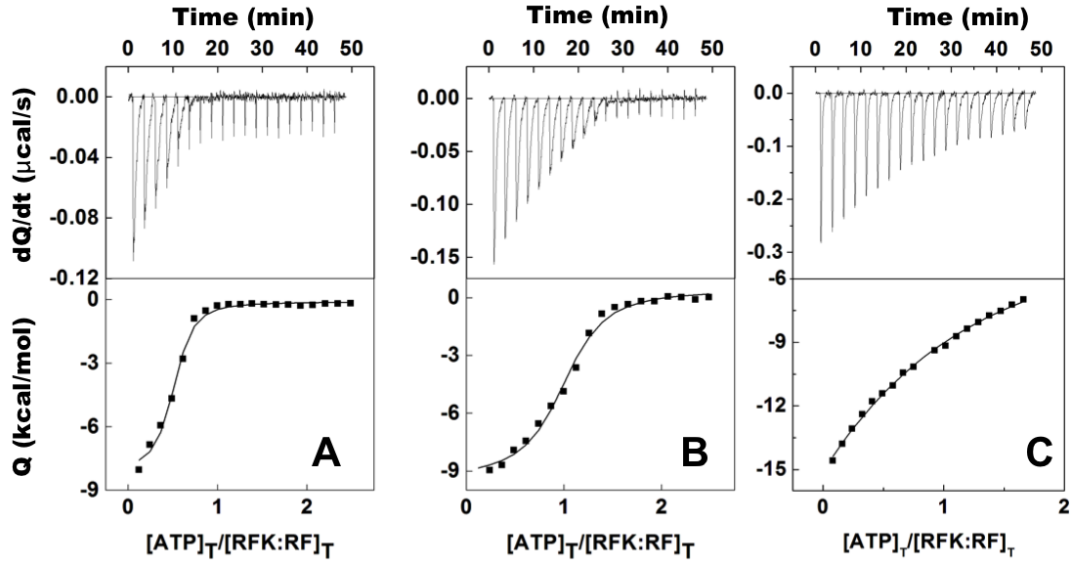

Figure 5.7. Calorimetric titrations with ATP of mixtures that contain different ratios of the RFK module and the RF ligand. Experiments were performed at (A) 7.5, (B) 15, and (C) 180 µM of RF with 25 µM RFK module in 20 mM PIPES, pH 7.0 at 25 ºC. Data were fit to a home-derived model for a single binding site. Within each panel, upper charts show thermograms for the different interactions and the lower panels the corresponding binding isotherms with integrated heats.

Thermograms for the titration of the RFK module with the individual ligands indicate that: i) FMN does not interact or interact with undetectable Δ*H*; ii) RF, ATP and ADP bind with appreciable enthalpic changes; iii) the presence of the Mg^{2+} cation modulates binding parameters (Table 5.3). When mixtures containing the RFK module and ANP (ATP or ADP) are titrated with FLV (RF or FMN), or *viceversa*, Mg^{2+} favors formation of ternary complexes, which are more stable than in the absence of the cation, as the more negative free binding energies show. This positive effect of the cation on the enzyme affinity for ligands in ternary complexes is, in general, consequence of the less unfavorable entropic contribution to the binding (Table 5.3, Fig. 5.6). Therefore, Mg^{2+} contributes to the overall conformation of the system in binary and particularly, ternary, interactions.

Fig. 5.8 summarizes the free energy values (Δ*G*) determined for all possible combinations of the RFK module, in binary and ternary complexes with different ligands, as well as the relative fraction of protein prone to interact, both in the presence (Fig. 5.8A) and in the absence of the divalent cation (Fig. 5.8B). All paths shown in the network compete with the one leading to the catalytically competent complex by decreasing the amount of the RFK module available to bind the substrates of the reaction, RF and ATP:Mg^{2+}. As shown in the figure, paths with and without Mg^{2+}, considerably differ both in the complex stability and in its production probability. Several remarkable facts need to be highlighted. We have no data for the reactive path containing RF and ATP:Mg^{2+} (the heat exchanged in the chemical reaction masks the binding one). We can include the path leading to a "pseudo reactive"-ternary complex in the absence of the cation, produced by titration of the RFK module:RF binary complex with ATP (shown in maroon in Fig. 4B), but in the absence of Mg^{2+} RF does not bind to the binary RFK module:ATP preformed complex. These data suggest that in the absence of the cation, the ATP substrate induces enzyme conformations that are not able to bind the RF substrate. All ternary interactions, as well as the single RF binding to the module, appear more favorable in the presence of Mg^{2+}, furthermore the cation also increases the protein fraction in the competent conformation to bind the ligands (as indicated by the thicker lines in Fig. 5.8A). Paths leading to transformation of binary complexes into ternary ones, despite not being competent for catalysis, are in general thermodynamically more favorable (as the more negative Δ*G* values show) than the "pseudo reactive" one. It is also noticeable that, despite direct binding of FMN to the RFK module is not detected by ITC (neither by stopped-flow), free energies for ANP

binding to the RFK module are considerably more favorable when FMN is in the mixture. These data indicate that FMN might act as a slow binding ligand [215] in its interaction with the RFK module in the absence of ANP, and also suggest a cooperative binding of both ligands.

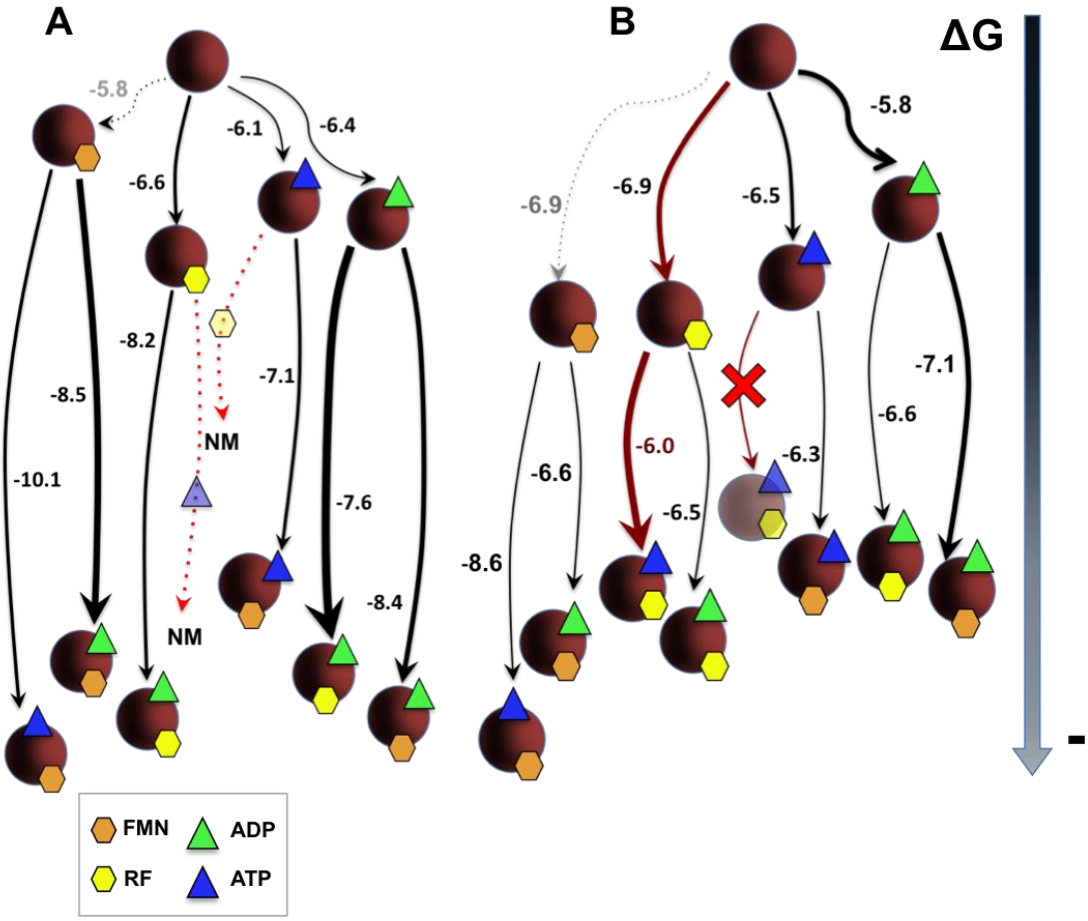

Figure 5.8. Free Gibbs energy flow in the interaction between the RFK module and its ligands. Diagrams resume the thermodynamic flow representing the interaction of the RFK module and the different combinations of its ligands as obtained through ITC at 25°C (A) in 20 mM PIPES, 0.8 mM $MgCl_2$, pH 7.0 and (B) in 20 mM PIPES, pH 7.0. The RFK module is represented as maroon spheres, RF and FMN as yellow and orange hexagons respectively and ATP and ADP as blue and green triangles respectively. Numbers indicate the ΔG value for each particular titration. The thickness of the arrows is proportional to the fraction of protein that is able to bind the ligand in each case and the length of the lines to the ΔG value associated to each process. Dash lines indicate processes not observed directly by ITC but whose values are indirectly estimated once known the cooperativity coefficients. Red lines indicate the path leading to the simultaneous binding of both substrates of the RFK activity in the absence of the cation.

Table 5.3. Thermodynamic interaction parameters for the combination of the RFK module with different ligands as obtained through ITC. Column named initial mixture indicates the starting composition of the calorimetric cell. Titrations were carried out at 25ºC in 20 mM PIPES, 0.8 mM $MgCl_2$, pH 7.0 (upper table) and in 20 mM PIPES, pH 7.0 (lower table).

0.8 mM $MgCl_2$					
initial mixture	**ligand**	**K_d (µM)**	**Δ*G* (kcal/mol)**	**Δ*H* (kcal/mol)**	**-*T* Δ (kcal/mol)**
RFK	ATP	28.7	-6.1	-5.6	-0.6
RFK	ADP	22.1	-6.4	-9.8	3.5
RFK	RF	15.2	-6.6	-10.6	4.1
RFK	FMN	n.d.[a]	n.d.[a]	n.d.[a]	n.d.[a]
RFK:RF	ADP	1.0	-8.2	-13.4	5.2
RFK:RF	ATP	n.m.[b]	n.m.[b]	n.m.[b]	n.m.[b]
RFK:FMN	ADP	0.6	-8.5	-10.3	1.8
RFK:FMN	ATP	0.04	-10.1	-19.5	9.3
RFK:ATP	FMN	6.6	-7.1	-6.9	-0.2
RFK:ATP	RF	n.m.[b]	n.m.[b]	n.m.[b]	n.m.[b]
RFK:ADP	FMN	0.8	-8.4	-6.4	-1.9
RFK:ADP	RF	2.3	-7.6	-19.2	11.5
0.0 mM $MgCl_2$					
Initial mixture	**ligand**	**K_d (µM)**	**Δ*G* (kcal/mol)**	**Δ*H* (kcal/mol)**	**-*T* Δ*S* (kcal/mol)**
RFK	ATP	16.3	-6.5	-5.5	-1.0
RFK	ADP	51.4	-5.8	-6.4	0.6
RFK	RF	19.5	-6.9	-5.9	-0.9
RFK	FMN	n.d.[a]	n.d.[a]	n.d.[a]	n.d.[a]
RFK:RF	ADP	17.1	-6.5	-31.8	25.4
RFK:RF	ATP	50.4	-5.9	-72.5	66.6
RFK:FMN	ADP	14.8	-6.6	-15.9	9.3
RFK:FMN	ATP	0.5	-8.6	-17.9	9.3
RFK:ATP	FMN	23.9	-6.3	-21.7	15.4
RFK:ATP	RF	n.d.[a]	n.d.[a]	n.d.[a]	n.d.[a]
RFK:ADP	FMN	6.4	-7.1	-17.7	10.6
RFK:ADP	RF	14.5	-6.6	-74.3	67.7

[a] n.d. Not detected. Not heat of interaction was detected for this titration. [b] n.m. Not measured. This combination of ligands in the presence of Mg^{2+} leads to the catalytic reaction, preventing determination of binding heats.

4. Adenine and flavin nucleotide ligands cooperate in their binding to the RFK module

To prove the cooperativity between ligands, we performed sets of ITC experiments in which samples of RFK module containing different FLV ligands proportions were titrated with ANP ligands (Fig. 5.7). These experiments allowed determining the apparent cooperativity constants for the ANP binding in the presence of the FLV ligand, $K_a^{app,ANP}$. Plots of $K_a^{app,ANP}$ *vs* FLV concentrations show different behaviors depending on the flavin-adenine nucleotide combination (Fig. 5.9A). FMN exhibits positive cooperativity with both ADP and ATP, as RF does with ADP. Although concentrations of the RF substrate up to 30 μM increase protein affinity for ATP (maximum cooperativity at ≈7.5 μM), higher RF concentrations hinder ATP binding (Fig. 5.9). This suggests that an excess of RF might block its binding.

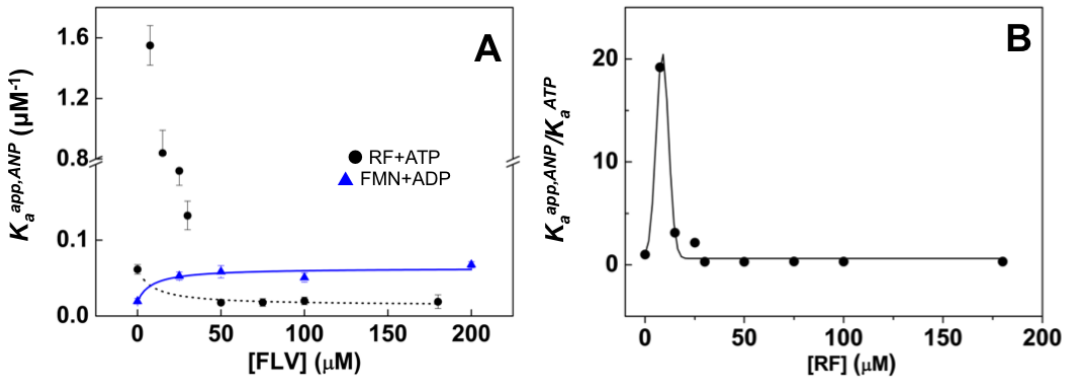

Figure 5.9. Cooperativity between the flavin and adenine nucleotide ligands to their binding to the RFK module. (A) Dependence of apparent ANP association constants, $K_a^{app,ANP}$, on the concentration of the flavinic ligand for the titration with ATP of mixtures of the RFK module with different amounts of RF (▲), as well as for the titration with ADP of mixtures of the RFK module with different amounts of FMN (●). (B) Evolution of the $K_a^{app,ATP}/K_a^{ATP}$ ratio as a function of the RF concentrations. All experiments were performed in 20 mM PIPES, pH 7.0 at 25 °C. Lines are included only as eye guides of the data evolution.

We performed additional ANP titrations at saturating FLV; namely 150 μM for RF or FMN, as well as at 7.5 μM RF for the ATP titration. The binding isotherms can be fit to a model that considers the reciprocal effect between the FLV and ANP ligands [187]. In this way, cooperativity coefficients (α), the fraction of protein sample able to bind the titrating ligand (N) and the enthalpy change associated to each process (Δh), can be determined. Data are summarized in Table 5.4. The presence of the cation

dramatically increases the binding cooperativity between flavin and adenine nucleotides (compare upper and lower parts of Table 5.4). It is also remarkable that α values are larger than one, which indicates positive cooperativity, with the only exception of the combination of the RF and ATP substrates at high RF concentrations that showed negative cooperativity (α<1). Therefore, although low concentrations of the RF substrate favor binding of the ATP substrate, an excess of RF has a negative impact in ATP binding (Figs. 5.7 and 5.9B, Table 5.4). The products of the reaction (FMN and ADP) always favor binding of the rest of substrates and products (Fig. 5.9A, Table 5.4). Moreover, the presence of either Mg^{2+} or ATP considerably enhances cooperativity, being particularly large the cooperativity for the FMN-ATP:Mg^{2+} combination (Table 5.4). This later observation probably relates to the fact that in the absence of ATP, FMN seems to act as a slow binding ligand, which makes its binding to the RFK module not detectable by fast kinetics or ITC methods. Once α values are known, the experimental $K_a^{app,ANP}$ can be also used to predict the association constant for FMN binding, K_a^{FMN}, to the free RFK module, as well as the corresponding ΔG values presented in Fig. 5.8 (gray dotted lines), by using Eqn. 2.17.

Table 5.4. Cooperativity coefficients (α) for the binding of the different combinations of FLV and ANP ligands to the RFK module. Experiments were carried out at 25°C in PIPES 20 mM, 0.8 mM $MgCl_2$, pH 7.0, as well as in the same buffer without $MgCl_2$. α represents the cooperativity coefficient between each pair of ligands, N the fraction of total protein able to bind the titrating ligand and Δ*h* the enthalpy change associated to each process. Errors were taken in general larger than the standard deviation between replicates and the numerical error after fitting analysis.

	ligands	**α**	**N**	**Δ*h* (kcal/mol)**
0.8 mM $MgCl_2$	FMN-ADP	56.0±4.5	0.6±0.01	-8.1±1.9
	FMN-ATP	917±70	0.2±0.01	-22.1±0.1
	RF-ADP	24.0±2.5	0.3±0.01	-7.1±0.3
0 mM $MgCl_2$	FMN-ADP	3.8±0.2	0.2±0.01	-9.7±0.8
	FMN-ATP	15.7±0.6	0.02±0.003	-30.0±0.8
	RF-ADP	3.3±0.1	0.2±0.02	-20.3±0.8
	RF-ATP[a]	19.2±5.7	0.5±0.06	-8.1±1.1
	RF-ATP[b]	0.8±0.1	0.8±0.07	-15.0±4.1

[a] Data from the titration at the maximum of cooperativity, 7.5 μM RF. [b] Data from the titration at 100 μM RF.

5. Discussion

The collective binding of adenine and flavin nucleotides induces important conformational changes in the CaFADS RFK module

Analysis of our steady-state, pre-steady-state and binding data in the context of the available structures for the RFK module, free and in the FMN:ADP:Mg^{2+} non-productive ternary complex (Fig. 5.10) [85, 99], allows inferring new insights about the binding and dissociation of substrates and products in the course of the enzyme catalytic cycle. Although changes in the RF fluorescence are not detected upon its fast mixing with the RFK module, ITC experiments reveal that RF is able to interact with the RFK module with moderate affinity (Table 5.3). Such way of RF binding is consistent with the wide-open cavity that the free RFK module shows at the ribityl and isoalloxazine binding sites (Fig. 5.10, panel B_1). Thus, RF can be somehow recognized by the RFK module, but its isoalloxazine is not enclosed within the protein. On the contrary, in the free protein crystal structure several loops and side-chains block the adenine nucleotide binding site, including the pocket for the phosphate groups [85, 99], (Fig. 5.10, panels B1 and C1). ATP (as well as ADP) reduces the access of the RF isoalloxazine to the solvent (Fig. 5.4, Table 5.3), suggesting its competent binding. This agrees with the formation of a ternary complex as the one in the RFK module:FMN:ADP:Mg^{2+} crystal structure (Fig. 5.10) [99]. Comparison of these two structures shows significant rearrangements. They include displacements of loops L3c, L5c and L1c-FlapI to allow the binding of the adenine nucleotide, as well as a noticeable change in the conformation of loop L4c-FlapII that encloses the isoalloxazine ring inside the protein (Fig. 5.10). The large unfavorable entropic and favorable enthalpic contributions for ATP binding to the RFK module:RF mixture, as well as for RF binding to the RFK module:ADP mixture (Table 5.3 and Fig. 5.6), further support such rearrangements occurring upon concerted ligand binding. Therefore, it appears that large conformational changes take place in the transformation of binary interactions into ternary complexes [99].

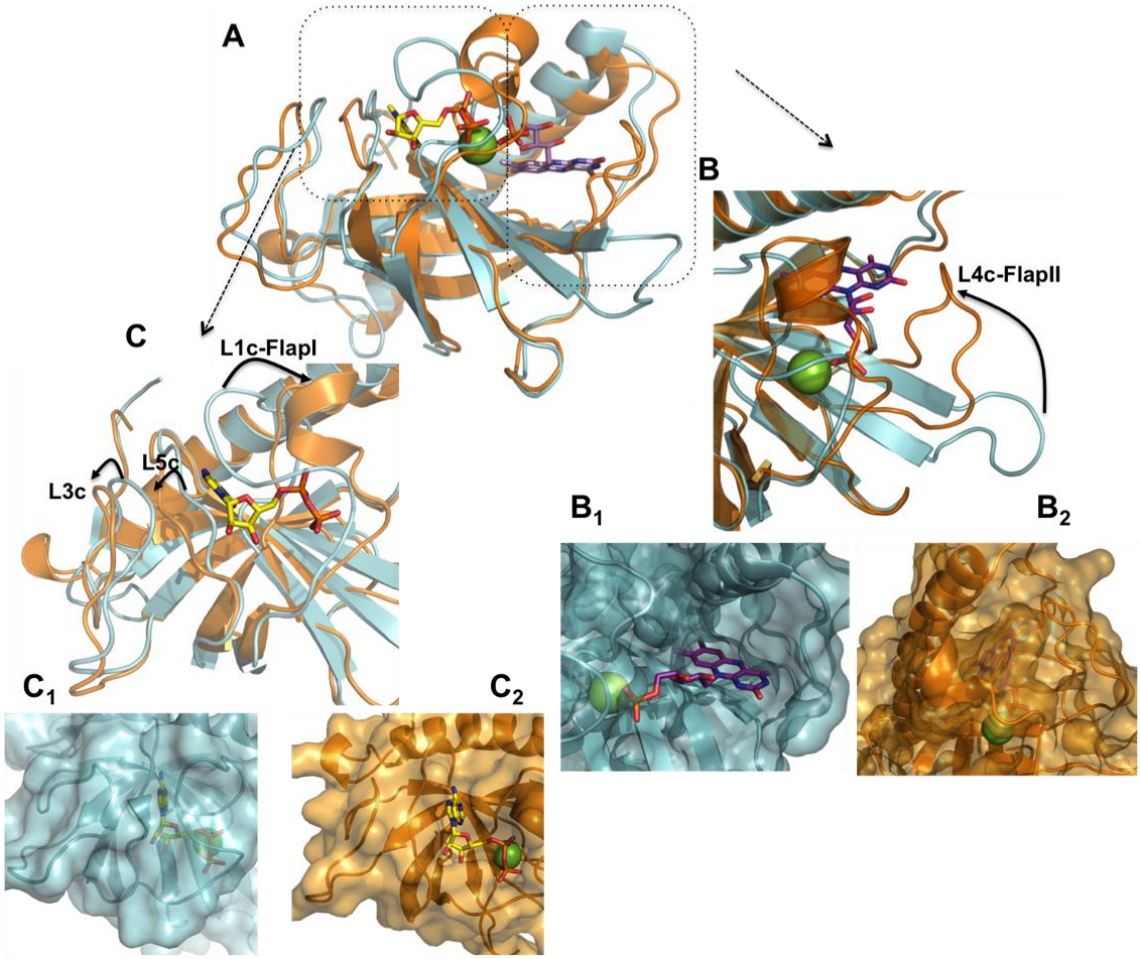

Figure 5.10. Structure of the RFK module of *Ca*FADS. Crystallographic structures for the RFK module when free (blue, PDB 2x0k) and in the ternary complex with the FMN and ADP:Mg^{2+} products (orange, PDB 5a89). (A) Superposition of the both structures. (B) Detail of the flavin nucleotide binding cavity. B_1 shows the open conformation of the cavity in the free enzyme, where the phosphate of FMN and the Mg^{2+} cation will find their binding site blocked by residues of L1c. B_2 shows the enclosed of the flavin ring by L4c in the ternary complex. (C) Detail of the adenine nucleotide binding cavity. C_1 shows the closed conformation of the ANP binding site in the free enzyme, where the phosphates of ANP and the Mg^{2+} cation will find their binding site blocked by residues of L1c. C_2 shows the open conformation of this cavity with bound ADP:Mg^{2+} in the ternary complex. In all panels the ligands correspond to those in the 5a89 structure. ADP and FMN ligands are shown in sticks and CPK colored with carbons in yellow and purple respectively, and the Mg^{2+} cation is shown as a green sphere.

Mg^{2+} and concerted fit of substrates to achieve the catalytically competent complex

Fast kinetic methods allowed to determining a dissociation constant in the low micromolar range for the productive RFK module:RF:ATP:Mg^{2+} ternary interaction

(Table 5.2). Such interaction, which is not thermodynamically detected in the absence of the cation, suggests that previous ATP:Mg^{2+} binding is required for the competent RF binding to the RFK module (Fig. 5.10). Three observations support this mechanism; i) the cation-mediated conformational changes which enclosures the flavin ring and fits the ribityl end in a competent geometry for its phosphorylation [99] ii) the previously reported molecular dynamics simulations, which show how phosphates Mg^{2+}-bridged to the active site promote the adenine binding site opening [99] and iii) the fact that RF is not able to interact with the preformed RFK module:ATP complex in the absence of the cation, but it is transformed into FMN when we mixed it with the RFK module:ATP:Mg^{2+} mixture. Collectively, these results indicate that a concerted binding of ATP:Mg^{2} and RF is necessary to achieve the substrates induced fit in the catalytic competent conformation.

The RFK activity is highly regulated by inhibition of substrates and products

The substrates of the RFK reaction showed positive cooperativity at low RF concentration, while higher RF concentrations hinder ATP binding (Fig. 5.9 and Table 5.4). This fact points to the formation of non-productive RFK module:RF interactions as the main cause for the RF substrate inhibition (Figs. 5.2A and 5.10) [95]. Fast kinetic data indicate that the opening of the flavin binding cavity to release the flavin products is the process prevented (Figs. 5.4 and 5.5), whereas cooperative binding data (Table 5.4) point to an increase in the protein occupation by ligands as the RF concentration increases. Such observations are consistent with excess of RF inducing binding modes that prevent conformational reorganizations which are required for products release to initiate a new catalytic cycle.

The FMN and ADP products, accumulating as the RFK reaction proceeds, also inhibit the RFK reaction through different mechanisms (Fig. 5.11). FMN is not able to bind fast enough to the free RFK module, but it behaves as an uncompetitive inhibitor that binds to the ATP-enzyme preformed complex and forms a highly stable dead-end complex (Table 5.1 and Table 5.3 and Figs. 5.6 and 5.8). Apparently, the phosphate group at the ribityl end in the FMN product might prevent the placement and enclosure of this cofactor (Fig. 5.10). When combining FMN and ATP with the RFK module, fast kinetic binding rates show a biphasic profile on the flavin concentration. The faster rates are produced in the lower range concentrations, but rates rapidly decrease with FMN concentration (Fig. 5.4E). The combination of these ligands also produces a huge cooperativity (Table 5.4) and very stable non-productive ternary complex (dead-end

complex), while FMN binding to the preformed enzyme:ATP binary complex is considerably less stable (Fig. 5.8). Considering that FMN and ATP are the substrates of the reaction catalyzed by the *Ca*FADS FMNAT module, it is likely that under situations which require FAD synthesis, the dead-end ternary complexes might facilitate channeling of FMN and ATP to the FMNAT module. This must be considered within the framework of the RFK-to-FMNAT modules head-to-tail disposition between protomers within trimers, in the dimer-of-trimers reported for the complete enzyme [85]. On its side, ADP acts as competitive inhibitor, competing with ATP for the same binding site (Fig. 5.11). The higher K_m/K_i ratio for FMN relative to ADP, ≈ 5 and ≈ 2.4 respectively, points to the flavinic product as a more potent inhibitor. This fact, together with the negative cooperativity between RF and ATP at high RF concentrations (Table 5.4), can explain why inhibition of the *Ca*FADS RFK activity by ADP has not been detected before.

Our data suggest that FMN and ADP are able to inhibit the RFK reaction through the formation of different non-productive ternary complexes (Fig. 5.8). The kinetic rising of flavin fluorescence, observed in samples containing ATP (not observed for ADP) after ternary complex formation (Fig. 5.4), suggests dissimilar organizations of complexes with the ANP substrate and product. This is also supported by differences in their thermodynamic binding parameters (Table 5.3 and Fig. 5.8). Noticeably, the binding of substrates is slower than the formation of all the non-productive adenine-flavin nucleotide combinations (Fig. 5.4E, Table 5.2), as well as less thermodynamically favorable. Therefore, all combinations of ternary complexes might compete with the catalytic one as the reaction progresses on, being the ternary non-productive interactions containing the ADP:Mg^{2+} product particularly populated (thicker lines in Fig. 5.8A) (Fig. 5.11). This contributes to reduce the number of enzyme molecules available to initiate a new catalytic RFK cycle. Moreover, the higher the concentration of one of the ligands in ternary non-productive complexes is, the stronger the second ligand binds (Fig. 5.9, Table 5.4). Thus, binding of substrates of the RFK reaction is less favorable when products accumulate.

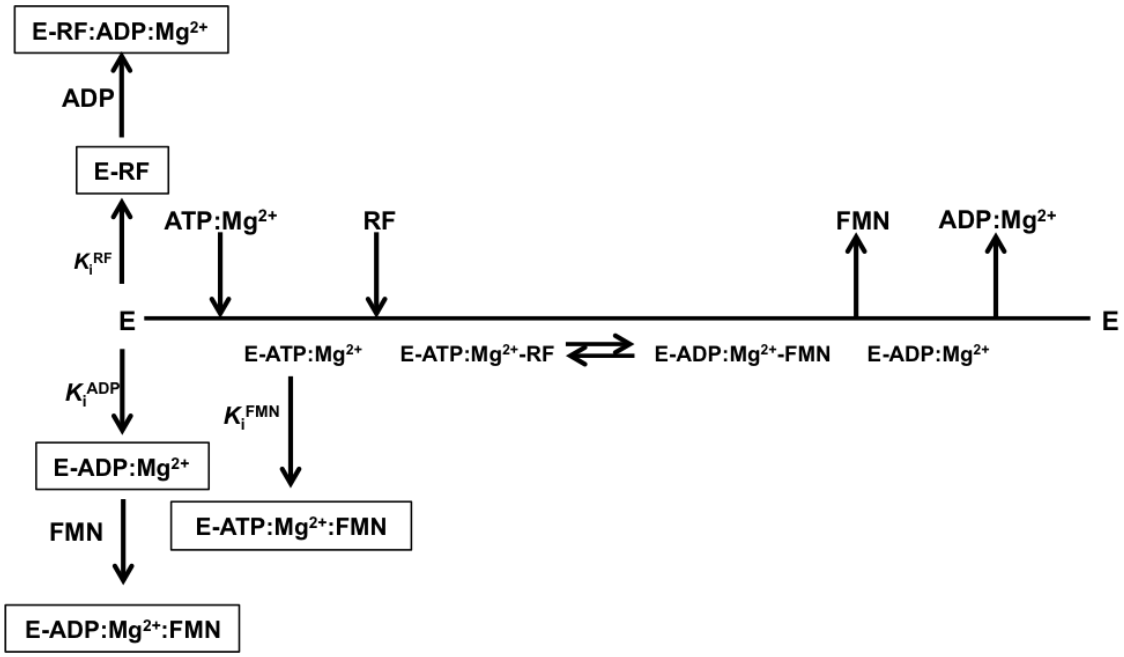

Figure 5.11. Cleland representation of the kinetic mechanism for the transformation of RF into FMN by the RFK module of *Ca*FADS. The different inhibition processes identified are summarized.

FMN synthesis is a key process that requires tight regulation

Our data indicate that FMN production by *Ca*FADS is highly regulated by substrates and products inhibition of its RFK activity, to avoid overproduction of flavin even though the RF substrate might reach high concentration in the media. Moreover, they show that the ADP and the ATP nucleotides bind similarly to the RFK module, while the binding pockets for RF and FMN are dissimilar. In addition, we must keep in mind that the FMNAT activity, at the N-terminus module, of the *Ca*FADS does not show any type of regulation by substrates or products inhibition [90]. Considering that selective inhibition of key enzymes is a common tool to regulate metabolic pathways [216-219], inhibition of the RFK activity by its substrates and products appears a useful tool to regulate the availability of both FMN and FAD in *C. ammoniagenes*. Most bacteria are able to synthesize their own RF [61, 220], as well as to assimilate it from the extracellular media [58, 60, 220, 221]. Therefore, mechanisms avoiding FMN and FAD overproduction when profusion of RF is produced must be relevant to maintain the cellular flavin homeostasis. Although characterization of additional family members is required to evaluate the generality of this mechanism, the few FADSs already characterized suggest strategies different from RFK inhibition to regulate FADS activity. Such differences among family members might provide with a framework to

the design of selective compounds targeting FADS for the treatment of diverse infectious diseases.

Chapter VI

The FAD synthetase from the human pathogen Streptococcus pneumoniae: a bifunctional enzyme exhibiting activity-dependent redox requirements

Up to now, only three crystallographic structures of bifunctional FADSs are available, those of *Thermotoga maritima* (*Tm*FADS, PDB 1MRZ [74, 75]) *Corynebacterium ammoniagenes* (*Ca*FADS PDB 2X0K [76]), and of the human pathogen *Streptococcus pneumoniae* (*Spn*FADS, PDB 3OP1). Except for the exhaustive biochemical and biophysical characterization of *Ca*FADS [84, 88, 90] the rest of family members have been poorly studied [79, 222, 223]. As indicated in Chapter I, section 3.3, *Spn*FADS shows the typical sequence and structural features of prokaryotic bifunctional FADSs, and therefore, it is likely to perform the RFK, FMNAT and FADpp activities as other bifunctional FADSs. *Spn*FADS structurally differs from the corresponding mammalian enzymes, and consequently, it can be exploded as a therapeutic target. Taking this into consideration, and also the fact that *S. pneumoniae* is the causative agent of invasive bacterial pneumoniae disease in children, in the elderly and in immunodepressed patients, *Spn*FADS appears as a protein worthy to be studied.

In this chapter we present a first biophysical characterization of *Spn*FADS, addressing the study of its both RFK and FMNAT activities, its oligomerization tendency as well as the thermodynamic of the interaction with its substrates.

1. *Spn*FADS is purified free of flavin ligands

Typically, the yield after purification was 3.5 mg of *Spn*FADS *per* liter of *E.coli* culture. Enriched *Spn*FADS fractions did not absorb notoriously at 450 nm along purification, and the final absorption spectrum of purified *Spn*FADS exhibits a single peak at 279 nm. Thus, in contrast to *Ca*FADSs [76] *Spn*FADS does not co-purify with FAD, suggesting a much lower affinity for the oxidized flavinic substrates/products. Far-UV CD spectrum of *Spn*FADS exhibits a negative band at 208 nm typical of secondary α-helix structure and a slightly less intense negative band around 222 nm (Fig. 6.1A). Analysis of the far-UV CD spectrum using the method of Raussens [224] predicted 28.3, 19.9, 12.5 and 34.5 % of content in α helix, ß strand, turn and random, respectively, in agreement with its 3D-structure containing 29% α helix and 28% β strand (Fig. 6.2B). Near-UV CD spectrum of *Spn*FADS shows a broad 265-290 nm negative band with minima at 280.5 and 287 nm related with the protein tertiary structure organization (Fig. 6.1B). Altogether these data indicate that the purified protein is correctly folded.

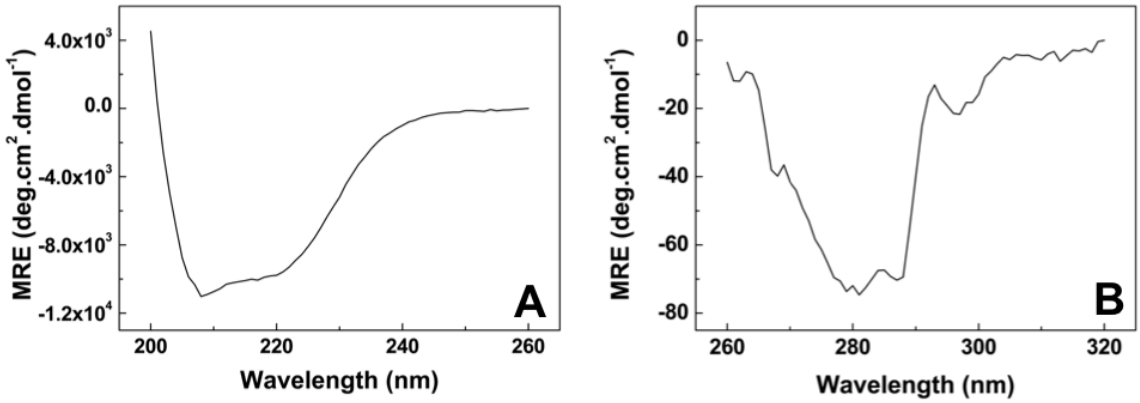

Figure 6.1. Spectroscopic properties of *Spn*FADS. (A) Far-UV circular dichroism spectrum of *Spn*FADS (5 µM). (B) Near-UV circular dichroism spectrum of *Spn*FADS (20 µM). Spectroscopic measurements were performed in 25 mM Tris/HCl, pH 7.5 at 20 ºC.

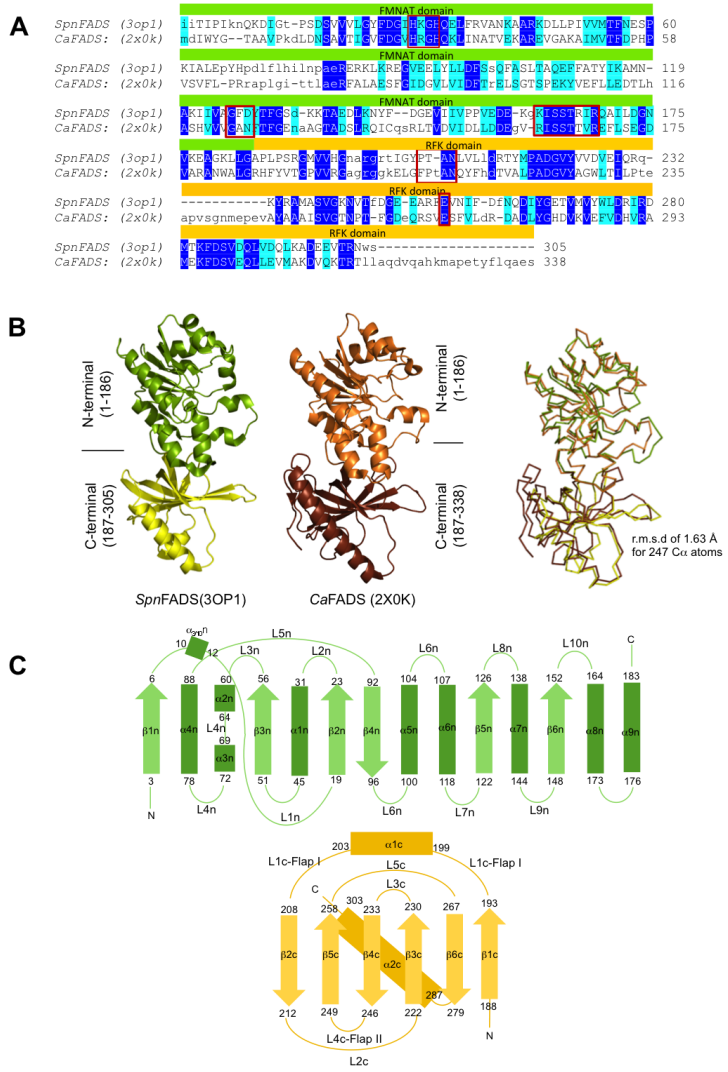

Figure 6.2. Structural properties of *Spn*FADS. **(**A) Structural alignment of *Spn*FADS (PDB 3op1) and *Ca*FADS (PDB 2x0k) according to the SSM server (http://www.ebi.ac.uk/msd-srv/ssm/). Identical residues are shown in dark blue and conservative ones in light blue. Consensus motives are highlighted with boxes. *Spn*FADS contains the 30-HKGH-33, 126-GFD-128 and 161-KISSTRIR-168 consensus motifs in the N-terminal module contributing to ATP stabilization for FMN adenylylation, as well as in FAD stabilization for the FADpp activity. The enzyme also conserves the 206-PTAN-209 motif and E254 at the RFK module to set up the catalytic site to transform RF into FMN. (*Spn*FADS numbering, highly conserved residues along family are shown in bold). (B) Three dimensional structures of *Spn*FADS (N- and C-terminal modules colored in green and yellow, respectively) and *Ca*FADS (orange and brown, respectively). On the right it is shown the superposition of both structures showing an r.m.s.d. of 1.63 Å for 247 Cα atoms (structural alignment by PyMol). (C) Topology of the N-terminal FMNAT module (green) and the C-terminal RFK module (orange) of *Spn*FADS. α helices are shown as solid dark rectangles and β strands as light arrows. Numbers indicates residue positions.

2. *Spn*FADS catalyzes the RFK, FMNAT and FADpp activities.

A qualitative assay was initially performed to evaluate whether *Spn*FADS was able to catalyze the RFK, FMNAT and FADpp activities by resolving the flavin reaction products by TLC. As shown in Figure 6.3A, *Spn*FADS catalyzes the conversion of RF into FMN, both in the absence and in the presence of a reducing agent. However, reducing conditions (2.5 mM of sodium dithionite) are required for the transformation of FMN into FAD (Fig. 6.3A) and *vice versa* (Fig. 6.3B).

3. The reduced state of flavins is critical for the FMNAT activity but not for the RFK one.

Prior to determining the kinetic parameters for the RFK activity of *Spn*FADS, we evaluated the influence of the reducing environment (sodium dithionite) as well as of Mg^{2+} on this reaction. Under saturating concentrations of substrates (RF and ATP) rates for RF transformation were independent on the reducing agent concentration in the media (Fig. 6.4A), indicating that the *Spn*FADS RFK activity does not depend on its redox environment. On the contrary, Mg^{2+} enhances the RFK activity, being the rate of the process practically constant at cation concentrations over 0.4 mM (Fig. 6.4B). Thus, herein a concentration of 0.8 mM $MgCl_2$ was used. Steady-state rates for the RFK activity showed saturation profiles for both of the substrates (Fig. 6.3C), contrary to *Ca*FADS that has strong inhibition by excess of RF [88, 90]. Thus, profiles for the RFK activity of *Spn*FADS were fit to the Michaelis-Menten model, allowing determination of k_{cat}, K_m^{RF} and K_m^{ATP} values of 18.7 min^{-1}, 0.9 µM and 54.0 µM, respectively. These values were only slightly influenced by the presence of the reducing agent (Table 6.1, Fig. 6.3C). Similarly, we also evaluated the effect of Mg^{2+} concentration and of reducing conditions on the FMNAT activity of *Spn*FADS before determining it. This activity was measured following the transformation of FMN into FAD. The presence of sodium dithionite was a requirement for the transformation of FMN into FAD (Fig. 6.4A), being the rate of the process constant over 2 mM sodium dithionite. On the contrary, the FMNAT activity was very poor in the presence of milder reducing agents as DTT (not shown), suggesting that strong reducing conditions are required to achieve catalysis. Maximal activity was observed in the range of 0.8-1.2 mM of the divalent cation (Fig. 6.4B), being the observed rates in its absence up to 5-fold lower. Thus, 0.8

mM $MgCl_2$ and 3 mM sodium dithionite were selected to further characterize the FMNAT kinetic parameters of *Spn*FADS.

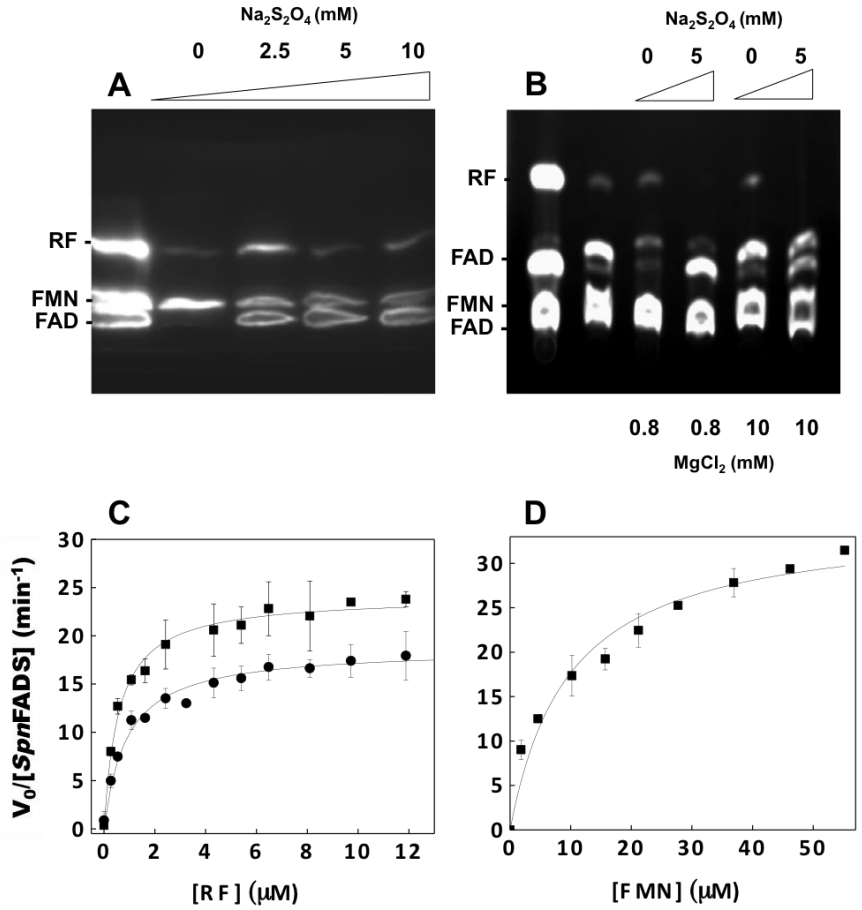

Figure 6.3. The RFK, FMNAT and FADpp activities of *Spn*FADS**.** (A) Thin layer chromatography of the products of the RFK and FMNAT activities. Reaction mixtures contained ~500 nM *Spn*FADS, 50 μM RF, 0.2 mM ATP, and several concentrations of sodium dithionite. First lane to the left corresponds to a standard solution containing RF, FMN and FAD at 50 μM each. (B) Thin layer chromatography of the products of FADpp activity. Reaction mixtures contained ~500 nM *Spn*FADS, 50 μM FAD, 0.2 mM PPi, and several concentrations of sodium dithionite. First lane corresponds to the standard solutions and second line to a free FAD sample with 10 mM $MgCl_2$. (C) Rates for RFK activity as a function of the RF concentration at saturating ATP (412 μM) without (●) and with 2.6 mM (■) sodium dithionite. (D) Rates for the FMNAT activity as a function of the FMN concentration at saturating ATP (252 μM) and 3 mM sodium dithionite. Unless otherwise stated all measurements were carried out at 25 ºC in 20 mM PIPES, pH 7.0, with 0.8 mM $MgCl_2$.

Observed rates exhibited Michaelis-Menten saturation profiles (Fig. 6.3D) with k_{cat}, K_m^{FMN} and K_m^{ATP} values of 34.9 min^{-1}, 9.8 μM and 31.6 μM, respectively (Table 6.1).

The need of reducing conditions for the FMNAT activity suggests that either the isoalloxazine ring of FMN needs to be reduced for the reaction to occur, or the reaction depends on a conformational change of the flavin binding site of the FMNAT module of *Spn*FADS induced by the redox environment. To clarify this matter an additional experiment was performed. The FMNAT activity of *Spn*FADS was measured under anaerobic conditions, but in the absence of dithionite, using as substrate the photo-reduced FMN. The HPLC analysis of the reaction products revealed that *Spn*FADS is able to transform FMN into FAD in the samples containing photo-reduced FMN in contrast with the negative controls where FMN is oxidized. Therefore, we demonstrate that FMN needs to be in its reduced form to get adenylylated by *Spn*FADS.

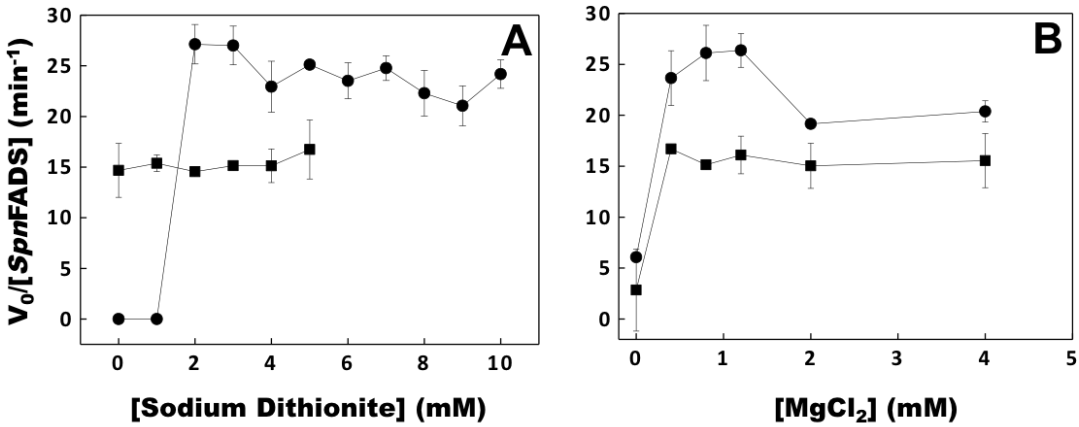

Figure 6.4. Rates of the RFK (■) and FMNAT (●) activities of *Spn*FADS as a function of (A) sodium dithionite and (B) $MgCl_2$ concentrations. Reaction mixtures contained ATP (~240 μM), RF (6 μM) and *Spn*FADS (25 μM) for the RFK activity; ATP (~250 μM), FMN (20 μM) and *Spn*FADS (25 μM) for the FMNAT activity. In all assays $MgCl_2$ was used at 0.8 mM when varying sodium dithionite, while sodium dithionite was used at 3 mM when varying $MgCl_2$.

Table 6.1. Steady-state kinetic parameters for the RFK and FMNAT activities of *Spn*FADS. Parameters obtained at 25 ºC in 20 mM PIPES, pH 7.0, 0.8 mM $MgCl_2$ and, when indicated 3 mM sodium dithionite as reductant. Estimated errors in k_{cat} and K_m are within ±10%.

RFK activity	***Reductant***	k_{cat} **(min^{-1})**	K_m^{RF} **(□M)**	k_{cat} / K_m^{RF} **(min^{-1} □M^{-1})**	k_{cat} **(min^{-1})**	K_m^{ATP} **(□M)**	k_{cat} / K_m^{ATP} **(min^{-1} □M^{-1})**
*Spn*FADS	-	18.7	0.9	21.0	19.5[a]	54.0	0.4
	+	24.1	0.6	41.5	13.4[a]	34.1	0.4
*Ca*FADS[a,b]	-	< 302	< 13	23.2	68	13.7	4.9
*Lm*FADSI[c]	+	0.40	6.9	0.057			
*Hs*RFK[e]	+	0.50	36	0.014			
*Bs*FADS[f]	+	0.70	55	0.013			
*Sd*FADS[f]	+	0.30	40	0.007			
*Ec*FADS[g]	+	0.39	2	0.20			

FMNAT activity		k_{cat} **(min^{-1})**	K_m^{FMN} **(μM)**	k_{cat} / K_m^{FMN} **(min^{-1} μM^{-1})**	k_{cat} **(min^{-1})**	K_m^{ATP} **(μM)**	k_{cat} / K_m^{ATP} **(min^{-1} μM^{-1})**
*Spn*FADS	+	34.9	9.8	3.6	23.2[e]	31.6	0.7
*Ca*FADS[a]	-	17.0	1.2	14.3	17.0	35.7	0.5
*Lm*FADSI[e]	+	4.39	29.2	0.15			
*Lm*FADSII[e]	+	0.51	12.9	0.04			
*Ec*FADS[g]	+	0.06	4	0.015			

[a] Data from [88]. Data were obtained at 25 ºC in 20 mM PIPES, pH 7.0 and 0.8 mM and 10 mM $MgCl_2$, respectively, for the RFK and FMNAT activities.
[b] Inhibition by substrate prevented the determination of true parameters and these correspond to apparent constants, $k_{cat,app}$, $K_{m,app}^{RF}$, $K_{m,app}^{ATP}$, $k_{cat,app}/K_{m,app}^{RF}$ and $k_{cat,app}/K_{m,app}^{ATP}$.
[c] Data from [79]. Data obtained in 50 mM potassium phosphate, pH 7.5.
[d] k_{cat} measured at 27.7 μM of FMN.
[e] Data from [225]. Data obtained in 50 mM potassium phosphate, pH 7.5.
[f] Data from [222]. Data obtained in 100 mM potassium phosphate, pH 7.5.
[g] Data from [226]. Data obtained in 50 mM potassium phosphate, pH 7.

4. *Spn*FADS does not bind oxidized flavins by itself

ITC thermograms for the titration of *Spn*FADS with oxidized RF, FMN or FAD, either in presence or absence of Mg^{2+}, indicated that under the assayed aerobic conditions none of these flavins binds to the protein with detectable enthalpic contribution (Fig. 6.5). Therefore, we also titrated *Spn*FADS with FMN and FAD in a flavin reducing buffer and in the presence of 0.8 mM Mg^{2+}. As shown in Fig. 6.6A, under such conditions binding of the reduced forms of FMN and FAD to the enzyme was detected. Both reduced cofactors bind to a single *Spn*FADS binding site (Fig. 6.6A and Table 6.2). K_d^{FMN} is in the low micromolar range, and binding of reduced FAD is 15-fold weaker. Enthalpic contributions to the binding are very similar for both flavins, but the entropic contributions favor FMN binding (Fig. 6.6C). Therefore, these results indicate that the FMNAT/FADpp sites of *Spn*FADS only bind the reduced states of FMN or FAD.

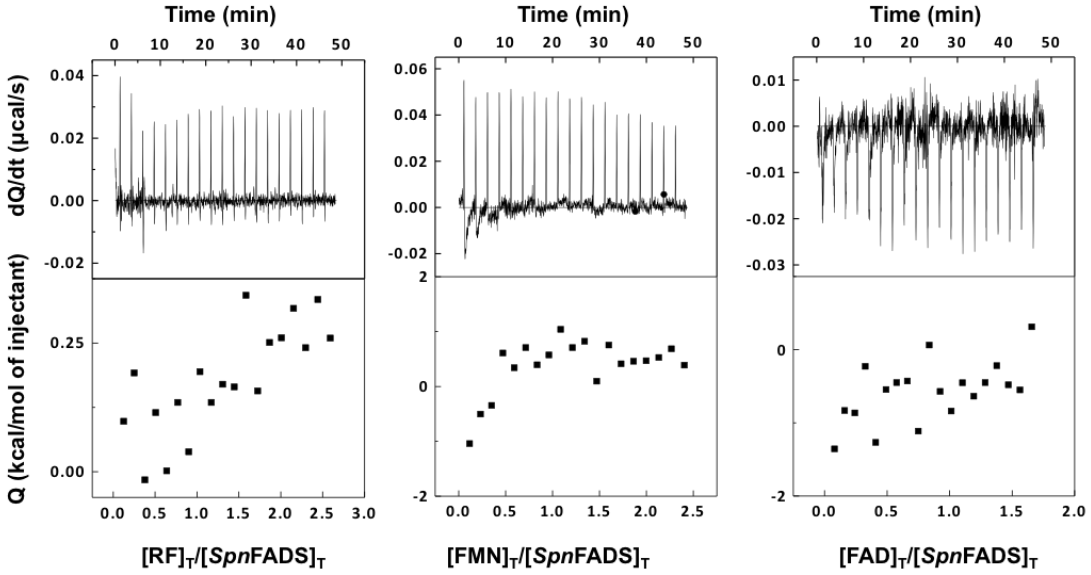

Figure 6.5. Representative calorimetric titrations of the interactions between *Spn*FADS with flavin cofactors: RF, FMN and FAD. The upper panels show the thermograms for the interactions and the lower panels show the corresponding binding isotherms with integrated heats. Experiments were carried out in 20 mM PIPES, pH 7.0 in 10 mM $MgCl_2$ at 20 °C and indicated flavins were not binding under these conditions.

Thermograms for the titration of *Spn*FADS with ATP indicated a single binding site for this nucleotide (presumably at the FMNAT site as in *Ca*FADS), both in the absence and presence of 0.8 mM of Mg^{2+} (Fig. 6.6A and Table 6.2), although binding affinities and interaction parameters differ between these two conditions. Thus, ATP

and ATP:Mg^{2+} allocate differently into the protein binding site, suggesting that the ion contributes to the nucleotide-protein-bound conformation. Titrations at higher Mg^{2+} concentrations showed two independent ATP binding sites, putatively related with each catalytic site, with similar affinities between them, and also similar to that of the site found at lower Mg^{2+} concentrations. However, enthalpic and entropic contributions to the ATP binding result highly influenced by Mg^{2+}; in its absence, and at low concentrations, the nucleotide binding is enthalpically driven with an opposing entropic contribution, while at high cation concentrations relatively mild entropic and enthalpic contributions favor the binding (Fig. 6.6B). Thermodynamic parameters for the *Spn*FADS titration with ADP also differ depending on Mg^{2+} concentration. In the absence of the cation, a single high affinity binding site is observed, being the binding driven by a favorable enthalpic contribution. At 10 mM of Mg^{2+}, a second binding site appears with lower affinity for the nucleotide, being the averaged K_d ($K_{d,av}$) at least 7-times higher. ADP binding in the presence of 10 mM Mg^{2+} is also enthalpically driven, but in this case the enthalpic contribution is much higher, being the entropic term mightily unfavorable. Thus high Mg^{2+} concentrations induce the generation of a second binding site for the adenine nucleotide ligands, both ATP and ADP, and influence the way the ligands allocate into the active site, as also supported by the different thermodynamic contributions to free energy of the binding.

Thermograms for the titration of mixtures containing *Spn*FADS plus ADP with oxidized RF or FMN showed that the presence of the adenine nucleotide promotes binding of both of these flavins (Fig. 6.6 and Table 6.2). Under these conditions RF in presence of 10 mM $MgCl_2$, apparently binds at two independent binding sites with moderate affinity, $K_{d,av}$ 51.3 µM, being the averaged binding enthalpically driven and the entropic contribution highly unfavorable. However, in the absence of Mg^{2+} only one binding site with strong affinity is detected. By contrast FMN binds at a single site with stronger affinity than those found for RF, being the binding driven by the enthalpic contribution and the binding parameters just modulated by the presence of Mg^{2+}. Finally, binding of FAD to *Spn*FADS in the presence of PPi could not be detected by enthalpic change, similarly to that occurred when titrating the PPi-free enzyme with FAD.

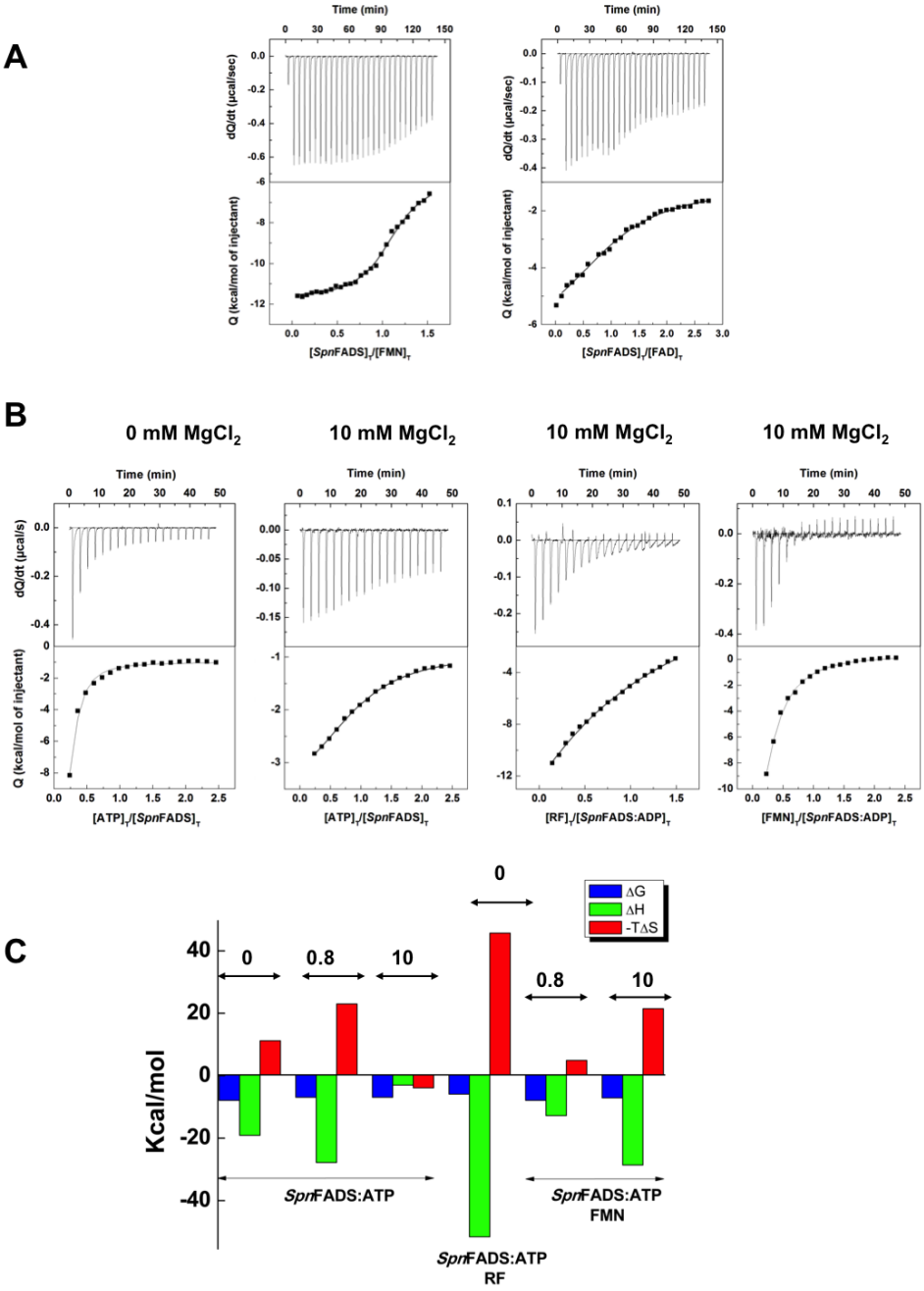

Figure 6.6. (A) Calorimetric titrations of *SpnF*ADS with reduced FMN and FAD, performed at 20 °C in 20 mM PIPES, pH 7.0, 0.8 mM $MgCl_2$, 4 mM sodium dithionite, 10 mM glucose, 0.5 U/ml glucose oxidase (degassed). (B) Calorimetric titrations of *SpnF*ADS with ATP and of the preformed *Spn*FADS:ADP complex with RF or FMN, at 20 °C in 20 mM PIPES, pH 7.0, and at the indicated concentrations of $MgCl_2$. In all titration figures upper panels show the thermograms for the interactions and the lower panels show the corresponding binding isotherms with integrated normalized heats. (C) Thermodynamic dissections of the interaction of *Spn*FADS with ATP, as well as of the preformed *Spn*FADS:ADP complex with RF and FMN. The binding Gibbs energy (ΔG), enthalpy (ΔH), and entropy ($-T\Delta S$) are represented in dark grey, light grey and white bars, respectively. $MgCl_2$ concentrations in mM used in each experiment are indicated by numbers.

Table 6.2. Thermodynamic parameters for the interaction of *Spn*FADS with the substrates and products of its activities obtained by ITC. Data obtained at 20 ºC in 20 mM PIPES, pH 7.0. Estimated errors in K_d are ±20 % and ±0.3 kcal/mol in ΔH and $-T\Delta S$.

	Ligand	$MgCl_2$ (mM)	K_d (μM)	ΔG (kcal/mol)	ΔH (kcal/mol)	$-T\Delta S$ (kcal/mol)	N
***Spn*FADS**	ATP	0	1.7	-7.9	-19.1	11.2	~1
		0.8	9.4	-6.9	-27.8	23.0	~1
		10	9.2 [a]	-6.9 [a]	-3.0 [a]	-3.9 [a]	~2
	ADP	0	4.1	-7.3	-12.9	5.5	~1
		10	30.0	-6.2	-19.4	13.3	~1
	RF, FMN, FAD	0	n.d.	n.d.	n.d.	n.d.	n.d.
		10					
	FMN[b]	0.8	0.8	-8.3	-5.8	-2.5	~1
	FAD[b]	0.8	12.5	-6.7	-5.6	-1.1	~1
***Spn*FADS: ADP**	RF	0	0.3	-9.0	-17.2	8.2	~1
		10	51.3 [a]	-5.9 [a]	-51.6 [a]	45.7 [a]	~2
	FMN	0	1.5	-7.9	-12.8	4.9	<1
		10	5.9	-7.1	-28.6	21.5	<1
***Spn*FADS: PP_i**	FAD	0	n.d.	n.d.	n.d.	n.d.	n.d.

[a] Data corresponding to average values of two similar and independent binding sites ($K_{d,av}$, ΔG_{av}, ΔH_{av}, $-T\Delta S_{av}$).
[b] Measurements performed in the presence of 4 mM sodium dithionite, 10 mM glucose and 0.5 U/ml glucose oxidase.
n.d. No enthalpic change was detected along the titration.

5. *Spn*FADS exists mainly as a monomer but other oligomeric states are populated during catalysis

*Spn*FADS eluted in a main peak with a small shoulder in the gel filtration column used as a last step in its purification. The presence of the shoulder might be indicative of freshly purified *Spn*FADS stabilizing quaternary assemblies, as described for *Ca*FADS [84]. To check for such possibility we passed through the gel filtration column a freshly purified *Spn*FADS fraction considered as monomeric. This protein eluted as a main broad peak at ~14.5 mL (~96% of the protein) but also produced a shoulder at ~13 mL (Fig. 6.7). The peak at ~14.5 mL deconvolutes in three populations with apparent MWs of 61.2, 63.7 and 70 kDa. These values are slightly higher than the theoretic one for the monomer (34.8 kDa), but the elongated structure of *Spn*FADS and the different conformations expected for its external loops suggests that they might be assigned to

either different conformers of monomers or dimers. In contrast, the apparent MW of the shoulder is 127.4 kDa, suggesting this small fraction is populated by high MW oligomers. These pure preparations of *Spn*FADS also migrated in two bands on native gel electrophoresis, although the one putatively assigned to the monomer was the most populated (Fig. 6.7B).

SDS-PAGE resolved the protein in a single band corresponding to the monomer MW, but pre-incubation of the protein with the BS3 crosslinker stabilized an additional band with an apparent MW of 78.6 kDa that can be assigned to a dimer (Fig. 6.7C). Altogether these data suggest that purified *Spn*FADS can be found in a monomer-dimer equilibrium that is mainly shifted towards the monomeric form, with traces of higher MW assemblies.

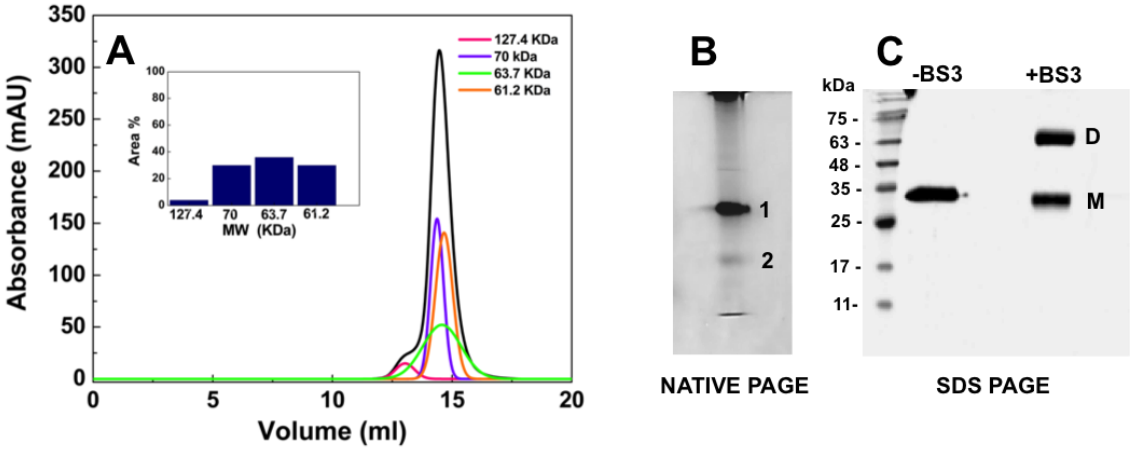

Figure 6.7. Hydrodynamic properties of *Spn*FADS. (A) Gel-filtration chromatogram of pure *Spn*FADS (20 µM) using a precalibrated Superdex™ 200 10/300 GL column (*GE Healthcare*) equilibrated with 50 mM Tris/HCl, pH 8.0, 150 mM NaCl, and calibrated with the Gel Filtration Calibration Kit LMW (*GE Healthcare*). The inset shows the percentage of the fractions obtained from the chromatogram. (B) 12% Native PAGE of pure *Spn*FADS and (C) 15% SDS-PAGE of *Spn*FADS without crosslinker and after incubation with the BS3 crosslinker.

We used AFM to shed light on the *Spn*FADS assembly in solution, as well as on the possible effect of ligands in the monomer-oligomer equilibrium (Fig. 6.8A-F). AFM topography images of free *Spn*FADS indicate a compact monomer (height ~7 ± 1 nm) (Fig. 6.8A). Incubation of the enzyme with different combinations of substrates and/or its reaction products produced some dimers and trimers, while ADP also promoted the formation of tetramers (Fig. 6.8 and Table 6.3). Two types of images were found for

dimers. In one of them the two protomers dispose parallel in the same plane with the tallest module of one interacting protomer with the smallest of the other, leaving the rest of these molecules free of contact (Fig. 6.8B). In the other dimer, the most frequent, both protomers are on the same plane establishing different angles and slightly overlapping one module of the first onto one of the modules of the other (Fig. 6.8C). Both dimers appear as intermediate steps in the formation of the two trimeric species visualized in the images (Figs. 6.8D and 6.8E), which situate an additional monomer over one of the monomers of the dimeric structures. Considering the disposition adopted by the three molecules present in the asymmetric unit of the *Spn*FADS crystal (Fig. 6.8G), where each protomer is situated in a different plane, the trimers in solution differ from such crystallographic association. Finally, tetramers form two layers of two overlapped monomers (Fig. 6.8F). Incubation of *Spn*FADS with ATP and FMN, ADP and FMN, or FAD and PP_i, produced the higher ratios of trimeric species, ~41 %, while the RFK activity reactants, ATP and RF, generated 30 % of dimeric molecules and only 16 % of trimers. ATP by itself produced 37 % of trimers, meanwhile ADP makes 20 % of trimers and 47 % of tetramers (Table 6.3). Incubation with the reactants of the FMNAT and FADpp activities resembles the same oligomeric yields. Since neither oxidized FMN nor FAD are able to bind to *Spn*FADS in the absence of adenine nucleotides, these data suggest that binding of adenine nucleotides (ATP and ADP) promotes the observed quaternary assemblies.

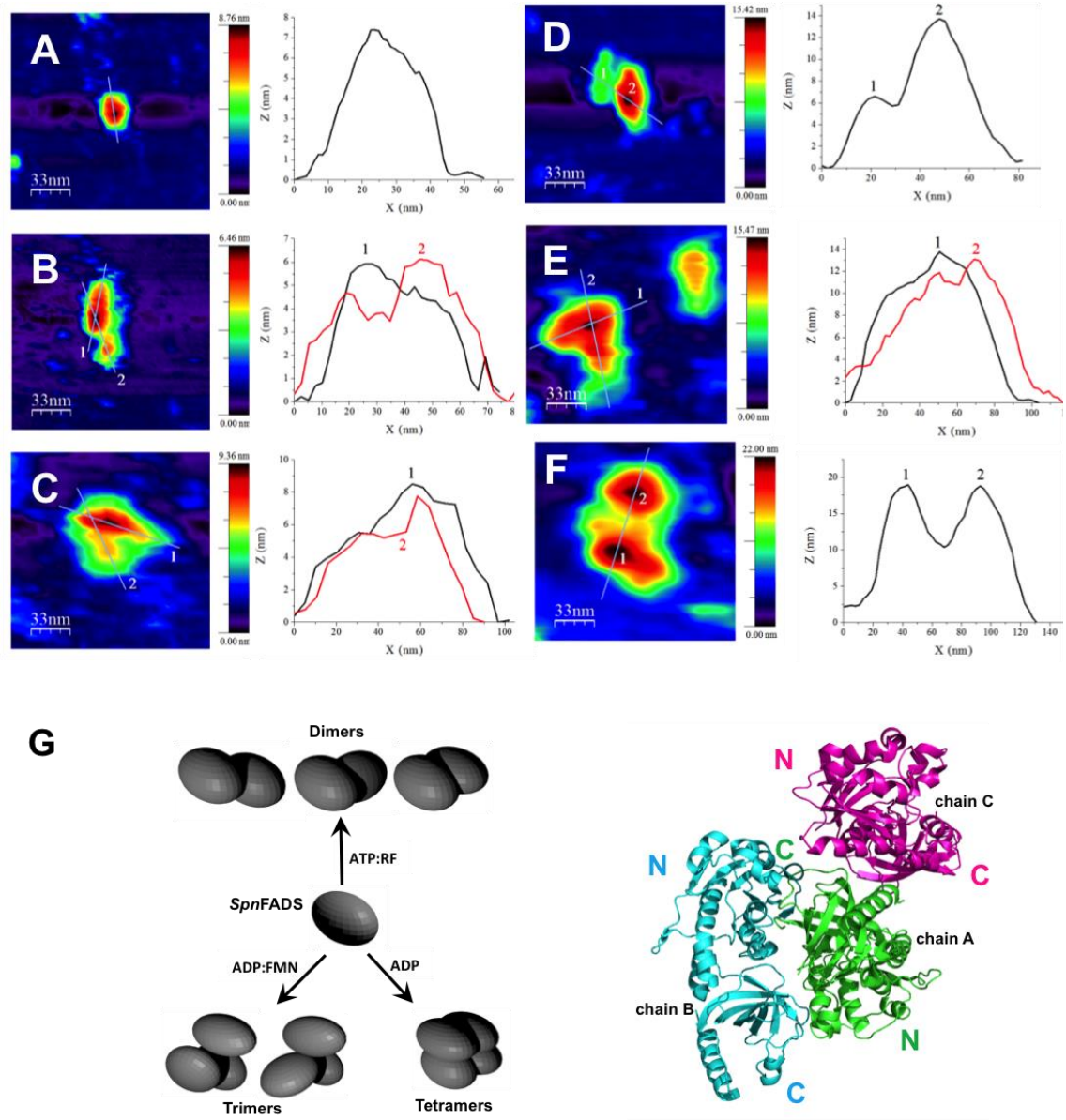

Figure 6.8. Image analysis of *Spn*FADS assemblies. Topography AFM images of a scanned area of 167 x 167 nm and Z-height profiles associated to the lines on the features of *Spn*FADS samples. (A) Monomer. (B) Dimer on the same plane. (C) Dimer with an overlapping on a monomer on the other. (D) Trimer from (B) showing an overlapped dimer interacting with a monomer. (E) Trimer from (C) showing overlapping of the dimer on a monomer. The different sizes of the original scanned images slightly change the roughness of the surface and the lateral resolution. This affects the size of the features in X-Y but not the Z-height measured in the profiles. (F) Tetramer. (G) Blender simulation of different assemblies according to the presence or absence of ligands and assembly of the three *Spn*FADS molecules in the crystal asymmetric unit (PDB 3op1).

Table 6.3. Percentages of *Spn*FADS assemblies imaged by AFM. Samples of 0.5 μM *Spn*FADS were analyzed in 20 mM PIPES, pH 6.0, 2 mM DTT and 0.8 mM $MgCl_2$ at room temperature. When indicated, ADP, ATP or PP_i were added at 250 μM, while oxidized FAD, FMN and RF were used at 50 μM. Features correspond to image units, while molecules refer to the amount of individual protein monomers in the corresponding image units. Error associated to percentage determination was ± 10 %.

		Association State			
Ligands	**Units**	**Monomers (%)**	**Dimers (%)**	**Trimers (%)**	**Tetramers (%)**
	Features	97	3	----	----
	Molecules	94	6	----	----
ADP	Features	60	7	13	20
	Molecules	31	7	20	47
ATP	Features	70	12	18	----
	Molecules	47	16	37	----
ATP, RF	Features	73	20	7	----
	Molecules	54	30	16	----
ATP, FMN	Features	73	7	20	----
	Molecules	50	9	41	----
ADP, FMN	Features	63	15	22	----
	Molecules	40	19	41	----
FAD, PPi	Features	73	7	20	----
	Molecules	50	9	41	----

6. Discussion

Sequence alignments, structural comparisons [76, 85, 99] and ligand binding models (Fig. 6.2A and Fig. 6.9A) suggested that *Spn*FADS contains all the features of prokaryotic FADSs that contribute to substrates stabilization and catalysis. Accordingly, we show here that the enzyme catalyzes the RFK, FMNAT and FADpp activities, but we also highlight different requirements for catalysis and binding of ligands relative to other family members. Interestingly while transformation of RF into FMN by *Spn*FADS occurs similarly under both aerobic and reducing conditions, the FMNAT and FADpp activities require reduced flavins (Fig. 6.3). Reducing conditions hardly influence any of the *Ca*FADS activities [88, 90] (Table 6.1), but some bifunctional FADSs as well as the monofunctional *Hs*RFK are more active in the presence of high concentrations of reducing agents [79, 222, 225, 226]. Moreover, studies of enriched samples of the

FADS from *Bacillus subtilis* (*Bs*FADS) early suggested specificity for reduced flavins in all its activities [223].

Despite the differences in the redox requirements for the RFK and FMNAT activities between *Spn*FADS and *Ca*FADS, both enzymes showed the highest efficiency for the synthesis of FMN and FAD compared to the other family enzymes reported up to now (Table 6.1) [79, 88, 90, 225] with the lack of inhibition by the RF substrate for the RFK activity in *Spn*FADS (Fig. 6.3C) as a notable difference between these two enzymes. Our ITC data indicate that *Spn*FADS does not bind any of its oxidized flavinic substrates when adenine nucleotides are not present (Fig. 6.5), contrary to *Ca*FADS [88, 90]. Reducing conditions are not a requirement for the binding of adenine nucleotides (ATP and ADP) (Fig. 6.6), and the presence of the adenine nucleotide also induces binding of oxidized RF or FMN. Nevertheless, ternary interactions in *Spn*FADS are slightly weaker than in *Ca*FADS [84]. Moreover, in the presence of the adenine nucleotide, oxidized FMN only binds at one site, which according to the enzyme capability to transform oxidized RF into FMN must be the RFK site (Table 6.2). The fact that oxidized RF does not bind to free *Spn*FADS, the lack of inhibition by RF, and the enzyme being catalytically efficient at low RF concentrations, suggest a dissimilar RFK mechanism between this enzyme and *Ca*FADS [81]. Furthermore, the enzymatic and ligand binding characterizations of *Spn*FADS altogether confirm that competent flavin binding for catalysis at the FMNAT site requires the flavin ring in its reduced state. In addition, *Spn*FADS needs higher concentrations of substrates than *Ca*FADS to achieve maximal efficiency.

The need for reduced flavinic substrates in *Bs*FADS was interpreted as the geometry of the active site only allowing the incorporation of isoalloxazine rings in the reduced bended conformations, contrary to the highly stable planar organization adopted by their oxidized states [39, 223, 227]. Despite the high conservation grade in overall folding (Fig. 6.2B) and key active sites residues, *Ca*FADS and *Spn*FADS are dissimilar in some regions involved in ligand binding (Figs. 6.9B and 6.2C). In the FMNAT module of *Spn*FADS helixes $\alpha 3_{10}$n and α5n break loops L4n and L6n, respectively. These regions form the external part of the cavity where substrates for the FMNAT and FADpp activities bind. The sites for the ribityl and isoalloxazine moieties are formed in both enzymes by hydrophobic and aromatic side-chains (Fig. 6.10A), whose differential spatial position might determine cavity volumes and, therefore, modes for flavin binding. The cavity appears slightly broader and deeper in *Spn*FADS

than in *Ca*FADS, although in *Spn*FADS the isoalloxazine binding site surface is rougher and shows a more negative surface electrostatic potential (Fig. 6.10B). The side chains of two Met residues, M54 and M118, form also part of the flavin ring cavity in *Spn*FADS, with M54 particularly prone to contact with the inner isoalloxazine ring (Fig. 6.10C). These Met residues are not conserved in most family members, which have instead hydrophobic residues [76]. Moreover, M54 forms part of a conserved sequence motif that is included only in few members such as *Bs*FADS.

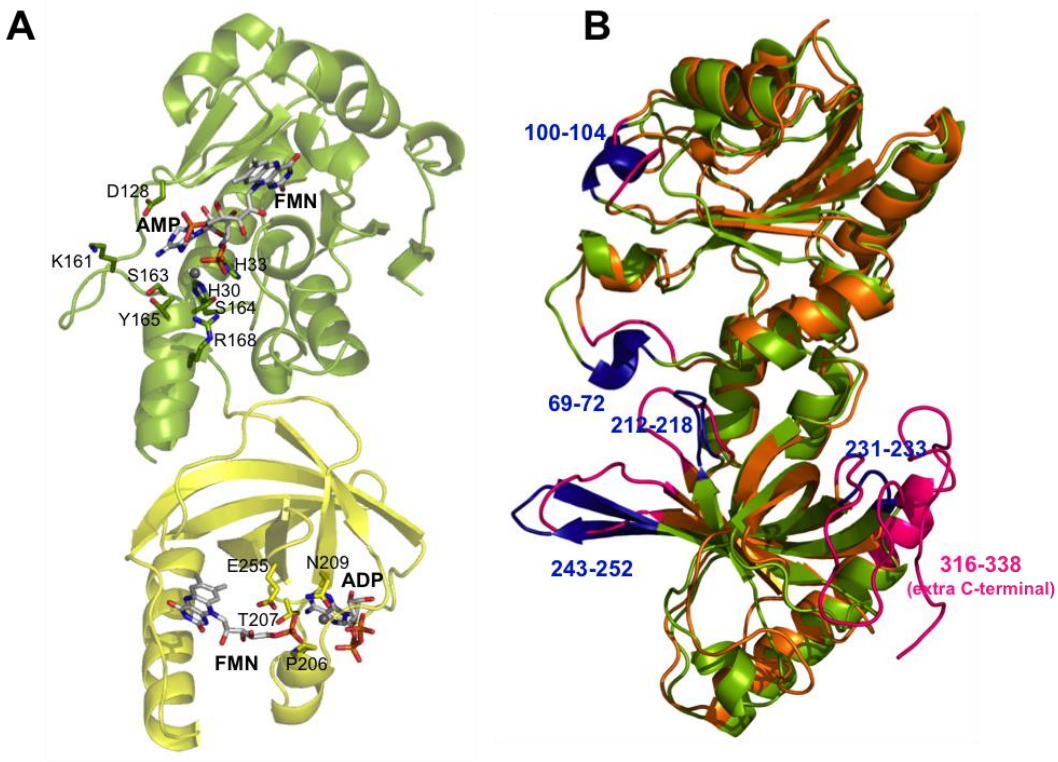

Figure 6.9. The structure of *Spn*FADS. (A) Model (based on PDB 3op1) for the interaction of *Spn*FADS with its ligands. The FMNAT module is shown in green and the RFK in yellow. Flavin and adenine nucleotide ligands are in CPK colored sticks with carbons in white. Mg^{2+} ions are shown as grey balls. Modelling performed using PyMol. (B) Superposition of the structures of *Spn*FADS (green, PDB 3op1) and *Ca*FADS (orange, PDB 2x0k). Dissimilar regions are highlighted in blue and pink, respectively, including the numbers of implicated residues in *Spn*FADS.

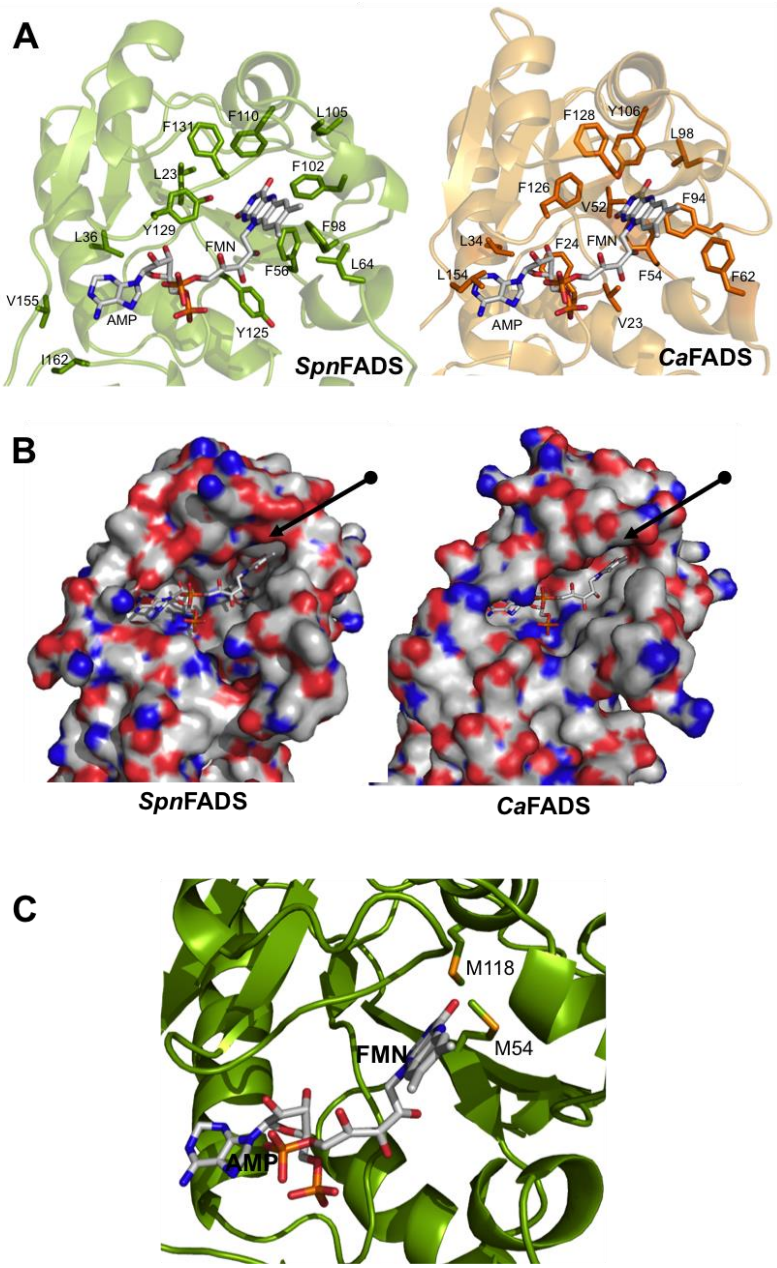

Figure 6.10. Comparative analysis of the *Spn*FADS and *Ca*FADS active sites in the FMNAT module. (A) Site for ligands binding in *Spn*FADS (green) and *Ca*FADS (orange). Hydrophobic and aromatic side chains are shown in sticks. (B) Surface electrostatic potential for the isoalloxazine binding cavity in *Spn*FADS (left panel) and *Ca*FADS (right panel). Arrows point to differences in sign of surface electrostatic potential at the *Spn*FADS and *Ca*FADS isoalloxazine sites. (C) Relative disposition of M54 and M118 regarding the isoalloxazine moiety of the flavin substrate. In all panels, FMN and AMP have been modelled on the crystals structures of *Spn*FADS (PDB 3op1) and *Ca*FADS (PDB 2x0k) and represented in CPK sticks with carbons in grey [85].

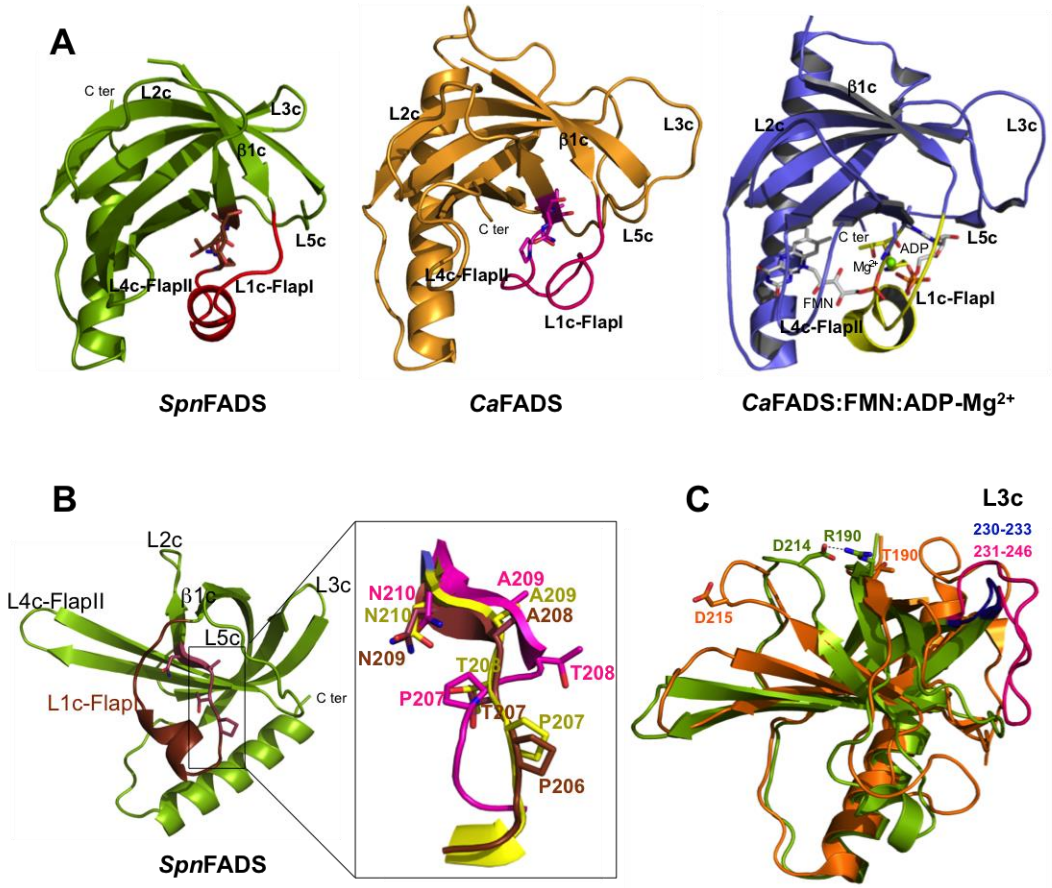

Figure 6.11. Comparative analysis of the RFK sites of *Spn*FADS, *Ca*FADS and the *Ca*FADS:FMN:ADP-Mg^{2+} ternary complex. (A) Cartoon representation of the RFK domains of *Spn*FADS (green, PDB 3op1), *Ca*FADS (orange, PDB 2x0k) and ternary complex of the RFK module of *Ca*FADS (blue, PDB 5a8a). L1c-FlapI is highlighted in red, pink and yellow, respectively. Residues of the PTAN motif are in CPK sticks. The FMN and ADP ligands bound to the *Ca*FADS RFK module are in white CPK and Mg^{2+} is included as a green sphere. (B) Detail of the PTAN motif in *Spn*FADS and superposition of the PTAN motives of the three structures. (**C)** Superposition of the RFK domain of *Spn*FADS (green) and *Ca*FADS (orange). The salt bridge between D214 at L2c and R190 at β1c of *Spn*FADS is in black dashes. Equivalent residues in *Ca*FADS, D215 and T190, are drawn in sticks. Loops L3c are colored in blue (*Spn*FADS) and pink (*Ca*FADS).

Structural differences are also observed when comparing the *Spn*FADS RFK module with the structures available for the *Ca*FADS RFK module free and in complex with ligands (Figs. 6.9 and 6.11) [99] : i) D214 at loop L2c of *Spn*FADS salt bridges R190 at β1c; ii) loop L3c is 12 residues shorter; iii) the C-terminal is considerably shorter; and iv) an extra α helix, α1c, breaks loop L1c-Flap I. In addition, conformations of the conserved PTAN motif and of L1c-FlapI in free *Spn*FADS resemble those

elements in the *Ca*FADS:FMN:ADP-Mg^{2+} complex. Such organization leaves the adenine nucleotide binding site open and the PTAN motif ready to stabilize the ligand (Fig. 6.11), contrary to free *Ca*FADS [99]. Thus, the weaker affinity of *Spn*FADS for the RFK activity products might be related with the lack of large conformational changes at the active site for substrates association and products dissociation during catalysis. These traits surely also contribute to the lack of inhibition by the RF substrate in *Spn*FADS.

Table 6.4. List of probable quaternary structures in solution for *Spn*FADS and *Ca*FADs as predicted by the PISA server

Composition	Stable	Surface area Å²	Buried area Å²	ΔG^{int} kcal/mol	ΔG^{diss} kcal/mol
***Spn*FADS**					
CC´	yes	24440	7030	-82.0	9.2
AB	yes	28530	5090	-33.2	2.9
B´C	yes	28190	4580	-52.6	0.3
***Ca*FADS**					
A_3B_3	yes	82800	19770	-189.0	22.5
B_3	yes	45020	6550	-73.0	3.1
A_3	yes	44480	6520	-72.0	2.7
AB	yes	31390	2800	-52.7	12.4

Finally, substrates and products of *Spn*FADS induce formation of dimers, tetramers and particularly trimers with head-to-tail contacts between the RFK module and the FMNAT module of different protomers (Table 6.3, Fig. 6.8). None of these organizations resembles the dimer-of-trimers reported for *Ca*FADS and in general the *Spn*FADS monomer appears to be majority [100]. The PDBePISA server predicts dimeric assemblies with head-to-tail fits (Table 6.4, Fig. 6.12), but it does not predict any higher oligomer as stable in solution. Differences in oligomerization profiles might relate with differences in protein oligomerization regions. In fact, a long L3c, only expected for *Corynebacterium* and *Mycobacterium* species, is predicted as a determinant to stabilize the dimer of trimers [100]. The shorter loop in *Spn*FADS agrees with this hypothesis, being less prone to oligomerization and establishing different contacts among protomers, which might also contribute to the dissimilar binding, kinetic and inhibition properties among species. The dimer-of-trimers in *Ca*FADS envisaged a controlled interplay between the regions involved in the formation of the

RFK and/or FMNAT catalytic sites of different protomers as well as in flavin delivery to client apoflavoproteins [87, 156]. However, such mechanism might not be required for *Spn*FADS, since in this enzyme the main regulation mechanism for the FAD synthesis seems to be the reducing environment.

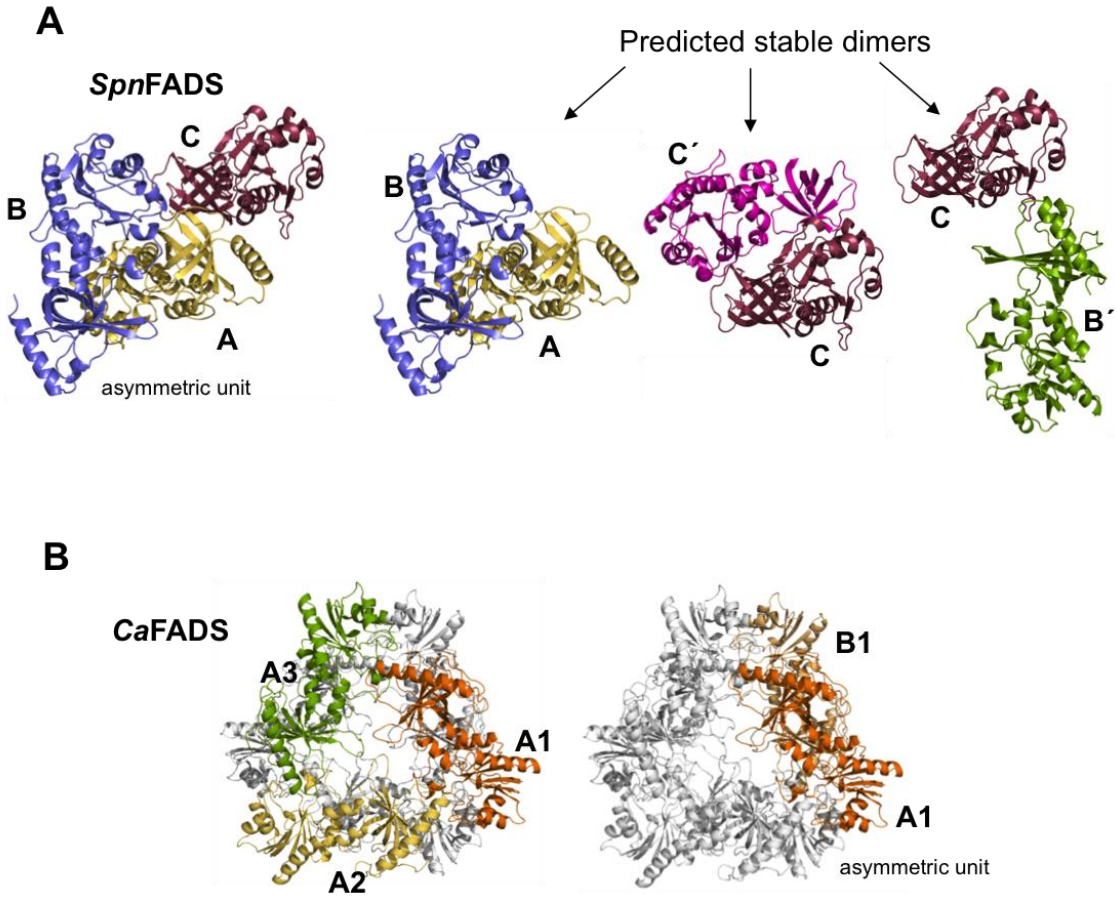

Figure 6.12. (A) Oligomeric organizations predicted by the PDBePISA server based on the structure of *Spn*FADS (PDB 3op1). The asymmetric unit contains three chains, A, B, and C, coloured in yellow, blue and red, respectively. Besides, the three predicted as possible stable dimers in solution. Chains A´ (pink) and C´ (green) belong to other asymmetry unit. (B) Oligomeric assembly predicted for *Ca*FADS as a dimer-of-trimers (hexamer, A_3B_3). The left panels show the protomers of the trimer at front coloured in orange, green and yellow and the others at the back in grey. The right panels show the location of the two chains of asymmetric unit (A_1B_1) in the dimer-of-trimers (orange and pale orange).

Chapter VII

The RFK catalytic cycle of the FADS from *Streptococcus pneumoniae*

The FADS from the human pathogen *S. pneumoniae* shows the consensus sequences assigned to the RFK, FMNAT and FADpp activities (Fig 1.11). Comparison of *Spn*FADS with *Ca*FADS reveals that the overall structures of both proteins are quite similar despite the fact that they only show 25% of sequence identity. Nevertheless, the previous study exposed in chapter 6, revealed important behavioral differences between both proteins. Among the dissimilarities, two stand out: Firstly, *Spn*FADS requires reduced FMN for its FMNAT reaction, while *Ca*FADS does not show such requirement. Secondly, contrary to *Ca*FADS, the RFK activity of *Spn*FADS does not show inhibition by excess of the RF substrate. Due to the potentiality of bifunctional FADSs as exploitable drug targets, the differences among them are worthy of study to take advantage of them when designing species-specific drugs.

The first issue was addressed in the previous chapter, while in the present one we tackle the apparent lack of inhibition of the RFK activity of *Spn*FADS. For that purpose, we performed a complete kinetic and thermodynamic characterization of the RFK catalytic cycle of the enzyme, similar to that displayed in chapter 5 for the RFK module of *Ca*FADS. Comparison of the results obtained for both enzymes might reveal key aspects of their RFK activity.

1. The RFK activity of *Spn*FADS is inhibited by the products of the reaction

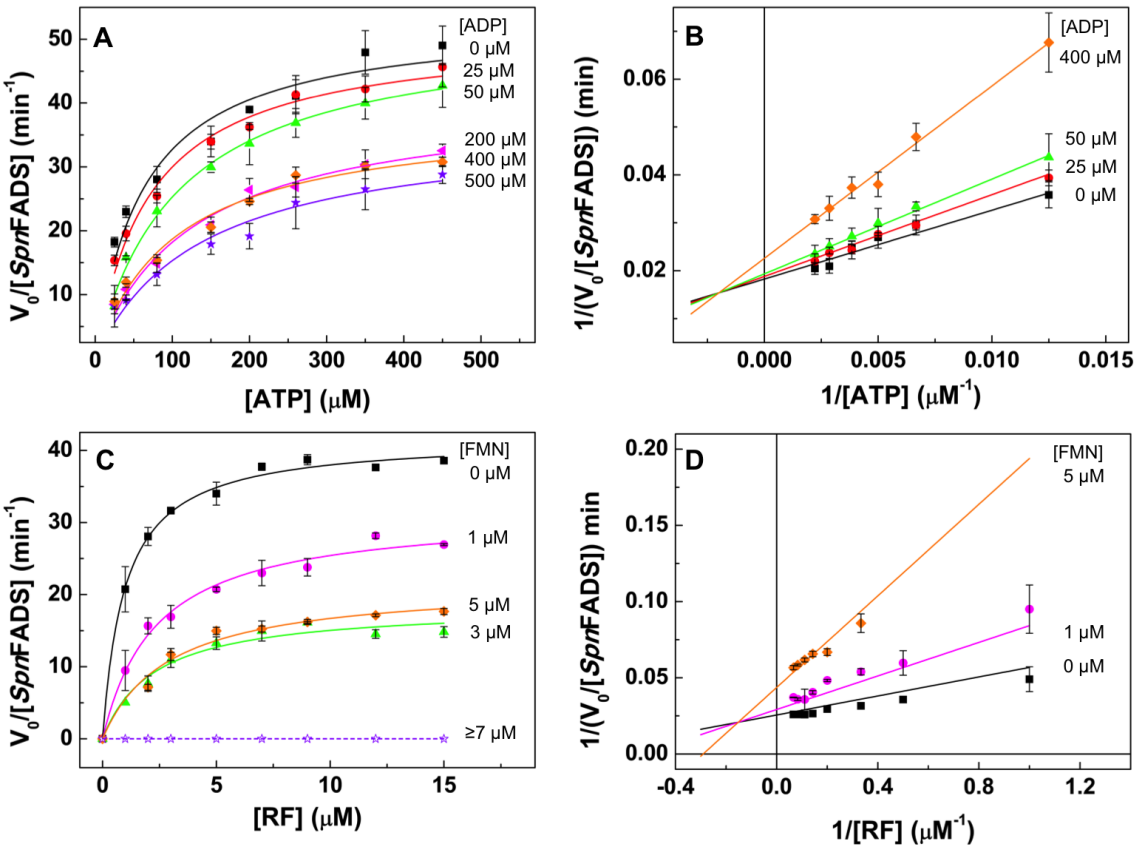

Figure 7.1. Inhibitory effects produced by the FMN and ADP products of the *Spn*FADS RFK reaction. (A) Michaelis-Menten plots as a function of ATP obtained at different concentrations of the ADP product. (B) Lineaweaver-Burk representation at different ADP concentrations with global fit to the equation for mixed inhibition. (C) Michaelis-Menten plots as a function of RF obtained at different concentrations of the FMN product. (D) Lineaweaver-Burk representation at different FMN concentrations with global fit to the equation for mixed inhibition. All the experiments were performed at 25ºC in 20mM PIPES, pH7.0, 0.8 mM $MgCl_2$. Reaction rates represented in (A) and (B) were obtained at 10 μM RF and variable concentrations of the ATP substrate (25-450 μM) and of the ADP product (25-500 μM). Reaction rates displayed in (C) and (D) were obtained at 350 μM ATP and variable concentrations of the RF substrate (1-15 μM) and of the FMN product (1-14 μM). Experiments were carried out in triplicate.

Table 7.1. Steady-state kinetic parameters obtained for the *Spn*FADS RFK activity in presence and absence of the products of the reaction. Data obtained at 25 °C in 20 mM PIPES, 0.8 mM $MgCl_2$, pH 7.0.

Kinetic parameters as determined in the absence of products of the reaction

[ADP] (μM)	k_{cat} (min^{-1})	K_m^{ATP} (μM)	[FMN] (μM)	k_{cat} (min^{-1})	K_m^{RF} (μM)
0	53±3	62±12	0	42±1	1.0±0.1

Kinetic parameters as determined at different concentrations of reaction products

[ADP] (μM)	k_{cat} (min^{-1})	K_m^{ATP} (μM)	[FMN] (μM)	k_{cat} (min^{-1})	K_m^{RF} (μM)
25	51±12	71±8	1	31±1***	2.3±0.3**
50	52±2	107±10	3	18±1***	2.3±0.5**
200	41±2***	125±18**	5	21±1***	2.9±0.6**
400	38±2***	105±14**	7	N.A.	N.A.
500	36±3***	136±30**	9	N.A.	N.A.

Data showing statistical significance differences when compared with the activity of *Spn*FADS in the absence of the products of the reaction (***, $p<0.0001$; **, $0.0021>p>0.0001$.
N.A. Not applicable. The complete inhibition of the enzyme prevented the determination of any kinetic parameter.

Kinetic parameters determined by global fitting to the Lineweaver-Burk equation

K_i^{ADP} a (μM)	$K'_i{}^{ADP}$ (μM)	k_{cat} (min^{-1})	K_m^{ATP} (μM)	K_i^{FMN} (μM)	$K'_i{}^{FMN}$ (μM)	k_{cat} (min^{-1})	K_m^{RF} (μM)
130.7±16.4	844±97	55±2	75±7	1.3±0.4	7.1±1	39±3	1.2±0.3

The RFK reaction of *Spn*FADS follows a bisubstrate Michaelis-Menten kinetics, with K_m^{ATP}, K_m^{RF} and k_{cat} values of ~62± 13 μM, ~1.0± 0.1 μM and ~50± 3 min^{-1}, respectively (Fig. 7.1, Table 7.1). To evaluate if the products of the RFK reaction (ADP and FMN) inhibit this activity, we also studied the evolution of the steady-state rates at increasing concentrations of ADP and FMN (Figs. 7.1A and 7.1C). Michaelis-Menten plots obtained as a function of the ATP substrate at increasing concentrations of the ADP product revealed that both k_{cat} and K_m^{ATP} were altered. k_{cat} decreased while K_m^{ATP} increased with the ADP concentration (Fig. 7.1A, Table 7.1). Similar results were observed for plots obtained as a function of the RF substrate when increasing the FMN product concentration. This behavior (both k_{cat} and K_m are modified) is typical of mixed and uncompetitive inhibitors. We used then Lineweaver-Burk representations to discerning between these two mechanisms of inhibition. Lines intersected at negative

values of the x-axis and positive ones of the y-axis for both reaction products, indicating that both ADP and FMN are mixed inhibitors of the RFK activity. Thus, FMN and ADP can bind to the free enzyme as well as to a *Spn*FADS:ATP or *Spn*FADS:RF complex, respectively. However, affinities for the free protein and for the complex differ (Table 7.1). Global fitting of the double inverses plots (Figs. 7.1B and 7.1C) to the model describing mixed inhibition (Eqn. 2.21), yielded the inhibition constants for ADP and FMN, being K_i^{ADP} and $K'_i{}^{ADP}$ 131± 16 μM and 844± 97 μM, respectively; and K_i^{FMN} and $K'_i{}^{FMN}$ 1.3± 0.4 μM and 7.1± 1.3 μM, respectively. These data indicate that FMN is a stronger inhibitor than ADP, and that both inhibitors bind preferentially to the free enzyme.

2. Fast kinetics in the pre-steady state RFK reaction of *Spn*FADS

We used stopped-flow spectrophotometry to kinetically identify the different processes that might take place during the RFK reaction of *Spn*FADS. As in chapter 5, the magnitude change we follow is the fluorescence of the oxidized FLV ligands [51]. Two aspects must be considered at this point. Since RF and FMN show the same fluorescence spectra and yields [55], we do not expect to observe the transformation of the first into the second one. Thus, we will follow changes affecting the isoalloxazine ring environment (such as its binding or dissociation to the protein or conformational changes in its surroundings). The second relates to the FMNAT module of *Spn*FADS that only binds and transforms flavins in their reduced state, as indicated in chapter 6. Taking advantage of this, working under oxygen atmosphere will allow us to independently study flavin binding processes to the RFK module of the protein. When we mixed *Spn*FADS with FLV ligands, we only distinguished very slow linear fluorescence decays, whose slopes linearly decreased with the FLV concentration. The rates for these decays were within the photobleanching range ($4.5 \cdot 10^{-3} \pm 1.2 \cdot 10^{-4}$ min^{-1} and $4.1 \cdot 10^{-3} \pm 2.4 \cdot 10^{-4}$ min^{-1} for RF and FMN, respectively) (Fig. 5.3B). As discussed elsewhere, these data indicate that *Spn*FADS, and particularly its RFK module, is neither able to bind oxidized FLV ligands, nor to internalize their isoalloxazine rings (Chapter 5, section 2).

We next mixed *Spn*FADS simultaneously with ANP and FLV ligands, observing fluorescence changes that were considerably faster and more intense that those related to photobleaching. The number of processes identified in these kinetic traces depends on the nature of the ANP ligand in the mixture (Fig. 7.2A). All mixtures show a

fluorescence decay within the 5 s after mixing (Fig. 7.2A-D), but mixtures containing ATP also show a subsequent rising of the flavin fluorescence up to the initial values. In a previous study with the RFK module of the *Ca*FADS enzyme, we suggested that the initial fluorescence decay was related to flavin binding and internalization within the protein previously bound to the ANP ligand (Chapter 5, section 2). Noticeably, it is apparent that under the assayed conditions the amplitude of the fluorescence kinetic decay is considerably larger when mixing *Spn*FADS with the substrates of the RFK reaction, RF and ATP, than with any other FLV-ANP combination (Fig. 7.2A). These data indicate a greater fraction of protein prone to bind the RF and ATP substrates. The fitting of the fluorescent decay traces to a single exponential equation (Eqn. 2.9) yields k_{obs1} values (Fig. 7.3A) that, in general, follow a linear dependence on the FLV concentration for mixtures containing RF-ATP or FMN-ADP. However, when mixing *Spn*FADS with RF-ADP k_{obs1} values exhibit an upward curvature, indicating that as the RF concentration increases the *Spn*FADS:ADP binary complex internalizes it faster. As a consequence, at low RF concentrations its binding to *Spn*FADS is faster when induced by the ATP substrate than by the ADP product, while as RF concentration increases this behavior is inverted. The fitting of the k_{obs1} values to Eqn 2.11 allows calculating the corresponding flavin association rate constants, $k_{on,}$ and the dissociation rate constants, k_{off}, whose values are summarized in Table 7.2 together with the kinetic dissociation constants derived from them. The binding of the RFK substrates, RF and ATP, is in general the faster process, and only at high RF concentrations RF and ADP binding is slightly faster. This observed effect of RF concentration on its internalization rate in the presence of ADP, might be due to the two different paths that lead to the formation of the non-productive *Spn*FADS:RF:ADP ternary complex (Fig. 7.4B). Thus, no matter which ligand binds the protein firstly, the binding of the second one induces the conformational change that encloses the RF within the active site. As our inhibitory study in the steady state revealed, ADP act as a mixed inhibitor, being able to bind both the free protein and the preformed *Spn*FADS:RF binary complex (being these processes characterized by the inhibition constants K_i^{ADP} and $K'_i{}^{ADP}$, respectively). Since $K'_i{}^{ADP} > K_i^{ADP}$, at low RF concentrations ADP might bind the protein first and then RF would do it. Higher RF concentrations increase the amount of the *Spn*FADS:RF binary complex, and under these conditions, ADP might be in fact the second ligand binding the protein. The two different slopes observed when plotting k_{obs1} on RF concentration might be related with variations in the RF internalization rates, which depend on the order in

which the ligands get bound. Thus, RF binding to *Spn*FADS:ADP (and its internalization), which predominates at low concentrations of this flavin (k_{on1} ~ 102 ± 6 min^{-1}), is slower than ADP binding to *Spn*FADS:RF (k'_{on1} ~ 297 ± 9), which is favored at high RF concentrations. In contrast, the FMN binding to *Spn*FADS in the presence of ATP is a very slow process. Considering also the small amplitude of the fluorescence change in this process, this combination of ligands is the least favored (from the kinetic point of view) for flavin enclosure within the RFK module of *Spn*FADS.

Table 7.2. Pre-steady-state kinetic parameters for the binding and dissociation of flavins to *Spn*FADS in the presence of the adenine nucleotides. Experiments were carried out in 20 mM PIPES, 0.8 mM $MgCl_2$, pH 7.0.

Ligands combination	k_{on} **($min^{-1}\mu M^{-1}$)**	k_{off} **(min^{-1})**	K_d **(μM)**	ΔG **(kcal/mol)**
FMN-ATP	[a]	[a]		
RF-ADP	102 ± 6 [b]	84 ± 11 [b]	0.83 ± 0.12	-8.3 ± 1.4
RF-ATP	128 ± 14	73 ± 16	0.57 ± 0.14	-8.5 ± 2.0
FMN-ADP	85 ± 7	65 ± 20	0.80 ± 0.24	-8.3 ± 2.5

[a] The k_{obs1} values close to 0 prevented the determination of k_{on} and k_{off} values.
[b] Values obtained when [RF]≤ 3 μM. When [RF] ≥ 3 μM, k_{on} ~ 297 ± 9, k_{off} could not been determined.

Kinetic traces obtained when mixing *Spn*FADS with FLV-ATP mixtures show a subsequent exponential rising of fluorescence (Fig. 7.2A green and black lines, 7.2C and 2D). This process has been previously related with an "ATP-induced" conformational change in the isoalloxazine environment that increases its solvent accessibility (Chapter 5, section 2). The fitting of the kinetic traces to an exponential equation provides with k_{obs2} values (Fig. 7.3B) that show a linear dependency on RF concentration. On the contrary, k_{obs2} values for processes with FMN and ATP are considerably slower and even exhibit a biphasic behavior on FMN concentration. This indicates that the conformational rearrangement is considerably faster when the RF substrate is the flavin initially bound to the active site (Fig. 7.3B). Comparison of k_{obs1} and k_{obs2} values indicates that the binding and internalization of the reaction substrates is at least 4 times faster than the subsequent conformational change that might lead to flavin release.

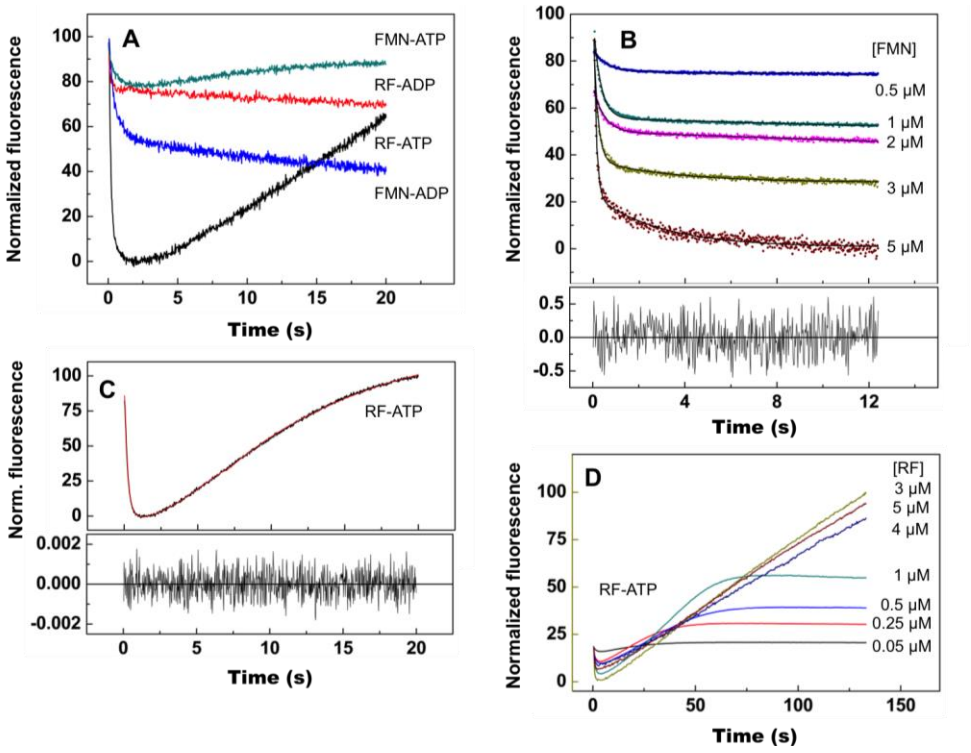

Figure 7.2. Pre-steady state stopped-flow kinetics for the binding of flavins to *Spn*FADS in the presence of adenine nucleotides. (A) Kinetic traces for the flavin fluorescence evolution upon mixing the protein (0.2 μM) with RF (1 μM) at saturating ATP (250 μM) or ADP (250 μM), as well as with FMN (1 μM) at saturating ATP (250 μM) and ADP (250 μM). (B) Evolution of kinetic traces for FMN fluorescence when *Spn*FADS is mixed in the presence of 250 μM ADP with increasing FMN concentrations. Traces are fit to a mono-exponential decay with steady-state. Residual is shown at the bottom for fitting of the 2 μM FMN trace. (C) Dissection of the exponential processes for kinetic traces observed upon mixing the *Spn*FADS (0.2 μM) at saturating ATP (250 μM) with RF (1 μM). The panel shows the fit to a two exponential process. Fitting residual is shown at the bottom. (D) Evolution of kinetic traces when mixing *Spn*FADS (0.2 μM) at saturating ATP (250 μM) with increasing RF concentrations. All the experiments were carried out in the stopped-flow equipment at 25°C in 20 mM PIPES, 0.8 mM $MgCl_2$, pH 7.0. All concentrations indicated are final ones in the mixing cell.

Finally, since k_{on} and k_{off} values obtained for processes involving RF and ATP, are in the range of the k_{cat} for the RF phosphorylation (~50 min^{-1}), both of the observed processes are relevant for catalysis.

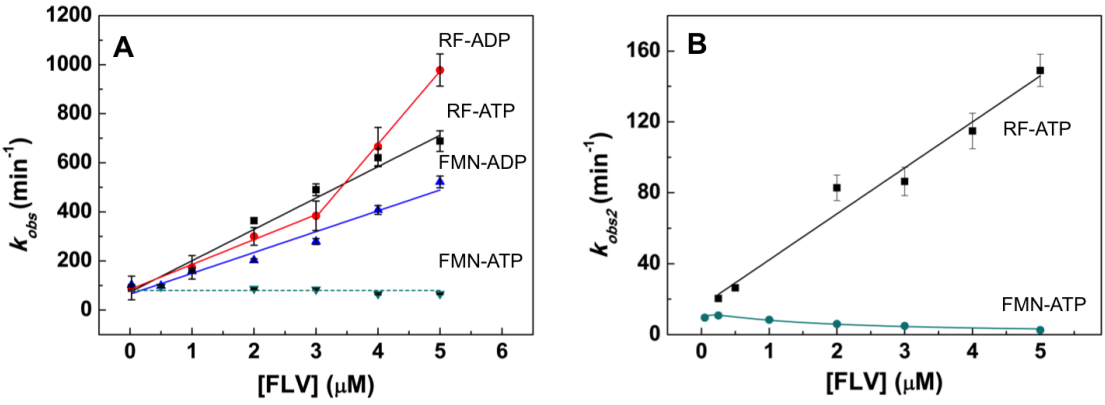

Figure 7.3. Dependence of the pre-steady-state observed rates on the flavin ligand concentration. (A) Evolution of k_{obs1} for the mixing of *Spn*FADS with RF-ATP (black), RF-ADP (red), FMN-ADP (blue) and FMN-ATP (green). For those data showing linear dependences slopes are related with the k_{on} for the binding and the independent term with the k_{off}. (B) Evolution of k_{obs2} values on the flavin concentration for mixtures of *Spn*FADS with (A) RF+ATP (black) and with (B) FMN+ATP (green). k_{obs2} exhibits a linear dependence on the RF concentration, while in the case of FMN shows a biphasic behavior with a maximum at 0.25 μM. Experimental conditions as in Fig. 7.1.

3. Thermodynamics of the interactions of *Spn*FADS with its ligands

Then we performed ITC experiments to determine whether the processes identified in our pre-steady state kinetic study were relevant to reach the thermodynamic equilibrium. We titrated with the substrates and the products of the RFK reaction, both free *Spn*FADS and its binary mixtures with either ANP or FLV ligands. These experiments provided us with the dissociation constant (K_d), the protein fraction available to bind the ligand (N), as well as with Gibbs free energy (ΔG), enthalpy (ΔH) and entropy (-T ΔS), for each interaction (Table 7.3, Figs. 7.4 and 7.5). The titrations were performed both in the presence of 0.8 mM $MgCl_2$, Mg^{2+} concentration at which the RFK activity of *Spn*FADS shows its maximum activity (Fig. 6.4), and in the absence of the divalent cation, to avoid catalysis in those titrations that involve both reaction substrates (the reaction heat would mask the binding enthalpy). Fig. 7.4 illustrates all the possible interactions pathways of *Spn*FADS with substrates and products of the RFK reaction, as well as the protein fraction prone to interact with a specific ligand (N) as the thickness of the arrows.

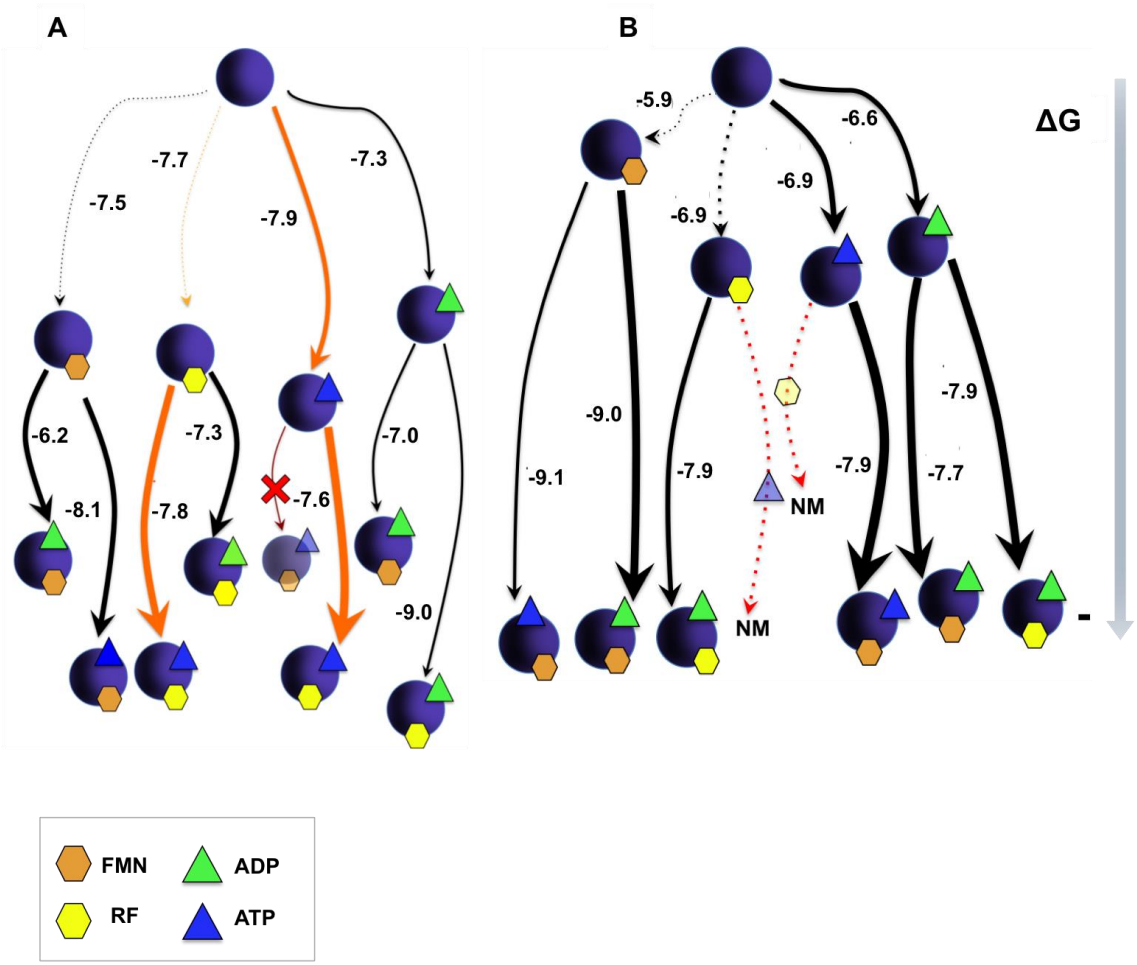

Figure 7.4. Free Gibbs energy diagrams for the interaction of *Spn*FADS with its ligands. Diagrams resuming the thermodynamic flow representing the interaction of the RFK module and the different combinations of its ligands as obtained by ITC at 20 ºC in (A) in 20 mM PIPES, pH 7.0 and (B) in 20 mM PIPES, 0.8 mM $MgCl_2$, pH 7.0. *Spn*FADS is shown as violet spheres, RF and FMN as yellow and orange hexagons respectively and ATP and ADP as blue and green triangles respectively. Numbers indicate the ΔG value in Kcal/mol for each titration. Thickness of the arrows is proportional to the fraction of protein able to bind the ligand in each case, and the length of the lines is related to the ΔG value associated to each process. Dashed lines indicate processes not observed directly by ITC but whose values are indirectly estimated once known the cooperativity coefficients. Orange lines indicate the paths leading to the simultaneous binding of both substrates of the RFK activity in the absence of Mg^{2+}. NM accounts for processes where the heat exchanged in the catalytic reaction masks the interaction heat.

Table 7.3. Thermodynamic interaction parameters for the combination of *Spn*FADS with different ligands as obtained through ITC. Column named initial mixture indicates the starting composition of the calorimetric cell. Titrations were carried out at 20ºC in 20 mM PIPES, pH 7.0 (upper table) and in 20 mM PIPES, pH 7.0, 0.8 mM $MgCl_2$ (lower table). Errors in ΔG, ΔH and $-T\Delta S$ were estimated in ± 0.3 kcal/mol, taken in general larger than the standard deviation between three replicates and the numerical error after fitting analysis.

0.0 mM $MgCl_2$

Initial mixture	Ligand		K_d (μM)	ΔG (kcal/mol)	ΔH (kcal/mol)	$-T\Delta S$ (kcal/mol)
*Spn*FADS	ATP		1.7	-7.9	-19.1	11.2
*Spn*FADS	ADP		4.1	-7.3	-12.9	5.5
*Spn*FADS	RF		n.d.[a]	n.d.[a]	n.d.[a]	n.d.[a]
*Spn*FADS	FMN		n.d.[a]	n.d.[a]	n.d.[a]	n.d.[a]
*Spn*FADS:RF	ADP		4.6	-7.3	-4.8	-2.5
*Spn*FADS:RF	ATP	(1)	0.32	-8.9	-17.6	8.8
		(2)	2.0	-7.8	-9.3	1.5
*Spn*FADS:FMN	ADP		27.7	-6.2	-25.6	19.4
*Spn*FADS:FMN	ATP		1.2	-8.1	-15.6	7.5
*Spn*FADS:ATP	FMN		n.d.[a]	n.d.[a]	n.d.[a]	n.d.[a]
*Spn*FADS:ATP	RF		2.5	-7.6	-1.9	-5.7
*Spn*FADS:ADP	FMN		7.9	-7.0	-21.9	14.9
*Spn*FADS:ADP	RF		0.3	-9.0	-17.2	8.2

0.8 mM $MgCl_2$

Initial mixture	Ligand	K_d (μM)	ΔG (kcal/mol)	ΔH (kcal/mol)	$-T\Delta S$ (kcal/mol)
*Spn*FADS	ATP	8.1	-6.9	-11.8	4.9
*Spn*FADS	ADP	14.2	-6.6	-7.0	0.4
*Spn*FADS	RF	n.d.[a]	n.d.[a]	n.d.[a]	n.d.[a]
*Spn*FADS	FMN	n.d.[a]	n.d.[a]	n.d.[a]	n.d.[a]
*Spn*FADS:RF	ATP [b]	n.m.	n.m.		
*Spn*FADS:RF	ADP	1.7	-7.9	-17.1	9.2
*Spn*FADS:FMN	ADP	0.24	-9.0	-7.8	-1.2
*Spn*FADS:FMN	ATP	0.23	-9.1	-17.1	8.1
*Spn*FADS:ATP	FMN	1.6	-7.9	-6.0	-1.9
*Spn*FADS:ATP	RF [b]	n.m.	n.m.		
*Spn*FADS:ADP	FMN	2.3	-7.7	-8.1	0.4
*Spn*FADS:ADP	RF	1.6	-7.9	-6.9	-1.0

[a] n.d. Not detected. Not heat of interaction was detected for this titration. [b] n.m. Not measured. This combination of ligands in the presence of Mg^{2+} leads to the catalytic reaction, preventing determination of binding heats

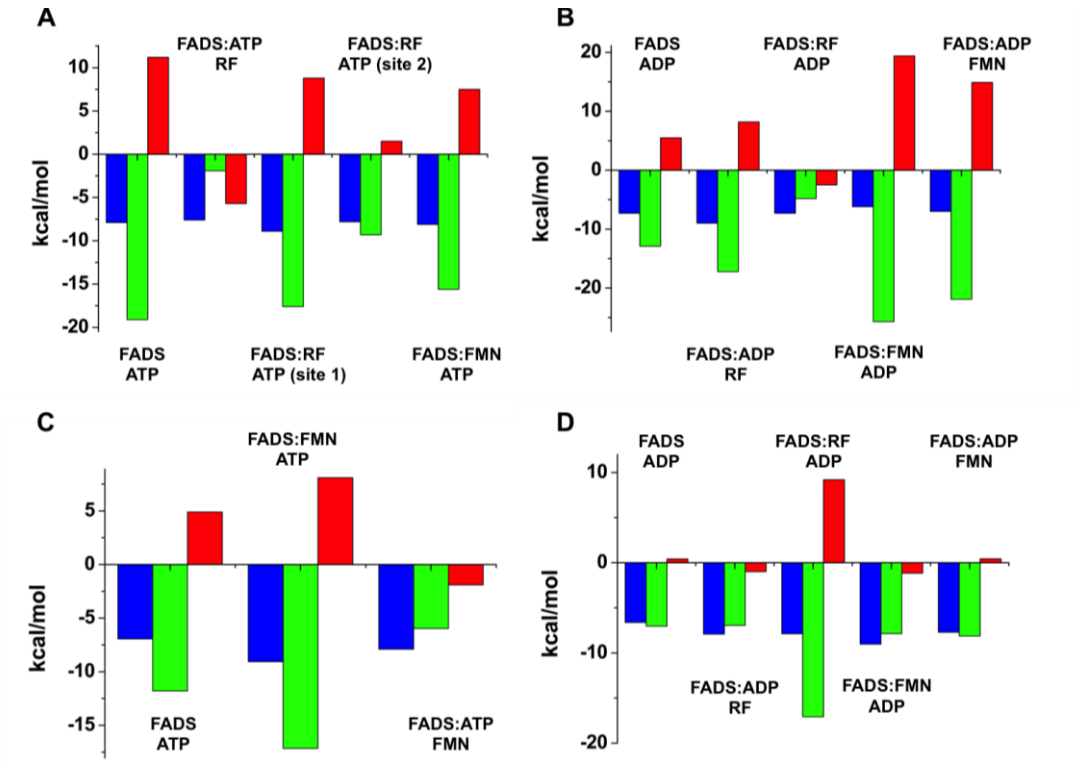

Figure 7.5. Thermodynamic dissection of the interaction of different ligands with either free *Spn*FADS, or with preformed mixtures of the protein with different ligands (indicated as FADS:X). Measurements were performed in 20 mM PIPES, pH 7.0 (A and B) and in 20 mM PIPES, 0.8 mM $MgCl_2$, pH 7.0 (C and D). The binding Gibbs energy (ΔG), enthalpy (ΔH), and entropy ($-T\Delta S$) contributions to the binding are represented in blue, green and red bars, respectively.

Several aspects are highlighted when evaluating these results. First, paths in the presence and in the absence of $MgCl_2$ considerably differ. The divalent cation alters both the stability of the complexes and the protein fraction binding a specific ligand. Mg^{2+} makes highly more favorable the formation of all ternary complexes but the *Spn*FADS:RF:ADP one, and considerably destabilizes *Spn*FADS:ANP binary complexes. Stabilization of ternary complexes by Mg^{2+} is mainly a consequence of the less unfavorable, or even favorable, entropic contributions to the binding (Fig. 7.5, Table 7.3). The cation also increases the amount of protein prone to interact and, consequently, the probability of a particular path to occur. All these data suggest different conformations in binary and ternary complexes with and without $MgCl_2$. As shown in chapter 6, binding of FLV ligands to the free protein is not directly observed either with or without Mg^{2+}. Nevertheless, the presence of the FLV ligands considerably modifies the affinity of the protein for the ANP ligands when Mg^{2+} is in the reaction

medium, and only slightly alters it in the absence of the cation (compare in Fig. 7.4B, the *ΔG* values for the titration of the free protein with ANP ligands with those for *Spn*FADS:FLV complexes). In that way, *ΔG* values for FLV binding to *Spn*FADS can be indirectly estimated [183, 187]. These results suggest that FLV ligands bind the protein either without an appreciable enthalpy change or too slowly (and in that case flavins act as slow binding ligands) to detect their binding within the experimental time [215].

4. FLV and ANP ligands show cooperative effects in their binding to *Spn*FADS

The presence of FLV ligands modifies the binding of ANP ones to *Spn*FADS, and *vice versa* (compare titrations with a particular ligand, of the free protein and of binary complexes, Fig. 7.4 and Table 7.3). Two facts are especially remarkable regarding these observations; ANP ligands facilitate the FLV binding to *Spn*FADS (no FLV binding is detected in the absence of ANP), and RF induces ATP binding to a second site (upper part of Table 7.3). To further analyze these cooperative effects, we fit the thermograms for titrations of *Spn*FADS:FLV mixtures with ANP to a home-derived model (Fig 7.6) [187], that considers the reciprocal effect between ANP and FLV ligands. This allows us to calculate cooperativity coefficients (α), the protein fraction able to bind the titrating ligand (N), and the enthalpy change associated to each process (*Δh*) (Table 7.4). This model also allows inferring association constants for the FLV binding to *Spn*FADS (K_a^{FMN} and K_a^{RF}), and subsequently the *ΔG* values for the formation of the *Spn*FADS:FLV binary complexes that could not be directly determined (dashed lines in Fig. 7.4).

As α values show (Table 7.4), cooperativity between ligands highly depends on the presence of Mg^{2+}. In its absence, the affinity of *Spn*FADS for the ANP ligands is, in general, only slightly affected by the RF or FMN presence. In this way, FMN barely favors ATP binding to the enzyme, as the α value hardly higher than 1 indicates (upper part of Table 7.4). In addition, both FLV ligands only slightly hinder ADP binding (α < 1), having FMN a more negative impact. This agrees with ANP nucleotides binding preferably to the FMNAT active site in the absence of the cation (as discussed in Chapter 6, section 4).

Special attention requires the cooperative binding of the substrates of the reaction. RF induces the formation of a second binding site for ATP, even in the absence of

$MgCl_2$, but it does not alter the ATP binding to the site existing in the absence of the flavin (compare in Table 7.3 the titrations with ATP in the presence and in the absence of RF).

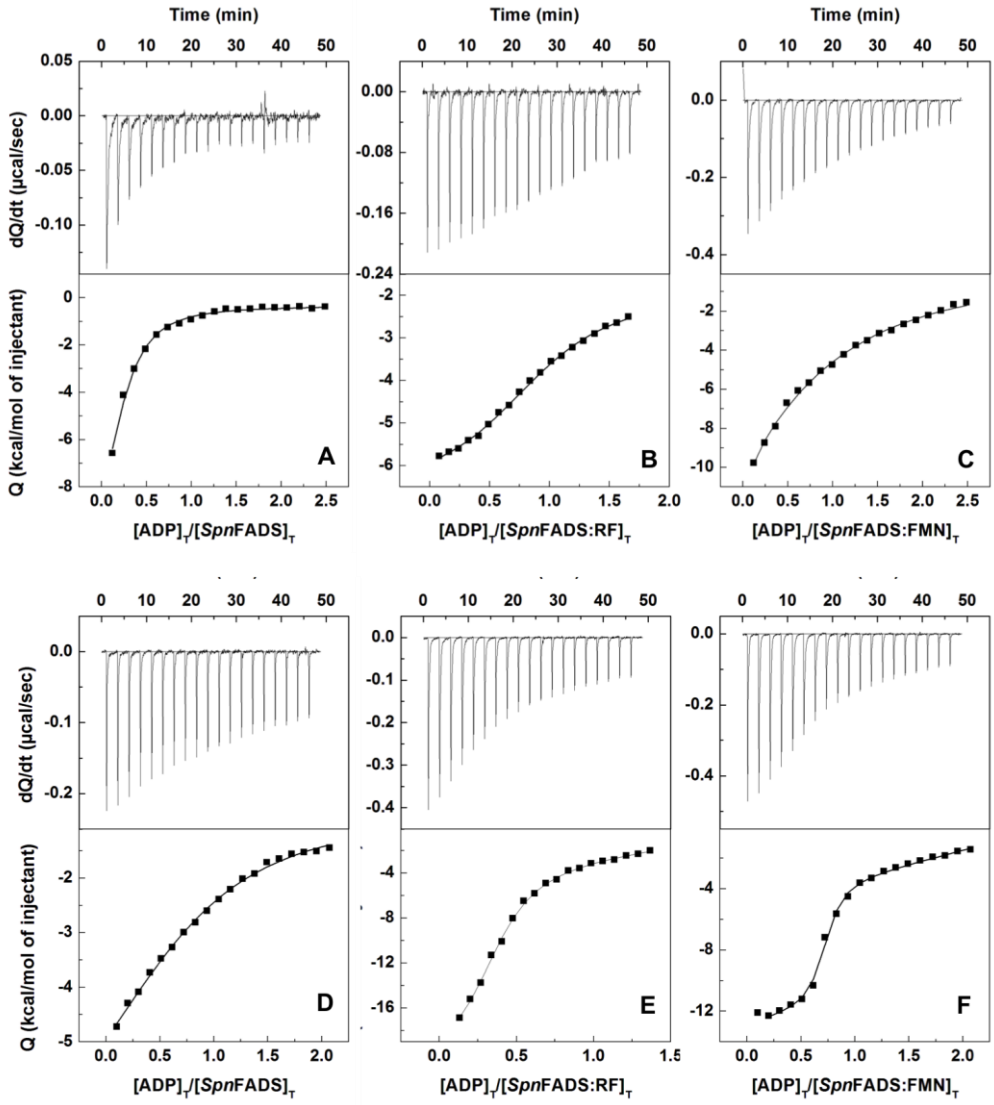

Figure 7.6. Calorimetric titrations with ADP of free *Spn*FADS, and of binary *Spn*FADS-FLV mixtures. (A, D) Titrations of the free protein with ADP. (B, E) titrations of *Spn*FADS-RF mixtures with ADP, (C, F) titrations of SpnFADS-FMN mixtures with ADP. Experiments were performed at 20ºC, in 20 mM PIPES, pH 7.0, without Mg^{2+} (A, B and C), and in the presence of 0.8 mM $MgCl_2$ (D, E and F). The concentration of *Spn*FADS was 25 µM in all the experiments, being the ADP concentration 300 µM (A, B and C) or 250 µM (D, E and F). In titrations of the preformed mixtures of *Spn*FADS with flavin ligands, these were included at saturating concentrations (200 µM RF or 250 µM FMN) with the protein in the sample cell. Data were fit to a home-derived model for a single binding site. Within each panel, upper charts show thermograms for the different interactions and the lower panels the corresponding binding isotherms with integrated heats.

Table 7.4. Cooperativity coefficients (α) for the binding of the different combinations of FLV and ANP ligands to *Spn*FADS. Experiments were carried out at 20°C in 20 mM PIPES, 0.8 mM $MgCl_2$, pH 7.0, or in 20 mM PIPES, pH 7.0. α is the cooperativity coefficient between each pair of ligands, n the fraction of total protein able to bind the titrating ligand and Δ*h* the enthalpy change associated to each process. Errors were taken in general larger than the standard deviation between replicates and the numerical error after fitting analysis.

	Ligands	**α**	**n**	**Δ*h*** **(kcal/mol)**
0 mM $MgCl_2$	FMN-ADP	0.35 ± 0.06	0.40 ± 0.03	-58 ± 3
	FMN-ATP	1.3 ± 0.2	1.1 ± 0.1	-0.2 ± 0.05
	RF-ADP	0.7 ± 0.1	0.9 ± 0.1	2.1 ± 0.1
	RF-ATP[a]			
0.8 mM $MgCl_2$	FMN-ADP	24 ± 4	0.70 ± 0.01	-3.9 ± 0.4
	FMN-ATP	34 ± 4	1.0 ± 0.1	-2.4 ± 0.2
	RF-ADP	5.2 ± 0.8	0.40 ± 0.01	-15 ± 1

[a] Not aplicable

5. Discussion

Regardless of overall structural similarities between *Spn*FADS and *Ca*FADS, they differ in the conformation of structural elements located at the RFK module, such as the PTAN motif and the loops L2c, L3c and L4c (Fig. 7.7), and in the lack of RF substrate inhibition at the RFK activity of *Spn*FADS. Moreover, contrary to *Ca*FADS, *Spn*FADS requires reduced flavins for their binding and transformation in its FMNAT site. Taking advantage of this last observation, we are here able to characterize the mechanism of the RFK activity in *Spn*FADS, by kinetically and thermodynamically analyzing the binding of its ligands (substrates and products), as well as their potential as modulators of the activity. In addition, similar data available for the RFK module of *Ca*FADS are used to explain different behaviors along the RFK activity of these two bacterial FADSs.

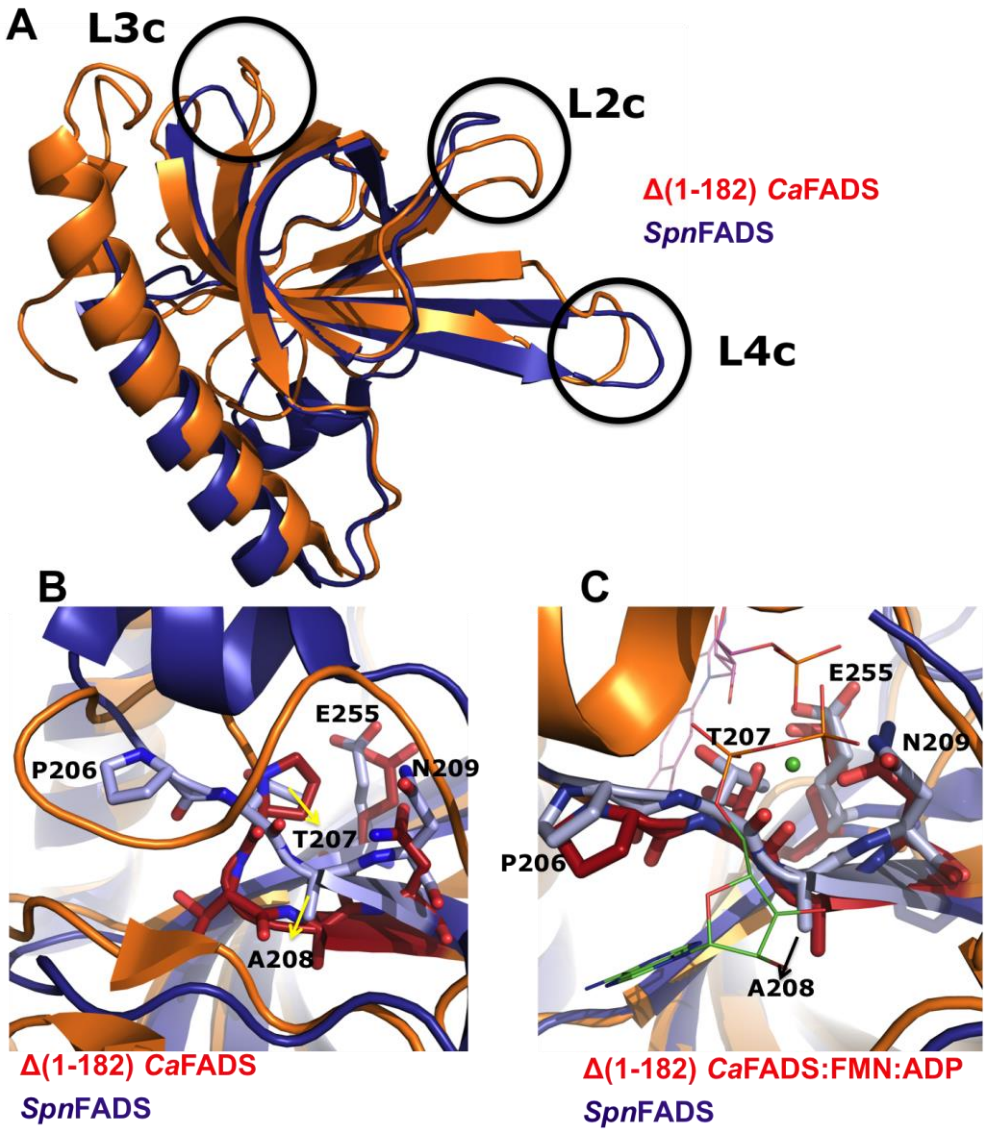

Figure 7.7. Structural alignment of the C-terminal modules of *Ca*FADS (PDB 2x0k) and *Spn*FADS (PDB 3op1). (A) Superposition of the overall structures of the RFK modules of *Spn*FADS (blue) and *Ca*FADS (orange). (B) Zoom into the PTAN consensus motif residues and the E255 putative catalytic base of *Spn*FADS (shown in CPK code, with carbons in light blue), corresponding residues in *Ca*FADS are also shown (CPK code, with carbons in red). (C) Comparison of the conformation of the PTAN motif in *Spn*FADS (CPK code, with carbons in light blue) and in the Δ(1-182)*Ca*FADS:FMN:ADP-Mg^{2+} ternary complex (PDB entry 5a89, CPK code, with carbons in red).

Mg^{2+} plays a key role in the binding of adenine and flavin nucleotides to SpnFADS

Our ITC thermodynamic parameters reveal that Mg^{2+} is key in the formation of *Spn*FADS:ANP:FLV ternary complexes (Figs. 7.4 and 7.6, Table 3). The cation increases the protein fraction prone to interact with a determined ligand, and favors the

formation of ternary complexes from the binary ones (compare Fig. 7.4A and 7.4B). This last point is related to the cooperativity enhancement between ANP and FLV ligands in the presence $MgCl_2$ (compare α values on upper and lower Table 7.4). Figure 7.8 shows the products of the RFK activity modeled [99] on RFK active site of *Spn*FADS. Contrary to that reported for *Ca*FADS, allocation of these ligands does not require major reorganizations in the free RFK active site (Fig. 7.8). Interestingly, our data show that Mg^{2+} has a negative impact in the stabilization of the binary complexes of the protein with ANP ligands, and especially with ATP (Fig. 7.4, Table 7.3). This fact appears *a priory* counterproductive for catalysis. However, it might have the opposite effect when considering the formation of the catalytically competent *Spn*FADS:RF:ATP-Mg^{2+} ternary complex. In this way, destabilization of the *Spn*FADS:ATP-Mg^{2+} complex increases the Gibbs free energy difference between the binary and the ternary complexes, making thermodynamically more favorable the formation of the last one.

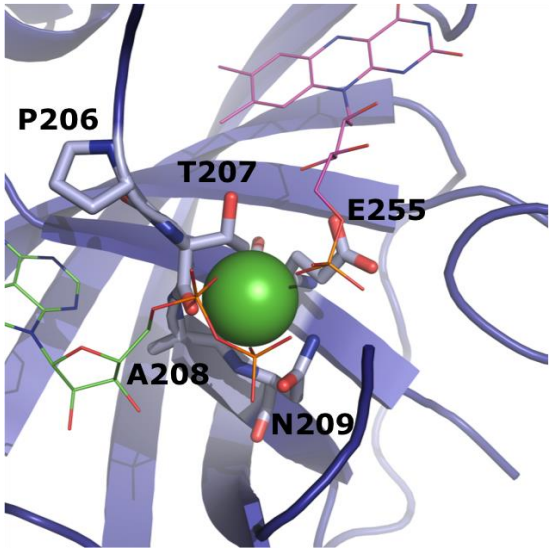

Figure 7.8. Detail of a structural model for the PTAN motif of *Spn*FADS in complex with FMN and ADP. The substrates of the RFK reaction are allocated as in the crystal structure of the Δ(1-182)*Ca*FADS:FMN:ADP-Mg^{2+} ternary complex. The residues are highlighted in sticks and colored in CPK code, with the carbons in light blue. FMN and ADP ligands are shown in lines colored in CPK code, with the carbons in purple and green, respectively. The Mg^{2+} cation is shown as a green sphere.

Considering now the Mg^{2+} effect on binding of FLV ligands to the free *Spn*FADS, the following conclusion can be extracted. Although we are not able to directly observe it, neither by stooped-flow nor by ITC, both RF and FMN are able to someway bind to

*Spn*FADS in the presence of the cation. This fact is evident through comparison of the *ΔG* values obtained when titrating with ANP ligands the free protein, and the binary *Spn*FADS-FLV mixtures. The large differences in *ΔG* (from -1.3 to -2.4 kcal/mol) can only be due to a cooperative effect of the FLV ligand previously interacting with the protein, specifically with the RFK module. These titrations also allow us to indirectly calculate, in addition to *ΔG* values (Fig. 7.4B), the *ΔH* for RF and FMN binding (-5.7 and -3.5 kcal/mol, respectively). This stabilizing effect of $MgCl_2$ was also reported for the ternary complexes of the *Ca*FADS RFK module with its flavin and adenine nucleotide ligands (Chapter 5).

The RFK catalytic cycle of SpnFADS

Taken together our kinetic and thermodynamic data allow shedding light on some aspects of the RFK catalytic cycle of *Spn*FADS, identifying similarities with the *Ca*FADS corresponding cycle, and highlighting differences. Stopped-flow experiments reveal that the presence of ANP is a requirement for FLV ligands binding and/or internalization (no FLV binding is observed in the absence of ANP). Thus, the initial abrupt decrease in fluorescence, observed upon mixing FADS with mixtures of ANP and FLV ligands is related to this process. In *Ca*FADS this fluorescence decrease was identified as the flavin internalization produced by the conformational change of L4c subsequent to the binding of FMN and ADP (Chapter 5). In the case of *Spn*FADS, we can reach the same conclusion. Nonetheless, the relative rate at which the different ANP-FLV mixtures bind the FADSs differs between both proteins. Binding of substrates of the RFK reaction (ATP:RF) is the fastest process for *Spn*FADS, but the slowest one for *Ca*FADS (Table 7.2). This fact, together with the high difference in the values of K_i^{ADP} for both proteins (approximately 10 times higher for *Ca*FADS), and in the K_i^{FMN}/K_m^{RF} ratio (~1 and 0.2, for *Spn*FADS and *Ca*FADS, respectively) might explain the larger inhibition by the products of the reaction observed for *Ca*FADS than for *SpnFADS*. Another important difference between both proteins appears when comparing k_{obs2} values (Figs. 7.3 and 5.5), which have been identified as an ATP-induced conformational change in both FADSs. During the RFK reaction of *Ca*FADS such conformational change results inhibited by increasing RF concentrations, while such inhibition is not detected for *Spn*FADS. That might be a determinant factor in the inhibition by the RF substrate that *Ca*FADS shows, and *Spn*FADS does not.

Considering all these data, we can conclude that although the steps occurring during the RFK reaction of *Ca*FADS and *Spn*FADS are the same, their rates differ. The final consequence of these differential behaviors is inhibition by products being less relevant at the kinetic level (both by RF and by the products of the reaction) in *Spn*FADS.

Differences in the inhibition of the SpnFADS and CaFADS RFK activities can be thermodynamically explained

The thermodynamic data of the interaction of both proteins with all the substrates and the products of the RFK reaction also expose important differences. Similar *ΔG* diagrams can be established upon titration of the proteins with the substrates and the products of the reaction (Figs. 7.4 and 5.8), but important differences can be detected. The first noteworthy fact is that in Fig 7.4 two different paths lead to the "pseudoreactive" *Spn*FADS:RF:ATP ternary complex, while in *Ca*FADS this complex only can be reached through a single path. Apparently, RF cannot bind to the preformed *Ca*FADS:ATP complex, but it is able to bind to *Spn*FADS:ATP. This suggests that during the RFK catalytic cycles of both enzymes, the substrates get bound in different order. As described in chapter 5, the *Ca*FADS:RF:ATP catalytically competent complex is achieved through the concerted fit of the substrates, while *Spn*FADS seems to follow a random sequential binding of its substrates. Structurally, this important difference might be related to the simpler conformational changes postulated for *Spn*FADS to reach the ternary competent complex. Thus, Fig 7.7 shows the relative position of the PTAN motif in *Spn*FADS and *Ca*FADS (Fig. 7.7B), and in *Spn*FADS and *Ca*FADS:FMN:ADP (Fig. 7.7C). Remarkably, the position of this motif in *Spn*FADS resembles that of the *Ca*FADS ternary complex with the products of the RFK reaction. So, the conformational change of the PTAN motif, which is crucial for the RFK cycle of *Ca*FADS, is not necessary for *Spn*FADS, and this might allow some flexibility in the allocation order of the substrates in the active site of the latter enzyme.

Another important difference is the absence of specially stable *Spn*FADS:FLV:ANP complexes. *Ca*FADS establishes a highly stable ternary complex with FMN and ATP (Fig. 5.8), whose kinetic relevance was also discussed in chapter 5. Additionally to this complex, all the non-productive *Ca*FADS:FLV:ANP ternary complexes are more favored than the only *Ca*FADS:RF:ATP competent one. This situation is completely distinct in *Spn*FADS (Fig. 7.4), where the ternary complexes with RF and ATP are, together with *Spn*FADS:RF:ADP, the most stable ones. These dissimilar diagrams

involve important differences in the tendency of both enzymes to bind substrates or products, when the reaction draws on and the products start to accumulate. In that way, although FMN and ADP accumulate in the reaction media, *Spn*FADS would preferably bind the substrates of the reaction, and no inhibition would be detected, at least until reaching a high products/substrates ratio. *Ca*FADS shows the opposite behavior, and inhibition by products is quickly detected as soon as products accumulate.

Finally, *Spn*FADS and *Ca*FADS also exhibit dissimilarities in the cooperative binding of the substrates of the RFK reaction. Thus, as explained in chapter 5, RF and ATP show positive cooperativity during their binding to *Ca*FADS at low concentration of the flavin ligand, while high RF concentrations hinder ATP binding. This effect is not observed for *Spn*FADS, where RF and ATP have positive cooperativity at high RF concentration. This differential fact might explain the inhibition by the RF substrate that *Ca*FADS shows but not *Spn*FADS. Structurally, this effect might be also related with the conformation of the PTAN motif in both enzymes. In *Ca*FADS the occupation of the ANP binding site by a RF molecule might somehow prevent the ANP-Mg^{2+}-induced conformational change of the PTAN motif, and consequently the ATP binding. Nevertheless, the huge conformational change of the PTAN motif does not appear necessary for the ATP binding to *Spn*FADS, and therefore it might not be hindered by the RF excess.

Different organisms use distinct strategies to regulate flavin synthesis

FMN and FAD are involved in a huge amount of essential metabolic processes, acting as cofactors of flavoproteins and flavoenzymes [32, 33, 152]. Most bacteria are able to synthesize RF [220, 228], as well as to assimilate it from the extracellular media [58, 60, 220, 221]. Therefore, regulatory mechanisms to control RF transformation into FMN and FAD, when profusion of RF is produced, are required to maintain the flavin homeostasis. Having into account the data available for *Ca*FADS and *Spn*FADS, apparently different organisms use assorted strategies to regulate their FADSs. As discussed in the previous chapter, the FMNAT activity of *Spn*FADS only takes place with reduced FMN, which might constitute a regulatory point of the FAD synthesis in *S. pneumoniae*. This regulatory point is not observed in *Ca*FADS, whose FMNAT activity does not show any type of inhibition [90]. Consequently, and in agreement with our data, the RFK activity of *Ca*FADS might require a more carefully regulation by excess of substrates and products than the RFK activity of *Spn*FADS.

Such differences among members of the FADSs family might provide with a framework to design selective compounds targeting these enzymes for the treatment of some infectious diseases.

Chapter VIII
Discovery of antimicrobial compounds targeting bifunctional FAD synthetases

The emergence during the last decades of bacterial strains resistant antibiotics reveals the need to find new effective antibacterial targets, as well as compounds able to inhibit them. We propose prokaryotic bifunctional FADSs as exploitable drug targets. These proteins appear as a good option for several facts; i) the inhibition of FADSs avoids FMN and FAD synthesis, which prevent from the very beginning all the pathways that implicate flavoproteins and flavoenzymes [153, 154], ii) prokaryotic FADSs differ structurally and biochemically from the mammalian proteins that transform FMN into FAD [81, 88, 155, 229], so drugs that target these proteins are likely to be selective for bacteria [89], and iii) the availability of crystallographic structures of several bacterial FADSs facilitates the design of inhibitory drugs and activity assays [74, 75, 86].

In this chapter we present the results obtained for the activity-based HTS performed using the *Ca*FADS, as well as the subsequent characterization of the selected hits, their specificity, and their effect on the cellular growth of different bacterial strains.

1. Identification of Potential Inhibitors of the *Ca*FADS activities through HTS

Among the 1240 compounds of the chemical library, 140 (13.5 %) produced *Ca*FADS activity levels lower than the mean of the positive controls minus twice its standard deviation, and 37 (3.6 %) reduced the positive controls average rate for FAD formation in a factor higher than 0.5 (Fig. 8.1B). Those 37 compounds were selected as the primary HTS hits.

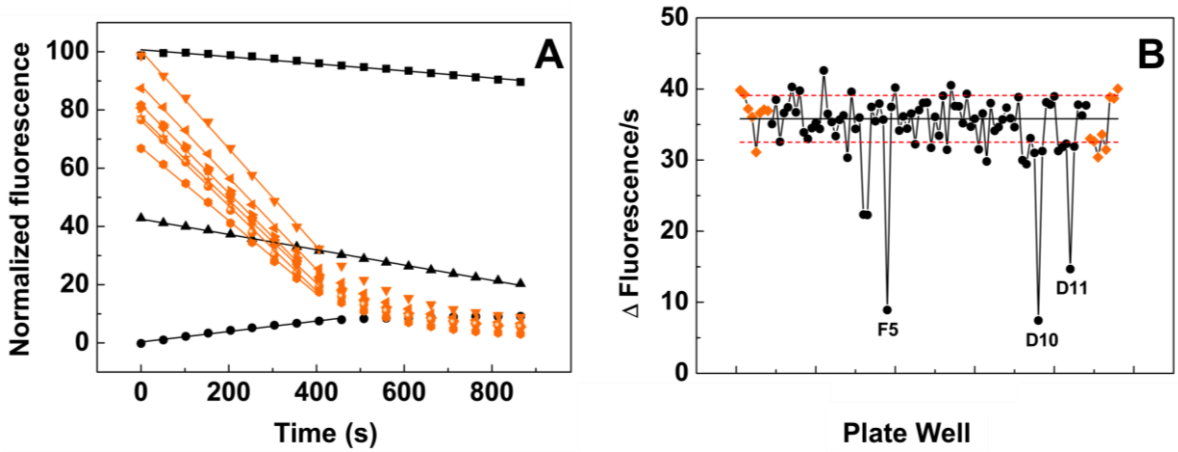

Figure 8.1. Activity-based high-throughput screening for the discovery of HTS hits inhibiting the RFK and/or the FMNAT activities of *Ca*FADS. (A) Example of the flavin fluorescence evolution over time for three of the identified hits (black) and for the controls of the assay (orange). Reaction mixtures were incubated at 25 °C and contained 5 µM RF, 50 µM ATP, 0.4 µM *Ca*FADS, 10 mM $MgCl_2$, in PIPES 20 mM, pH 7.0, 2.5 % DMSO, and when indicated (black symbols and lines) the corresponding compound of the library at 250 µM. (B) Initial velocities, determined as Δfluorescence/s, for the reactions in each of the wells of the HTS plates. Data from wells containing compounds of the chemical library are shown in black and those for controls in the absence of chemical library compounds are in orange. The solid line represents the average velocity obtained for the positive controls of the reaction and the dotted lines this average velocity minus and plus the standard deviation. The letters and numbers indicate the position of the well in the plate (row and a column respectively) for each specific selected measurement.

2. Effect of the HTS hits on RFK and FMNAT activities of *Ca*FADS

As indicated before, the FMNAT module of *Ca*FADS shares neither sequence nor structural homology with the corresponding mammal protein, while the RFK module belongs to the eukaryotic RFKs family. Therefore, we decided to continue the study with those HTS hits that inhibit the *Ca*FADS FMNAT activity, since they are more likely to be specific for the bacterial proteins. With this aim, we assayed the effect of the HTS hits both on the

*Ca*FADS RFK and FMNAT activities. Figure 8.2 and Table 8.1 summarize the results. Comparison of Fig. 8.2A and 8.2B shows that, in general and under the assayed conditions, HTS hits produced a stronger deleterious effect on the FMNAT activity (all decrease the activity of the controls in more than 50%) than on the RFK one. We choose to continue the study the HTS hits that decreased the FMNAT activity below 5 % of that of the controls, but maintained over 75% the RFK activity (Fig. 8.2, Table 8.1). Thus, among the 37 HTS hits, 9 compounds (C2, C11, C15, C17, C19, C24, C27, C31 and C43) were selected as FMNAT hits (Fig. 8.3).

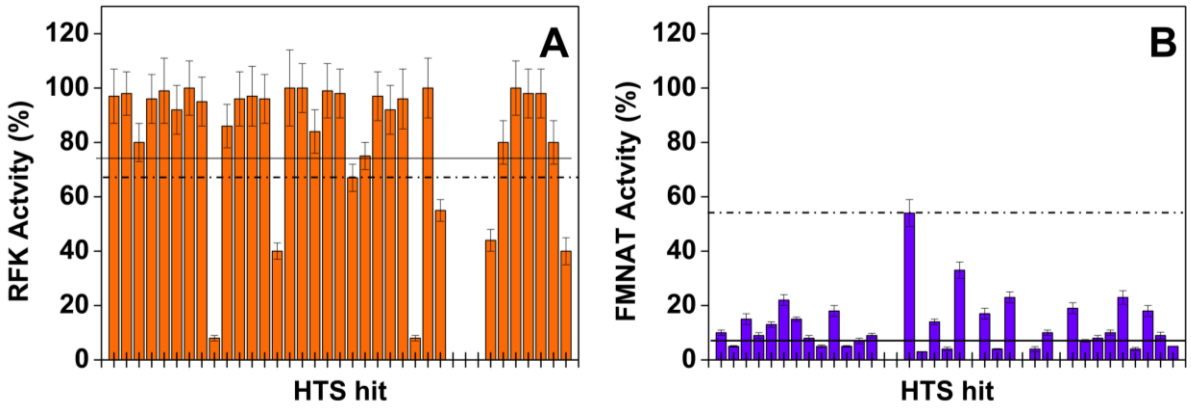

Figure 8.2. Effect of the HTS hits on the RFK and FMNAT activities of CaFADS. Residual (A) RFK activity and (B) FMNAT activity when assayed in the presence of 250 µM of the 37 HTS hits. In panel A, data below the dashed line show statistical significant inhibition ($p<0.002$, 67% remaining activity) for samples containing compounds regarding the control CaFADS RFK activity. In panel B, all hits produce statistical significant inhibition ($p<0.0001$, dashed line) when compared with the CaFADS FMNAT activity of controls in their absence. Solid lines indicate 75% and 5% of the control RFK and FMNAT activities, respectively. Those HTS hits displaying <5% of the control FMNAT activity and >75% of the control RFK one were selected to continue the study. Experiments were carried out in 20 mM PIPES, pH 7.0, 2.5 % DMSO at 25 ºC, with 7.5 µM RF, 350 µM ATP, 0.8 mM MgCl2 (for the RFK activity) or 15 µM FMN, 350 µM ATP, 10 mM MgCl2 (for the FMNAT activity) (n=3; mean ± SD).

Table 8.1. RFK and FMN residual activities of *Ca*FADS in the presence of HTS hits. Values measured at 25 ºC, in 20 mM PIPES, pH 7.0, 2.5 % DMSO, and 0.8 or 10 mM $MgCl_2$ when assaying the RFK or the FMNAT activities, respectively. The final concentration of each HTS compound was 250 µM and saturating concentrations of all the substrates were used. The compounds highlighted in black, which completely inhibited the FMNAT activity with minor effects on the RFK one, were selected as FMNAT hits to continue the study.

		% residual RFK activity			
		≤ 5	5-50	50-75	≥75
% residual FMNAT activity	≤ 5	C9, C29, C33, C37	C14, C47		**C2, C11, C15, C17, C19, C24, C27, C31, C43**
	5-50	C35	C38	C22, C32	C1, C3, C4, C5, C6, C7, C8, C10, C12, C13, C16, C18 C25, C28, C39, C40, C44, C46
	≥50	--	--	--	--

Table 8.2. Effect on the FMNAT activity of *Ca*FADS of the FMNAT hits. All the experiments were carried out at 25 ºC, in 20 mM PIPES, pH 7.0, 10 mM $MgCl_2$ at saturating concentrations of FMN and ATP. All samples contained 2.5% DMSO (n=3, mean ± SD).

FMNAT hit	**Residual activity[a] (%)**	**IC_{50}[b] (µM)**
C2	41.1 ± 5.2	8.9 ± 1.0
C11	34.6 ± 4.9	9.0 ± 1.3
C15	45.3 ± 4.2	40.7 ± 3.9
C17	33.5 ± 10.1	12.8 ± 3.4
C19	43.3 ± 3.9	20.8 ± 2.6
C24	3.6 ± 0.2	0.4 ± 0.1
C27	6.9 ±0.8	0.5 ± 0.1
C31	24.5 ± 1.9	6.6 ± 0.6
C43[c]	20.3 ± 5.2	1.0 ± 0.5

[a] Remaining activity in the presence of 50 µM of each compound. All data show statistical significance differences when compared with activity in the absence of compound (***, p<0.0001).
[b] Compounds assayed in the 0-100 µM concentration range.
[c] This compound shows very low water solubility, so it was discarded to continue the study even though its good properties.

To rate the power of these 9 FMNAT hits as inhibitors of the *Ca*FADS FMNAT activity, their IC_{50} values and the remaining activity at 50 μM of each compound, were determined (Fig. 8.4, Table 8.2). The 9 compounds yielded IC_{50} values in the micromolar range, reducing by over the half the activity of the controls. Considering both their IC_{50} value and residual activity, the more potent inhibitors were C24 (Chicago sky blue, IC_{50} = 0.4 ± 0.1 μM), C27 (Gossypol IC_{50} = 0.5 ± 0.1 μM) and C31 (Flunixin meglumine IC_{50} =6.6 ± 0.6 μM), the three of them producing residual activities below 25% of the controls ones. Compound C43 (oxaprozine) also showed high inhibitory potency, but due to its low solubility in the working buffer, it was discarded and only the effect of the three previous inhibitors was further characterized.

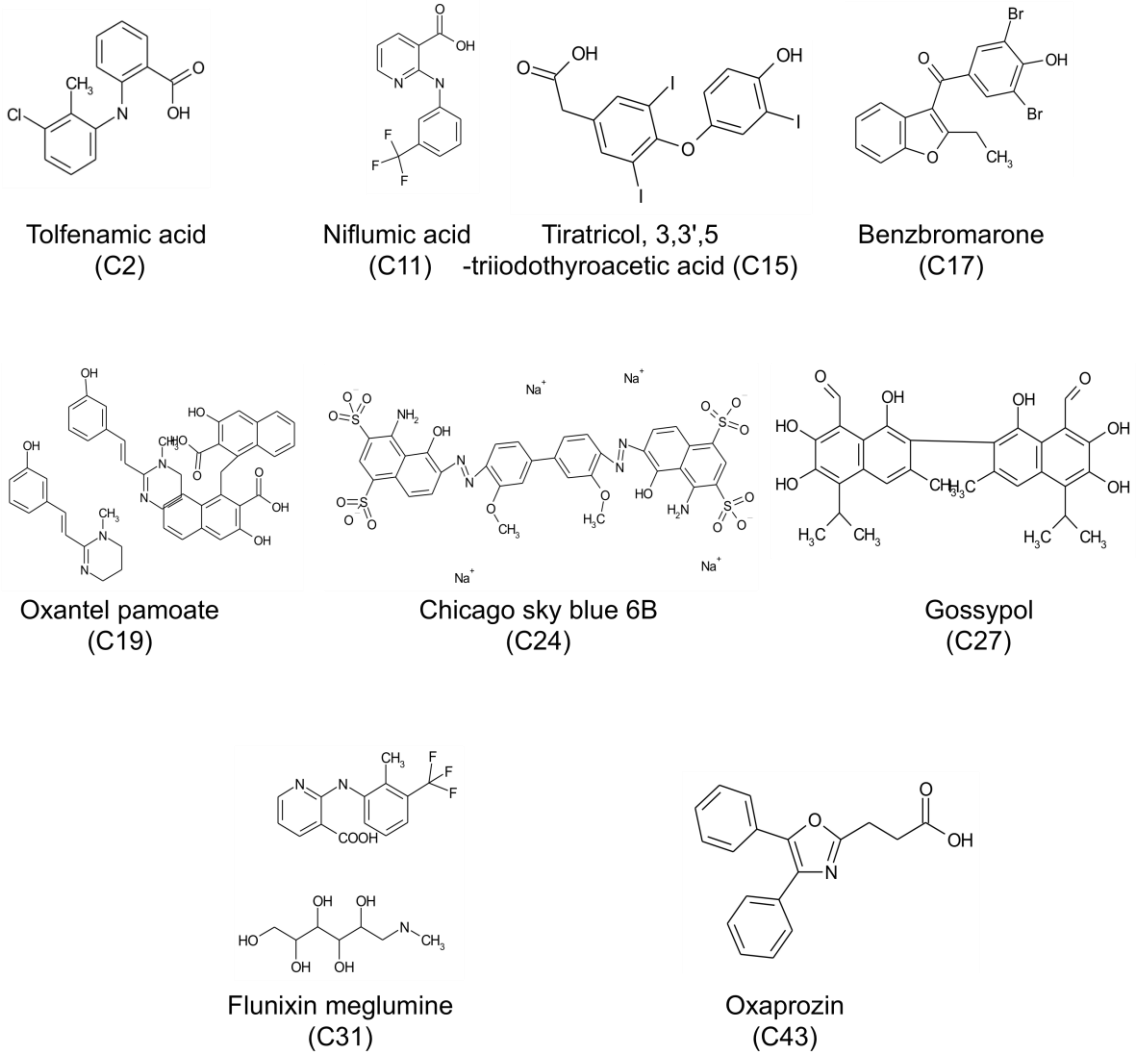

Figure 8.3. Chemical structures of compounds selected as FMNAT hits for *Ca*FADS.

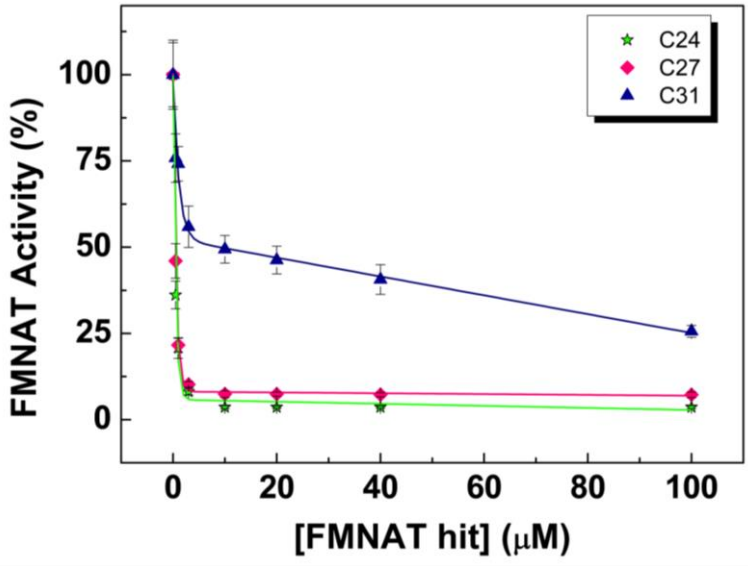

Figure 8.4. Dose-response curves for the FMNAT activity of *Ca*FADS in the presence of representative hits. IC_{50} values derived from these representations are included in Table 8.2. Experiments were performed at 25 ºC in 20 mM PIPES, pH 7.0, 10 mM $MgCl_2$, 2.5 % DMSO, with 15 μM FMN and 350 μM ATP (n=3, mean ± SD).

3. The Inhibition Mechanisms of C24, C27 and C31

To determine the inhibition mechanism of C24, C27 and C31, we measured the *Ca*FADS FMNAT activity in the presence of increasing concentrations of each of them, at i) saturating ATP concentration and a range of RF concentrations, and at ii) saturating RF concentration and increasing concentrations of ATP. Fitting of the experimental data to the Michaelis Menten equation (Figs. 8.5, 8.6, and 8.7, Table 8.3) allowed identifying the inhibitory mechanism of each hit. Additionally, through global fitting of Lineawever-Burk plots to a model that describes the corresponding inhibition mechanism, we obtained the inhibition constant/s (K_i or, K_i and K_i') for each compound (Table 8.4).

C24 inhibits *Ca*FADS in a non-competitive manner regarding the FMN (ATP saturating). Non-competitive inhibitors do not compete with the substrate of the reaction, since they bind to the enzyme at a position different from the substrate binding site. Therefore, k_{cat} decreases while K_m keeps constant because the inhibitor does not affect the affinity of the enzyme for the substrate (Fig. 8.5A and Table 8.3). Lineawever-Burk plots intercept on the negative part of the x-axis, which is also characteristic for non-competitive inhibitors, providing a K_i of 0.07 ± 0.01 μM (Table 8.4). On the other hand, regarding the ATP substrate (FMN saturating), C24 behaves as an uncompetitive inhibitor, which does not bind to the free enzyme but to a preformed enzyme-substrate complex resulting in a non-

catalytically competent complex. Through the law of mass action, this complex reduces the amount of free enzyme available to perform the reaction; therefore, both k_{cat} and K_m values are affected, and Lineawever-Burk plots run in parallel (Figs. 8.5C, 8.5D and Table 8.3). In this case, the K_i value for C24 was 0.08 ± 0.03 µM (Table 8.4).

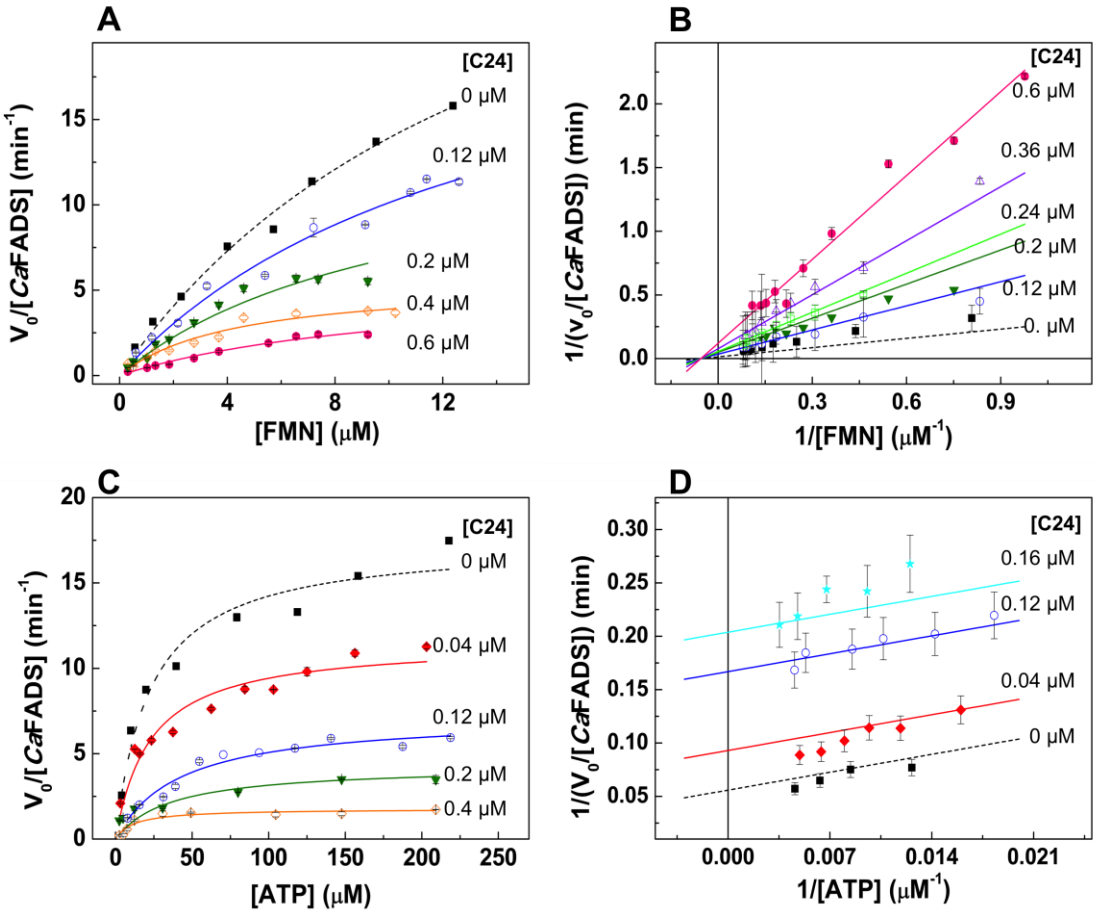

Figure 8.5. Hit C24 as inhibitor of the FMNAT activity of *Ca*FADS. Michaelis-Menten plots at different concentrations of C24 under obtained at saturation (A) of ATP and (B) of FMN. Lineaweaver-Burk representations with global fit to the equation for (C) non-competitive inhibition at saturating ATP and (D) for competitive inhibition at saturating FMN. Reaction rates were obtained in 20 mM PIPES, pH 7.0, 10 mM $MgCl_2$, 2.5 % DMSO, at 25 ºC, with 15 µM FMN and 10-450 µM ATP (FMN saturating) or with 350 µM ATP and 0.5-20 µM FMN (ATP saturating) (n=3, mean ± SD).

C27 also behaves as a non-competitive inhibitor regarding the FMN substrate. k_{cat} decreases and K_m does not significantly change, while Lineawever-Burk plots intercept on the negative part of the x-axis (Figs. 8.6A, 8.6B and Table 8.3). Regarding the ATP, C27 behaves as a competitive inhibitor (Lineawever-Burk plots intercept on the y-axis) (Fig. 8.6D), competing with this substrate for the active site of the *Ca*FADS FMNAT module. C27

reduces the affinity of the enzyme for ATP (K_m increases) while k_{cat} does not significantly change (Fig. 8.6C and Table 8.3). K_i values for C27, when acting as a FMN non-competitive and as an ATP competitive inhibitor, are 0.08 ± 0.01 μM and 0.06 ± 0.01 μM respectively (Table 8.4).

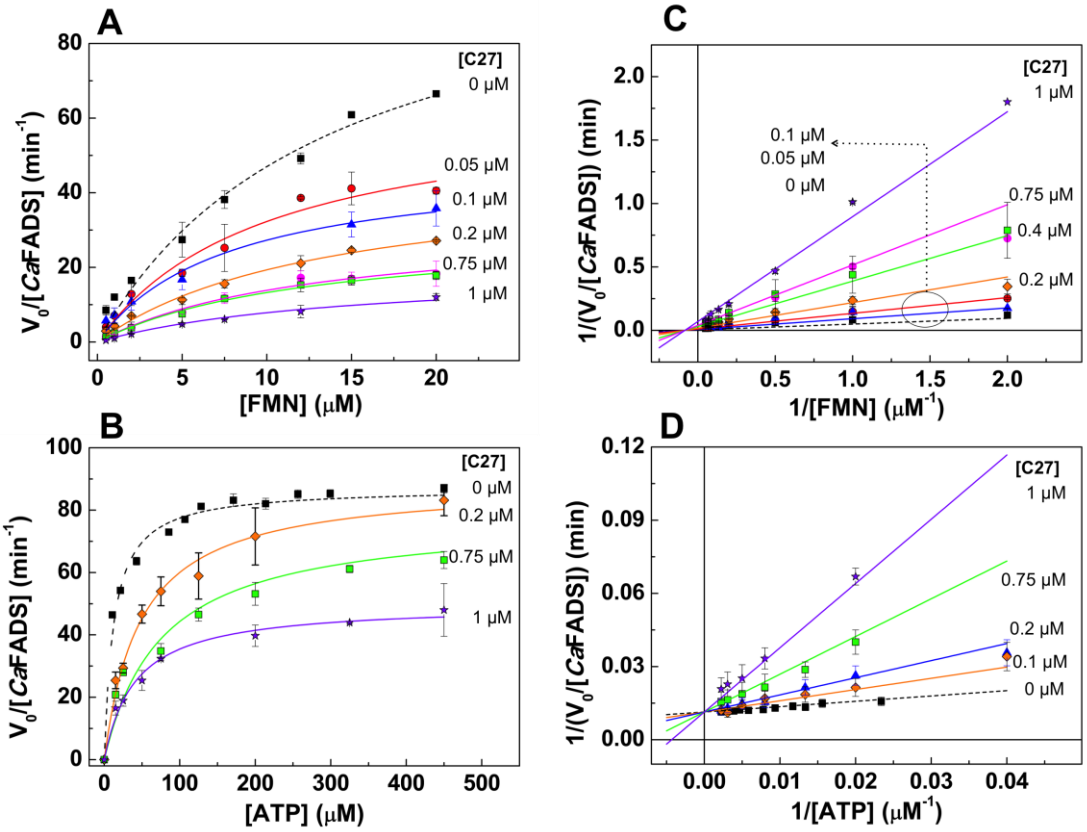

Figure 8.6. Hit C27 as inhibitor of the FMNAT activity of *Ca*FADS. Michaelis-Menten plots obtained at different concentrations of C27 under saturation (A) of ATP and (B) of FMN. Lineaweaver-Burk representations with global fit to the equation for (C) non-competitive inhibition at saturating ATP and (D) for competitive inhibition at saturating FMN. Reaction rates were obtained in 20 mM PIPES, pH 7.0, 10 mM $MgCl_2$, at 25 ºC, with 15 μM FMN and 10-450 μM ATP (FMN saturating) or with 350 μM ATP and 0.5-20 μM FMN (ATP saturating). All the samples contained 2.5% DMSO (n=3, mean ± SD).

C31 follows a similar inhibitory mechanism than C24 and C27 under ATP saturating conditions, being its K_i 0.09 ± 0.03 μM (Figs. 8.7A and 8.7B, Tables 8.3 and 8.4). Nevertheless, regarding the ATP substrate (FMN saturating), the inhibitory mechanism of C31 becomes more intricate. C31 acts as a mixed inhibitor. These inhibitors are able to bind both to the free enzyme and to an enzyme-substrate complex, reducing the k_{cat} and increasing the K_m (Fig. 8.7C and Table 8.3). Lineawever-Burk plots for mixed inhibition intercept at a negative value of the x-axis, but at the positive part of the y-axis and not on the x-axis (Fig.

8.7D). Although C31 is able to interact with *Ca*FADS and with the complex *Ca*FADS-ATP, it preferably binds to the free *Ca*FADS as its lower K_i value 3.5 ± 1.0 µM shows, being its K_i'18.4 ± 4.0 µM (Table 8.4).

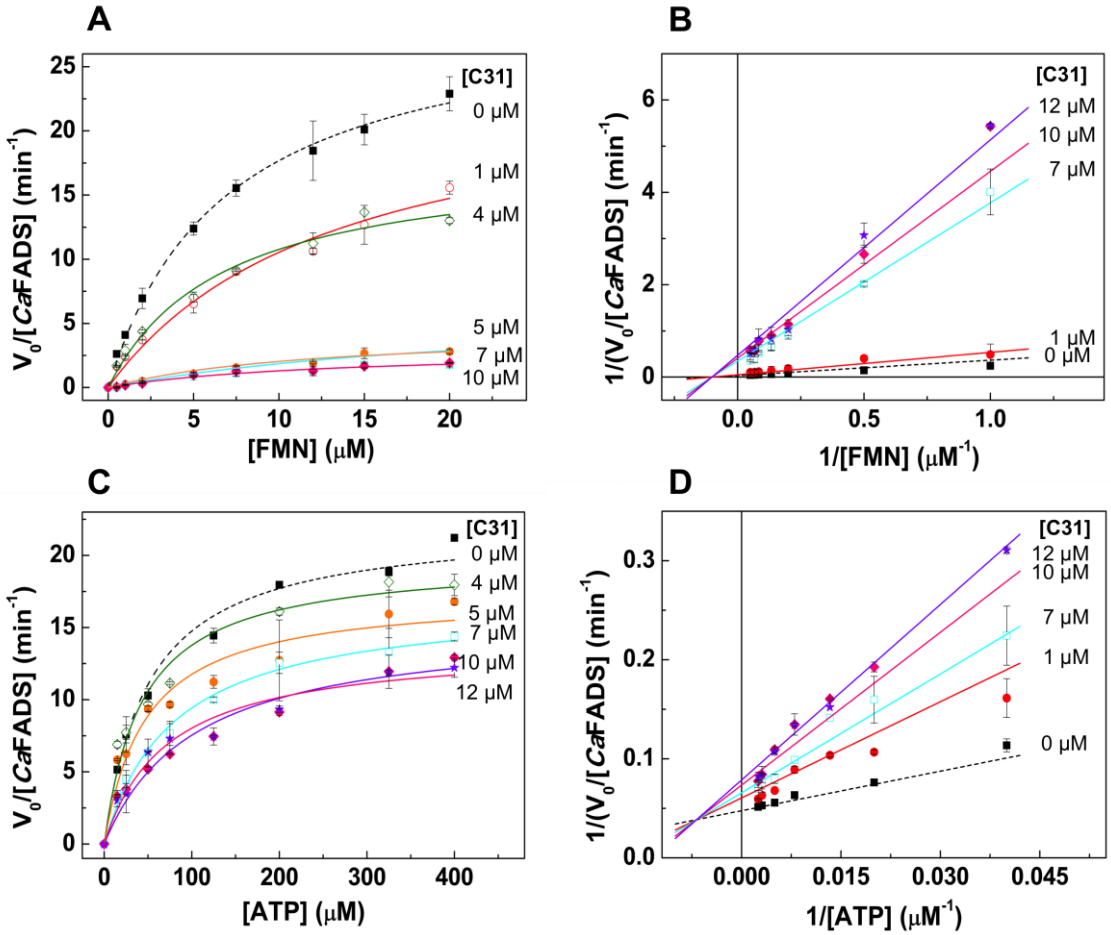

Figure 8.7. Hit C31 as inhibitor of the FMNAT activity of *Ca*FADS. Michaelis-Menten plots at different concentrations of C31 under saturation (A) of ATP and (B) of FMN. Lineaweaver-Burk representations with global fit to the equation (C) for non-competitive inhibition at saturating ATP, and (D) for competitive inhibition at saturating FMN. Reaction rates were obtained in 20 mM PIPES, pH 7.0, 10 mM $MgCl_2$, 2.5% DMSO, at 25 ºC, with 15 µM FMN and 10-450 µM ATP (FMN saturating) or with 350 µM ATP and 0.5-20 µM FMN (ATP saturating) (n=3, mean ± SD).

Table 8.3. Apparent kinetic parameters for the FMNAT activity of *Ca*FADS at different concentrations of the C24, C27 and C31 inhibitors. Data obtained at 25ºC in 20 mM PIPES, pH 7.0, 10 mM $MgCl_2$, 2.5% DMSO.

	Saturating ATP			Saturating FMN	
[C24] (µM)	**k_{cat} (min^{-1})**	**K_m (µM)**	**[C24] (µM)**	**k_{cat} (min^{-1})**	**K_m (µM)**
0	34 ± 3.8	16.3 ± 3.2	0	22.4 ± 0.7	29.4 ± 4.9
0.12	24.3 ± 4.1 [a]	14.0 ± 3.9	0.04	22.5 ± 4.8	11.5 ± 0.7 [a]
0.2	9.8 ± 1.3 [a]	10.6 ± 2.4	0.12	7.2 ± 0.4 [a]	42.1 ± 3.9 [a]
0.4	5.6 ± 0.6 [a]	4.3 ± 1.0 [a]	0.2	4.3 ± 0.4 [a]	35.8 ± 3.2
0.6	5.7 ± 1.3 [a]	11.1 ± 3.9	0.4	1.8 ± 0.1 [a]	12.0 ± 3.6 [a]

	Saturating ATP			Saturating FMN	
[C27] (µM)	**k_{cat} (min^{-1})**	**K_m (µM)**	**[C27] (µM)**	**k_{cat} (min^{-1})**	**K_m (µM)**
0	34 ± 3.8 [a]	16.3 ± 3.2	0	22.4 ± 0.7	29.4 ± 4.9
0.05	21.6 ± 2.9 [a]	10.1 ± 2.9	0.1	22.8 ± 1.3	59.7 ± 5.7 [a]
0.1	16.1 ± 1.7 [a]	7.7 ± 2.1	0.2	22.2 ± 1.4	48.2 ± 5.6 [a]
0.2	15.1 ± 1.5 [a]	13.5 ± 2.6	0.4	18.1 ± 1.6	51.8 ± 5.5 [a]
0.75	10.0 ± 0.8 [a]	12.8 ± 2.1	0.75	17.1 ± 3.3	51.5 ± 4.9 [a]
1	6.5 ± 0.2 [a]	15.0 ± 2.0	1	12.5 ± 0.5 [a]	40.9 ± 5.7

	Saturating ATP			Saturating FMN	
[C31] (µM)	**k_{cat} (min^{-1})**	**K_m (µM)**	**[C31] (µM)**	**k_{cat} (min^{-1})**	**K_m (µM)**
0	34 ± 3.8	16.3 ± 3.2	0	22.4 ± 0.7	29.4 ± 4.9
1	24.6 ± 2.9 [a]	13.3 ± 3.1	4	19.7 ± 1.0 [a]	43.3 ± 7.9
4	18.1 ± 1.4 [a]	6.8 ± 1.3	5	17.3 ± 1.1 [a]	47.5 ± 5.7 [a]
5	6.4 ± 1.2 [a]	24.4 ± 7.0	7	16.9 ± 0.6 [a]	79.1 ± 8.7 [a]
7	3.0 ± 0.4 [a]	13.3 ± 3.6	10	15.3 ± 1.3 [a]	103 ± 24 [a]
10	3.0 ± 0.4 [a]	12.3 ± 3.6	12	13.8 ± 1.0 [a]	92.1 ± 14.9 [a]

[a] Values showing statistically significant differences, $p < 0.002$, from the values in the absence of compounds, as determined by the one-way ANOVA test (n=3, confidence interval 95%).

Table 8.4. Kinetic parameters for the FMNAT activity of *Ca*FADS in the presence of the best FMNAT hits. Kinetic rates obtained at 25 ºC in 20 mM PIPES, pH 7.0, 10 mM $MgCl_2$, and in the presence of 2.5% DMSO. The kinetic parameters were calculated by globally fitting the experimental data to the corresponding Lineweaver-Burk inhibition model.

	Saturating ATP				**Saturating FMN**				
	k_{cat} **(min^{-1})**	K_m^{FMN} **(µM)**	K_i **(µM)**	**Inhibition Mechanism**	k_{cat} **(min^{-1})**	K_m^{ATP} **(µM)**	K_i **(µM)**	K'_i **(µM)**	**Inhibition Mechanism**
C24	75.5 ± 17.5	18.3 ± 4.0	0.07 ± 0.01	Non-competitive	13.4 ± 4.2	32.1 ± 9.8	0.08 ± 0.03	-	Uncompetitive
C27	87.1 ± 30.0	16.7 ± 6.2	0.08 ± 0.01	Non-competitive	21.8 ± 1.2	16.7 ± 6.2	0.06 ±0.01	-	Competitive
C31	29.8 ± 1.2	15.7 ± 5.2	0.09 ± 0.03	Non-competitive	21.0 ± 2.6	28.0 ± 9.0	3.5 ± 1.0	18.4 ± 4.0	Mixed

4. ITC constants for the *Ca*FADS interaction with C24, C27 and C31

The interaction of *Ca*FADS with C24, C27 and C31 was characterized using ITC. All the three compounds were able to bind the enzyme at, at least, one binding site (Fig. 8.8A, Table 4). *Ca*FADS presents a unique binding site of moderate affinity for C31 (N ≈ 1, K_d = 30.9 ± 2.8 μM), while shows two binding sites of high and equivalent affinity for C27 (N ≈ 2, $K_{d,av}$ = 0.7 ± 0.07 μM), as well as favorable enthalpic and entropic contributions to the binding. Therefore, parameters displayed in Table 8.5 for C27 are average values for both binding sites. The binding sites for C27 and C31 are expected to be located at the FMNAT domain of the enzyme, since that is the inhibited activity. The interaction between C24 and the enzyme resulted more complicated. C24 appears to bind to the protein at three sites, two of them equivalent and the third one independent from the other two. The two equivalents binding sites exhibit great affinity for C24 ($K_{d,av}$ = 1.1 ± 0.1 μM) and they are expected to be located at the FMNAT module of *Ca*FADS, while the third site is a low affinity binding site (K_d[a] = 161 ± 20 μM) and presumably it might be at the RFK domain, since C24 mildly inhibits this activity.

Table 8.5. Thermodynamic parameters for the interaction of *Ca*FADS with hits C24, C27 and C31. ITC experiments were performed at 25 ºC, in PIPES 20 mM, pH 7.0, 10 mM $MgCl_2$, 3% DMSO.

Compound		N	K_d (μM)	ΔG (kcal/mol)	ΔH (kcal/mol)	-TΔS (kcal/mol)
C24	Site 1	≈ 2	1.1 ± 0.1[a]	-8.1 ± 1.0[a]	-4.2 ± 0.5[a]	-3.9 ± 0.5[a]
	Site 2	≈ 1	161 ± 20	-5.2 ± 0.7	18.4 ± 2.2	-23.6 ± 1.9
C27		≈ 2	0.7 ± 0.07[a]	-8.4 ± 0.9[a]	-3.1 ± 0.05[a]	-5.3 ± 0.4[a]
C31		≈ 1	30.9 ± 2.8	-6.2 ± 0.6	-7.2 ± 0.4	1.1 ± 0.1

[a] These parameters correspond to average values for the binding of two hit molecules.

Regarding the enthalpic contributions to the binding free energy for the three different compounds; all of them (with the only exception of the low affinity binding site for C24, presumably at the RFK module) show favorable enthalpic contributions (Fig. 8.8B, Table 8.5). Negative binding enthalpies are related with a neat gain of hydrogen bonding and ion-pair interactions, which indicate a specific interaction

between the compound and the protein. Concerning the entropic contribution to the binding free energy (Fig. 8.8B, Table 8.5), it is small and favorable for C24 and C27, and slightly unfavorable for C31. Favorable entropic contributions, usually relate to a less important loss of freedom degrees by the ligand and the protein, or to a gaining of freedom degrees by the solvent, as a consequence of changes in the local structure of water surrounding both molecules [230].

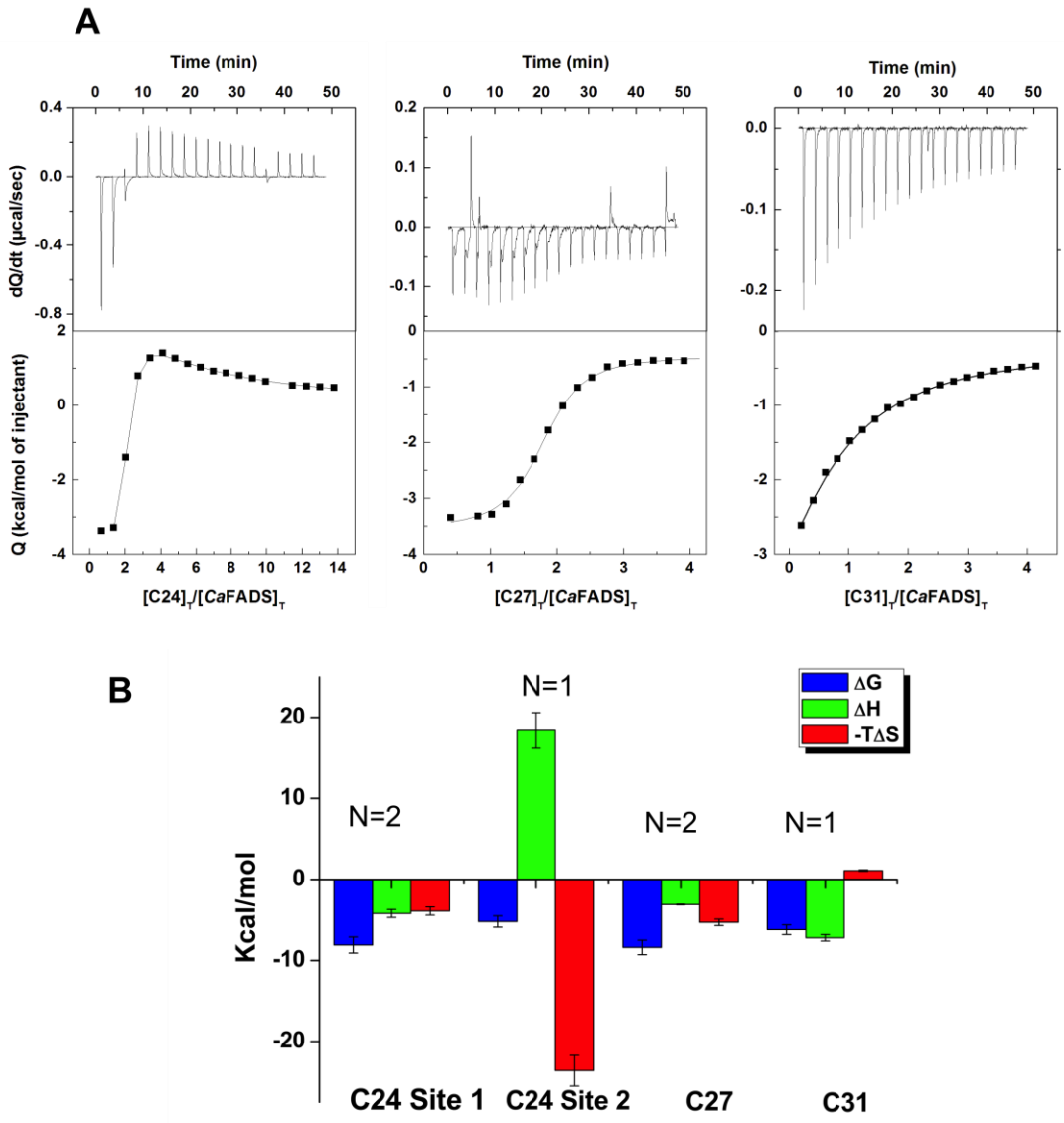

Figure 8.8. Thermodynamic analysis of the binding of selected FMNAT hits to *Ca*FADS. (A) Calorimetric titrations for the C24, C27 and C31 compounds. The upper panels show the thermograms for the interaction and the lower ones the corresponding binding isotherms with integrated heats. (B) Thermodynamic dissections of the interaction of *Ca*FADS with each of the selected compounds. The binding Gibbs energy (ΔG), enthalpy (ΔH), and entropy ($-T\Delta S$) are represented in black, gray and white bars, respectively. Experiments were carried out at 25 ºC, in 20 mM PIPES, pH 7.0, 10 mM $MgCl_2$ and 3% DMSO.

The predicted binding of C24 to the RFK module is driven by a hugely favorable entropic contribution that compensates the unfavorable binding enthalpy. That fact reveals that this C24 binding might not be specific, but takes places due to the hydrophobic nature and rigidity of this compound.

5. Effect of the HTS hits on the RFK and FMNAT activities of *Spn*FADS

Table 8.6. Effect of selected HTS hits on the RFK and FMNAT activities of *Spn*FADS. All the experiments were carried out at 25 ºC, in 20 mM PIPES pH 7.0, 10 mM $MgCl_2$ at saturating concentrations of FMN and ATP and in the presence of 2.5% DMSO. (n=3, mean ± SD).

	RFK activity		FMNAT activity	
HTS hit	**Res. activity [a] (%)**	**IC_{50} [b] (µM)**	**Res. activity [a] (%)**	**IC_{50} [b] (µM)**
C1	100 ± 15	--	0 ± 0 ***	69 ± 5
C2	78 ± 10	>100	100 ± 12	--
C7	92 ± 10	>100	0 ± 0 ***	73 ± 7
C9	0 ± 0 ***	6 ± 1	7 ± 1 ***	78 ± 6
C10	100 ± 12	--	0 ± 0 ***	68 ± 7
C14	100 ± 10	--	63 ± 7 ***	>100
C24	84 ± 9	>100	0 ± 0 ***	70 ± 6
C25	81 ± 8	>100	0 ± 0 ***	70 ± 6
C27	25 ± 4 ***	6 ± 1	0 ± 0 ***	51 ± 6
C29	71± 8*	>100	0 ± 0 ***	64 ± 5
C33	26 ± 3 ***	33 ± 4	93 ± 11	>100
C37	96 ± 10	>100	0 ± 0 ***	7 ± 1
C38	40 ± 5 ***	88 ± 6	68 ± 7 **	>100
C43	32 ± 3 ***	14 ± 2	100 ± 15	--

[a] Remaining activity in the presence of 100 µM of each compound. Data showing statistical significance differences when compared with activity in the absence of compound (***, $p<0.0001$; **, $0.0021>p>0.0001$; *, $0.033>p>0.0021$).
[b] Compounds assayed in the 0-100 µM concentration range.

To determine whether our HTS hits were specific for *Ca*FADS or might have effect on other similar bacterial FADS family members, we tested their effects on the RFK and FMNAT activities of the also bimodular and bifunctional *Spn*FADS. 16 out of 37 HTS hits did not inhibit the activity of *Spn*FADS, but 11 of the 37 HTS hits inhibited

either the RFK or the FMNAT activities of *Spn*FADS (Table 8.6). However, most of them exhibited IC_{50} values in the high micromolar range (>65 μM). Only C37 for the FMNAT activity, and C9 and C27 for the RFK one showed IC_{50} values lower than 10 μM. C37 and C9 inhibit completely the corresponding activity, but the residual activity for the RFK activity with C27 was too high to be considered as a good inhibitor.

6. Effect of selected HTS hits on different bacterial cells

Table 8.7. Minimal Inhibitory Concentration (MIC) of selected HTS hits against different microorganisms. FMNAT hits are shown in italics. Compounds were assayed in the 0.125-64 μM concentration range.

HTS HIT	*C. ammoniagenes* (μM)	*M. tuberculosis* (μM)	*S. pneumoniae* (μM)
C1	>64	>64	>64
C2	>64	>64	>64
C9	2	16	1-2
C11	>64	>64	>64
C14	0.25	8	2
C15	32	>64	64
C17	8	>64	>64
C24	16-32	16-32	>64
C27	64	>64	>64
C29	0.125	16-32	1
C31	32-64	>64	>64
C32	8	>64	64
C33	0.125	2-4	0.5
C35	16-32	>64	64
C37	>64	>64	>64
C38	32	>64	16-32
C47	2-4	8	4

To determine the effect of our HTS hits on the growth of different bacteria, we determined their minimal inhibitory concentration (MIC) (Table 8.7). With that aim, bacterial cells of *C. ammoniagenes*, *M. tuberculosis* and *S. pneumoniae* were growth in the presence of increasing concentrations of the selected HTS hits. Among the 37 HTS hits, only 11 and 5 inhibited, respectively, the growth of *C. ammoniagenes* and *M. tuberculosis*. From them, only C9, C14, C29, C33, and C47 showed MIC values for *C. ammoniagenes* lower than 2 μM, while C17, C24, C32, and C35 show values between 2 and 16 μM. (Table 8.7). Interestingly, those compounds that present better properties against the *Ca*FADS FMNAT activity (C24, C27 and C31) have poor growth inhibitory effect on whole bacterial cells (C24 and C27 have MIC ≈ 32 and 64 μM, respectively, whereas the MIC of C31 was >64 μM). However, it is worth to notice the effect as

growth inhibitors of compounds C9, C14, C29, C33 and C47, which show in common their ability to inhibit considerably both *Ca*FADS enzymatic activities (Table 8.1, Fig. 8.8). Regarding *M. tuberculosis* growth, C9, C8, C24 and C29 produced mild effects on cell growth, but only C14 and C33 showed MIC values below 8 µM. Table 8.7 also summarizes the effect of some selected compounds on *S. pneumoniae*, indicating that C9, C14, C29 and C33 inhibit moderately their growth.

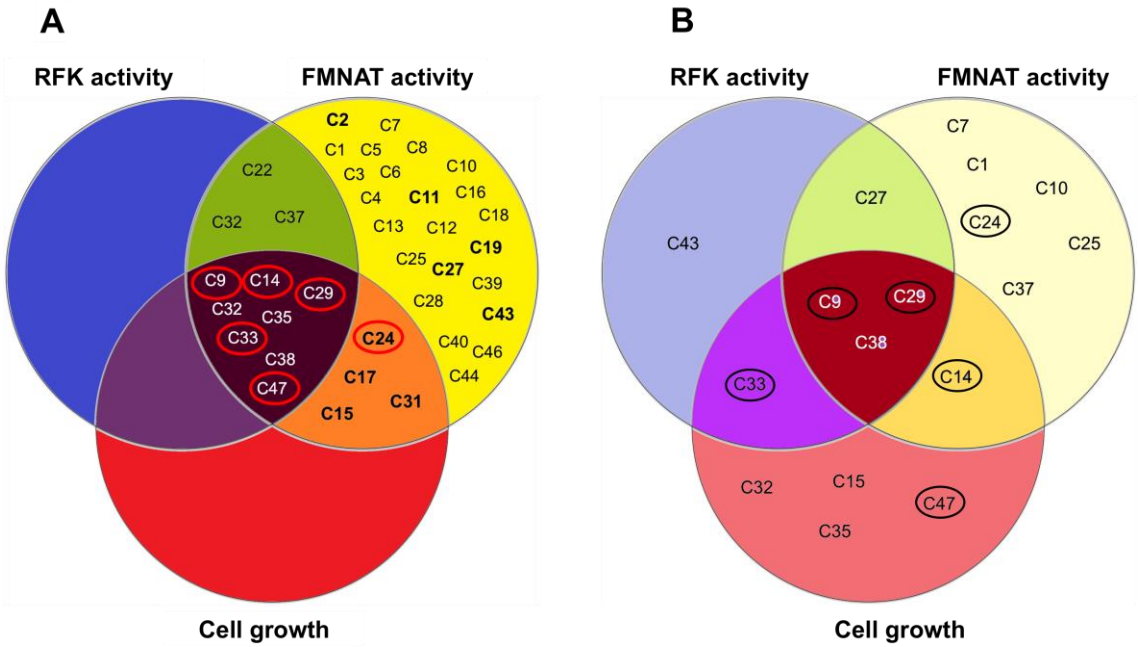

Figure 8.8. Venn diagrams for the effects of the HTS hits on *C. ammoniagenes* and *S. pneumoniae*. (A) Effect of the HTS hits on the RFK and FMNAT activities of *Ca*FADS as well as on the growth of *C. ammoniagenes* cells. (B) Effect of the HTS hits on the RFK and FMNAT activities of *Spn*FADS and on the *S. pneumoniae* cellular growth. The HTS hits including within each circle inhibit (with statistical significance) the specified activity or the cell growth. The hits highlighted in bold in (A) (those that completely inhibited the FMNAT activity without affecting the RFK one), were selected to continue the study. Hits rounded, both in (A) and (B), were also able to inhibit the proliferation of *M. tuberculosis*.

7. Discussion

Validation of the HTS protocol

Here we have designed and optimized an enzymatic activity-based HTS protocol to discover specific inhibitors for *Ca*FADS. In this protocol, the direct evaluation of the FMNAT enzymatic activity allows maximizing the specificity [194]. Our HTS protocol is simple, effective and consumes scant protein quantity, 1.5 ng/compound, against the ~5 µg/compound required for some differential scanning fluorescence-based HTSs

[190]. Our protocol directly monitors the activity of the enzyme that we want to inhibit (Fig. 8.1A), therefore, the number of false positives and PAINS is minimized. In addition, since chemicals in the library are approved drugs, their toxicity in mammalian cells will be limited. The 37 HTS hits obtained in this way (3.6% of the chemical library) were further assayed against the RFK and FMNAT activities of *Ca*FADS. Nine of the HTS hits (when assayed at 250 μM) almost completely inhibited the FMNAT activity without practically affecting the RFK one (Table 8.1). Since the FMNAT activity of the enzyme appeared as a more useful target, due to its difference in active site geometry regarding eukaryotic enzymes, these FMNAT hits were selected to continue the study.

Inhibitors targeting the FMNAT activity of CaFADS.

We choose the three FMNAT hits showing the lowest IC_{50} and residual activity (C24, C27 and C31, 8% of the HTS hits) (Table 8.2) to further determine their binding affinities to the enzyme and inhibition mechanisms. The first one was Chicago Sky Blue (CSB), here C24. It is an allosteric inhibitor of the Macrophage Inhibitor Factor, and shows promising *in vivo*-effects for the treatment of spinal cord injury [231]. Additionally, CSB appears to act an anticancer drug through the specific inhibition of Rad 51, as well as a potential resource for the Alzheimer disease treatment by inhibiting the binding of β-amyloid to the prion protein [232, 233]. Furthermore, the inhibition of vesicular glutamate transporters by CSB seems to attenuate expressions of behavioral sensitization [234]. In our study, CSB is the most potent inhibitor of the *Ca*FADS FMNAT activity as shown by its lowest values of residual activity and IC_{50} (Table 8.2), targeting both the free enzyme and an ATP-protein complex (Table 8.4, Fig. 8.5). CSB binds to both modules of the enzyme, being its binding to the FMNAT one highly favorable and enthalpically driven (Table 8.5, Fig. 8.8). This fact is positive for an inhibitor, since high binding enthalpy denotes lots of specific interactions, H-bounding and/or Van der Waals interactions, formed upon binding [195].

Gossypol, here C27, was used some years ago in China as a masculine contraceptive [235], although its side effects stopped its pharmacological use. More recently, gossypol has demonstrated anticancer effects through the inhibition of antiapoptotic proteins that belong to the Bcl-2 family and of molecules implicated in tumor progression [236, 237]. Additionally, gossypol inhibits the HIV-1 replication *in vitro* [238]. Gossypol is a potent inhibitor of the *Ca*FADS FMNAT activity that shows low IC_{50} and residual activity values (Table 8.2), while it does not affect the RFK one

(Table 8.1, Fig. 8.2). This compound competes with ATP for its binding at the FMNAT site of the protein (Table 8.4, Fig. 8.6). The lower K_d value for gossypol when compared with that of FMN [84], makes the inhibitor a preferred ligand for *Ca*FADS.

C31, or flunixin meglumine (flunixin is the bioactive part and meglumine the excipient), is a non-steroidal anti-inflammatory drug, analgesic and antipyretic extensively used in horses, pigs and cattle [239-241]. This fact guarantees that flunixin can be used securely in mammals. In this study, flunixin arises as a mixed inhibitor of the *Ca*FADS FMNAT activity. Although flunixin is the less potent inhibitor of the three here characterized (Table 8.2, Fig. 8.4), its great binding thermodynamic properties, together with its bio-security in mammals, reveal its potentiality as a drug.

Antimicrobial activity of the FMNAT hits

S. pneumoniae is the causative agent of more than 25 % of all cases of community-acquired pneumonia [112], causing more deaths than any other vaccine-preventable bacterial disease. On the other hand, *M. tuberculosis* causes tuberculosis, one of the most common causes of death from infectious disease (World Health Organization, 2015). *S. pneumoniae* FADS (*Spn*FADS) shows only 29% sequence identity with *Ca*FADS, but it owns the consensus sequences of prokaryotic FADSs and both proteins show very similar structures (Fig 8.9). The *M. tuberculosis* FADS (*Mt*FADS) sequence shows 45% identity with *Ca*FADS and 59% of conservative substitutions [76]. Since so far attempts to produce stable purified *Mt*FADS have failed, *Ca*FADS is considered a good model for the formers, as well as for other proteins of these two genera [242]. Thus, we tested the inhibitory activity of the best FMNAT hits on the growth of *C. ammoniagenes*, *S. pneumoniae* and *M. tuberculosis* cultures. CSB shows moderate effects on *C. ammoniagenes* and *M. tuberculosis* growth (Table 8.7, Fig. 8.8), although it does not inhibit at all the pneumococci growth. *A priori*, gossypol and flunixin do not inhibit the growth of *C. ammoniagenes*, *S. pneumoniae* and *M. tuberculosis* cells. This might be due to their inability to enter in the bacterial cell, or because efflux pumps eject them once in the bacterial cytoplasm. However, derivatization of these compounds in second generation hits, the utilization of vehiculization systems to move drugs across the membrane, or the use of efflux pumps inhibitors might be tools to favor their bactericide effects [243-245]. Among the other FMNAT hits not further characterized, only C15, C17 and C31 show mild inhibitory activity on the growth of *C. ammoniagenes*, not having any effect on *S. pneumoniae* and *M. tuberculosis* cultures (Fig 8.8).

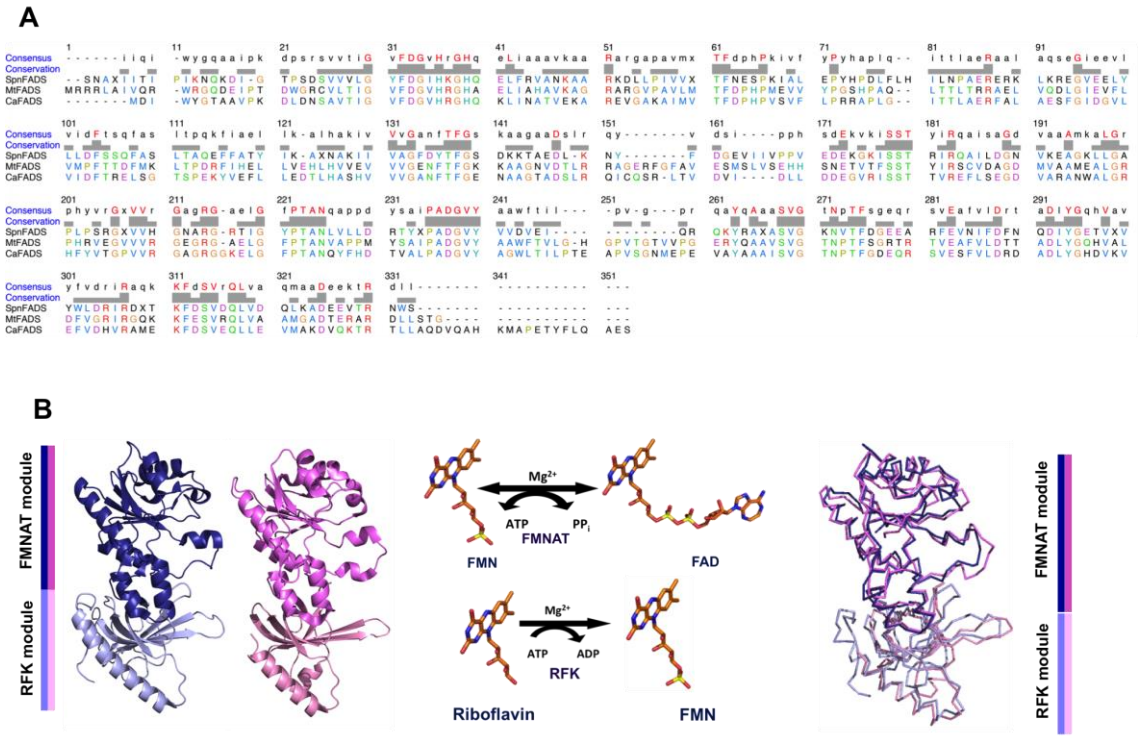

Figure 8.9. Sequence and structure similarity within selected members of the bacterial bifunctional FADS family. (A) Sequence alignment of *Ca*FADS (Q59263), *Spn*FADS (A0A0H2UPY5) and *Mt*FADS (NP_217302.1) obtained using the CLUSTAL W algorithm (http://www.ebi.ac.uk/clustalw/) with default parameters. The consensus sequence is indicated. Equivalent residues at each position are shown in the same color. (B) Crystallographic structures of *Ca*FADS (PDB 2x0k), with the FMNAT and RFK modules shown in blue and light blue respectively, and of *Spn*FADS (PDB 3op1), with the FMNAT and RFK modules shown in pink and light pink respectively, and structural alignment, showing an r.m.s.d. of 1.63 Å for 247 Cα atoms. Structural alignment and figures produced with PyMol [246]. The reaction catalyzed by each module is shown next to the corresponding module structure.

Selectivity of the HTS hits

The specificity of the HTS hits for *Ca*FADS was also tested by determining their effects on the *Spn*FADS RFK and FMNAT activities. Thus, regarding the three FMNAT hits: CSB has a poor inhibitory effect on *Spn*FADS (Table 8.6), which might be of interest for a selective inhibitor; gossypol inhibits both *Ca*FADS and *Spn*FADS activities (Tables 8.6 and 8.7), appearing as a broad inhibitor of FADS; and flunixin has no effect on *Spn*FADS (Table 8.6), indicating the specificity of this compound for *Ca*FADS. Furthermore, only 30% of the HTS hits have inhibitory effects on *Spn*FADS, despite conservation of sequential and structural motives among both proteins (Fig.

8.9), In addition, high values for residual activities and IC_{50} reveal that they are worse inhibitors for *Spn*FADS than for *Ca*FADS (Table 8.6).

Among the HTS hits C9, C27, C37 and C43 appear as interesting inhibitors of *Spn*FADS (Table 8.6). Curiously, C27 and C43, which did not reduce the *Ca*FADS RFK activity (Table 8.1), have an important effect on the *Spn*FADS one. C9, thonzonium bromide, inhibits both *Spn*FADS activities (Table 8.6). This compound is a monocationic detergent that has been commonly used in cortisporin-TC ear drops to help penetration of active ingredients through cellular debris. Additionally, thonzonium bromide has appeared as an inhibitor of the vacuolar ATPase, showing cytotoxic effects at concentrations higher than 10 μM [247], and a inhibitor of the RANK-L induced osteoclast formation [248]. C37, fluvastatin sodium salt, inhibited both *Ca*FADS activities, but only affects the FMNAT one in *Spn*FADS. Fluvastatin inhibits the HMG-CoA reductase being used to treat hypercholesterolemia [249]. Fluvastatin seems to have positive effects in myocardial fibrosis by favoring ACE2 expression, and also appears to inhibit modestly the replication of hepatitis C virus [250, 251]. Oxaprozine, here C43, is used as analgesic (inhibits anandamide hydrolase in neurons) and an anti-inflammatory drug [252, 253] and acts as a nonselective cyclooxigenase inhibitor. Additionally, it inhibits NF-κβ in activated monocytes, being a promising drug for the treatment of rheumatoid arthritis [254].

Recent studies [79, 99, 100, 222], as well as the presented in the chapters 6 and 7, have revealed important differences in the catalytic cycle of bifunctional FADS, which might be related to dissimilarities in the conformation of the active sites during catalysis. That fact is consistent with the differential inhibitory activity of the HTS hits against *Ca*FADS and *Spn*FADS, as we have observed in the present work. Such mechanistic variations appear to determine the capability of hits to bind and/or to produce inhibition. These observations highlight the potentiality of our method to find selective drugs targeting a specific protein of a particular microorganism, without affecting homologous proteins in other microorganisms. The development of such species-selective drugs is of great importance in the treatment of infections, in order to avoid undesired side-effects on the normal microbioma of the host [255], and to minimize the selection of resistant bacterial strains.

Besides FMNAT hits whose inhibitory activity on *Ca*FADS only had mild or no effects on bacterial cells, 5 HTS hits (C9, C14, C29, C33 and C47) appear as strongly inhibitors of the *C. ammoniagenes* growth (Table 8.6, Fig. 8.8). These 5 HTS hits also

inhibit the growth of *S. pneumoniae* (Table 8.7, Fig. 8.8), while only the first four mildly affect *M. tuberculosis*. Noticeably, these 5 HTS hits are good inhibitors of both *Ca*FADS activities (Table 8.1, Fig. 8.8). C9 and C29 also appear as potent inhibitors of the *Spn*FADS RFK and/or FMNAT activities respectively. The effect of the others as *Spn*FADS inhibitors is milder, suggesting that in these cases mechanisms that do not involve FADS prevent cell proliferation. Considering our results collectively, the development of drugs targeting both activities of bifunctional FADSs appears as a strategy to consider in the discovery of new antibacterial drugs. In this context, the non-selective antimicrobial properties of C9 and C29 seem interesting tools to explore.

Chapter IX
General discussion

1. Quaternary organizations of bifunctional prokaryotic FAD synthetases

The crystal structure of *Ca*FADS suggested the formation of a transient oligomeric assembly that consists on a dimer of trimers [85, 100]. Such quaternary organization might approach the RFK and FMNAT active sites of neighboring protomers, facilitating the channeling of the FMN produced in the RFK module of a protomer to the FMNAT site of the contiguous one, for its transformation into FAD [85]. Besides the dimer of trimers, other oligomeric assemblies of lower molecular weights (dimers, trimers and tetramers) have been observed both *in vitro* and *in vivo* assays [100]. Additionally, it has been proven that the presence of different substrates and products of the RFK and FMNAT reactions promotes the transformation of some oligomers into others [100]. All these data suggested that the dimer of trimers might play an active role in the catalytic cycle of the *Ca*FADS, as well as in the regulation of FMN and FAD synthesis.

Structural analysis of the *Ca*FADS dimer of trimers suggested that loop L3c (only present in FADS from *Corynebacterium* and *Mycobacterium* genera) might be key for the stabilization of that structure [85]. Additionally, loops L4n, L1c-FlapI and L6c together with helix α1c form the interface between two protomers within each trimer, contributing to the structure of the active sites [85]. With the purpose to clarify the relevance of such elements of secondary structure in the stabilization of the quaternary assembly, we produced point mutations at L4n (R66, which forms a salt bridge with the E268 that is the catalytic base of the RFK activity), L1c-FlapI (K202, E203 and F206), L6c (D298), and α1c (V300, E301 and L304).

Among the mutated residues, R66 was the only one located at the N-terminus module (specifically at the loop L4n) [85]. Mutants of this residue (R66A and R66E) showed altered RFK and FMNAT activities, as well as modified affinities for the ligands, both at the RFK and FMNAT binding sites. Even though the substitution of R66 did not prevent the stabilization of oligomeric assemblies, surface and charge complementarities within these organizations decreased regarding the WT. Considering that within a monomer, R66 at the FMNAT module is far enough from the RFK active site to affect the activity and ligands binding to this second site, the effects observed upon mutation of R66 only can be explained in the context of the dimer of trimers. Thus, all these data revealed that the salt bridge between R66 of a monomer and E268 of the neighboring protomer contributes to the stabilization of the trimer within the

dimer of trimers, validating the hypothesis of the formation of quaternary organizations. Nevertheless, this salt bridge is not the main determinant in the stabilization of such structure, where other secondary structure elements, such as loop L3c, might have a more relevant role.

Mutations in L1c-FlapI (K202, E203 and F206) altered the kinetic parameters for the *Ca*FADS RFK activity, as well as ligand binding parameters in the C-terminal module, revealing the implication of these residues in the achievement of the appropriate RFK catalytic geometry. F206 interacts with F62 of helix α2n, while K202 and E203 establish salt bridges with E103 and N131, respectively, from loop L8n of the N-terminus module of the neighboring protomer. Substitutions of these residues would prevent such interactions, and consequently the shape of the flavins cavity in the FMNAT module would change, explaining the decreased fraction of protein able to bind FMN and FADS at this module.

Mutations in L6c (D298) and in the helix α1c (V300, E301 and L304) highly modulated kinetic parameters for both RFK and FMNAT activities, reducing as well the affinity for FMN and FAD. That fact revealed the implication of these residues inflavins binding to the FMNAT module and in the stabilization of quaternary organizations. Thus, L6c and the N-terminal end of helix α1c contribute to close the FMNAT flavin binding site of the neighboring protomer within the trimer. Mutation of D298 might prevent its H-bound with T165 that is critical for flavin binding and the FMN adenylylation, which would explain the obtained results. Similarly, substitutions of E301 and L304 might hinder its interaction with T127 and A132, respectively, affecting van der Waals contacts between α1c and L8n, within the timer. These facts would explain the altered parameters for flavin binding that the mutants show. V300 is expected to directly interact with the isoalloxazine ring in the FMNAT module of the adjacent protomer, therefore the altered binding constants that the variants of this residue showed were the expected ones. Finally, the mutations also modified flavin binding at the RFK module, consistently with the conformational changes in L1c-FlapI, L4c-FlapII, L6c and helix α1c induced by substrates binding.

All these data revealed that despite none of the mutated residues is by itself determinant for the stabilization of quaternary assemblies, neither for the RFK or FMNAT activities of *Ca*FADS, they modulate the oligomerization equilibrium, altering as well the RFK and FMNAT activities and the thermodynamic parameters for ligands binding, specially to the FMNAT module. Therefore, among the secondary structure

elements proposed as key in the formation of the dimer of trimers, the loop L3c acquires special relevance. This hypothesis is supported by the fact that the dimer of trimers is neither predicted, nor experimentally observed for *Spn*FADS. During The RFK and FMNAT catalytic cycles, and despite the fact that the monomer was the most populated state, *Spn*FADS appeared to stabilize dimers, tetramers and specially trimers. Nevertheless, none of these structures resembles the dimer of trimers observed for *Ca*FADS. Having into account that *Spn*FADS presents a loop L3c that is 12 residues shorter than *Ca*FADS, the results obtained for *Spn*FADS reinforce the supposition of the key role of L3c in the stabilization of the dimer of trimers.

2. Catalytic cycles of *Ca*FADS and *Spn*FADS

*Ca*FADS and *Spn*FADS only share 25% of sequence identity, although both proteins present the consensus sequences related to the RFK and FMNAT activities [76]. Despite the low sequence homology, both FADSs display great similarity in their overall structures. Regarding their catalytic cycle, *Ca*FADS and *Spn*FADS are able to transform RF into FMN, and FMN into FAD but the RFK and FMNAT activities of these enzymes show important differences. Thus, the RFK activity of *Spn*FADS is not inhibited at high concentrations of the RF substrate (as that of *Ca*FADS is), and their FMNAT activity only takes place under strong reducing conditions.

During the FMNAT catalytic cycle of *Spn*FADS, and contrary to that observed for *Ca*FADS, FMN only is transformed into FAD when it is in the reduced form. The reduced isoalloxazine ring seems to be an absolute requirement for flavins binding to the FMNAT module of the enzyme, and for its subsequent transformation. This could be due to the FMNAT active site of *Spn*FADS only allows the incorporation of the isoalloxazine ring in their reduced bended conformation. Such difference might be a consequence of important changes in regions involved in ligands binding, for instance in loops L4n and L6n, which form the external part where substrates and products of the FMNAT activity bind. Additionally, the flavin cavity at the FMNAT module of *Spn*FADS is slightly broader and deeper than that of *Ca*FADS, which might influence the way in which flavins bind to this cavity.

The RFK catalytic cycle of *Ca*FADS and *Spn*FADS also presents important differences, being the most obvious one the lack of inhibition by excess of the RF substrate that *Spn*FADS shows. Thus, the *Ca*FADS RFK activity is noticeably inhibited at RF concentrations higher than ~5 μM. A more detailed study revealed that besides

the RF inhibition, the products of the reaction (FMN and ADP) also affected the RFK activity of *Ca*FADS. ADP acts as a competitive inhibitor, while FMN performs a uncompetitive inhibition mechanism, yielding a *Ca*FADS:ATP:FMN dead-end complex. Nevertheless, inhibition constants for RF and FMN are considerably lower than that for ADP, which makes both flavins more potent inhibitors than ADP and also explains the fact that inhibition by ADP stayed unnoticed up today. A similar analysis of the RFK activity of *Spn*FADS revealed that, although the RF substrate does not produce any inhibitory effect, the FMN and ADP products do. The inhibitory mechanism carry out by these products differs from those observed for *Ca*FADS, and in this case both FMN and ADP are uncompetitive inhibitors, being FMN more potent as inhibitor than ADP. Nevertheless, the K_i^{FMN}/ K_m^{RF} ratio is approximately 5 times higher for *Spn*FADS than for *Ca*FADS, which explains the apparent lack of inhibition of the *Spn*FADS RFK activity.

Rapid mixing stopped flow experiments allowed inferring some evidences of the RFK catalytic cycle for both enzymes. Both proteins are not able to either bind or internalize FLV ligands in the absence of ANP ligands, but ATP and ADP promote flavins binding and/or its internalization through a conformational change in loop L4c that closes the flavin binding cavity [99]. Nonetheless, the rates at which the ANP-FLV mixtures bind the FADSs differ between these proteins, being the ATP-RF substrate binding the fastest and the slowest process for *Spn*FADS and *Ca*FADS, respectively. As a consequence of that, as the RFK reaction draws on and the products start to accumulate, they would bind the *Ca*FADS preferably, producing kinetic inhibition. In the case of *Spn*FADS, although products accumulate the ATP-RF binding would be the most favored process. When mixing ATP-RF with FADSs, an ATP-induced conformational change is observed for both proteins (characterized by k_{obs2}), although the behavior of k_{obs2} on RF concentration differs. Thus, during the *Ca*FADS RFK reaction, increasing RF concentration inhibits such conformational change, while this inhibition is not observed for *Spn*FADS. These differences might be explained considering the conformational rearrangement of the PTAN motif required to reach the catalytically competent conformation by *Ca*FADS but not by *Spn*FADS. Hence, we can conclude that although the steps occurring during the RFK reactions of *Ca*FADS and *Spn*FADS are similar, their rates differ being the final consequence the lesser kinetic inhibition level that *Spn*FADS shows.

Regarding the thermodynamic data of the interactions of both proteins with all the substrates and products of the RFK reaction, some aspects need to be pointed. *Spn*FADS can reach the "pseudoreactive" ternary complex with RF and ATP through two paths, while just one path leads to the *Ca*FADS:RF:ATP ternary complex. The interaction diagram also suggest that the substrates bind the protein in different order, since RF cannot bind to the preformed *Ca*FADS:ATP binary complex. Thus, *Ca*FADS seems to reach the catalytically competent complex through the concerted fit of the substrates, while *Spn*FADS apparently follows a random sequential binding of its substrates. Another important difference is the relative stability of the FADS:ANP:FLV ternary complexes. *Ca*FADS establishes a highly stable ternary complex with FMN and ATP, and also all the *Ca*FADS:ANP:FLV ternary complexes are more favored than *Ca*FADS:ATP:RF. For its part, the *Spn*FADS:RF:ATP together with the *Spn*FADS:RF:ADP are the most stable complexes. All these observations explain from the thermodynamic point of view, the more potent inhibition profiles observed for *Ca*FADS. Additionally, for *Ca*FADS the substrates of the RFK reaction present different cooperation tendency depending on the RF concentration. Thus, RF and ATP show high positive cooperation at low RF concentrations, while their cooperation is negative at high concentrations of this flavin. This fact, which is not observed for *Spn*FADS, might explain the inhibition by the RF substrates that *Ca*FADS presents and *Spn*FADS does not.

All these regulatory differences between both proteins might be due to dissimilar strategies to regulate FMN and FAD synthesis to keep the flavoproteome homeostasis. So, considering the huge amount of processes in which FMN and FAD are involved, acting as cofactors of flavoproteins, regulation of the synthesis of these flavins appears as a highly important process. Since the FMNAT activity of *Ca*FADS does not appear to present any type of regulation, its RFK activity requires a more carefully control than *Spn*FADS, whose FMNAT activity needs strong reducing conditions.

3. Discovery of antibacterial drugs targeting bifunctional FADSs

The apparition during the last decades of resistant bacterial strains [11], together with the fact that effective antibiotics have not been developed since the 90s [256], reveal the need to explore new effective antibacterial targets, as well as drugs against them. Among the possible new targets, bifunctional FADSs appear as attractive candidates for different reasons. i) They are essential proteins and their inhibition prevent from the

beginning all the routes in which FMN and FAD are involved [153, 154]. ii) Bifunctional FADSs, and especially the FMNAT module, differ from the eukaryotic proteins that synthetize FMN and FAD [81, 90, 155, 229], thus, drugs targeting these proteins are more likely to not affect the human proteins. iii) There are available several crystallographic structures of FADSs, which facilitates the design of inhibitory assays and the improvement of the drugs [74, 75, 86]. Therefore, taking all these facts into consideration, we decide to explode the potentiality of FADSs as drug targets, searching inhibitors of such proteins using as model the member of the family best characterized, that is *Ca*FADS [76, 84, 85, 87, 89, 95, 99].

Using an activity-based HTS against *Ca*FADS, we identified 37 compounds with potential inhibitory effect on the RFK or FMNAT activities. Among these HTS hits, 9 inhibited the FMNAT activity (FMNAT hits), having no effect on the RFK one. Since hits that only altered the FMNAT activity were more likely to not inhibit the corresponding human enzymes (the RFK module of bacterial FADSs and mammal RFKs highly differ) [74, 85, 155], we continue the study characterizing the three most potent hits among the 9 FMNAT ones. We determined the inhibition mechanism performed by each hit, as also the thermodynamic parameters that lead their interaction with *Ca*FADS. Among these three compounds, namely Chicago Sky Blue, Gossypol and Flunixin meglumine, the last one appeared as a promising inhibitor. Despite Flunixin meglumine is the least potent inhibitor, it stands out as potential drug due to its great thermodynamic binding properties and the fact that its biosecurity in mammals has been proven before.

The specificity of the HTS hits was tested on *Spn*FADS. In general the HTS hits are less potent inhibitors of the *Spn*FADS activities than of *Ca*FADS, highlighting the ability of our method to find specie-specific inhibitors.

When we checked the ability of the HTS hits to inhibit the growth of *C. ammoniagenes, M. tuberculosis* and *S. pneumoniae* cells, we found that just a few compounds have inhibitory effect at the cellular level. That might be due to their inability to enter in the bacterial cell, or because efflux pumps eject them once in the bacterial cytoplasm. However, derivatization of these compounds in second generation hits, the utilization of vehiculization systems to move drugs across the membrane, or the use of efflux pumps inhibitors might be tools to favor their bactericide effects [243-245]. Noticeably, those hits that inhibited both the RFK and the FMNAT activities of

*Ca*FADS and *Spn*FADS were the most effective inhibiting the bacterial growth, which point to the inhibition of both activities of bacterial FADSs as the best strategy.

Chapter X
Conclusions

1. The FADS from *C. ammoniagenes*

- In *Ca*FADS the residue R66, located at the FMNAT module of the protein, modulates the RFK activity of the C-terminal module.
- R66 stabilizes the substrates of the RFK reaction, RF and ATP, during catalysis.
- The salt bridge that R66 establishes with E268 of a contiguous protomer contributes to the stabilization of the trimer within the *Ca*FADS dimer of trimers, reinforcing the theory of the formation of transient quaternary organizations during both RFK and FMNAT activities of the enzyme
- The R66-E268 salt-bridge is not the only and main determinant in the stabilization of *Ca*FADS quaternary organization.
- R66 does not play any key role in the FMNAT activity, and only has a minor contribution to substrates/products location in this active site.
- Residues K202, E203 and F206 in loop L1c-FlapI, D298 in L6c and V300, E301 and L304 in helix α1c of the *Ca*FADS RFK module are not unique determinants in the formation of quaternary assemblies, but modulate the oligomerization profiles.
- K202, E203, F206, D298, V300, E301 and L304 modulate binding and kinetic parameters of the RFK and FMNAT activities.
- The conformation of the secondary structural elements containing these residues is modulated by their nature. Therefore, the nature of these residues also modulates the packing architecture within the quaternary assemblies, as well as ligand binding and kinetic parameters.
- The RFK activity of *Ca*FADS, is inhibited by the RF substrate, as well as by both products (FMN and ADP) of the RFK reaction. ADP acts as a competitive inhibitor, being its inhibition constant 17.0 μM, while FMN is an uncompetitive inhibitor with an inhibition constant of 1.4 μM. Having into account that the K_m values for the RF and ATP substrates are 10.4 and 60.3 μM, respectively, both products of the reaction are very potent inhibitors.
- During the RFK catalytic cycle, the collective binding of adenine and flavin nucleotides induces important conformational changes in the RFK module.
- The RFK catalytic cycle of *Ca*FADS requires Mg^{2+} and the concerted fit of the substrates to achieve a catalytically competent geometry.

- All possible combinations of adenine and flavin nucleotides produce inhibition of the RFK activity. The binding of substrates of the RFK reaction is the slowest process, as well as the least favored one from a thermodynamic approach. Thus, All possible RFK:ANP:FLV ternary complexes compete kinetically and thermodynamically with the catalytically competent one (with RF and ATP).
- The careful regulation of the RFK activity of *Ca*FADS might have a relevant role at the physiological level for the production of flavins according to *C. ammoniagenes* cellular needs.

2. The FADS from *S. pneumoniae*

- *Spn*FADS is a prokaryotic bifunctional FADS that folds in two modules, the C-terminal module has RFK activity, and the N-terminal one FMNAT and FADpp activities.
- Both the RFK and FMNAT activities show Michaelis-like kinetic profiles. The k_{cat}, K_m^{RF}, and K_m^{ATP} for the RFK activity are 18.7 min^{-1}, 0.9 μM and 54.0 μM, respectively. For the FMNAT activity the k_{cat}, K_m^{FMN}, and K_m^{ATP} are 34.9 min^{-1}, 9.8 μM and 31.6 μM, respectively.
- *Spn*FADS shows three main behavioral differences regarding *Ca*FADS:
  - The *Spn*FADS FMNAT module only binds and transforms flavins in their reduced state.
  - The *Spn*FADS RFK activity does not show inhibition by the RF substrate.
  - Only dimers and trimers are stabilized during catalysis.
- The RFK activity of *Spn*FADS is inhibited by both products of the RFK reaction (FMN and ADP). FMN and ADP are mixed inhibitors, being K_i^{FMN} and K'_i^{FMN} 1.3 and 7.1 μM, respectively; and K_i^{ADP} and K'_i^{ADP} 131 and 844 μM, respectively. Thus, the inhibition by ADP suffered by *Spn*FADS is weaker than that experimented by *Ca*FADS.
- During the *Spn*FADS RFK catalytic cycle, RF and ATP get allocated within the active site through a random sequential binding.
- Although all the *Spn*FADS:ANP:FLV complexes can be formed in complex mixtures of substrates and products of the RFK reaction, the binding of RF and ATP substrates is the fastest and thermodynamically the most favored process. That explains that inhibition is less relevant for the RFK activity in *Spn*FADS than in *Ca*FADS.

- Using reduced flavin as substrates, substrate inhibition, or the formation of oligomeric assemblies reflect different regulation mechanisms used by prokaryotic FADSs.
- Dissimilar behaviors among prokaryotic FADS family members provide with a framework to design species-selective compounds targeting bacterial FADSs.

3. Discovery of antibacterial compounds targeting prokaryotic FADS

- We have optimized a HTS protocol that can be used for the discovery of new antibacterial drugs, targeting RFK and/or FMNAT activities of bifunctional prokaryotic FADSs. The method is quick, effective and requires a small quantity of protein, additionally minimizes the number of PAINS.
- Among the 1240 compounds contained in the library, 37 inhibited *Ca*FADS, and three were selected as good inhibitors of its FMNAT activity.
- Two of the three selected compounds were not species-selective, since they also affected *Spn*FADS, but the third one, C31, was selective for *Ca*FADS. Therefore, we can identify promising compounds at the non-selective or selective enzyme inhibitors level.
- The three selected compounds do not produce observable antimicrobial effects, probably due to a poor uptake, efficient efflux, or a fast degradation by other bacterial enzymes.
- The HTS hits with the best antimicrobial properties against the different bacteria analyzed were those that inhibited both the RFK and FMNAT activities.
- Bacterial FADS are promising species-selective drug targets.

.

Capítulo X
Conclusiones

1. La FADS de *C. ammoniagenes*

- El residuo R66, situado en el módulo N-terminal de *Ca*FADS, tiene un papel fundamental en la modulación de la actividad RFK del módulo C-terminal.
- Durante la catálisis, R66 estabiliza los substratos RF y ATP.
- El puente salino formado entre R66 y E268 contribuye a la estabilización del trímero en el dímero de trímeros descrito para *Ca*FADS, reforzando la teoría de la formación transitoria de estructuras cuaternarias durante las sus actividades RFK y FMNAT.
- El puente salino entre R66 y E268 no es el determinante más relevante en la estabilización de los ensamblados cuaternarios de *Ca*FADS.
- El residuo R66 no juega ningún papel relevante en la actividad FMNAT y sólo contribuye ligeramente a la colocación de sustratos y productos en el sitio activo.
- Aunque los residuos del módulo RFK de *Ca*FADS K202, E203 y F206 del bucle L1c-FlapI, D298 en L6c y V300, E301 y L304 de la hélice α1c no determinan por sí solos la capacidad de la enzima para formar agregados cuaternarios, modulan los perfiles de oligomerización.
- K202, E203, F206, D298, V300, E301 y L304 modulan los parámetros cinéticos y de unión de las actividades RFK y FMNAT de *Ca*FADS.
- La conformación de los elementos de estructura secundaria que contiene estos residuos depende de la naturaleza de sus cadenas laterales. Por tanto, su naturaleza determina la arquitectura de las estructuras cuaternarias, así como los parámetros cinéticos y de unión.
- La actividad RFK de *Ca*FADS resulta inhibida tanto por el substrato RF como por ambos productos de la reacción (FMN y ADP) . El ADP actúa como un inhibidor competitivo, siendo su constante de inhibición 17.0 μM. Por su parte, el FMN es un inhibidor acompetitivo, y con una constante de inhibición de 1.4 μM. Teniendo en cuenta que los valores de K_m para RF y ATP son de 10.4 y 60.3 μM, respectivamente, los dos productos de la reacción son inhibidores muy potentes.

- Durante el ciclo catalítico de la actividad RFK, la unión conjunta de nucleótidos de flavina y adenina induce importantes cambios conformacionales en este módulo.

- Para alcanzar una geometría catalíticamente competente durante el ciclo catalítico de la actividad RFK de *Ca*FADS, es necesaria la intervención del cation Mg^{2+} y la unión concertada de los sustratos.
- Todas las combinaciones posibles de nucleótidos de adenina y flavin producen la inhibición de la actividad RFK. La unión de los sustratos es el proceso más lento tanto desde el punto de vista cinético como desde el termodinámico. Por tanto, todos los complejos ternarios RFK:ANP:FLV compiten cinética y termodinámicamente con el catalíticamente competente (con RF y ATP)
- La intrincada regulación de la actividad RFK de *Ca*FADS podría tener un papel relevante para laproducción de flavinas de acuerdo a las necesidades celulares de *C. ammoniagenes.*

2. La FADS de *S. pneumoniae*

- *Spn*FADS es una enzima procariota bifuncional que se pliega en dos módulos: el C-terminal cataliza la actividad RFK y el N-terminal las actividades FMNAT y FADpp.
- Tanto la actividad RFK como la actividad FMNAT de *Spn*FADS presentan perfiles cinéticos que siguen el modelo de Michaelis. Los valores de k_{cat}, K_m^{RF}, y K_m^{ATP} son 18.7 min^{-1}, 0.9 μM y 54.0 μM, respectivamente, para la actividad RFK. Para la actividad FMNAT, los valores de k_{cat}, K_m^{FMN}, y K_m^{ATP} son 34.9 min^{-1}, 9.8 μM y 31.6 μM, respectivamente.
- *Spn*FADS presenta tres diferencias fundamentales respecto a *Ca*FADS
    - El módulo FMNAT de *Spn*FADS únicamente une y transforma flavinas en su estado reducido.
    - La actividad RFK de *Spn*FADS no presenta inhibición por el sustrato RF.
    - *Spn*FADS sólo estabiliza dímeros durante ambos ciclos catalíticos.
- La actividad RFK de *Spn*FADS es inhibida por ambos productos de la reacción (FMN y ADP). Ambos actúan como inhibidores mixtos, siendo los valores de K_i^{FMN} y $K'_i{}^{FMN}$ de 1.3 y 7.1 μM, respectivamente; y los de K_i^{ADP} y $K'_i{}^{ADP}$ 131 y 844 μM, respectivamente.
- Durante el ciclo catalítico de la actividad RFK de *Spn*FADS, RF y ATP ocupan el sitio activo de la enzima siguiendo un mecanismo secuencial aleatorio.
- Aunque todos los posibles complejos *Spn*FADS:ANP:FLV pueden formarse en mezclas complejas de *Spn*FADS con los sustratos y los productos de la actividad

RFK, la unión de los productos, RF y ATP, es el proceso más rápido y termodinámicamente más favorable. Este hecho explica el menor nivel de regulación a través de la inhibición que presenta *Spn*FADS en comparación con *Ca*FADS.

- La necesidad de flavinas oxidadas o reducidas, la presencia o ausencia de inhibición por sustrato y las estabilización de diferentes especies oligoméricas durante las actividades RFK y FMNAT, ponen de manifiesto diferentes estrategias de regulación para la producción de los cofactores flavínicos utilizadas por distintas FADSs procariotas.
- Los distintos comportamientos observados entre miembros de la familia de las FADSs bifuncionales proporcionan una herramienta útil para el desarrollo de nuevos compuestos antimicrobianos dirigidos contra estas dianas de forma que sean especie-selectivos.

3. Desarrollo de nuevos compuestos antibacterianos

- Se ha optimizado un protocolo de cribado de alto rendimiento (HTS) que puede ser utilizado para identificar fármacos utilizando como dianas las actividades RFK y/o FMNAT de FADSs bacterianas. El método es rápido, efectivo y consume muy poca cantidad de proteína. Además, minimiza el número de compuestos de interferencia (PAINS) detectado.
- De entre los 1240 compuestos que componen la librería de compuestos ensayada, 37 inhiben alguna de las actividades de *Ca*FADS. De estos 37 compuestos, tres son buenos inhibidores selectivos de actividad FMNAT.
- Dos de los tres compuestos seleccionados, dos no son selectivos de especie, dado que también inhiben *Spn*FADS. El tercero, C31, es selectivo para *Ca*FADS. Por tanto nuestro método ha permitido identificar prometedores inhibidores de la enzima que sean o bien selectivos o no selectivos.
- Estos tres compuestos no presentan efectos antibacterianos, lo que puede deberse a una internalización deficiente, a que las bacterias expulsan el compuesto mediante bombas de eflujo, o a que los compuestos son degradados por la acción de otras enzimas bacterianas.
- Los compuestos identificados en el cribado con mejores propiedades antibacterianas son aquellos que inhibenn tanto la actividad RFK como la FMNAT.

- Las FADSs bacterianas son prometedoras dianas terapéuticas para la identificación de compuestos antimicrobianos selectivos para una especie. .

Bibliography

1 Koch, R. (1884) An Address on Cholera and its Bacillus. Br Med J. **2**, 453-459

2 Koch, R. (1876) Die Ätiologie der Milzbrand-Krankheit, begründet auf die Entwicklungsgeschichte des Bacillus Anthracis. Kreisphysikus in Wollstein

3 Pouillard and J. (2002) A forgotten discovery:doctor of medicine Ernest Duchesne´s thesis (1874-1912. ed.)^eds.). pp. 11-20, Hist. Sci. Med.

4 Ehrlich, P. (1913) Address in Pathology, ON CHEMIOTHERAPY: Delivered before the Seventeenth International Congress of Medicine. Br Med J. **2**, 353-359

5 Fleming and A. (1929) On the antibacterial action of cultures of a penicillium, with special reference to their use in the isolation of B. influenzae. Br. J. Exp. Pathol. **10**, 226-236

6 Chain, E., Florey, H. W., Adelaide, M. B., Gardner, A. D., Heatley, N. G., Jennings, M. A., Orr-Ewing, J. and Sanders, A. G. (1993) Penicillin as a chemotherapeutic agent. 1940. Clin Orthop Relat Res, 3-7

7 Parascandola, J. (1980) The history of antibiotics: a symposium. American Institute of the History of Pharmacy

8 Dubos, R. J. and Hotchkiss, R. D. (1941) The production of bactericidal substances by aerobis sporulating bacili. J Exp Med. **73**, 629-640

9 Bbosa, G. S., Mwebaza, N., Odda, J., Kyegombe, D. B. and Ntale, M. (2014) Antibiotics/antibacterial drug use, their marketing and promotion during the post-antibiotic golden age and their role in emergence of bacterial resistance. Health. **Vol.06No.05**, 16

10 Fischbach, M. A. and Walsh, C. T. (2009) Antibiotics for emerging pathogens. Science. **325**, 1089-1093

11 Brown, E. D. and Wright, G. D. (2016) Antibacterial drug discovery in the resistance era. Nature. **529**, 336-343

12 Fajardo, A., Martínez-Martín, N., Mercadillo, M., Galán, J. C., Ghysels, B., Matthijs, S., Cornelis, P., Wiehlmann, L., Tümmler, B., Baquero, F. and Martínez, J. L. (2008) The neglected intrinsic resistome of bacterial pathogens. PLoS One. **3**, e1619

13 Abraham, E. P. and Chain, E. (1940) An enzyme from bacteria able to destroy penicilin. Nature. **146**, 837

14 Andersson, D. I. and Hughes, D. (2011) Persistence of antibiotic resistance in bacterial populations. FEMS Microbiol Rev. **35**, 901-911

15 Gross, E., Kastner, D. B., Kaiser, C. A. and Fass, D. (2004) Structure of Ero1p, source of disulfide bonds for oxidative protein folding in the cell. Cell. **117**, 601-610

16 Parsons, H. G. and Dias, V. C. (1991) Intramitochondrial fatty acid metabolism: riboflavin deficiency and energy production. Biochem Cell Biol. **69**, 490-497

17 Myllykallio, H., Lipowski, G., Leduc, D., Filee, J., Forterre, P. and Liebl, U. (2002) An alternative flavin-dependent mechanism for thymidylate synthesis. Science. **297**, 105-107

18 Susin, S. A., Lorenzo, H. K., Zamzami, N., Marzo, I., Snow, B. E., Brothers, G. M., Mangion, J., Jacotot, E., Costantini, P., Loeffler, M., Larochette, N., Goodlett, D. R., Aebersold, R., Siderovski, D. P., Penninger, J. M. and Kroemer, G. (1999) Molecular characterization of mitochondrial apoptosis-inducing factor. Nature. **397**, 441-446

19 Joosten, V. and van Berkel, W. J. (2007) Flavoenzymes. Curr Opin Chem Biol. **11**, 195-202

20 A., W. B. (1897) The composition of cows' milk in health and disease. **35**, 530-538
21 Kuhn, R. and Weygand, F. (1934) Synthetic vitamin B2. ed.)^eds.). pp. 2084–2085, Berichte der deutschen chemischen Gesellschaf
22 P., K., K., S. and F., B. (1935) Synthesen von Flavinen IV. Helv Chim Acta. **18**, 426–429
23 Warburg, O. and Christian, W. (1933) The yellow enzyme and its functions. Biochem Z. **266**, 377–411
24 Theorell, H. (1935) Reindarstellung der Wirkungsgruppe der gelben Ferment. Biochem. Z. **275**, 344-349
25 Krebs, H. A. (1935) Metabolism of amino-acids: Deamination of amino-acids. Biochem J. **29**, 1620-1644
26 Warburg, O. and Christian, W. (1938) Isolierung der prosthetischen Gruppe der D-Aminosaureoxidase. Biochem. Z. **298**, 150-155.
27 Christie, S. M. H., Kenner, G. W. and Todd, A. R. (1954) Nucleotides. Part XXV. A synthesis of flavin-adenine dinucleotide. J Chem Soc, 46-52
28 Kupke, T., Stevanović, S., Sahl, H. G. and Götz, F. (1992) Purification and characterization of EpiD, a flavoprotein involved in the biosynthesis of the lantibiotic epidermin. J Bacteriol. **174**, 5354-5361
29 White, M. D., Payne, K. A., Fisher, K., Marshall, S. A., Parker, D., Rattray, N. J., Trivedi, D. K., Goodacre, R., Rigby, S. E., Scrutton, N. S., Hay, S. and Leys, D. (2015) UbiX is a flavin prenyltransferase required for bacterial ubiquinone biosynthesis. Nature. **522**, 502-506
30 Roberts, D. L., Frerman, F. E. and Kim, J. J. (1996) Three-dimensional structure of human electron transfer flavoprotein to 2.1-A resolution. Proc Natl Acad Sci U S A. **93**, 14355-14360
31 Serre, L., Medina, M., Gomez-Moreno, C., Fontecilla-Camps, J. C. and Frey, M. (1991) Crystals of Anabaena PCC 7119 ferredoxin-NADP+ reductase. J Mol Biol. **218**, 271-272
32 Lienhart, W. D., Gudipati, V. and Macheroux, P. (2013) The human flavoproteome. Arch Biochem Biophys. **535**, 150-162
33 Gudipati, V., Koch, K., Lienhart, W. D. and Macheroux, P. (2014) The flavoproteome of the yeast Saccharomyces cerevisiae. Biochim Biophys Acta. **1844**, 535-544
34 Macheroux, P., Kappes, B. and Ealick, S. E. (2011) Flavogenomics-a genomic and structural view of flavin-dependent proteins. Febs J. **278**, 2625-2634
35 Manstein, D. J., Massey, V., Ghisla, S. and Pai, E. F. (1988) Stereochemistry and accessibility of prosthetic groups in flavoproteins. Biochemistry. **27**, 2300-2305
36 Mulo, P. and Medina, M. (2017) Interaction and electron transfer between ferredoxin-NADP(+) oxidoreductase and its partners: structural, functional, and physiological implications. Photosynth. Res.
37 Couto, N., Wood, J. and Barber, J. (2016) The role of glutathione reductase and related enzymes on cellular redox homoeostasis network. Free Radic Biol Med. **95**, 27-42
38 Margoliash, E. (1963) Primary structure and evolution of cytochrome C. Proc Natl Acad Sci U S A. **50**, 672-679
39 Massey, V. (2000) The chemical and biological versatility of riboflavin. Biochem Soc Trans. **28**, 283-296
40 Dym, O. and Eisenberg, D. (2001) Sequence-structure analysis of FAD-containing proteins. Protein Sci. **10**, 1712-1728

41 Fontecave, M., Eliasson, R. and Reichard, P. (1987) NAD(P)H:flavin oxidoreductase of Escherichia coli. A ferric iron reductase participating in the generation of the free radical of ribonucleotide reductase. J Biol Chem. **262**, 12325-12331

42 Fieschi, F., Nivière, V., Frier, C., Décout, J. L. and Fontecave, M. (1995) The mechanism and substrate specificity of the NADPH:flavin oxidoreductase from Escherichia coli. J Biol Chem. **270**, 30392-30400

43 Shi, Z., Zachara, J. M., Shi, L., Wang, Z., Moore, D. A., Kennedy, D. W. and Fredrickson, J. K. (2012) Redox reactions of reduced flavin mononucleotide (FMN), riboflavin (RBF), and anthraquinone-2,6-disulfonate (AQDS) with ferrihydrite and lepidocrocite. Environ Sci Technol. **46**, 11644-11652

44 Edwards, A. M. (2006) General Properties of Flavins. Flavins Photochemistry and Photobiology. The Royal Society of Chemistry

45 Heels, P. (1982) The photophysical and photochemical properties of flavins (isoalloxazines), Chem Soc Rev

46 Michaelis, L., Schubert, M. P. and Smythe, C. V. (1936) The seminquinone of the flavine dyes, including vitamin B2. Science. **84**, 138-139

47 Michaelis, L. and Schwarzenbach, G. (1938) The intermediate forms of oxidation-reduction of the flavins. J. Biol. Chem. **123 (2)**, 527-542

48 Massey, V. (1994) Activation of molecular oxygen by flavins and flavoproteins. J Biol Chem. **269**, 22459-22462

49 Ghisla, S. and Massey, V. (1986) New flavins for old: artificial flavins as active site probes of flavoproteins. Biochem J. **239**, 1-12

50 CLARK, W. M. and LOWE, H. J. (1956) Studies on oxidation-reduction. XXIV. Oxidation-reduction potentials of flavin adenine dinucleotide. J Biol Chem. **221**, 983-992

51 Weber, G. (1950) Fluorescence of riboflavin and flavin-adenine dinucleotide. Biochem J. **47**, 114-121

52 van den Berg, P. W. A., Feenstra, K. A., Mark, A. E., Berendsen, H. J. C. and Visser, A. J. W. G. (2002) Dynamic conformations of flavin adeninde dinucleotide: simulated molecular dynamics of the flavin cofactor related to the time-resolved fluorescence characteristics. J. Phys. Chem. B. **106**, 8858-8869.

53 Massey, V. and Palmer, G. (1966) On the existence of spectrally distinct classes of flavoprotein semiquinones. A new method for the quantitative production of flavoprotein semiquinones. Biochemistry. **5**, 3181-3189

54 Dawson, R. M. C., Elliot, D. C., Elliot, W. H. and Jones, K. M. (1969) Data for biochemical research. ed.)^eds.), Oxford University Press.

55 Sun, M., Moore, T. A. and Song, P. S. (1972) Molecular luminescence studies of flavins. I. The excited states of flavins. J Am Chem Soc. **94**, 1730-1740

56 Keilin, D. and Hartree, E. F. (1946) Prosthetic group of glucose exidase (notatin). Nature. **157**, 801

57 Straub, F. B. (1939) Isolation and properties of a flavoprotein from heart muscle tissue. Biochem J. **33**, 787-792

58 Vogl, C., Grill, S., Schilling, O., Stulke, J., Mack, M. and Stolz, J. (2007) Characterization of riboflavin (vitamin B_2) transport proteins from *Bacillus subtilis* and *Corynebacterium glutamicum*. J Bacteriol. **189**, 7367-7375

59 Fischer, M., Haase, I., Feicht, R., Schramek, N., Kohler, P., Schieberle, P. and Bacher, A. (2005) Evolution of vitamin B_2 biosynthesis: riboflavin synthase of Arabidopsis thaliana and its inhibition by riboflavin. Biol Chem. **386**, 417-428

60 Abbas, C. A. and Sibirny, A. A. (2011) Genetic control of biosynthesis and transport of riboflavin and flavin nucleotides and construction of robust biotechnological producers. Microbiol Mol Biol Rev. **75**, 321-360
61 Fischer, M. and Bacher, A. (2005) Biosynthesis of flavocoenzymes. Nat Prod Rep. **22**, 324-350
62 Lee, S. S. and McCormick, D. B. (1985) Thyroid hormone regulation of flavocoenzyme biosynthesis. Arch Biochem Biophys. **237**, 197-201
63 Lee, S. S., Ye, J. H., Jones, D. P. and McCormick, D. B. (1983) Correlation of H_2O_2 production and liver catalase during riboflavin deficiency and repletion in mammals. Biochem Biophys Res Commun. **117**, 788-793
64 Santos, M. A., Jimenez, A. and Revuelta, J. L. (2000) Molecular characterization of FMN1, the structural gene for the monofunctional flavokinase of *Saccharomyces cerevisiae*. J Biol Chem. **275**, 28618-28624
65 Wu, M., Repetto, B., Glerum, D. M. and Tzagoloff, A. (1995) Cloning and characterization of FAD1, the structural gene for flavin adenine dinucleotide synthetase of *Saccharomyces cerevisiae*. Mol Cell Biol. **15**, 264-271
66 Barile, M., Brizio, C., Valenti, D., De Virgilio, C. and Passarella, S. (2000) The riboflavin/FAD cycle in rat liver mitochondria. Eur J Biochem. **267**, 4888-4900
67 Torchetti, E. M., Brizio, C., Colella, M., Galluccio, M., Giancaspero, T. A., Indiveri, C., Roberti, M. and Barile, M. (2010) Mitochondrial localization of human FAD synthetase isoform 1. Mitochondrion. **10**, 263-273
68 Galluccio, M., Brizio, C., Torchetti, E. M., Ferranti, P., Gianazza, E., Indiveri, C. and Barile, M. (2007) Over-expression in Escherichia coli, purification and characterization of isoform 2 of human FAD synthetase. Protein Expr Purif. **52**, 175-181
69 Sandoval, F. J. and Roje, S. (2005) An FMN hydrolase is fused to a riboflavin kinase homolog in plants. J Biol Chem. **280**, 38337-38345
70 Yruela, I., Arilla-Luna, S., Medina, M. and Contreras-Moreira, B. (2010) Evolutionary divergence of chloroplasts FAD synthetase proteins. BMC Evol Biol. **10**, 311
71 Giancaspero, T. A., Locato, V., de Pinto, M. C., De Gara, L. and Barile, M. (2009) The occurrence of riboflavin kinase and FAD synthetase ensures FAD synthesis in tobacco mitochondria and maintenance of cellular redox status. Febs J. **276**, 219-231
72 Mashhadi, Z., Xu, H., Grochowski, L. L. and White, R. H. (2010) Archaeal RibL: a new FAD synthetase that is air sensitive. Biochemistry. **49**, 8748-8755
73 Medina, M. (2012) FAD synthetase and FAD biosynthesis, Flavoproteins Handbook
74 Wang, W., Kim, R., Yokota, H. and Kim, S. H. (2005) Crystal structure of flavin binding to FAD synthetase of *Thermotoga maritima*. Proteins. **58**, 246-248
75 Wang, W., Kim, R., Jancarik, J., Yokota, H. and Kim, S. H. (2003) Crystal structure of a flavin-binding protein from *Thermotoga maritima*. Proteins. **52**, 633-635
76 Frago, S., Martínez-Júlvez, M., Serrano, A. and Medina, M. (2008) Structural analysis of FAD synthetase from *Corynebacterium ammoniagenes*. BMC Microbiol. **8**, 160
77 Krupa, A., Sandhya, K., Srinivasan, N. and Jonnalagadda, S. (2003) A conserved domain in prokaryotic bifunctional FAD synthetases can potentially catalyze nucleotide transfer. Trends Biochem Sci. **28**, 9-12
78 Arilla-Luna, S. (2013) Enzymes involved in the metabolismof flavins in prokayotic organism:structure-function relationship. ed.)^eds.), Zaragoza

79 Matern, A., Pedrolli, D., Großhennig, S., Johansson, J. and Mack, M. (2016) Uptake and Metabolism of Antibiotics Roseoflavin and 8-Demethyl-8-Aminoriboflavin in Riboflavin-Auxotrophic Listeria monocytogenes. J Bacteriol. **198**, 3233-3243
80 Crooks, G. E., Hon, G., Chandonia, J. M. and Brenner, S. E. (2004) WebLogo: a sequence logo generator. Genome Res. **14**, 1188-1190
81 Efimov, I., Kuusk, V., Zhang, X. and McIntire, W. S. (1998) Proposed steady-state kinetic mechanism for *Corynebacterium ammoniagenes* FAD synthetase produced by *Escherichia coli*. Biochemistry. **37**, 9716-9723
82 Manstein, D. J. and Pai, E. F. (1986) Purification and characterization of FAD synthetase from *Brevibacterium ammoniagenes*. J Biol Chem. **261**, 16169-16173
83 Rossmann, M. G., Moras, D. and Olsen, K. W. (1974) Chemical and biological evolution of nucleotide-binding protein. Nature. **250**, 194-199
84 Frago, S., Velázquez-Campoy, A. and Medina, M. (2009) The puzzle of ligand binding to *Corynebacterium ammoniagenes* FAD synthetase. J Biol Chem. **284**, 6610-6619
85 Herguedas, B., Martinez-Julvez, M., Frago, S., Medina, M. and Hermoso, J. A. (2010) Oligomeric state in the crystal structure of modular FAD synthetase provides insights into its sequential catalysis in prokaryotes. J Mol Biol. **400**, 218-230
86 Herguedas, B., Martínez-Júlvez, M., Frago, S., Medina, M. and Hermoso, J. A. (2009) Crystallization and preliminary X-ray diffraction studies of FAD synthetase from *Corynebacterium ammoniagenes*. Acta Crystallogr Sect F Struct Biol Cryst Commun. **65**, 1285-1288
87 Serrano, A., Sebastian, M., Arilla-Luna, S., Baquedano, S., Pallares, M. C., Lostao, A., Herguedas, B., Velazquez-Campoy, A., Martinez-Julvez, M. and Medina, M. (2015) Quaternary organization in a bifunctional prokaryotic FAD synthetase: Involvement of an arginine at its adenylyltransferase module on the riboflavin kinase activity. BBAPRO-14-491R2
88 Serrano, A., Frago, S., Herguedas, B., Martínez-Júlvez, M., Velázquez-Campoy, A. and Medina, M. (2013) Key residues at the riboflavin kinase catalytic site of the bifunctional Riboflavin kinase/FMN adenylyltransferase from *Corynebacterium ammoniagenes*. Cell Biochem Biophys. **65**, 57-68.
89 Serrano, A., Ferreira, P., Martínez-Júlvez, M. and Medina, M. (2013) The prokaryotic FAD synthetase family: a potential drug target. Curr Pharm Des. **19**, 2637-2648
90 Serrano, A., Frago, S., Velázquez-Campoy, A. and Medina, M. (2012) Role of key residues at the flavin mononucleotide (FMN):adenylyltransferase catalytic site of the bifunctional riboflavin kinase/flavin adenine dinucleotide (FAD) synthetase from *Corynebacterium ammoniagenes*. Int. J. Mol. Sci. **13**, 14492-14517
91 Spencer, R., Fisher, J. and Walsh, C. (1976) Preparation, characterization, and chemical properties of the flavin coenzyme analogues 5-deazariboflavin, 5-deazariboflavin 5'-phosphate, and 5-deazariboflavin 5'-diphosphate, leads to 5'-adenosine ester. Biochemistry. **15**, 1043-1053
92 Thorpe, C. and Massey, V. (1983) Flavin analogue studies of pig kidney general acyl-CoA dehydrogenase. Biochemistry. **22**, 2972-2978
93 Krauth-Siegel, R. L., Schirmer, R. H. and Ghisla, S. (1985) FAD analogues as prosthetic groups of human glutathione reductase. Properties of the modified enzyme species and comparisons with the active site structure. Eur J Biochem. **148**, 335-344
94 Hagihara, T., Fujio, T. and Aisaka, K. (1995) Cloning of FAD synthetase gene from *Corynebacterium ammoniagenes* and its application to FAD and FMN production. Appl Microbiol Biotechnol. **42**, 724-729

95 Serrano, A., Frago, S., Herguedas, B., Martinez-Julvez, M., Velazquez-Campoy, A. and Medina, M. (2013) Key residues at the riboflavin kinase catalytic site of the bifunctional riboflavin kinase/FMN adenylyltransferase from Corynebacterium ammoniagenes. Cell Biochem Biophys. **65**, 57-68
96 Bauer, S., Kemter, K., Bacher, A., Huber, R., Fischer, M. and Steinbacher, S. (2003) Crystal structure of *Schizosaccharomyces pombe* riboflavin kinase reveals a novel ATP and riboflavin-binding fold. J Mol Biol. **326**, 1463-1473
97 Karthikeyan, S., Zhou, Q., Mseeh, F., Grishin, N. V., Osterman, A. L. and Zhang, H. (2003) Crystal structure of human riboflavin kinase reveals a beta barrel fold and a novel active site arch. Structure. **11**, 265-273
98 Karthikeyan, S., Zhou, Q., Osterman, A. L. and Zhang, H. (2003) Ligand binding-induced conformational changes in riboflavin kinase: structural basis for the ordered mechanism. Biochemistry. **42**, 12532-12538
99 Herguedas, B., Lans, I., Sebastián, M., Hermoso, J. A., Martínez-Júlvez, M. and Medina, M. (2015) Structural insights into the synthesis of FMN in prokaryotic organisms. Acta Crystallogr D Biol Crystallogr. **71**, 2526-2542
100 Marcuello, C., Arilla-Luna, S., Medina, M. and Lostao, A. Detection of a quaternary organization into dimer of trimers of Corynebacterium ammoniagenes FAD synthetase at the single-molecule level and at the in cell level. Biochim Biophys Acta. **1834**, 665-676
101 Drijkoningen, J. J. and Rohde, G. G. (2014) Pneumococcal infection in adults: burden of disease. Clin Microbiol Infect. **20 Suppl 5**, 45-51
102 Todar. Online Texbook of Bacteriology
103 Weinberger, D. M., Trzciński, K., Lu, Y. J., Bogaert, D., Brandes, A., Galagan, J., Anderson, P. W., Malley, R. and Lipsitch, M. (2009) Pneumococcal capsular polysaccharide structure predicts serotype prevalence. PLoS Pathog. **5**, e1000476
104 Jedrzejas, M. J. (2001) Pneumococcal virulence factors: structure and function. Microbiol Mol Biol Rev. **65**, 187-207 ; first page, table of contents
105 Mitchell, A. M. and Mitchell, T. J. (2010) Streptococcus pneumoniae: virulence factors and variation. Clin Microbiol Infect. **16**, 411-418
106 Zhang, J. R., Mostov, K. E., Lamm, M. E., Nanno, M., Shimida, S., Ohwaki, M. and Tuomanen, E. (2000) The polymeric immunoglobulin receptor translocates pneumococci across human nasopharyngeal epithelial cells. Cell. **102**, 827-837
107 Braathen, R., Sandvik, A., Berntzen, G., Hammerschmidt, S., Fleckenstein, B., Sandlie, I., Brandtzaeg, P., Johansen, F. E. and Lauvrak, V. (2006) Identification of a polymeric Ig receptor binding phage-displayed peptide that exploits epithelial transcytosis without dimeric IgA competition. J Biol Chem. **281**, 7075-7081
108 Canvin, J. R., Marvin, A. P., Sivakumaran, M., Paton, J. C., Boulnois, G. J., Andrew, P. W. and Mitchell, T. J. (1995) The role of pneumolysin and autolysin in the pathology of pneumonia and septicemia in mice infected with a type 2 pneumococcus. J Infect Dis. **172**, 119-123
109 Löfling, J., Vimberg, V., Battig, P. and Henriques-Normark, B. (2011) Cellular interactions by LPxTG-anchored pneumococcal adhesins and their streptococcal homologues. Cell Microbiol. **13**, 186-197
110 Radin, J. N., Orihuela, C. J., Murti, G., Guglielmo, C., Murray, P. J. and Tuomanen, E. I. (2005) beta-Arrestin 1 participates in platelet-activating factor receptor-mediated endocytosis of Streptococcus pneumoniae. Infect Immun. **73**, 7827-7835

111 Birgitta Henriques-Normark and Tuomanen, E. I. (2016) The Pneumococcus: Epidemiology, Microbiology, and Pathogenesis. Cold Spring Harbor Perspectives in Medicine
112 Torres, A., Blasi, F., Peetermans, W. E., Viegi, G. and Welte, T. (2014) The aetiology and antibiotic management of community-acquired pneumonia in adults in Europe: a literature review. Eur J Clin Microbiol Infect Dis. **33**, 1065-1079
113 Feldman, C. and Anderson, R. (2016) Epidemiology, virulence factors and management of the pneumococcus. F1000Res. **5**, 2320
114 Fuller, J. D., McGeer, A. and Low, D. E. (2005) Drug-resistant pneumococcal pneumonia: clinical relevance and approach to management. Eur J Clin Microbiol Infect Dis. **24**, 780-788
115 Steel, H. C., Cockeran, R., Anderson, R. and Feldman, C. (2013) Overview of community-acquired pneumonia and the role of inflammatory mechanisms in the immunopathogenesis of severe pneumococcal disease. Mediators Inflamm. **2013**, 490346
116 Karchmer, A. W., &lt, style&gt, W., A. and Karchmer. (2004) Increased Antibiotic Resistance in Respiratory Tract Pathogens: PROTEKT US—An Update, Clinical Infectious Diseases
117 Collins, D. M. (1996) In search of tuberculosis virulence genes. Trends Microbiol. **4**, 426-430
118 Cole, S. T., Brosch, R., Parkhill, J., Garnier, T., Churcher, C., Harris, D., Gordon, S. V., Eiglmeier, K., Gas, S., Barry, C. E., Tekaia, F., Badcock, K., Basham, D., Brown, D., Chillingworth, T., Connor, R., Davies, R., Devlin, K., Feltwell, T., Gentles, S., Hamlin, N., Holroyd, S., Hornsby, T., Jagels, K., Krogh, A., McLean, J., Moule, S., Murphy, L., Oliver, K., Osborne, J., Quail, M. A., Rajandream, M. A., Rogers, J., Rutter, S., Seeger, K., Skelton, J., Squares, R., Squares, S., Sulston, J. E., Taylor, K., Whitehead, S. and Barrell, B. G. (1998) Deciphering the biology of Mycobacterium tuberculosis from the complete genome sequence. Nature. **393**, 537-544
119 Brosch, R., Gordon, S. V., Marmiesse, M., Brodin, P., Buchrieser, C., Eiglmeier, K., Garnier, T., Gutierrez, C., Hewinson, G., Kremer, K., Parsons, L. M., Pym, A. S., Samper, S., van Soolingen, D. and Cole, S. T. (2002) A new evolutionary scenario for the Mycobacterium tuberculosis complex. Proc Natl Acad Sci U S A. **99**, 3684-3689
120 Dubos, R. J. and Middlebrook, G. (1947) Media for tubercle bacilli. Am Rev Tuberc. **56**, 334-345
121 Brennan, P. J. and Nikaido, H. (1995) The envelope of mycobacteria. Annu Rev Biochem. **64**, 29-63
122 Song, H., Sandie, R., Wang, Y., Andrade-Navarro, M. A. and Niederweis, M. (2008) Identification of outer membrane proteins of Mycobacterium tuberculosis. Tuberculosis (Edinb). **88**, 526-544
123 Wolfe, L. M., Mahaffey, S. B., Kruh, N. A. and Dobos, K. M. (2010) Proteomic definition of the cell wall of Mycobacterium tuberculosis. J Proteome Res. **9**, 5816-5826
124 Barry, C. E. (2001) Interpreting cell wall 'virulence factors' of Mycobacterium tuberculosis. Trends Microbiol. **9**, 237-241
125 Takayama, K., Wang, C. and Besra, G. S. (2005) Pathway to synthesis and processing of mycolic acids in Mycobacterium tuberculosis. Clin Microbiol Rev. **18**, 81-101
126 Hunter, R. L., Olsen, M. R., Jagannath, C. and Actor, J. K. (2006) Multiple roles of cord factor in the pathogenesis of primary, secondary, and cavitary tuberculosis,

including a revised description of the pathology of secondary disease. Ann Clin Lab Sci. **36**, 371-386
127 Rajni, Rao, N. and Meena, L. S. (2011) Biosynthesis and Virulent Behavior of Lipids Produced by Mycobacterium tuberculosis: LAM and Cord Factor: An Overview. Biotechnol Res Int. **2011**, 274693
128 Silva, C. L., Ekizlerian, S. M. and Fazioli, R. A. (1985) Role of cord factor in the modulation of infection caused by mycobacteria. Am J Pathol. **118**, 238-247
129 Spargo, B. J., Crowe, L. M., Ioneda, T., Beaman, B. L. and Crowe, J. H. (1991) Cord factor (alpha,alpha-trehalose 6,6'-dimycolate) inhibits fusion between phospholipid vesicles. Proc Natl Acad Sci U S A. **88**, 737-740
130 Azuma, I., Kimura, H. and Yamamura, Y. (1968) Chemical and immunological properties of polysaccharides of wax D extracted from Mycobacterium tuberculosis strain Aoyama B. J Bacteriol. **96**, 567-568
131 Houben, E. N., Nguyen, L. and Pieters, J. (2006) Interaction of pathogenic mycobacteria with the host immune system. Curr Opin Microbiol. **9**, 76-85
132 Suarez, J., Ranguelova, K., Schelvis, J. P. and Magliozzo, R. S. (2009) Antibiotic resistance in Mycobacterium tuberculosis: peroxidase intermediate bypass causes poor isoniazid activation by the S315G mutant of M. tuberculosis catalase-peroxidase (KatG). J Biol Chem. **284**, 16146-16155
133 Alteri, C. J., Xicohténcatl-Cortes, J., Hess, S., Caballero-Olín, G., Girón, J. A. and Friedman, R. L. (2007) Mycobacterium tuberculosis produces pili during human infection. Proc Natl Acad Sci U S A. **104**, 5145-5150
134 Pieters, J. (2001) Entry and survival of pathogenic mycobacteria in macrophages. Microbes Infect. **3**, 249-255
135 Wayne, L. G. (1994) Dormancy of Mycobacterium tuberculosis and latency of disease. Eur J Clin Microbiol Infect Dis. **13**, 908-914
136 Deretic, V. and Fratti, R. A. (1999) Mycobacterium tuberculosis phagosome. Mol Microbiol. **31**, 1603-1609
137 Fenton, M. J. and Vermeulen, M. W. (1996) Immunopathology of tuberculosis: roles of macrophages and monocytes. Infect Immun. **64**, 683-690
138 Ehlers, M. R. and Daffé, M. (1998) Interactions between Mycobacterium tuberculosis and host cells: are mycobacterial sugars the key? Trends Microbiol. **6**, 328-335
139 Cosma, C. L., Sherman, D. R. and Ramakrishnan, L. (2003) The secret lives of the pathogenic mycobacteria. Annu Rev Microbiol. **57**, 641-676
140 Behar, S. M., Martin, C. J., Booty, M. G., Nishimura, T., Zhao, X., Gan, H. X., Divangahi, M. and Remold, H. G. (2011) Apoptosis is an innate defense function of macrophages against Mycobacterium tuberculosis. Mucosal Immunol. **4**, 279-287
141 Yuan, Y., Crane, D. D., Simpson, R. M., Zhu, Y. Q., Hickey, M. J., Sherman, D. R. and Barry, C. E. (1998) The 16-kDa alpha-crystallin (Acr) protein of Mycobacterium tuberculosis is required for growth in macrophages. Proc Natl Acad Sci U S A. **95**, 9578-9583
142 Clark-Curtiss, J. E. and Haydel, S. E. (2003) Molecular genetics of Mycobacterium tuberculosis pathogenesis. Annu Rev Microbiol. **57**, 517-549
143 Flynn, J. L. and Chan, J. (2005) What's good for the host is good for the bug. Trends Microbiol. **13**, 98-102
144 Tortoli, E., Cichero, P., Piersimoni, C., Simonetti, M. T., Gesu, G. and Nista, D. (1999) Use of BACTEC MGIT 960 for recovery of mycobacteria from clinical specimens: multicenter study. J Clin Microbiol. **37**, 3578-3582
145 Mendel, F. (1908) Die von Pirquet'sche Hautreaktion und die

intravenöse Tuberkulinbehandlung. Medizinische Klinik. **4**, 402-404
146 Pérez-Stable, E. J. and Hopewell, P. C. (1989) Current tuberculosis treatment regimens. Choosing the right one for your patient. Clin Chest Med. **10**, 323-339
147 Kaufmann, S. H., Weiner, J. and von Reyn, C. F. (2017) Novel approaches to tuberculosis vaccine development. Int J Infect Dis. **56**, 263-267
148 O'Brien, R. J. (1994) Drug-resistant tuberculosis: etiology, management and prevention. Semin Respir Infect. **9**, 104-112
149 Maitre, T., Aubry, A., Jarlier, V., Robert, J., Veziris, N. and CNR-MyRMA. (2017) Multidrug and extensively drug-resistant tuberculosis. Med Mal Infect. **47**, 3-10
150 Manjelievskaia, J., Erck, D., Piracha, S. and Schrager, L. (2016) Drug-resistant TB: deadly, costly and in need of a vaccine. Trans R Soc Trop Med Hyg. **110**, 186-191
151 Kumar, V. A., AK. Fausto, N. and Mitchell, R. (2007) Robbins Basic Pathology (8th ed.), Saunders Elsevier
152 Barile, M., Giancaspero, T. A., Leone, P., Galluccio, M. and Indiveri, C. (2016) Riboflavin transport and metabolism in humans. J Inherit Metab Dis. **39**, 545-557
153 Sassetti, C. M., Boyd, D. H. and Rubin, E. J. (2003) Genes required for mycobacterial growth defined by high density mutagenesis. Mol Microbiol. **48**, 77-84
154 Griffin, J. E., Gawronski, J. D., Dejesus, M. A., Ioerger, T. R., Akerley, B. J. and Sassetti, C. M. (2011) High-resolution phenotypic profiling defines genes essential for mycobacterial growth and cholesterol catabolism. PLoS Pathog. **7**, e1002251
155 Barile, M., Passarella, S., Bertoldi, A. and Quagliariello, E. (1993) Flavin adenine dinucleotide synthesis in isolated rat liver mitochondria caused by imported flavin mononucleotide. Arch Biochem Biophys. **305**, 442-447
156 Giancaspero, T. A., Colella, M., Brizio, C., Difonzo, G., Fiorino, G. M., Leone, P., Brandsch, R., Bonomi, F., Iametti, S. and Barile, M. (2015) Remaining challenges in cellular flavin cofactor homeostasis and flavoprotein biogenesis. Front Chem. **3**, 30
157 Dagert, M. and Ehrlich, S. D. (1979) Prolonged incubation in calcium chloride improves the competence of Escherichia coli cells. Gene. **6**, 23-28
158 Bradford, M. M. (1976) A rapid and sensitive method for the quantitation of microgram quantities of protein utilizing the principle of protein-dye binding. Anal Biochem. **72**, 248-254
159 Whitmore, L. and Wallace, B. A. (2008) Protein secondary structure analyses from circular dichroism spectroscopy: methods and reference databases. Biopolymers. **89**, 392-400
160 Fasman, G. D. (1996) Circular dichroism and the conformational analysis of biomolecules, Springer
161 Greenfield, N. J. (2006) Using circular dichroism spectra to estimate protein secondary structure. Nat Protoc. **1**, 2876-2890
162 Holzwarth, G. and Doty, P. (1965) The ultraviolet circular dichroism of polypeptides. J Am Chem Soc. **87**, 218-228
163 Gehring, K., Bao, K. and Nikaido, H. (1992) UV difference spectroscopy of ligand binding to maltose-binding protein. FEBS Lett. **300**, 33-38
164 Saito, T., Nishino, T. and Massey, V. (1989) Differences in environment of FAD between NAD-dependent and O2-dependent types of rat liver xanthine dehydrogenase shown by active site probe study. J Biol Chem. **264**, 15930-15935
165 Halle, B. and Davidovic, M. (2003) Biomolecular hydration: from water dynamics to hydrodynamics. Proc Natl Acad Sci U S A. **100**, 12135-12140
166 Kirchner, J. G., Miller, J. M. and Keller, G. J. (1951) Separation and identification of Some Terpenes by New Chromatographic Technique. Anal. Chem, 420-425

167 Poole, C. F. and Poole, S. K. (1991) Chromatogrphy Today, Elsevier Science
168 Blum, F. (2014) High performance liquid chromatography. Br J Hosp Med (Lond). **75**, C18-21
169 Michaelis, L. and Menten, M. L. (1913) Die Kinetik der Invertinwerkung. Biochem. Z. **49**, 333
170 Leskovac, V. (2003) Comprehensive enzyme kinetics. Kluwer Adacemic / Plenum Publishers, New York
171 Simondsen, R. P. and Tollin, G. (1983) Transient kinetics of redox reactions of flavodoxin: effects of chemical modification of the flavin mononucleotide prosthetic group on the dynamics of intermediate complex formation and electron transfer. Biochemistry. **22**, 3008-3016
172 Cornish-Bowden, A. (1973) A Simple Method for Determinig the Inhibition Constants of Mixed, Uncompetitive and Non-Competitive Inhibitors. ed.)^eds.). pp. 143-144, Biochem.J.
173 Lineweaver, H. and Burk, D. (1934) The determination of enzyme dissociation constants. J. Am. Chem. Soc. **56**, 658-666
174 Hofstee, B. H. (1959) Non-inverted versus inverted plots in enzyme kinetics. Nature. **184**, 1296-1298
175 Yamada, Y., Merrill, A. H., Jr. and McCormick, D. B. (1990) Probable reaction mechanisms of flavokinase and FAD synthetase from rat liver. Arch Biochem Biophys. **278**, 125-130
176 Drewe, W. F., Koerber, S. C. and Dunn, M. F. (1989) Application of rapid-scanning, stopped-flow spectroscopy to the characterization of intermediates formed in the reactions of L- and D-tryptophan and beta-mercaptoethanol with Escherichia coli tryptophan synthase. Biochimie. **71**, 509-519
177 West, J. M., Xia, J., Tsuruta, H., Guo, W., O'Day, E. M. and Kantrowitz, E. R. (2008) Time evolution of the quaternary structure of Escherichia coli aspartate transcarbamoylase upon reaction with the natural substrates and a slow, tight-binding inhibitor. J Mol Biol. **384**, 206-218
178 Lew, J., Taylor, S. S. and Adams, J. A. (1997) Identification of a partially rate-determining step in the catalytic mechanism of cAMP-dependent protein kinase: a transient kinetic study using stopped-flow fluorescence spectroscopy. Biochemistry. **36**, 6717-6724
179 O'Brien, R., Ladbury, J. E. and B.Z., C. (2000) Isothermal titration calorimetry of biomolecules. In Protein-Ligand interactions: hydrodynamics and calorimetry, Oxford University Press
180 Pierce, M. M., Raman, C. S. and Nall, B. T. (1999) Isothermal titration calorimetry of protein-protein interactions. Methods. **19**, 213-221
181 Velazquez-Campoy, A., Leavitt, S. A. and Freire, E. (2004) Characterization of protein-protein interactions by isothermal titration calorimetry. Methods Mol Biol. **261**, 35-54
182 Ladbury, J. E. and Chowdhry, B. Z. (1996) Sensing the heat: the application of isothermal titration calorimetry to thermodynamic studies of biomolecular interactions. Chem Biol. **3**, 791-801
183 Velazquez-Campoy, A., Goñi, G., Peregrina, J. R. and Medina, M. (2006) Exact analysis of heterotropic interactions in proteins: Characterization of cooperative ligand binding by isothermal titration calorimetry. Biophys J. **91**, 1887-1904
184 Feeney, J., Birdsall, B., Kovalevskaya, N. V., Smurnyy, Y. D., Navarro Peran, E. M. and Polshakov, V. I. (2011) NMR structures of apo L. casei dihydrofolate reductase and its complexes with trimethoprim and NADPH: contributions to positive

cooperative binding from ligand-induced refolding, conformational changes, and interligand hydrophobic interactions. Biochemistry. **50**, 3609-3620
185 Abeliovich, H. (2005) An empirical extremum principle for the hill coefficient in ligand-protein interactions showing negative cooperativity. Biophys J. **89**, 76-79
186 Aramaki, H., Kabata, H., Takeda, S., Itou, H., Nakayama, H. and Shimamoto, N. (2011) Formation of repressor-inducer-operator ternary complex: negative cooperativity of d-camphor binding to CamR. Genes Cells. **16**, 1200-1207
187 Martínez-Júlvez, M., Medina, M. and Velázquez-Campoy, A. (2009) Binding thermodynamics of ferredoxin:NADP+ reductase: two different protein substrates and one energetics. Biophys J. **96**, 4966-4975
188 Caraus, I., Alsuwailem, A. A., Nadon, R. and Makarenkov, V. (2015) Detecting and overcoming systematic bias in high-throughput screening technologies: a comprehensive review of practical issues and methodological solutions. Brief Bioinform. **16**, 974-986
189 Hann, M. M. and Oprea, T. I. (2004) Pursuing the leadlikeness concept in pharmaceutical research. Curr Opin Chem Biol. **8**, 255-263
190 Aubi, O., Flydal, M. I., Zheng, H., Skjærven, L., Rekand, I., Leiros, H. K., Haug, B. E., Cianciotto, N. P., Martinez, A. and Underhaug, J. (2015) Discovery of a Specific Inhibitor of Pyomelanin Synthesis in Legionella pneumophila. J Med Chem. **58**, 8402-8412
191 Pey, A. L., Ying, M., Cremades, N., Velazquez-Campoy, A., Scherer, T., Thony, B., Sancho, J. and Martinez, A. (2008) Identification of pharmacological chaperones as potential therapeutic agents to treat phenylketonuria. J Clin Invest. **118**, 2858-2867
192 Dillon, M. B., Bachovchin, D. A., Brown, S. J., Finn, M. G., Rosen, H., Cravatt, B. F. and Mowen, K. A. (2012) Novel inhibitors for PRMT1 discovered by high-throughput screening using activity-based fluorescence polarization. ACS Chem Biol. **7**, 1198-1204
193 Hu, Y., Chen, G. Y. and Yao, S. Q. (2005) Activity-based high-throughput screening of enzymes by using a DNA microarray. Angew Chem Int Ed Engl. **44**, 1048-1053
194 Deu, E., Yang, Z., Wang, F., Klemba, M. and Bogyo, M. (2010) Use of activity-based probes to develop high throughput screening assays that can be performed in complex cell extracts. PLoS One. **5**, e11985
195 Klebe, G. (2015) Applying thermodynamic profiling in lead finding and optimization. Nat Rev Drug Discov. **14**, 95-110
196 Freire, E. (2015) The Binding Thermodynamics of Drug Candidates
197 Pesch, K. and Simmert, U. (1929) Combined assays for lactose and galactose by enzymatic reactions. ed.)^eds.)
198 Anoopkumar-Dukie, S., Carey, J. B., Conere, T., O'sullivan, E., van Pelt, F. N. and Allshire, A. (2005) Resazurin assay of radiation response in cultured cells. Br J Radiol. **78**, 945-947
199 Delano, W. L. (2002) The PyMOL Molecular Graphics System. ed.)^eds.)
200 Grishin, N. V. and Phillips, M. A. (1994) The subunit interfaces of oligomeric enzymes are conserved to a similar extent to the overall protein sequences. Protein Sci. **3**, 2455-2458
201 Moreno, M. A., Abramov, A., Abendroth, J., Alonso, A., Zhang, S., Alcolea, P. J., Edwards, T., Lorimer, D., Myler, P. J. and Larraga, V. (2014) Structure of tyrosine aminotransferase from Leishmania infantum. Acta Crystallogr F Struct Biol Commun. **70**, 583-587

202 Wubben, T. J. and Mesecar, A. D. (2010) Kinetic, thermodynamic, and structural insight into the mechanism of phosphopantetheine adenylyltransferase from Mycobacterium tuberculosis. J Mol Biol. **404**, 202-219
203 Garavaglia, S., D'Angelo, I., Emanuelli, M., Carnevali, F., Pierella, F., Magni, G. and Rizzi, M. (2002) Structure of human NMN adenylyltransferase. A key nuclear enzyme for NAD homeostasis. J Biol Chem. **277**, 8524-8530
204 Zhai, R. G., Rizzi, M. and Garavaglia, S. (2009) Nicotinamide/nicotinic acid mononucleotide adenylyltransferase, new insights into an ancient enzyme. Cell Mol Life Sci. **66**, 2805-2818
205 Izard, T. and Geerlof, A. (1999) The crystal structure of a novel bacterial adenylyltransferase reveals half of sites reactivity. EMBO J. **18**, 2021-2030
206 Izard, T. (2002) The crystal structures of phosphopantetheine adenylyltransferase with bound substrates reveal the enzyme's catalytic mechanism. J Mol Biol. **315**, 487-495
207 Akiva, E., Itzhaki, Z. and Margalit, H. (2008) Built-in loops allow versatility in domain-domain interactions: lessons from self-interacting domains. Proc Natl Acad Sci U S A. **105**, 13292-13297
208 Gabizon, R. and Friedler, A. (2014) Allosteric modulation of protein oligomerization: an emerging approach to drug design. Front Chem. **2**, 9
209 Marsh, J. A. and Teichmann, S. A. (2015) Structure, dynamics, assembly, and evolution of protein complexes. Annu Rev Biochem. **84**, 551-575
210 Marsh, J. A. and Teichmann, S. A. (2014) Protein flexibility facilitates quaternary structure assembly and evolution. PLoS Biol. **12**, e1001870
211 Korennykh, A. V., Egea, P. F., Korostelev, A. A., Finer-Moore, J., Stroud, R. M., Zhang, C., Shokat, K. M. and Walter, P. (2011) Cofactor-mediated conformational control in the bifunctional kinase/RNase Ire1. BMC Biol. **9**, 48
212 Liuzzi, V. C., Giancaspero, T. A., Gianazza, E., Banfi, C., Barile, M. and De Giorgi, C. (2012) Silencing of FAD synthase gene in Caenorhabditis elegans upsets protein homeostasis and impacts on complex behavioral patterns. Biochim Biophys Acta. **1820**, 521-531
213 Torchetti, E. M., Bonomi, F., Galluccio, M., Gianazza, E., Giancaspero, T. A., Lametti, S., Indiveri, C. and Barile, M. (2011) Human FAD synthase (isoform 2): a component of the machinery that delivers FAD to apo-flavoproteins. Febs J. **278**, 4434-4449
214 Krissinel, E. and Henrick, K. (2007) Inference of macromolecular assemblies from crystalline state. J Mol Biol. **372**, 774-797
215 Bollen, Y. J., Westphal, A. H., Lindhoud, S., van Berkel, W. J. and van Mierlo, C. P. (2012) Distant residues mediate picomolar binding affinity of a protein cofactor. Nat Commun. **3**, 1010
216 Gulve, E. A. and Dice, J. F. (1989) Regulation of protein synthesis and degradation in L8 myotubes. Effects of serum, insulin and insulin-like growth factors. Biochem J. **260**, 377-387
217 Cárdenas, M. L., Cornish-Bowden, A. and Ureta, T. (1998) Evolution and regulatory role of the hexokinases. Biochim Biophys Acta. **1401**, 242-264
218 Gerhart, J. (2014) From feedback inhibition to allostery: the enduring example of aspartate transcarbamoylase. FEBS J. **281**, 612-620
219 Rogers, M. A., Liu, J., Song, B. L., Li, B. L., Chang, C. C. and Chang, T. Y. (2015) Acyl-CoA:cholesterol acyltransferases (ACATs/SOATs): Enzymes with multiple sterols as substrates and as activators. J Steroid Biochem Mol Biol. **151**, 102-107

220 Cecchini, G., Perl, M., Lipsick, J., Singer, T. P. and Kearney, E. B. (1979) Transport and binding of riboflavin by *Bacillus subtilis*. J Biol Chem. **254**, 7295-7301
221 Grill, S., Yamaguchi, H., Wagner, H., Zwahlen, L., Kusch, U. and Mack, M. (2007) Identification and characterization of two *Streptomyces davawensis* riboflavin biosynthesis gene clusters. Arch Microbiol. **188**, 377-387
222 Grill, S., Busenbender, S., Pfeiffer, M., Kohler, U. and Mack, M. (2008) The bifunctional flavokinase/flavin adenine dinucleotide synthetase from *Streptomyces davawensis* produces inactive flavin cofactors and is not involved in resistance to the antibiotic roseoflavin. J Bacteriol. **190**, 1546-1553
223 Kearney, E. B., Goldenberg, J., Lipsick, J. and Perl, M. (1979) Flavokinase and FAD synthetase from *Bacillus subtilis* specific for reduced flavins. J Biol Chem. **254**, 9551-9557
224 Raussens, V., Ruysschaert, J. M. and Goormaghtigh, E. (2003) Protein concentration is not an absolute prerequisite for the determination of secondary structure from circular dichroism spectra: a new scaling method. Anal Biochem. **319**, 114-121
225 Pedrolli, D. B., Nakanishi, S., Barile, M., Mansurova, M., Carmona, E. C., Lux, A., Gartner, W. and Mack, M. (2011) The antibiotics roseoflavin and 8-demethyl-8-amino-riboflavin from *Streptomyces davawensis* are metabolized by human flavokinase and human FAD synthetase. Biochem Pharmacol. **82**, 1853-1859
226 Langer, S., Hashimoto, M., Hobl, B., Mathes, T. and Mack, M. (2013) Flavoproteins are potential targets for the antibiotic roseoflavin in Escherichia coli. J Bacteriol. **195**, 4037-4045
227 Massey, V. (1995) Introduction: flavoprotein structure and mechanism. FASEB J. **9**, 473-475
228 Fischer, M., Romisch, W., Illarionov, B., Eisenreich, W. and Bacher, A. (2005) Structures and reaction mechanisms of riboflavin synthases of eubacterial and archaeal origin. Biochem Soc Trans. **33**, 780-784
229 Mack, M., van Loon, A. P. and Hohmann, H. P. (1998) Regulation of riboflavin biosynthesis in *Bacillus subtilis* is affected by the activity of the flavokinase/flavin adenine dinucleotide synthetase encoded by ribC. J Bacteriol. **180**, 950-955
230 Olsson, T. S., Williams, M. A., Pitt, W. R. and Ladbury, J. E. (2008) The thermodynamics of protein-ligand interaction and solvation: insights for ligand design. J Mol Biol. **384**, 1002-1017
231 Saxena, T., Loomis, K. H., Pai, S. B., Karumbaiah, L., Gaupp, E., Patil, K., Patkar, R. and Bellamkonda, R. V. (2015) Nanocarrier-mediated inhibition of macrophage migration inhibitory factor attenuates secondary injury after spinal cord injury. ACS Nano. **9**, 1492-1505
232 Normand, A., Rivière, E. and Renodon-Cornière, A. (2014) Identification and characterization of human Rad51 inhibitors by screening of an existing drug library. Biochem Pharmacol. **91**, 293-300
233 Risse, E., Nicoll, A. J., Taylor, W. A., Wright, D., Badoni, M., Yang, X., Farrow, M. A. and Collinge, J. (2015) Identification of a Compound That Disrupts Binding of Amyloid-β to the Prion Protein Using a Novel Fluorescence-based Assay. J Biol Chem. **290**, 17020-17028
234 He, Z., Yan, L., Yong, Z., Dong, Z., Dong, H. and Gong, Z. (2013) Chicago sky blue 6B, a vesicular glutamate transporters inhibitor, attenuates methamphetamine-induced hyperactivity and behavioral sensitization in mice. Behav Brain Res. **239**, 172-176

235 Soufir, J. C. (2017) Hormonal, chemical and thermal inhibition of spermatogenesis: contribution of French teams to international data with the aim of developing male contraception in France. Basic Clin Androl. **27**, 3
236 Ferdek, P. E., Jakubowska, M. A., Nicolaou, P., Gerasimenko, J. V., Gerasimenko, O. V. and Petersen, O. H. (2017) BH3 mimetic-elicited Ca(2+) signals in pancreatic acinar cells are dependent on Bax and can be reduced by Ca(2+)-like peptides. Cell Death Dis. **8**, e2640
237 Xiong, J., Li, J., Yang, Q., Wang, J., Su, T. and Zhou, S. (2017) Gossypol has anti-cancer effects by dual-targeting MDM2 and VEGF in human breast cancer. Breast Cancer Res. **19**, 27
238 Polsky, B., Segal, S. J., Baron, P. A., Gold, J. W., Ueno, H. and Armstrong, D. (1989) Inactivation of human immunodeficiency virus in vitro by gossypol. Contraception. **39**, 579-587
239 Burkett, B. N., Thomason, J. M., Hurdle, H. M., Wills, R. W. and Fontenot, R. L. (2016) Effects of Firocoxib, Flunixin Meglumine, and Phenylbutazone on Platelet Function and Thromboxane Synthesis in Healthy Horses. Vet Surg. **45**, 1087-1094
240 Kleinhenz, M. D., Van Engen, N. K., Gorden, P. J., KuKanich, B., Rajewski, S. M., Walsh, P. and Coetzee, J. F. (2016) The pharmacokinetics of transdermal flunixin meglumine in Holstein calves. J Vet Pharmacol Ther. **39**, 612-615
241 Newby, N. C., Leslie, K. E., Dingwell, H. D., Kelton, D. F., Weary, D. M., Neuder, L., Millman, S. T. and Duffield, T. F. (2017) The effects of periparturient administration of flunixin meglumine on the health and production of dairy cattle. J Dairy Sci. **100**, 582-587
242 Seidel, M., Alderwick, L. J., Sahm, H., Besra, G. S. and Eggeling, L. (2007) Topology and mutational analysis of the single Emb arabinofuranosyltransferase of Corynebacterium glutamicum as a model of Emb proteins of Mycobacterium tuberculosis. Glycobiology. **17**, 210-219
243 Stermitz, F. R., Lorenz, P., Tawara, J. N., Zenewicz, L. A. and Lewis, K. (2000) Synergy in a medicinal plant: antimicrobial action of berberine potentiated by 5'-methoxyhydnocarpin, a multidrug pump inhibitor. Proc Natl Acad Sci U S A. **97**, 1433-1437
244 Ladbury, J. E., Klebe, G. and Freire, E. (2010) Adding calorimetric data to decision making in lead discovery: a hot tip. Nat Rev Drug Discov. **9**, 23-27
245 Rodrigues, L., Parish, T., Balganesh, M. and Ainsa, J. A. (2017) Antituberculosis drugs: reducing efflux=increasing activity. Drug Discov Today
246 Xu, D. and Zhang, Y. (2013) Toward optimal fragment generations for ab initio protein structure assembly. Proteins. **81**, 229-239
247 Chan, C. Y., Prudom, C., Raines, S. M., Charkhzarrin, S., Melman, S. D., De Haro, L. P., Allen, C., Lee, S. A., Sklar, L. A. and Parra, K. J. (2012) Inhibitors of V-ATPase proton transport reveal uncoupling functions of tether linking cytosolic and membrane domains of V0 subunit a (Vph1p). J Biol Chem. **287**, 10236-10250
248 Zhu, X., Gao, J. J., Landao-Bassonga, E., Pavlos, N. J., Qin, A., Steer, J. H., Zheng, M. H., Dong, Y. and Cheng, T. S. (2016) Thonzonium bromide inhibits RANKL-induced osteoclast formation and bone resorption in vitro and prevents LPS-induced bone loss in vivo. Biochem Pharmacol. **104**, 118-130
249 Weng, T. C., Yang, Y. H., Lin, S. J. and Tai, S. H. (2010) A systematic review and meta-analysis on the therapeutic equivalence of statins. J Clin Pharm Ther. **35**, 139-151

250 Shin, Y. H., Min, J. J., Lee, J. H., Kim, E. H., Kim, G. E., Kim, M. H., Lee, J. J. and Ahn, H. J. (2016) The effect of fluvastatin on cardiac fibrosis and angiotensin-converting enzyme-2 expression in glucose-controlled diabetic rat hearts. Heart Vessels
251 Bader, T., Fazili, J., Madhoun, M., Aston, C., Hughes, D., Rizvi, S., Seres, K. and Hasan, M. (2008) Fluvastatin inhibits hepatitis C replication in humans. Am J Gastroenterol. **103**, 1383-1389
252 Dallegri, F., Bertolotto, M. and Ottonello, L. (2005) A review of the emerging profile of the anti-inflammatory drug oxaprozin. Expert Opin Pharmacother. **6**, 777-785
253 Kara, I. M., Polat, S., Inci, M. F., Ince, F. and Gümüş, C. (2010) Analgesic and anti-inflammatory effects of oxaprozin and naproxen sodium after removal of impacted lower third molars: a randomized, double-blind, placebo-controlled crossover study. J Oral Maxillofac Surg. **68**, 1018-1024
254 Montecucco, F., Bertolotto, M., Ottonello, L., Quercioli, A., Mach, F. and Dallegri, F. (2009) Oxaprozin-induced apoptosis on CD40 ligand-treated human primary monocytes is associated with the modulation of defined intracellular pathways. J Biomed Biotechnol. **2009**, 478785
255 Lewis, K. (2013) Platforms for antibiotic discovery. Nat Rev Drug Discov. **12**, 371-387
256 Conly, J. and Johnston, B. (2005) Where are all the new antibiotics? The new antibiotics paradox. Canadian Journal of Infectious Diseases and Medical Microbiology. **16**, 159-160

Abbreviations

3D	Three-dimensional
α	Cooperativity constant
Å	Angstrom
Abs	Absorbance
ADP	Adenosine 5´-diphosphate
AMP	Adenosine 5'-monophosphate
ANP	Adenine nucleotide (denotes for either ADP or ATP)
$^{app}k_{cat}$	Apparent catalytic constant
BCG	*Bacillus Calmette –Guérin*
BSA	Bovine Serum Albumin
BS_3	bis(sulfosuccinimidyl)suberate
*Ca*FADS	FAD synthetase from *Corynebacterium ammoniagenes*
cal	Calorie
CD	Circular Dichroism
CPK	Corey, Pauling, Koltun, colors code for atoms
CSB	Chicago Sky Blue
CTP	Cytosine 5'-triphosphate
Δ	Increment / deletion
DEAE	Diethylaminoethyl
DMSO	Dimethylsulfoxide
DNA	Deoxyribonucleic acid
O.D.	Optical density
DTT	Dithiothreitol
ε	Molar extinction coefficient
EC	Enzyme commission
EDTA	Ethylenediaminetetraacetic acid
EMA	European Medicines Agency
$E_{ox/sq}$	Redox potential for the oxidized and the semiquinone species
Eqn	Equation
$E_{sq/hq}$	Redox potential for the semiquinone and the reduced species
et. al.	*Et alia* (and collaborators)
FAD	Flavin adenine dinucleotide
FADasa	FAD hydrolase
FADpp	FAD pyrophosphorilase
FADS	FAD Synthetase
FDA	Food and Drug Administration
FHy	FMN hydrolase
Fig	Figure
FLV	Flavins (denotes for either RF or FMN)
FMN	Flavin mononucleotide / Riboflavin 5'-monophosphate
FMNAT	FMN adenylyltransferase
FPLC	Fast Protein Liquid Chromatography
G	Gibbs free energy
GST	Glutathione transferase
GTP	Guanosin 5'-triphosphate

H	Enthalpy
HPLC	High Performance Liquid Chromatography
*Hs*RFK	Riboflavin kinase from *Homo sapiens*
HSS	High Strength Silica
IPTG	Isopropyl β-D-1-thiogalactopyranoside
ITC	Isothermal Titration Calorimetry
K_a	Association constant
$K_a^{app, ANP}$	Apparent association constant for ANP ligands
K_d	Dissociation constant
kDa	kDalton
K_m	Michaelis-Menten constant
k_{cat}	Catalytic constant
K_i	Inhibition constant
λ	Wavelength
LB	Lysogeny-Broth
*Lm1*FADS	Type I-FAD synthetase from *Listeria monocytogenes*
*Lm2*FADS	Type II-FAD synthetase from *Listeria monocytogenes*
Mt	*Mycobacterium tuberculosis*
*Mt*FADS	FAD synthetase from *Mycobacterium tuberculosis*
MRE	Molar residue ellipticity
MW	Molecular weight
N	Stoichiometry for an interaction
N-PAGE	Native-Polyacrylamide gel electrophoresis
O.N	Over night
PAIN	Pan-assay Interference Compound
PDB	Protein Data Bank
pH	Potential of Hydrogen
PIPES	1,4-Piperazine diethane sulfonic acid
PMSF	Phenylmethylsulfonyl Fluoride
PP_i	Pyrophosphate
RF	Riboflavin
RFK	Riboflavin kinase
r.m.s.d.	Root Mean Square Deviation
r.p.m	Revolutions per minute
S	Entropy
SB	Sample buffer
SDS	Sodium Dodecyl Sulphate
SDS-PAGE	Denaturing electrophoresis with SDS
*Spn*FADS	FAD Synthetase from *Streptococcus pneumoniae*
*Sp*RFK	Riboflavin kinase from *Schizosaccharomyces pombe*
TB	Tuberculosis
θ	Ellipticity
$[\theta]_{mr}$	Molar ellipticity per residue
TLC	Thin Layer Chromatography
T_m	Melting Temperature
*Tm*FADS	FAD Synthetase from *Thermotoga maritima*
Tris	Tris(hydroxymethyl)aminomethane
UV	Ultraviolet
UV-vis	Ultraviolet-visible
V_{max}	Maximum reaction velocity

WT	Wild Type

Name of the mutants: the mutants were named as R_1nR_2, where R_1 is the residue of the WT protein, n is the position of the substituted residue in the protein sequence, and R_2 is the residue that replace R_1 in the mutant protein.